X-ray Study of the Virgo Cluster of Galaxies with ASCA

Hironori Matsumoto

Department of Physics, Kyoto University, Sakyo-ku, Kyoto, Japan 606-8502

Abstract

We present the ASCA results of spatially resolved X-ray spectra in the central regions of the Virgo cluster, near to the central elliptical galaxy M87. We also present the results of the mapping observations of the northwest region of the Virgo cluster. Since the spectra of the M87 regions are complex, an adequate fit requires at least two thin thermal-plasma components. The temperatures of the hot and cool components are approximately 2.9 and 1.3 keV, respectively, and the temperatures of these components are both nearly constant over the central $10'$ radius from the center of M87. However, the flux of the cool component is more concentrated toward the center than that of the hot component. Furthermore the surface brightness profile of the hot component can be extrapolated smoothly to that of the intracluster medium (ICM) beyond $40'$ from the center. These suggest that the cool component of M87 can be attributed to the interstellar matter of M87, while the hot component is the ICM of the Virgo main body. The abundances of Fe, Si, and S rise towards the center of M87, although the ratios of Si/Fe and S/Si remain constant. We also found, contrary to the Einstein results, that the abundance ratio of oxygen to iron (O/Fe) is smaller than the solar value. These strongly constrain the chemical evolution scenario. The X-ray spectra of the ICM at regions beyond $40'$ from the center of M87 can be represented by a single-temperature plasma. The temperature of the ICM decreases with radius from $0'$ to $50'$, and it becomes almost constant beyond the $50'$ radius. The metal abundances also decrease with radius from $0'$ to $50'$, then become constant beyond the radius of $50'$. These temperature and abundance profiles can be clues to investigate the cluster formation history and cosmological parameters.

Contents

List of Figures

List of Tables

Chapter 1

Introduction

The intergalactic space of a cluster of galaxies is filled with a hot ($\sim$ 1 – 10 keV) and tenuous ($\sim 1\times10^{-3}$ cm^{-3}) plasma, which is called the intracluster medium (ICM). The mass of the ICM is equal to or greater than that in the stellar component of the member galaxies. Therefore, the ICM plays an essential role for the structure and evolution of clusters of galaxies as well as those of member galaxies.

Major fraction of the total gravitating mass of a cluster of galaxies is attributed to the dark matter, which cannot be observed at any wavelength. However, since the ICM is thought to be bounded in the gravitational potential of the cluster, one can estimate the mass and distribution of the dark matter using the spatial distributions of density and temperature of the ICM.

The Big Bang synthesized only hydrogen and helium nuclei. However, heavy elements such as C, N, O, Ne, Mg, Si, S, Ar, Ca, Fe, Ni, and so on, which are called metals in astrophysics, are rich in the present universe. One of the major subjects of astrophysics is to investigate how and when metals have been enriched in the universe. The ICM contains a huge amount of heavy elements, hence materials processed through stars contaminate the ICM, because heavy elements can only be produced by thermonuclear reactions in stars and supernovae. Conversely, chemical evolution of the universe can be traced by measuring the spatial distribution of abundances of heavy elements in the ICM.

The physical conditions of the ICM are, consequently, largely related to the nature of the dynamical and chemical evolution and the dark-matter distributions of clusters, and are predominantly investigated using the X-ray band.

The ASCA satellite (Tanaka et al. 1994 [147]) has good energy resolution over the wide energy band of 0.4 – 10 keV, which has not been available with previous satellites. Since Virgo

is the nearest cluster which lies only $\sim$ 15 Mpc away from us, spatially resolved spectroscopy is possible even with the moderate spatial resolution of ASCA.

Furthermore, the high flux of Virgo provides the best quality X-ray data at present. In particular, measurement of the spatial distribution of oxygen is realistic only in the Virgo cluster. Since the O/Fe ratio is a key for the chemical evolution, X-ray observation of the Virgo cluster with ASCA is essential.

Since the Virgo cluster is not relaxed yet (Binggeli et al. 1987 [13]), X-ray is the unique tool to trace the distribution of the gravitating mass. For example, comparison of the distribution of the gravitating mass with that of the member galaxies may give important information on the formation of member galaxies and the evolution of clusters in the huge gravitating mass.

The origin of metals in the ICM is considered to be early-type galaxies (ellipticals and S0 galaxies), because the iron mass in the ICM is proportional to the total optical luminosity from early-type galaxy members (Arnaud et al. 1992 [5]). However, how to synthesize and transfer such a large amount of iron into the ICM is still debatable question. The Virgo cluster has the central dominant elliptical galaxy, M87. Because we can spatially resolve M87 with ASCA, we can study the metal distribution from the center of M87 to outer regions of the Virgo cluster, which tells us how much metals were made in M87 and how they diffused out from M87 to the vast intracluster space.

Luminous early-type galaxies have generally X-ray emitting hot interstellar medium (ISM) (e.g. Forman, Jones and Tucker (1985) [48]). Since the hot ISM is dense and cool compared with the ICM, the hot ISM should be affected by the surrounding ICM. However, observational evidence for the interaction between the ISM and ICM is sparse. Since ASCA can resolve the ISM of M87 and the ICM of the Virgo simultaneously, the question how the ISM and ICM interact with each other would be largely addressed.

With ASCA, we performed pointing observations at M87 in 1993, and proceeded mapping observations near the northwest regions of the Virgo cluster in 1996 and 1997. In this thesis, we present detailed analyses of the ASCA data in the $10'$ circle centered at M87, and those from the mapping observations of the Virgo cluster. Then we discuss the spatial distribution of the temperature and chemical abundances of the ICM.

We assume the distance of M87 to be 15 Mpc, hence $1'$ angular size corresponds to 4.4 kpc (see chapter 4). Furthermore, we assumed that $H_0 = 50$ km/s/Mpc and $q_0 = 0.5$ throughout this thesis.

Chapter 2

Review of Clusters of Galaxies

2.1 Overview of Clusters of Galaxies

Clusters of galaxies are gravitationally bound systems comprising tens to thousands of galaxies. They are among the largest known hierarchy in the universe, with typical dimensions of roughly 1 – 6 Mpc across.

Observations suggest that most galaxies belong to groups of various sizes. However, only 5 – 10 % of all galaxies in the universe reside in highly populated clusters or rich clusters. Thus, although very rich clusters of galaxies are spectacular objects, they are relatively rare systems.

Galaxy distribution in rich clusters is usually smooth and centrally peaked at the cluster center. On the other hand, poor clusters usually show asymmetric and poorly condensed galaxy distribution even at the center. The closest example of a very rich regular cluster is the Coma cluster which lies at a distance of $\sim$ 70 Mpc, while the Virgo cluster, which is the nearest cluster, is a typical example of a poor irregular cluster.

Clusters can also be classified according to the galaxy populations. In rich regular clusters, elliptical and S0 galaxies are dominated, with only a small fraction of spirals; the former comprise by far the majority in the central region, while the later usually located in the outer regions. In fact, among the brightest galaxies in the Coma cluster, 80 % may be ellipticals, and a few spirals are only found at the outer regions of the cluster. In contrast, galaxies in small groups, or field galaxies are mostly spirals. Irregular clusters have a mixture of different galaxy types. For example, more than half of the brightest member galaxies in the Virgo cluster are spirals.

At the central region, some clusters often harbor the largest known elliptical galaxy in the universe, called the cD galaxy. The characteristic of a cD galaxy is the presence of a largely

extended envelope of diffuse stellar light around the nucleus; it is, otherwise, a normal elliptical galaxy. In the visible light, cD galaxies are 10 – 100 time larger than normal galaxies in visible light, hence the total luminosity associated with cDs is extremely large. Since many cD galaxies have multiple nuclei, they would be created by merging of smaller galaxies.

In clusters, the member galaxies are moving under the control of the total gravity. Although three dimensional velocities can not be measured, we can estimate the line-of-sight velocity (the radial velocity, v_r) by measuring the redshift of the galaxy. Such measurements show that the member galaxies are all moving with different speeds about the cluster. It has been conventional to characterize this velocity distribution by the dispersion σ_r of radial velocities,

$$\sigma_r = \sqrt{\langle (v_r - \langle v_r \rangle)^2 \rangle}, \tag{2.1}$$

which is a measure of the typical speed with which the galaxies are moving relative to the cluster center. The typical value of a rich cluster is $\sim$ 1000 km/s. In many clusters, the velocity dispersion shows systematic decrease with increasing distance from the cluster center. This effect must necessarily occur if clusters are finite, bound systems. Then, the velocities of member galaxies at any point in the cluster cannot exceed the escape velocity at that position. Because the escape velocity decreases with increasing distance from the cluster center, the velocity dispersion must also decrease with increasing distance from the center.

The crossing time of member galaxies in the inner region of rich clusters is generally of the order of 10^9 yr (see Equation (2.21)), which is less than the age of the universe (the Hubble time, $\sim 10^{10}$ yr). Therefore clusters of galaxies can be well mixed within the Hubble time. Regular clusters, in particular, are well relaxed to dynamically equilibrium condition. On the other hand, irregular clusters are not relaxed systems, due possibly to the younger evolutional ages.

For simplicity, we consider circular Kepler motion of a test particle of mass m which is rotating around an object of mass of M (assuming $M \gg m$). For the velocity of the test particle v and the orbital radius r, the equation of motion is written as

$$m\frac{v^2}{r} = G\frac{Mm}{r^2}, \tag{2.2}$$

where G is the gravitational constant. Writing the kinematic and gravitational energies of the particle as $T = mv^2/2$ and $W = -GMm/r$, respectively, this equation is converted to

$$2T + W = 0. \tag{2.3}$$

Equation (2.3) is also derived from the virial theorem, which can be applied to even more complex cases in dynamical equilibrium. Assuming the clusters of galaxies to be in dynamical

equilibrium, we can determine the total gravitating mass using the virial theorem. In this case, for the total gravitating mass of the cluster M_{tot} and the characteristic size of the cluster R, we get from Eq.(2.3)

$$M_{tot} = \frac{\langle v^2 \rangle R}{G}. \tag{2.4}$$

Since $\langle v^2 \rangle = 3\sigma_r^2$, we have

$$M_{tot} = \frac{3R\sigma_r^2}{G} = 7.0 \times 10^{14} M_\odot \left[\frac{\sigma_r}{1000 \text{ km/sec}}\right]^2 \left[\frac{R}{1\text{Mpc}}\right]. \tag{2.5}$$

The visible mass is estimated by the optical luminosity integrated over the whole number of galaxies and is usually found to be less than 10 % of the virial gravitating mass. The X-ray emitting ICM also carries significant fraction of visible mass; often exceeds that of the optical. Total visible mass is still in the order of 10 % of the virial gravitating mass.

The lack of the mass is called the missing mass problem, which is one of the most important unsolved problems of the modern astrophysics. What implication can we get from the fact that about 90 % of the gravitating mass in clusters is invisible in any wave length? The invisible matter is called the dark matter, and many suggestions for the origin such as, faint low-mass stars or black holes, and rather speculative ideas invoking exotic particles predicted by elementary particle physics, have been proposed. However, at present, no convincing scenario for the origin or nature of the dark matter is still found.

2.2 X-ray Properties of Clusters of Galaxies

In this section, we summarize the X-ray properties of the clusters of galaxies. Since we focus particularly on the recent ASCA results, all the observational results given in this section are those made with ASCA, unless otherwise quoted.

2.2.1 Overview

The luminous material in clusters of galaxies is primarily composed of two components: (1) the visible galaxies; (2) the hot ($\sim 10^8$ K) and tenuous gas ($\sim 10^{-3}$ cm^{-3}) called the intracluster medium (ICM), which fills the whole region of the clusters of galaxies. Although X-rays from individual galaxies in a cluster are not negligible in some selected galaxies, the primary source of X-rays from clusters of galaxies is the hot ICM. The X-ray luminosity of clusters ranges from 10^{42} to 10^{45} erg/s. The temperatures of ICM are in the range of 2 – 10 keV, and are comparable

Table 2.1: Cluster morphology and dynamical evolution (Forman and Jones 1982).

	Non-x-ray-dominant galaxy (nXD)	X-ray-dominant galaxy (XD)
Irregular (less evolved)	Low $L_x \lesssim 10^{44}$ ergs/sec Cool gas $T_g = 1-4$ keV X-ray emission around many galaxies Irregular x-ray distribution High spiral fraction $>40\%$ Low central galaxy density Prototype: A1367	Low $L_x \lesssim 10^{44}$ ergs/sec Cool gas $T_g = 1-4$ keV Central galaxy x-ray halo Irregular x-ray distribution High spiral fraction $>40\%$ Low central galaxy density Prototype: Virgo/M87
Regular (more evolved)	High $L_x \gtrsim 10^{44}$ ergs/sec Hot gas $T_g \gtrsim 6$ keV No cooling flow Smooth x-ray distribution Low spiral fraction $\lesssim 20\%$ High central galaxy density Prototype: Coma (A1656)	High $L_x \gtrsim 3\times 10^{44}$ ergs/sec Hot gas $T_g \gtrsim 6$ keV Cooling flow onto central galaxy Compact, smooth x-ray distribution Low spiral fraction $\lesssim 20\%$ High central galaxy density Prototype: Perseus (A426)

to those estimated by the velocity dispersions of galaxies in the cluster (i.e. $\beta_{spec} \sim 1$; see section 2.3).

The ICM usually comprises the major fraction of the visible matter, with the mass equal to or greater than that in the stellar component of the galaxies. However, the visible galaxies and the X-ray emitting ICM occupy still a small fraction of the gravitation mass of clusters; the most part is the dark matter. Although the dark matter is not directly observable at any wavelength as literally, one can estimate the mass and distribution of the dark matter using the X-ray data.

2.2.2 Morphology

Using the results of the Einstein satellite, Forman and Jones (1982) [47] and Jones and Forman (1984) [77] proposed a cluster classification scheme, according to the X-ray morphology of a member galaxy, in which the X-ray morphology is related to the evolutionary state of the cluster determined by its optical properties. In their scheme, an X-ray cluster having a central dominant galaxy is called an XD cluster, while a cluster with no central dominant galaxy is called a nXD cluster. The clusters classified by this scheme is summarized in table 2.1. The Virgo cluster is a typical example of the XD and irregular (less evolved) cluster.

2.2.3 Gas Temperature

If the gas density in the central region of clusters is large enough, then the radiation cooling time scale is relatively short ($\sim 10^9$ yr), compared with the ages of clusters (possibly $\sim 10^{10}$ yr). The cooled gas is then expected to flow toward the cluster center, which is called the cooling flow (see section 2.3.4; a detailed review of the cooling flow can be seen in Fabian (1994) [39]).

Fukazawa (1997) [51] observed a large sample of XD clusters, and found that the XD clusters have at least two-temperature plasma components at the central region. Since the cool component can not be found in the outer region of the clusters, it is attributable to the central dominant galaxy, possibly due to the cooling flow. On the other hand, the hot component is likely to be the ICM of the clusters.

Markevitch et al. (1997) [95] analyzed spatially resolved X-ray spectra of 26 bright clusters, and found that most of them show a temperature gradient; it decreases with increasing radius. Honda et al. (1996) [69] found that the Coma cluster has significant temperature variation from region to region. This strongly suggests that the Coma cluster is not a dynamically relaxed system, although its optical appearance is quite smooth and rich in galaxies. Like these, temperature profile can be a clue to investigate the cluster formation history and cosmological parameters.

2.2.4 Metal Abundance

Emission lines from highly ionized irons and other heavy elements have been found in the energy spectra of the ICM. Since heavy elements can be produced only by thermonuclear reactions in stars and supernovae, the presence of the emission lines imply that material processed in stars, supernovae, and both largely contaminate the ICM. Good correlation of total iron mass to total light from member early-type galaxies suggests that the metals in the ICM are attributable to early-type galaxies in the past star burst activities (frequent supernovae). Galactic winds driven by the supernova (SN) would be a driving force to contaminate the ICM with the heavy elements (Arnaud et al. 1992 [5]; Tsuru 1993 [153]). The type Ia SNe, whose progenitors are old, medium mass stars, make mainly iron, while the type II SNe, which occur at the death of massive stars, make mainly the α elements (O, Ne, Mg, Si, and S) (figure 2.1). Since the ages of the medium mass stars are larger than the massive stars, SNe Ia may be more important for the chemical enrichment in relatively recent epochs, while SNe II would be more important in the early phase of evolution of clusters. Since the heavy elements originated from each galaxies would gradually diffuse out in the ICM, we can investigate the chemical evolution of

the universe by measuring the spatial distribution of each heavy elements. The abundance ratio of α element (especially oxygen) to iron is one of the most important parameters, because the origins are different with each other, as we already noted.

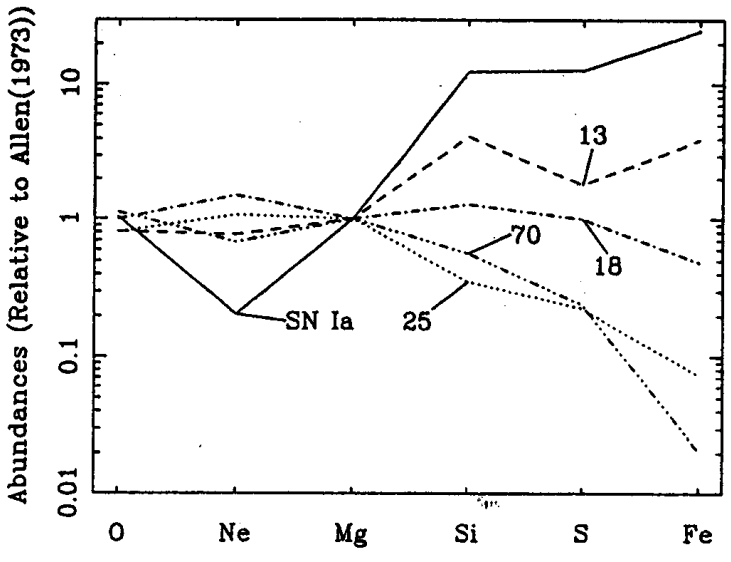

Figure 2.1: The predicted relative abundances of synthesized heavy elements (Tsujimoto et al. 1995). The ratios to the cosmic abundance of Allen (1973) are plotted for SN Ia and SN II of 13, 18, 25, and 70$M_{\odot}$ stars.

The iron abundances in rich clusters lie within rather narrow range (0.25 – 0.4 solar) (e.g. Edge and Stewart 1991 [35]; Yamashita 1992 [161]), in contrast of the wide abundance range found in poor clusters from 0.1 (NGC2300; Davis et al. 1996 [29]) to 1.0 solar (central region of Centaurus; Fukazawa et al. 1994 [49]). This suggests that rich clusters constitute a homogeneous system.

Mushotzky et al. (1996) [118] determined the abundances of O, Ne, Mg, Si, S, Ca, Ar, and Fe for 4 clusters of galaxies using the ASCA data, and found that the abundance ratio is similar to that of the SN II.

Some XD clusters such as the Centaurus (Fukazawa et al. 1994 [49]; Ikebe 1996 [71]), AWM7 (Ohashi et al. 1994 [120]; Xu et al. 1997 [159]; Ezawa et al. 1997 [38]), and Hydra-A clusters (Ikebe et al. 1997 [73]) are found to exhibit abundance gradient; the abundance increases towards the cluster centers. Fukazawa (1997) [51], using a larger sample of XD clusters, showed that the abundance increase is commonly found in the XD clusters. They therefore attributed the origin of metals to the dominant galaxies.

One exception is found in A1060 by Tamura et al. (1996) [146]; A1060 is an XD cluster, but shows no abundance gradient. This may be due to the different dynamical nature of the dominant galaxy, which is accompanied by another giant elliptical galaxy at the projected distance of 35 kpc; these are very likely to form a tight binary galaxy system.

Ezawa et al. (1997) [38] reported that the iron distribution of AWM7 well traces the galaxy

distribution. This discovery and the metal concentrations around dominant galaxies are the direct evidence that metals are ejected from member galaxies.

Fukazawa et al. (1998) [52] investigated the abundances of Si and Fe as a function of the ICM temperature. As is demonstrated in figure 2.2, the Fe abundance is almost constant to be 0.3 solar, while the Si abundance increases with the increasing ICM temperature. Si is considered to be mainly produced in SNe II, which occurred in the early galaxy formation phase, and is injected into the cluster space by the galactic winds. Since the temperature of ICM would be proportional to the depth of the gravitational potential of the cluster, high-velocity galactic wind containing Si can easily escape from clusters with shallow gravitational potential, or clusters of low temperature ICM (see Eqs. (2.33) and (2.37)). On the other hand, Fe would be more recently supplied by SNe Ia, when no violent galactic wind existed. Therefore the Fe ejection would be due to stripping by galaxy friction, hence slowly dissipated. Then the Fe abundance shows little dispersion around a constant value of 0.3 solar.

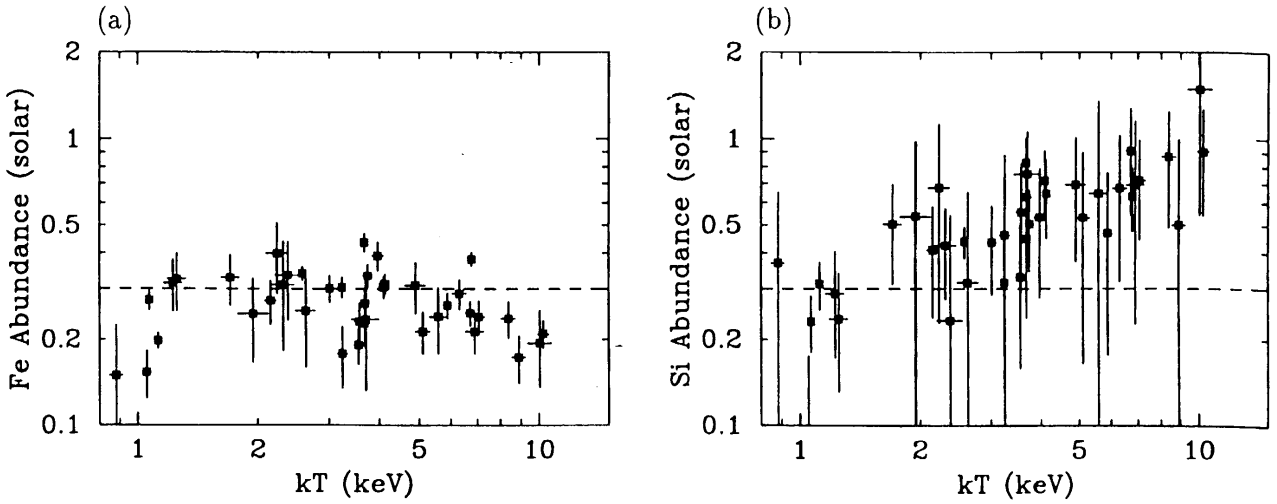

Figure 2.2: Spatially averaged metal abundances of clusters excluding central regions plotted against the ICM temperature for (a) Fe and (b) Si (Fukazawa et al. 1998).

2.2.5 Gravitational Potential

The observed X-ray surface brightness distribution can be converted to the density profile of the ICM. Assuming the hydrostatic equilibrium of the ICM, one can estimate the structure of the gravitational potential of the clusters of galaxies (see section 2.3).

Many XD clusters have been found to exhibit excess emissions at the central regions over the predicted X-ray surface brightness profile from the β model of (Eq. (2.40)), (Jones and

Forman 1984 [77]). This central excess was considered to be due to the cooling flow in the cluster core, because the flow is expected to make the gas density to be high at the central region of the cluster, hence the X-ray flux become higher than that given by a simple β model. The cooling flow predicts no central excess of the X-ray surface brightness in the high energy band (> 4 keV) even near the center. Ikebe et al. (1997) [73], however, analyzed the X-ray brightness profile of the cooling flow cluster, Hydra-A, and found central excess even in the high energy band. Almost identical structure is found from the Centaurus clusters (Ikebe 1996 [71]). These discoveries suggest that the central excess is not due to the dense cool gas, but is due to the structure of the gravitational potential of the cluster. The potential structure must have an additional central dimple associated with the central dominant galaxy, which suggests that the dark matter exhibits hierarchical structure like visible matters.

Another support was obtained by the observation of the Fornax cluster (Ikebe et al. 1996 [72]). The temperature of the ICM of the Fornax cluster is almost spatially constant at ~ 1 keV, indicating no cooling flow. Nevertheless, the surface brightness profile can not be fitted with a single-component β model, but can be fitted with a two-component β model. The angular sizes of the two components correspond to those of the central dominant galaxy NGC1399 and the whole region of the Fornax cluster. Thus they claimed the discovery of hierarchy structure in the gravitation potential (figure 2.3).

We should note, however, whether the central excess emission is due to the cooling flow or due to the hierarchy structure of the dark matter is still debatable. Although we certainly see the hierarchical structure of the dark matter in figure 2.3, we see no significant structure in the stellar distribution profile, in which hierarchy structure does exist. Since the β model is not a good approximation of the ICM distribution beyond 5 times the core radius (see section 2.3), the impressive shoulder-like structure of the dark matter distribution may or may not be an artificial structure due to the incomplete modeling.

2.2.6 Evolution of Clusters of Galaxies

The X-ray luminosity of cluster (L_X) is correlated with the temperature (T_g) as $L_X \propto T_g^3$ (Mushotzky 1984 [112]; Edge and Stewart 1991 [35]; Hatsukade [63]; David et al. 1993 [27]), although significant dispersion is found. This correlation is considered to be the evidence of cluster evolution (see section 2.3).

Since the X-ray emitting ICM comprise the major components of the visible matter of the clusters, to investigate evolution of X-ray properties of clusters is a key study of cosmology.

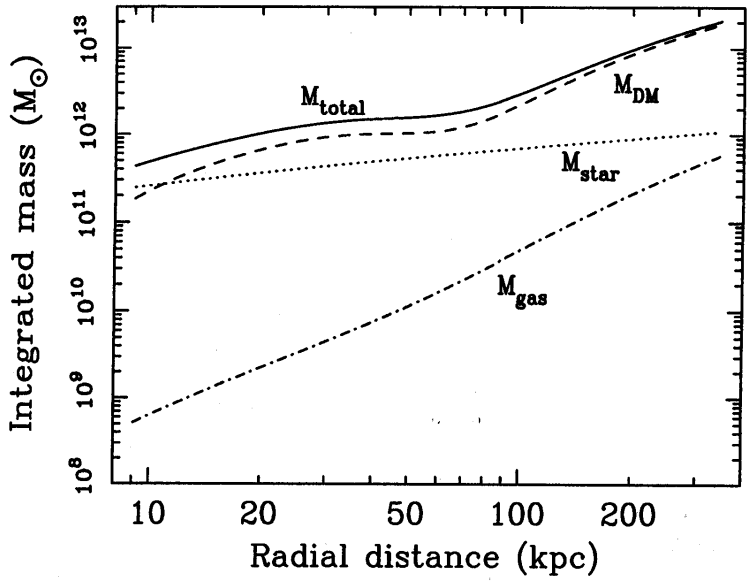

Figure 2.3: Distribution of various mass components in the Fornax cluster (Ikebe 1996).

The most important result in this field made with the Einstein satellite is the detection of the negative evolution of the X-ray luminosity function of luminous clusters at redshift lower than 0.6; the number density of clusters decreases as increasing redshift (Gioia et al. 1990 [56]; Henry et al. 1992 [67]). Following their pioneer works, many groups have investigated the evolution of X-ray luminosity function from various surveys with the ROSAT observatory (e.g. Castander et al. 1995 [24]; Collins et al. 1997 [26]; Romer et al. 1997 [126]; Ebeling et al. 1997 [34]; Scharf et al. 1997 [134]). Though Castander et al. (1995) [24] suggest the negative evolution, many others indicate no negative evolution at the redshift lower than 0.7. However, none of these ROSAT surveys cover an area large enough to probe the evolution of the luminous clusters. Therefore their results of no-evolution are not fully inconsistent with the Einstein results. Recently Vikhlinin et al. (1998) [157] present the first ROSAT analysis of the evolution of luminous ($L_X > 3\times10^{44}$ erg/s) distant clusters. They found that the number of the luminous clusters decreases significantly at z > 0.3, confirming the Einstein results. At lower luminosities ($L_X = (1-3)\times10^{44}$ erg/s), such evolution is not detected, which is also consistent with the previous ROSAT results.

Mushotzky and Loewenstein (1997) [116] found no evolution of metal abundance for clusters of z < 0.5. This strongly constrains high-Ω hierarchical theories in which clusters rapidly grow from z$\sim$0.3 to z$\sim$0. Furthermore, Mushotzky and Scharf (1997) [117] found no evidence for evolution in the $L_X - T_g$ relation below z $\sim$ 0.5. Similar results have been obtained by Tsuru et al. (1997a) [154] and Tsuru et al. (1997b) [155]. These results are consistent either with models in which the cluster core entropy is dominated by pre-heating, or low-Ω models in which cluster structure does not evolve strongly with time. Scharf and Mushotzky (1997) [133] found

a correlation between iron abundance and the relative deviation of a cluster from the mean $L_X - T_g$ relationship; clusters with higher iron abundances are more luminous than clusters of "normal" abundance, even if the temperatures are same. They argue that the observed results can be explained by tuning the cluster formation epochs within that expected by a hierarchical universe scenario. They suggest the oldest clusters were formed at $z \gtrsim 2$.

Hattori et al. (1997) [64] discovered an X-ray cluster, AXJ2019+1127 at z=1, which has been known as a gravitational lensing object. Although only two member galaxies has been found, this cluster contains as much iron as those in nearby clusters. Furthermore, Tsuru (1997b) [155] found that the iron mass of another high-z cluster MS1054-0321 at $z \sim 0.8$ is quite different from AXJ2019+1127. The gas masses of these two clusters and some other clusters with $z \sim 0.6$ are significantly lower than those of nearby clusters having the same gas temperature. These facts would be a hint of evolution of clusters of galaxies at the epoch around $z \sim 0.8 - 1.0$.

2.2.7 Hot ISM in Early-type galaxies

As already noted, metal abundances in the ICM should be closely related to that in the ISM of early-type galaxies. Furthermore, since the ISM is usually surrounded by the ICM, they must be interacting with each other. However due to the poor energy resolution of previous satellites before ASCA, critical parameters for investigating the nature of the ISM in early-type galaxies, such as the gas temperature, mass and metal abundance, have not been well constrained. Accordingly, several important issues, including relationship between the ISM and ICM on metal enrichment, and the effect of early-type galaxies on the ICM, are not well understood. For these studies, we will overview quickly on the ISM of the early-type galaxies.

The Einstein satellite discovered X-ray emitting hot ISM in luminous early-type galaxies (e.g. Forman, Jones, and Tucker 1985 [48]). This discovery forced us to revise the previous consensus that elliptical galaxies are gas-poor systems. Typical temperature and particle density of the ISM are ~ 1 keV and ~ 0.01 cm^{-3}, respectively.

Awaki et al. (1994) [7] observed three early-type galaxies with ASCA and found that the temperature and metal abundance of the hot ISM are about 0.8 keV and 0.4 solar, respectively. The inferred metal abundance is lower than expected from theoretical models (~ 5 solar) and lower than those determined at other wavelengths (e.g. stellar abundance determined with optical light is about 1 solar). Therefore, the ASCA observations are challenging against the current models for the evolution of galaxies. Matsushita et al. (1994) [99] analyzed ASCA data

of five early-type galaxies, including the sample of the three galaxies in Awaki et al. (1994) [7], and confirmed the conclusion of Awaki et al. (1994) [7]. Further "mystery" is the discovery of even lower metallicities (< 0.2 solar) in two other elliptical galaxies (Loewenstein et al. 1994 [89] and in the outer regions of NGC 4636 (Mushotzky et al. 1994 [115]).

Using larger sample of 12 early-type galaxies, Matsumoto et al. (1997) [98] confirmed that the metal abundances of the hot ISM are systematically lower than solar, with a mean value of about 0.3 solar. They found no systematic correlation between the X-ray properties and the galaxy environment, hence found no strong interaction between the ISM and ICM.

Recently Matsushita et al. (1997) [101] analyzed the ASCA data of deep pointing observations of NGC4636. They argued that the Fe abundance of 1 solar is possible by including the systematic error in the 0.4 – 1.6 keV band spectrum, the energy band which contains the serious problem of plasma coding of Fe L line complex (e.g. see chapter B). The 1 solar abundance of Fe is, however, still lower than the theoretical expectations. Furthermore, Matsushita et al. (1998) [102] found the double structure similar to figure 2.3 in the mass distribution around NGC4636, which suggests the presence of an optically dark galaxy group surrounding NGC4636.

2.3 Theoretical Backgrounds

In this section, we briefly summarize several physical processes which are closely related to X-rays from clusters of galaxies.

2.3.1 X-ray Emission from Thin Thermal Plasma

Because the ICM is low density ($\sim 10^{-3}$ cm^{-3}) and high temperature ($\sim 10^{8}$ K) plasma, it emits most of its energy into the X-ray band. We summarize some theoretical aspects to deduce physical condition of the ICM such as temperature, metallicity, density, and so on, using the X-ray spectral information from the ICM.

Electromagnetic radiation from thermal electrons in hot plasma are divided into three processes, based on their primarily transition processes;

1. free-free emission

   A free electron emits photons when it is scattered by the Coulomb field of an ion. This radiation is called bremsstrahlung, or free-free emission. This mechanism contributes to X-ray continuum emission.

2. free-bound emission

   Free-bound emission is accompanied by recombination of a free electron to a bound state of ion. Therefore this radiation is called recombination emission, too. This mechanism also contributes to continuum emission, but leave discontinuity at the transition edge energy.

3. bound-bound emission

   Radiation accompanied by transition of an electron bound to an atomic nucleus between different energy levels is called bound-bound emission. This is generally known as line emission. However, if two photons are emitted by one transition, which is called two-photon decay, this mechanism contributes to continuum emission.

The emissivity is defined as the emitted energy per unit time, frequency and volume. For the free-free and free-bound emissions, it is clear that the emissivities of these processes are proportional to a rate of collision of ions with electrons. Because the ICM is low density and high temperature, the coronal limit is usually assumed (e.g. Sarazin 1986 [129], p66). In this case, a rate of the bound-bound emission is determined by the number of excited ions, and thus

by a rate of collisional excitation. Therefore the emissivity of the bound-bound process also depends on the rate of collision of ions with electrons. Thus the total emissivity, $\frac{dL}{dVd\nu}$, where L is the X-ray luminosity, V is the volume, and ν is the frequency, can be expressed as

$$\frac{dL}{dVd\nu} = \sum_{X,i} \zeta_\nu(X^i, T_g) n(X^i) n_e, \tag{2.6}$$

where ζ_ν is the emission per ion at unit electron density, and T_g , n_e and $n(X^i)$ are, respectively, plasma temperature, number density of electron and the ion X^i (X is the element). The ionization degree τ is defined as $\tau = n_e \times \mathrm{T_{age}}$, where $\mathrm{T_{age}}$ is the plasma age in the unit of second. If $\tau \gtrsim 10^{12}$ sec cm^{-3}, the plasma is considered to be in collisional ionization equilibrium (Masai 1994 [96]). Since n_e and $\mathrm{T_{age}}$ of the ICM are typically 1×10^{-3} cm^{-3} and 10^{10} yr (3×10^{17} sec), respectively, the ICM is in collisional ionization equilibrium. Therefore, if $n(X)$ is the total density of the element X, the ionization fractions $f(X^i) \equiv n(X^i)/n(X)$ depend only on the temperature. Thus Eq. (2.6) becomes

$$\frac{dL}{dVd\nu} = n_p n_e \sum_{X,i} \frac{n(X)}{n(H)} [f(X^i, T_g)\zeta_\nu(X^i, T_g)] \tag{2.7}$$

$$\equiv n_p n_e \epsilon_\nu(T_g, A_1, A_2, ...), \tag{2.8}$$

where $n_p (= n(H))$ is the number density of protons and $A_X \equiv n(X)/n(H)$ is the abundance of the element X. $\epsilon_\nu(T_g, A_1, A_2, ...)$ is called the spectral emissivity. We define the emission integral EI as

$$EI \equiv \int n_e n_p dV. \tag{2.9}$$

Then the shape of the spectrum depends only on the abundance of each element and the distribution of temperatures $d(EI)/dT_g$.

We consider the simple case that the ICM is isothermal. The continuum emission at 10^8 K is mainly comes from the free-free emission (see figure 2.4). Furthermore, since hydrogen is the most common element, the continuum emission is mainly due to collisions of protons with electrons. Therefore we can deduce T_g and $\int n_e n_p dV$ from the continuum. Another way to deduce the temperature is to estimate flux ratio between two lines, each of which comes from the same element but from different ionization state, because the ratio reflects the ionization fraction $f(X)$, and $f(X)$ depends only on the temperature. Measuring the line flux, we can also deduce $\int n_e n_X dV$. Therefore we can estimate the abundance of the element X by combined information of $\int n_e n_p dV$ and $\int n_e n_X dV$.

Many authors calculated $\epsilon_\nu(T_g, A_1, A_2, ...)$ and they are often different from each other, especially around 1 keV ($\nu \sim 2.42\times10^{17}$ Hz). This is mainly due to the difference of the

treatment of the Fe L emission lines (Fabian et al. 1994 [40]; Fukazawa et al. 1996 [50]; Arimoto et al. 1997 [3]; Matsushita 1997 [100]; Matsushita et al. 1997 [101]). In this thesis, we use two spectral emissivities. One is the revised version of the Raymond-Smith model (Raymond and Smith, 1977 [122]) and the other is the Mewe-Kaastra-Liedahl model (Mewe, Gronenschild, and van den Oord 1985 [106]; Mewe, Lemen, and van den Oord 1986 [107]; Kaastra 1992 [78]; Liedahl, Osterheld, and Goldstein 1995 [86]; Arnaud and Rothenflug 1985 [4]). For example, the differences of these two models can be seen in figure B.1.

The bolometric emissivity $\Lambda(T_g, A_X)$, which is defined as

$$\Lambda(T_g, A_1, A_2, ...) \equiv \int \epsilon_\nu(T_g, A_1, A_2, ...) d\nu, \tag{2.10}$$

is called the cooling function. We show an example of $\Lambda(T_g, A_1, A_2, ...)$ calculated using the Raymond-Smith model and assuming the cosmic abundances of Allen (1973) [1] in figure 2.4 (Gehrels and Williams 1993 [55]). As can be seen from this figure, X-ray emission from a cluster of galaxies is dominated by the bremsstrahlung continuum; the line emissions contribute only small fraction. Therefore we can express the X-ray luminosity of a cluster of galaxies L approximately as

$$L \sim EI \times \Lambda^{ff} \propto n_e n_p V \sqrt{T_g}, \tag{2.11}$$

where Λ^{ff} is the cooling function on the part of the free-free emission which is proportional to $\sqrt{T_g}$ (e.g. Rybicki and Lightman 1979 [128]).

2.3.2 Mass Distribution

We summarize below some theoretical aspects to derive the ICM mass and total gravitating mass from X-ray data.

The King Model (Distribution of Gravitating Matter)

We discuss simple cases of spherically symmetric mass distribution of isothermal gravitating matter. We, hence, assume as follows;

1. Velocity distribution of particles of the gravitating matter is isotropic and independent of position.

2. The radial velocity distribution has a Gaussian profile, and the velocity dispersion is independent of position (i.e. isothermal).

3. The particle distribution is stationary.

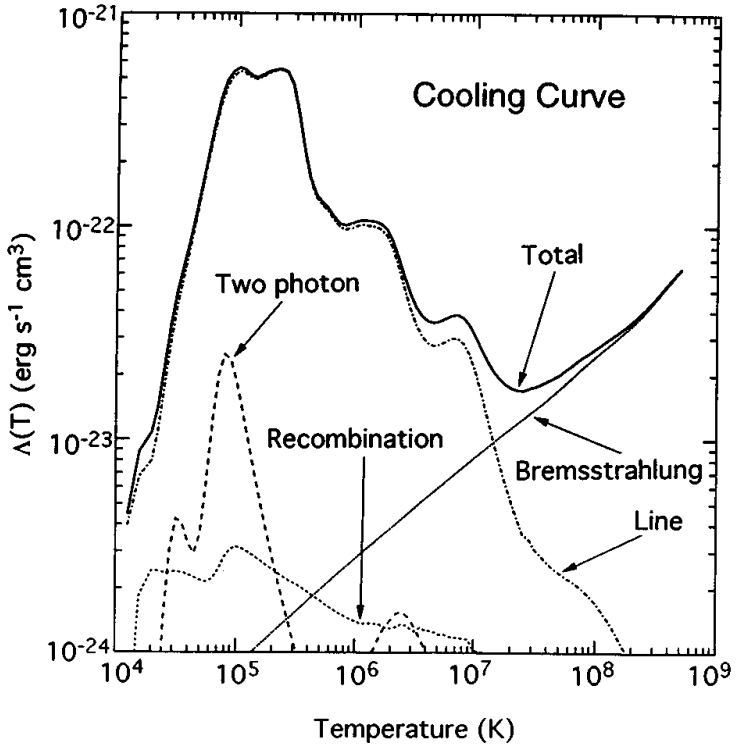

Figure 2.4: The temperature dependence of the cooling function and its components for an optically thin plasma of the cosmic abundance of Allen (1973) (Gehrels and Williams 1993).

4. Particle positions are uncorrelated.

Then we can write the particle phase-space density $f(\vec{r},\vec{v})$, as

$$f(\vec{r},\vec{v})d^3rd^3v = n(R) \times \frac{1}{(2\pi{\sigma_r}^2)^{3/2}} \exp\left[-\frac{1}{2}\left(\frac{v}{\sigma_r}\right)^2\right] d^3rd^3v, \tag{2.12}$$

where $\vec{r}$, $\vec{v}$ and σ_r are, respectively, position, velocity and the (radial) velocity dispersion, and $n(R)$ is the number density of particles at a (three-dimensional) radius of R.

If the gravitating particle is collisionless, the phase space density f is a function of only the integrals of the motion. Because we consider the velocity distribution is isotropic, the integral of the motion cannot be the orbital angular momentum of particles, and can only be the energy per unit mass ε, which can be expressed as

$$\varepsilon = \frac{v^2}{2} + \phi(R), \tag{2.13}$$

where $\phi(R)$ is the gravitational potential. In this case, we can express $n(R)$ as

$$n(R) = n_0 \exp\left[-\frac{\phi(R)}{\sigma_r^2}\right], \tag{2.14}$$

where n_0 is the central density. Poisson's equation for the gravitational potential is

$$\nabla\phi = 4\pi G m \int f(\vec{r},\vec{v})d^3v, \tag{2.15}$$

where m is the mass per particle and $G = 6.67\times10^{-8}$ dyne cm^2 g^{-2} is the gravitational constant. Substituting Eqs. (2.12) and (2.14) for Eq. (2.15), we get

$$\frac{1}{R^2}\frac{d}{dr}\left[R^2\frac{d\phi}{dR}\right] = 4\pi G\rho_0 \exp\left(-\frac{\phi}{\sigma_r^2}\right), \tag{2.16}$$

where $\rho_0 = n_0 m$. If we define the mass density distribution, $\rho(R)$, as

$$\rho(R) \equiv m\int f(\vec{r},\vec{v})d^3v \tag{2.17}$$

$$= \rho_0 \exp\left(-\frac{\phi}{\sigma_r^2}\right), \tag{2.18}$$

Eq. (2.16) becomes

$$\frac{d}{dR}\left(R^2\frac{d\ln\rho}{dR}\right) = -\frac{4\pi G R^2\rho}{\sigma_r^2}. \tag{2.19}$$

This differential equation has a solution of $\rho(R) = \dfrac{\sigma_r^2}{2\pi G R^2}$. However, we usually do not use this solution, because this function diverges at $R = 0$. The function of

$$\rho(R) = \rho_0\left[1+\left(\frac{R}{R_c}\right)\right]^{-\frac{3}{2}}, \qquad R_c \equiv \sqrt{\frac{9\sigma_r^2}{4\pi G\rho_o}} \tag{2.20}$$

was found to be a good approximation to the inner region of the numerical solution of Eq. (2.19) which is obtained with boundary conditions of $\rho(0) = \rho_0$ and $d\rho/dR = 0$ at $R = 0$. R_c is called the core radius. This function was first presented by King (1962) [81] to represent surface density distributions of globular clusters and is called the King approximation or King model. In figure 2.5, we show the numerical solution of Eq. (2.19) and the King model. As can be seen from this figure, the King model is not a good approximation beyond $R/R_c \sim 5$.

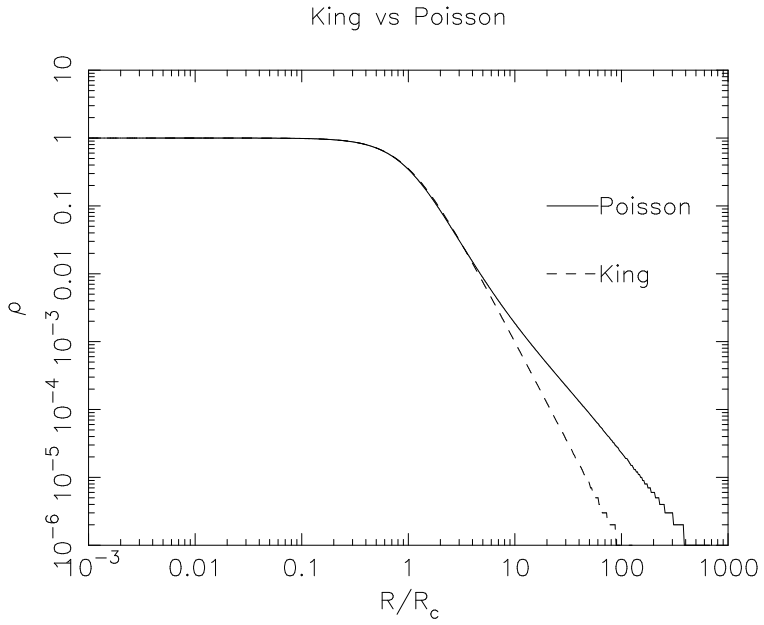

Figure 2.5: Numerical solution of Poisson's equation (solid line) and the King model (dashed line).

The crossing time of member galaxies $t_{cr}(R)$ can be expressed as

$$t_{cr}(R) = \frac{R}{\sigma_r} \sim 1{\times}10^9 \mathrm{yr} \left[\frac{R}{1\ \mathrm{Mpc}}\right] \left[\frac{\sigma_r}{1000\ \mathrm{km/sec}}\right]^{-1}. \tag{2.21}$$

The two body gravitational interaction time scale t_{gr} is estimated to be larger than $3{\times}10^{11}$ years (Sarazin 1986 [129], p20). Because $t_{cr} \ll t_{gr}$, the member galaxies can be considered to be a collisionless gas. Real distribution of member galaxies in a relaxed cluster can be fitted with the King model with $R_c \sim 250$ kpc.

The β Model (Distribution of the ICM)

The sound speed in plasma which consist of hydrogen, c_s, can be expressed as

$$c_s = \sqrt{\frac{2\gamma k T_g}{m_p}} = 1.7\times10^8 \mathrm{cm/s} \left[\frac{T_g}{10^8 \mathrm{K}}\right]^{\frac{1}{2}}, \tag{2.22}$$

where γ is the ratio of specific heats (Spitzer 1962 [139], p58), and k is Boltzmann's constant $= 1.38\times10^{-16}$ erg K^{-1}. Then the sound crossing time of the ICM, t_s, is given by

$$t_s \sim 5.8\times10^8 \text{ yr} \left[\frac{T_g}{10^8 \mathrm{K}}\right]^{-\frac{1}{2}} \left[\frac{D}{1 \text{ Mpc}}\right], \tag{2.23}$$

where D is the cluster diameter. The cooling time due to the free-free emission t_{cool} is

$$t_{cool} = 8.5\times10^{10} \text{ yr} \left[\frac{n_p}{10^{-3}\mathrm{cm}^{-3}}\right]^{-1} \left[\frac{T_g}{10^8 \mathrm{K}}\right]^{\frac{1}{2}}. \tag{2.24}$$

If we consider the heating of the ICM due to infall of the primordial gas into the cluster and compression, the heating time scale t_{heat} is equal to the free-fall time scale, and is given by

$$t_{heat} = 3.1\times10^9 \mathrm{yr} \left[\frac{D}{1 \text{ Mpc}}\right]^{\frac{3}{2}} \left[\frac{M}{10^{14} M_\odot}\right]^{-\frac{1}{2}}, \tag{2.25}$$

where M is the total mass of the cluster. Because t_s is less than the Hubble time ($\sim 10^{10}$ yr), t_{cool} and t_{heat}, the ICM can be considered to be hydrostatic:

$$\nabla P = -\rho_g \nabla \phi(R), \tag{2.26}$$

where P is the gas pressure and ρ_g is the gas mass density, which can be expressed as

$$\rho_g = n_e m_e + n_p m_p \equiv n_g \mu m_p, \tag{2.27}$$

where m_e and m_p are the masses of an electron and a proton, respectively, $n_g \equiv n_p + n_e$ is the gas number density, and μ is the mean molecular weight. We assume $\mu = 0.6$ in this thesis. Because of the low density and high temperature, the ICM can be treated as an ideal gas, and the equation of state is given by

$$P = n_g k T_g = \frac{\rho_g k T_g}{\mu m_p}. \tag{2.28}$$

Equation (2.26) reduces to

$$\frac{1}{\rho_g}\frac{dP}{dR} = -\frac{d\phi(R)}{dR} = -G\frac{M(<R)}{R^2}, \tag{2.29}$$

where $M(<R)$ is the total mass of the cluster within a radius R.

If we assume that the cluster gravitational potential is that of a self-gravitating isothermal sphere, we can use the King model as the mass density profile of the gravitating matter, approximately. Therefore the mass density, total cluster mass, and gravitational potential are given by

$$\rho(R) = \rho_0(1+x^2)^{-\frac{3}{2}} \tag{2.30}$$

$$M(<R) = 4\pi\rho_0 R_c^3 \left(\ln[x+\sqrt{1+x^2}] - \frac{x}{\sqrt{1+x^2}}\right) \tag{2.31}$$

$$\phi(R) = -4\pi G\rho_0 R_c^2 \frac{\ln[x+\sqrt{1+x^2}]}{x}, \tag{2.32}$$

where $x \equiv R/R_c$. Using Eq. (2.20),

$$\sigma_r^2 = \frac{4\pi G\rho_0 R_c^2}{9} = -\frac{\phi(0)}{9}. \tag{2.33}$$

Then we consider the situation that the ICM is bound in the gravitational potential given by equation (2.32). Substituting the equation of state (2.28) for Eq. (2.29), we get

$$\frac{d\ln\rho_g}{dR} = -\frac{\mu m_p}{kT_g}\frac{d\phi(R)}{dR}. \tag{2.34}$$

Integrating Eq. (2.34), we get

$$\rho_g(R) = \rho_{g0}\exp\left(-\frac{\mu m_p}{kT_g}[\phi(R)-\phi(0)]\right), \tag{2.35}$$

where ρ_{g0} is the central mass density of the ICM.

Substituting Eq. (2.32) for Eq. (2.35), $\rho_g(R)$ can be approximately expressed only at small radii ($R \lesssim 6R_c$) as

$$\rho_g(R) = \rho_{g0}\left[1+\left(\frac{R}{R_c}\right)^2\right]^{-\frac{3}{2}\beta} \tag{2.36}$$

$$\beta \equiv \frac{\mu m_p \sigma_r^2}{kT_g} = 0.73\left[\frac{\sigma_r}{1000\mathrm{km/s}}\right]^2\left[\frac{T_g}{10^8\mathrm{K}}\right]^{-1}. \tag{2.37}$$

β is the ratio of the kinematic energy of the gravitating matter per unit mass to the thermal energy of the ICM per unit mass. Equation (2.36) is called the β model. We show Eq. (2.35) and the beta model in figure 2.6. Note that the beta model is not a good approximation of Eq. (2.35) beyond $R \sim 6R_c$.

X-ray Surface Brightness Distribution

The X-ray surface brightness at a projected radius r is proportional to the emission measure, EM, defined as

$$EM \equiv \int n_e n_p dl, \tag{2.38}$$

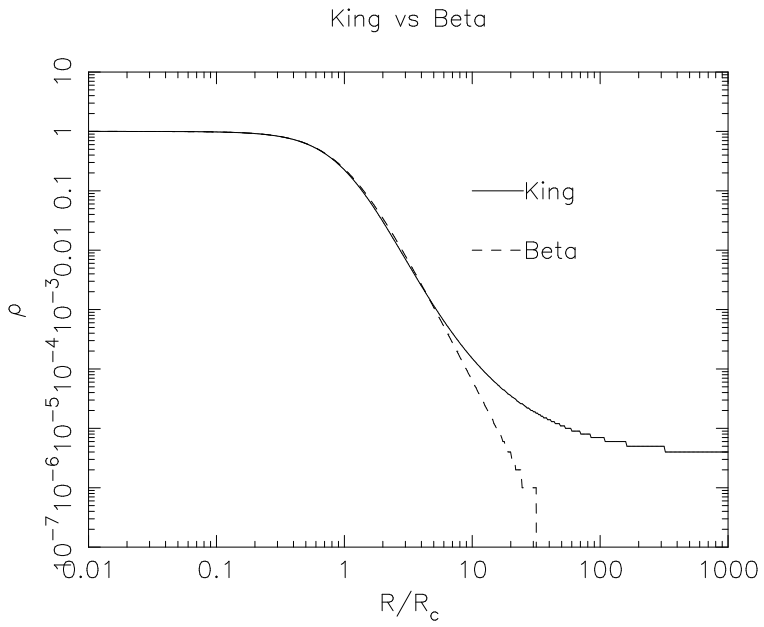

Figure 2.6: Distribution of the ICM.
Solid line shows Eq. (2.35), while dashed line shows the β model.

where l is the distance along the line-of-sight through the cluster at a projected radius r. If we use the β model as the distribution of the ICM, the emission measure is,

$$EM = \sqrt{\pi}\left(\frac{n_{e0}}{n_{p0}}\right) n_{p0}^2 R_c \frac{\Gamma(3\beta - 1/2)}{\Gamma(3\beta)}\left[1 + \left(\frac{r}{R_c}\right)^2\right]^{-3\beta+\frac{1}{2}} \qquad (\beta > \frac{1}{6}), \tag{2.39}$$

where Γ is the gamma function and n_{p0} and n_{e0} are the central number densities of protons and electrons. Therefore the X-ray surface brightness $S(r)$ can be expressed as

$$S(r) = S_0\left[1 + \left(\frac{r}{R_c}\right)^2\right]^{-3\beta+\frac{1}{2}}, \tag{2.40}$$

where S_0 is the central surface brightness density. The average value of β determined by fits to the X-ray surface brightness of a large number of clusters was found to be

$$\beta_{fit} \sim 0.65 \tag{2.41}$$

(Jones and Forman 1984 [77]).

Another way to estimate β is to use Eq. (2.37) assuming the distribution of the member galaxies ρ_{gal} is proportional to that of the gravitating matter, which means

$$\rho_g \propto \rho_{gal}^{\beta}. \tag{2.42}$$

In this case, the velocity dispersion of the member galaxies can be considered to be the same as that of the gravitating matter. Substituting the velocity dispersion of the galaxies and the gas temperature deduced from the X-ray spectrum for Eq. (2.37), the average value of β is

$$\beta_{spec} \sim 1.2 \sim 2 \times \beta_{fit} \tag{2.43}$$

(Sarazin 1986 [129]). This discrepancy between β_{spec} and β_{fit} is called the β problem. Many suggestions have been made as to the origin of this discrepancy (e.g. Kent and Sargent 1983 [79]; Mushotzky 1984 [112]; Henriksen and Mushotzky 1985 [66]; Bahcall and Lubin 1994 [9]). For example, this discrepancy may suggest that the velocity dispersion of the galaxies are not the same as that of the gravitating matter (Metzler and Evrard [104]).

It is important to note that both the King and β models are not good approximations beyond five times the core radius (figures 2.5 and 2.6). Therefore we have to pay attention to adopt the β profile to the whole region of the cluster.

Total Gravitating Mass

From Eq. (2.29), the total gravitating matter within a radius R can be expressed as

$$\begin{aligned} M(<R) &= -\frac{kT_g R^2}{\mu m_p G}\frac{d\ln(n_g T_g)}{dR} \\ &= -\frac{kT_g R}{\mu m_p G}\left(\frac{d\ln T_g}{d\ln R} + \frac{d\ln n_g}{d\ln R}\right). \end{aligned} \tag{2.44}$$

Therefore measurements of the gas density distribution and the temperature distribution are the key to estimate the mass of the total gravitating matter.

2.3.3 Simple Model for Cluster Evolution

We consider two simple models for evolution of the clusters of galaxies: (a) spherical clusters contract fixing the mass of gas and dark matter to be constant. (b) gas and dark matter come into a cluster of a fixed radius R. The schematic view of them are shown in figure 2.7. In both cases, we assume that the gas mass is proportional to the total mass of the cluster M.

In these cases, since $T_g \propto GM/R$, $V \propto R^3$, and $n_p \sim n_e \propto M/R^3$, Eq. (2.11) reduces to

$$L \propto \left(\frac{M}{R^3}\right)^2 R^3 \left(\frac{M}{R}\right)^{\frac{1}{2}} = M^{\frac{5}{2}} R^{-\frac{7}{2}}. \tag{2.45}$$

For the case of (a), eliminating R from Eq. (2.45), we get

$$L \propto T_g^{3.5}. \tag{2.46}$$

For the case of (b), eliminating M from Eq. (2.45), we get

$$L \propto T_g^{2.5}. \tag{2.47}$$

The real evolution is probably the intermediate between (a) and (b). Therefore the relation of $L \propto T_g^{\alpha}$ with $\alpha \sim 3$ is expected. Though our model is too simple, this expected value is consistent with the observation. Therefore the observed relation of $L \propto T_g^3$ can be considered to be the evidence of the evolution of clusters of galaxies.

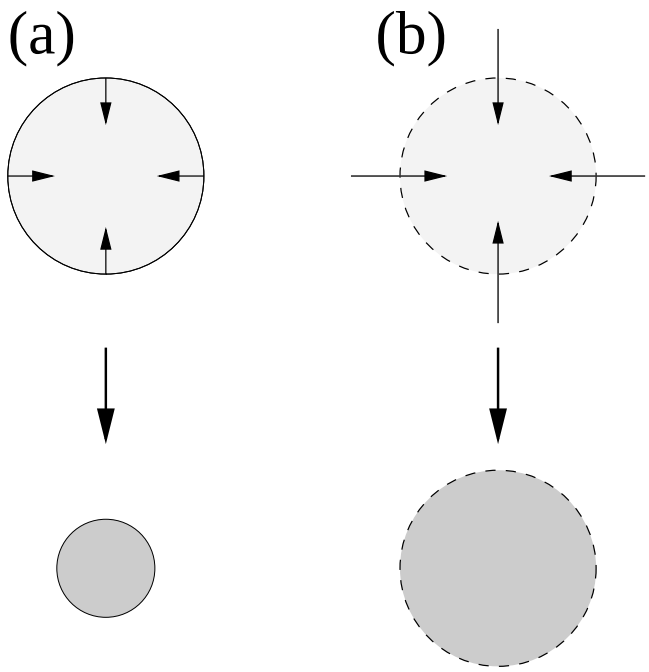

Figure 2.7: Schematic view of the simple models for the cluster evolution. (a) the total mass of the cluster is fixed. (b) the radius of the cluster is fixed.

2.3.4 Cooling Flow Model

The cooling time of the ICM is sometimes shorter than the Hubble time at the center of the cluster, where the density of the ICM is dense enough. Then the ICM loses energy by emission and falls into the center of the cluster. This is called the cooling flow. In this section, we summarize the constant pressure cooling flow model.

We assume the spherical symmetry and a steady state flow. If the flow speed v is much slower than the sound speed of the ICM, the ICM is approximately in the hydrostatic equilibrium. For the mass accretion rate $\dot{M}$, the mass conservation law is written as

$$\dot{M} = 4\pi R^2 \rho_g v. \tag{2.48}$$

The hydrostatic equilibrium can be written as

$$\frac{dP}{dR} = -\rho_g \frac{d\phi}{dR}. \tag{2.49}$$

The energy conservation law (the Bernoulli theorem) is

$$\rho_g v \frac{d}{dR}\left(\frac{v^2}{2}+\frac{P}{\rho_g}+\frac{3}{2}\frac{kT_g}{\mu m_p}+\phi\right) = n_e n_p \Lambda(T_g, A_1, A_2, ...). \tag{2.50}$$

Because the flow speed v is much slower than the sound speed of the ICM ($\sim \sqrt{P/\rho_g}$), we neglect the term of $v^2/2$ in Eq. (2.50). Furthermore, we assume the constant pressure of the ICM. Then, we get from Eq. (2.49)

$$\frac{d\phi}{dR} = 0. \tag{2.51}$$

Therefore, using Eq. (2.48), Eq. (2.50) becomes

$$\frac{\dot{M}}{4\pi R^2}\frac{5k}{2\mu m_p}\frac{dT_g}{dR} = n_e n_p \Lambda(T_g, A_1, A_2, ...). \tag{2.52}$$

The ICM between R and $R+dR$, which has the temperature in the range T_g to $T_g + dT_g$, emit the total luminosity dL_{cool}:

$$dL_{cool} = n_e n_p \Lambda(T_g, A_1, A_2, ...) \times 4\pi R^2 dR \tag{2.53}$$

$$= \frac{5}{2}\frac{\dot{M}k}{\mu m_p} dT_g. \tag{2.54}$$

The luminosity per unit frequency of the ICM can be written as

$$d\left(\frac{dL_{cool}}{d\nu}\right) = n_e n_p \epsilon_\nu(T_g, A_1, A_2, ...) \times 4\pi R^2 dR \tag{2.55}$$

$$= \frac{5}{2}\frac{\dot{M}k\epsilon_\nu}{\mu m_p \Lambda} dT_g. \tag{2.56}$$

Therefore the bolometric luminosity emitted from the whole cooling flow region can be written as

$$L_{cool} = \frac{5}{2}\frac{\dot{M}}{\mu m_p} k(T_{max} - T_{min}), \tag{2.57}$$

and the cooling spectrum can be expressed as

$$\frac{dL_{cool}}{d\nu} = \frac{5}{2}\frac{\dot{M}k}{\mu m_p}\int_{T_{min}}^{T_{max}} \frac{\epsilon_\nu}{\Lambda} dT_g, \tag{2.58}$$

where T_{max} is the temperature from which the ICM cools down, and T_{min} is the temperature to which the ICM cools.

Chapter 3

Review of M87

3.1 Overview

M87 (NGC4486), which is associated with the radio source Virgo A, is a giant elliptical galaxy at the center of the Virgo cluster (figure 3.1). Its position is $(\alpha,\ \delta)_{J2000}$ = (12h30m49.7s, 12d23m24s), and its B magnitude, B_0^T, is 9.47 mag (de Vaucouleurs et al., 1991 [31]), which corresponds to $\log(L_B/L_\odot) = 10.73$ assuming the distance of 15 Mpc. Though it has fairly extended optical emission (de Vaucouleurs and Nieto 1978 [30]), it is not classified as a cD galaxy (Schombert 1986 [135]).

M87 is the first galaxy from which a jet was discovered. The jet can be seen both in the optical and radio bands (figure 3.2 (a) and (b)). Optical jet galaxies like M87 are rather rare. Most of the jets have been found only in the radio band. The jet shown here is about 3 kpc long emanating from a source in the core of M87. Complex substructure can be seen in the jet, as well as a sudden transition from well-collimated to more disordered flow. The mechanism of the optical and radio emissions of the jet is considered to be a synchrotron radiation due to high speed electrons in a magnetic field. This jet is located inside the envelope of a large radio halo (figure 3.3).

M87 is the first object which was identified to be an extragalactic X-ray source (Byram, Chubb, and Friedman 1966 [21]; Bradt et al. 1967 [19]). In the following section, we summarize the X-ray properties of M87, focusing particularly on the results of the Einstein and ROSAT satellites.

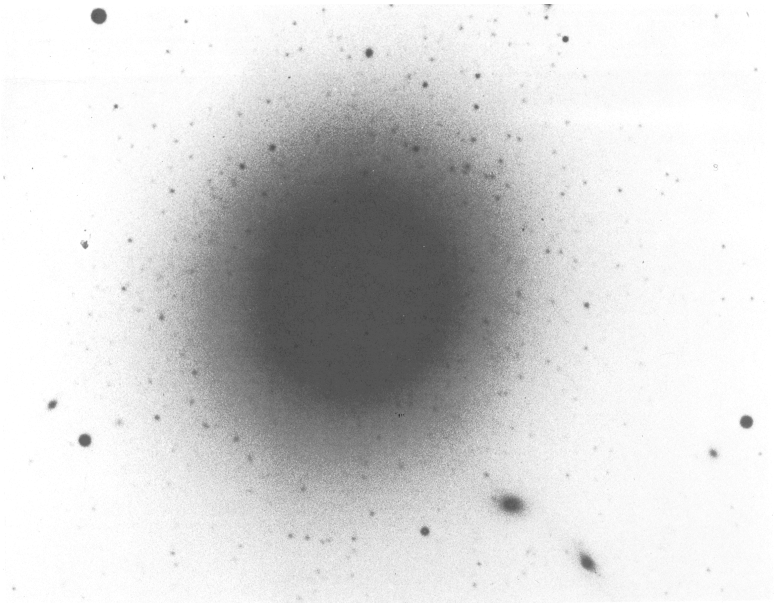

Figure 3.1: Giant elliptical galaxy M87. Several globular clusters can be seen in this photograph, appearing as small fuzzy points surrounding the core of M87 (Audouze and Israël 1994).

(a) (b)

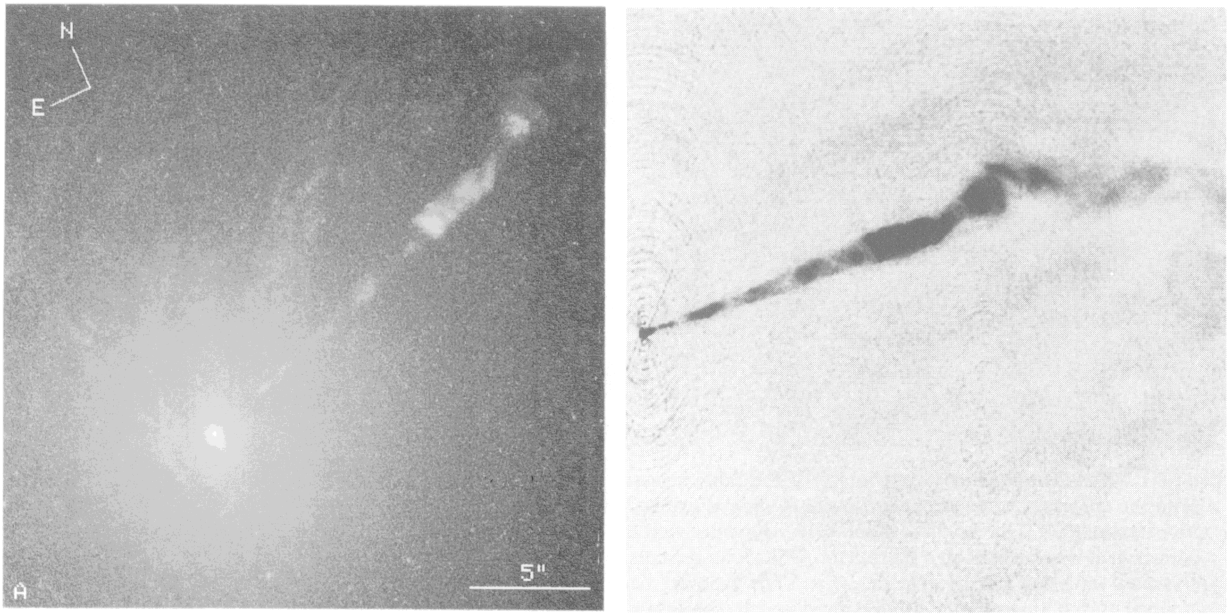

Figure 3.2: (a) HST image of M87 (Ford et al. 1994). (b) VLA image of M87 (Eilek 1992).

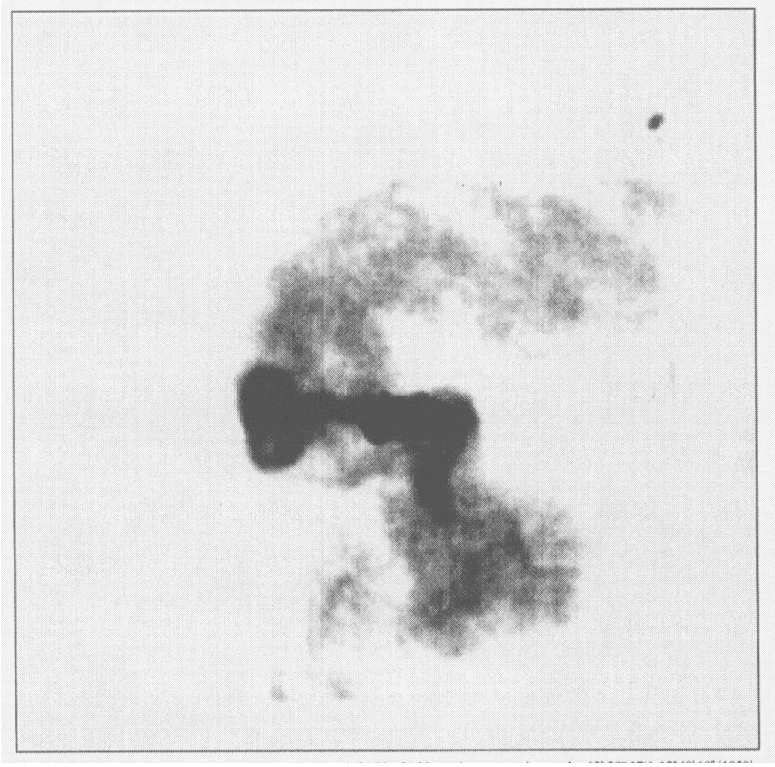

Figure 3.3: VLA image of M87 at 1667 MHz. The image is 21.33 × 21.33 arcmin square (Böhringer et al. 1995)

3.2 X-ray Properties

We show the X-ray image and surface brightness profile of M87 obtained with the Einstein IPC in figure 3.4 (a) and (b). As can be seen from this figure, the X-ray image of M87 is roughly circular. The X-ray surface brightness profile can be fitted by the β model with the core radius of $1'.6$ and the slope ($=3\beta - 1/2$) of 0.81 (Fabricant and Gorenstein (1983) [44]). This best-fit profile was converted to the density profile of the interstellar medium. Fabricant and Gorenstein (1983) [44] also fitted the spatially resolved X-ray spectra obtained with the IPC and determined the temperature profile, though the errors are rather large due to the limited energy resolution of IPC. Substituting the temperature profile and density profile for Eq. (2.44), they estimated the total gravitating mass as is shown in figure 3.6. The integral mass-to-light ratio of M87 (in solar unit) increases from 5 – 15 at $1'$ to over 180 at $20'$. This is further evidence for the massive dark halo of M87, which was suggested previously by Bahcall and Sarazin (1977) [8] and Fabricant, Lecar, and Gorenstein (1980) [43].

Though the IPC image is roughly circular, we can see X-ray emission produced in the nucleus and jet in a higher-resolution X-ray image of M87 (Schreier, Gorenstein, and Feigelson 1983 [138]; figure 3.5). Schreier, Gorenstein, and Feigelson (1982) found four components from these images: (1) a broad diffuse component associated with the hot gas in M87; (2) a diffuse, asymmetrical X-ray distribution to the east and southwest, which appears similar to the radio morphology and is consistent with an inverse Compton model; (3) an X-ray source centered on the nucleus of M87, which is extended by $2''$ – $3''$ and may be due to thermal bremsstrahlung; (4) a structure correlated with the radio-optical jet.

Feigelson et al. (1987) [45] studied the HRI image and VLA 1.4 GHz map. They subtracted a spherically symmetric component from the X-ray image, and compared the residual structure with the VLA image. They found that the residual X-ray emission and the radio halo are clearly associated with each other, but are not identical in structure. If this asymmetric component is due to the inverse Compton as suggested by Schreier, Gorenstein, and Feigelson (1982) [138], the average magnetic field must be 3 – 8 times weaker than the equipartition values of $\sim$ 2 – 5 μG. Therefore they suggested that the asymmetrical X-ray component is due to a local enhancement of thermal X-ray emission caused by compression of the interstellar medium by the outflowing jets. Biretta, Stern, and Harris (1991) [15] further analyzed the HRI images together with new optical and radio data, and argued that most of the core emission ((3) of Schreier, Gorenstein, and Feigelson (1982) [138]) was unresolved, and thus could be similar to a nuclear emission from other AGN.

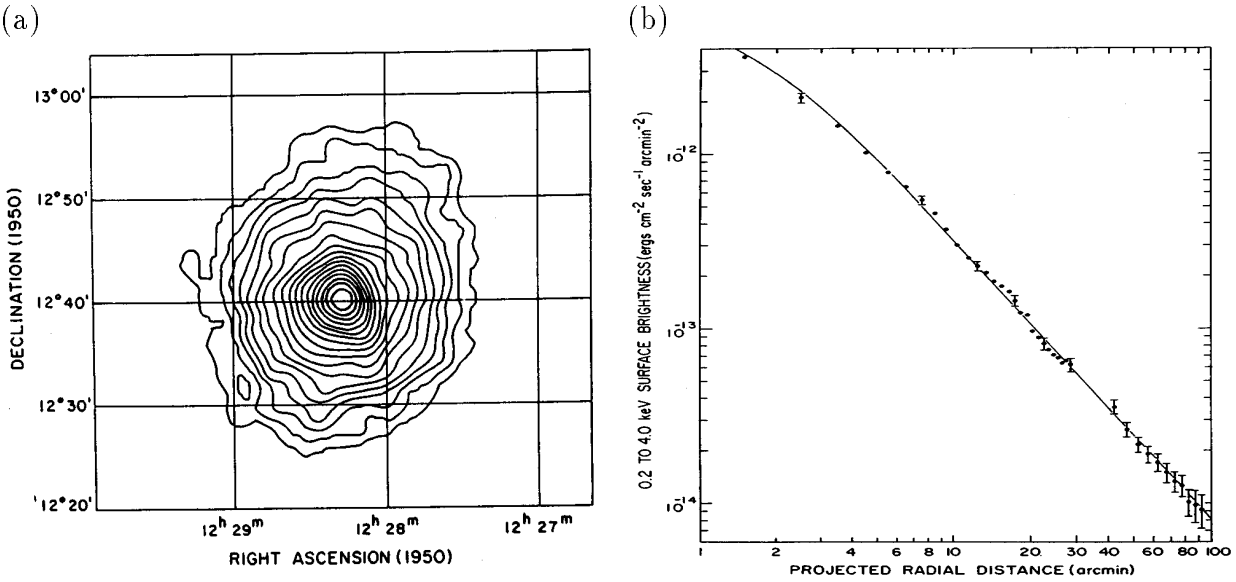

Figure 3.4: (a) X-ray contour map of M87 in the 0.3 – 4.0 keV band obtained with the Einstein IPC. (b) The 0.2 – 4.0 keV surface brightness profile of M87. The curve indicates $S \propto [1 + (r/1'.6)^2]^{-0.81}$. Both figures are from Fabricant and Gorenstein (1983).

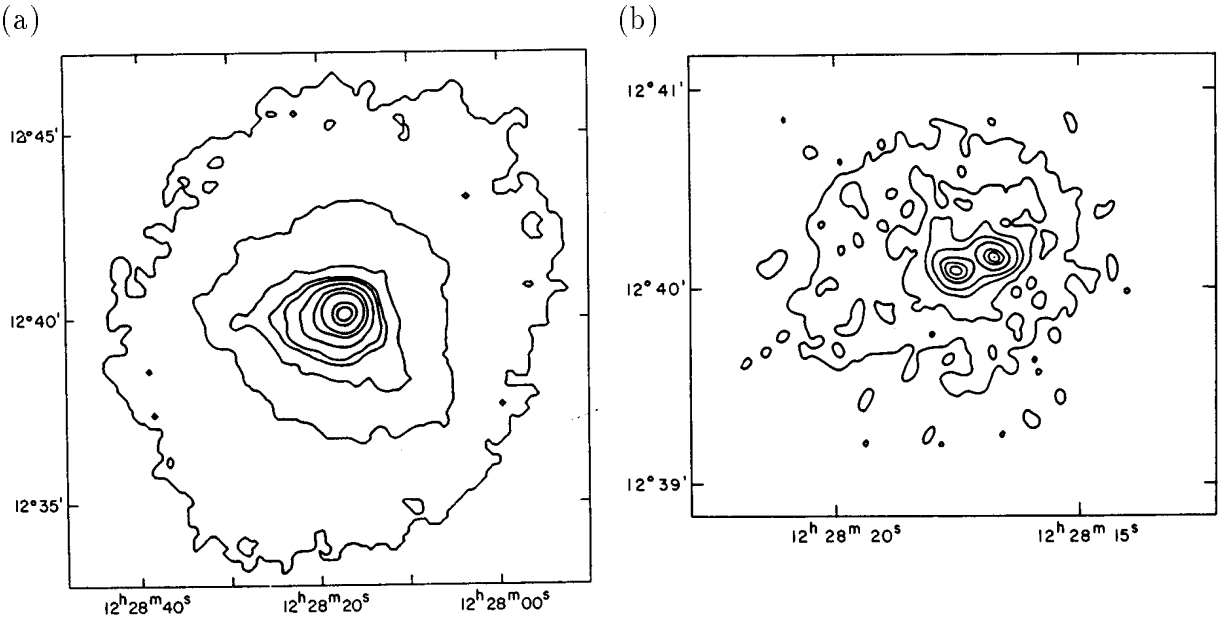

Figure 3.5: Higher-resolution X-ray image of M87 obtained with the Einstein HRI (Schreier, Gorenstein, and Feigelson 1982). (a) X-ray contour map of the 25′region centered on M87. (b) X-ray contour map of the central 2′region centered on M87.

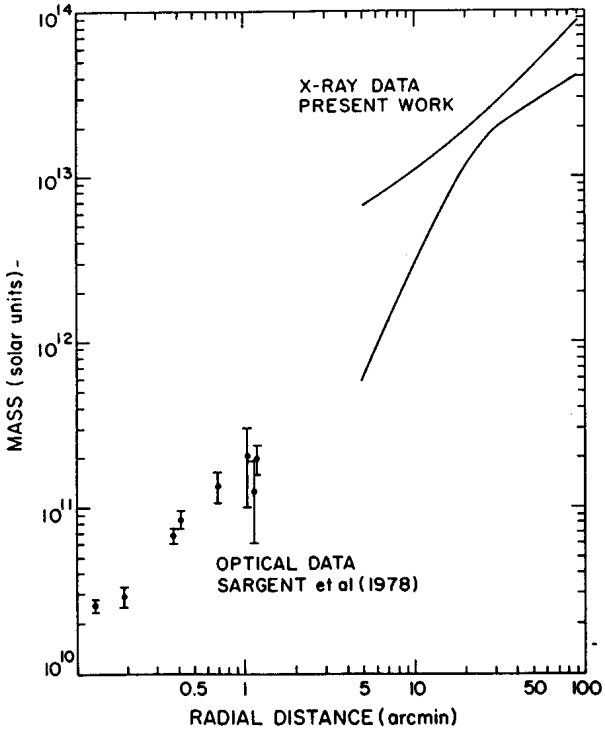

Figure 3.6: The total gravitating mass of M87 as a function of radius, summarizing both optical and X-ray results (Fabricant and Gorenstein 1983).

The Kα line from He-like Fe (6.7 keV) from the Virgo was detected with various instruments like OSO-8 (Serlemitsos et al. 1977 [136]; Mushotzky et al. 1978 [111]; Rothenflug and Arnaud 1985 [127]), HEAO-1 (Mushotzky 1984 [112]), EXOSAT (Edge, Stewart, and Smith 1988 [36]), and Ginga (Koyama, Takano and Tawara 1991 [82]; Takano 1990 [143]; Hatsukade 1989 [63]). The K lines from Mg, Si, and S and the L lines from Fe as well as the Fe K line were detected with the Einstein SSS (figure 3.7 (a); Lea et al. 1982 [84]). These lines indicate that the gas temperature is about 2 keV. The SSS spectrum can be represented with a two-temperature thermal plasma model plus a heavily absorbed power-law model. The temperatures of the plasmas are 0.6 and 1.4 keV with the metal abundances of about 1 solar. The photon index of the power component is fixed to be 1.75 (Lea et al. 1982 [84]). No cool component was detected at the region 7′ away from the center of M87. This suggests that the cool plasma is due to the cooling flow at the central region of M87. Comparing with the cooling flow model (Mathews and Bregman 1978 [97]), the mass accretion rate was deduced to be 10 – 20 $M_\odot$/yr. Since no power-law X-ray is found at the region 7′ away from the center, the power-law component is attributable to the nucleus of M87. Mushotzky and Szymkowiak [113] fitted the SSS spectrum with a cooling flow model and concluded that the mass accretion rate is about 4 $M_\odot$/yr.

Figure 3.7 (b) shows an example of the high-resolution X-ray spectrum of M87 obtained with the Einstein FPCS (Canizares et al. 1979 [22]). The OVIII Lyα line (0.65 keV) and the FeXVII line (0.83keV) were detected (Canizares et al. 1982 [23]; see table 6.9). Since the emissivities of

these two lines depend similarly on the plasma temperature, one can estimate the abundance ratio of oxygen to iron from their line flux ratio regardless of the plasma temperature or its distribution. Canizares et al. (1982) [23] concluded that the abundance ratio of oxygen to iron is 3 – 5 times of the solar ratio. Using other emission lines, Canizares et al. (1982) [23] derived the temperature distribution of the plasma, and concluded that the mass accretion rate is 3 – $4M_{\odot}/yr$.

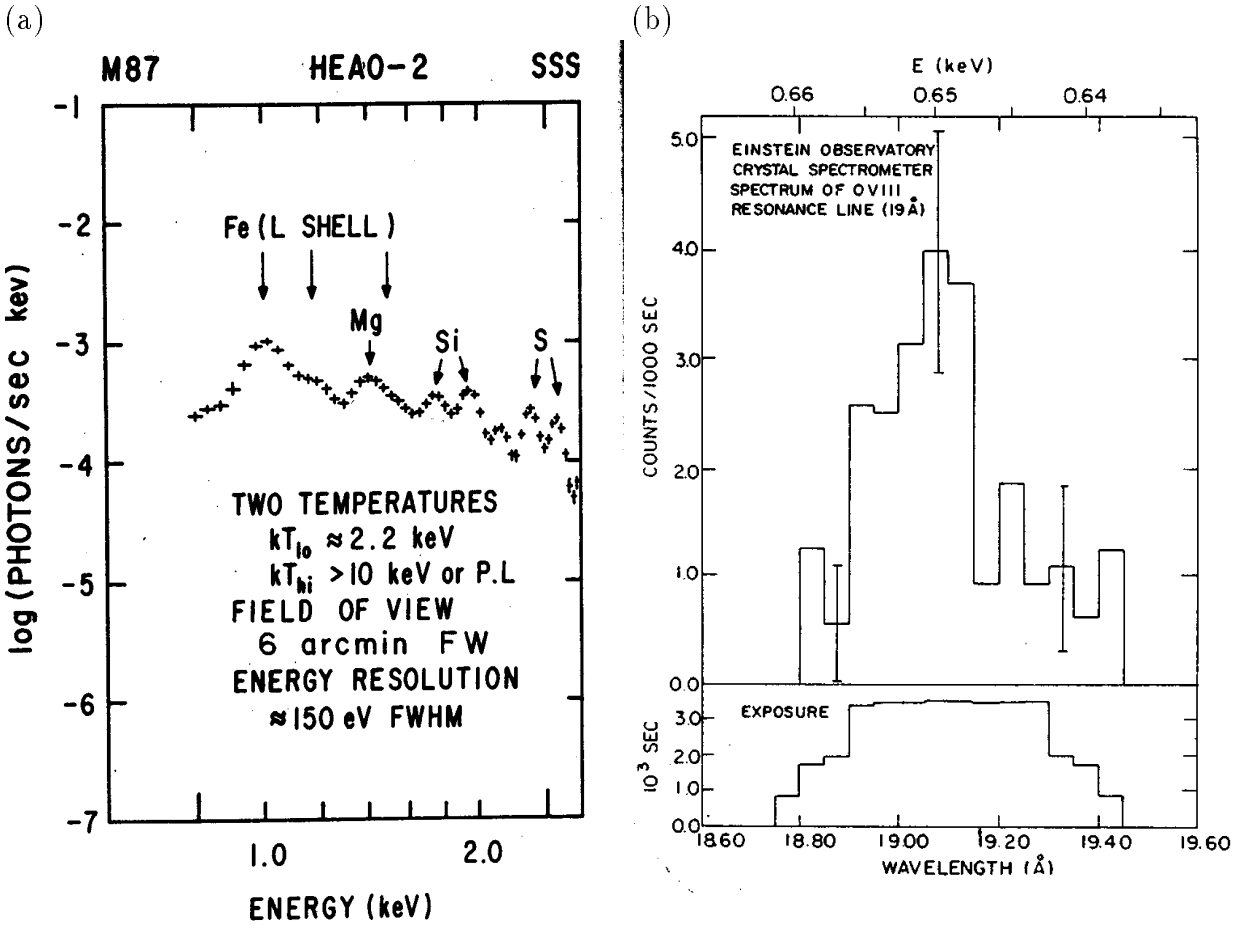

Figure 3.7: X-ray spectra obtained with the Einstein satellite. (a) The moderate-resolution spectrum obtained with the SSS (Lea et al. 1982). (b) The very high-resolution spectrum obtained with the FPCS (Canizares et al. 1979).

Stewart et al. (1984) [140] obtained the structure of the hot gas and gravitating matter around M87 with combined analyses of X-ray images and spectroscopy. They obtained the density and temperature distributions by the analysis of the Einstein IPC and HRI images under trial gravitational potentials, then made model spectra and compared to the spectra measured with the Einstein SSS and FPCS. By these iterative process, they determined the mass profile, which is consistent with that of Fabricant and Gorenstein (1983) [44] (figure 3.6).

They also found that the gas temperature varies slowly beyond 5′, and this profile is consistent with the cooling flow model. The mass accretion rate varies with radius as $\dot{M} \sim 3(R/10 \text{ kpc})^{2/3}$ $M_\odot$/yr from 1 to 70 kpc, assuming the distance of 15 Mpc; cooling flow rate is not constant, but increases as increasing radius.

Tsai (1994) [150] and Tsai (1994b) [151] reanalyzed the density and temperature profiles of the X-ray emitting gas around M87. For assumed density and temperature profile, he predicted surface brightness distributions as well as the line intensities, and compared with the Einstein HRI and IPC image as well as the FPCS spectrum. He found several models which give a nice fit to the data, and give a larger O/Fe abundance ratio than the solar ratio. However, these models failed to reproduce the SSS spectrum (figure 3.8). He suggests that there probably remain calibration problems in the SSS or both the SSS and FPCS data.

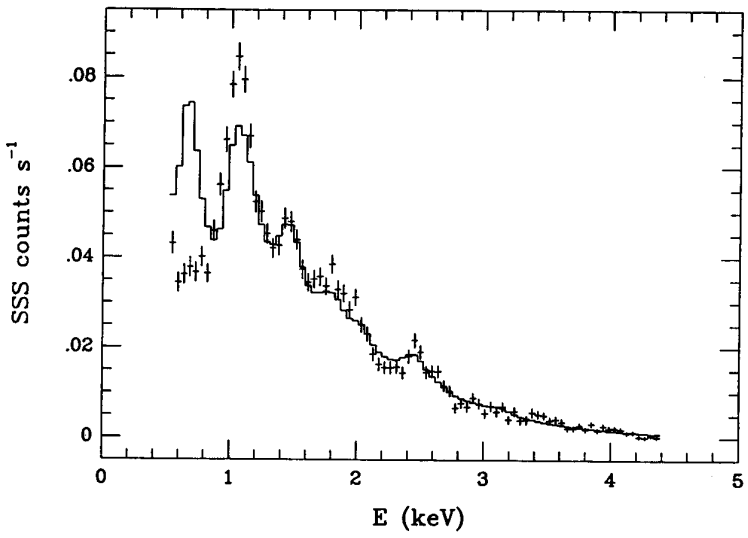

Figure 3.8: SSS spectrum of M87. The solid line shows the model giving a good fit to the data of IPC, HRI, and FPCS simultaneously (Tsai 1994).

We show the ROSAT PSPC image of M87 in figure 3.9 (a) and (b) (Böhringer et al. 1995 [17]: (a) is the X-ray contour map in the 0.5 – 2 keV band; (b) is the residuals of the X-ray image after subtraction of a spherically symmetric model from figure 3.9 (a). It is interesting that the X-ray residual structure to the east coincides with the radio feature of an "ear" shape (figure 3.3).

Furthermore, the radio "tail" bending down to the southwest is followed by X-ray residuals. These suggests the interaction between the radio halo and interstellar gas of M87. Böhringer et al. (1995) [17] found that the X-ray spectrum obtained with the ROSAT PSPC for the outer

part of the eastern residual can not fit a power-law model but can fit a thermal plasma model with a temperature of $\sim$ 1.3 keV, which is lower than that of the surrounding gas ($\sim$ 1.5 – 2 keV). This may imply that, relativistic plasmas and magnetic fields in the radio halo of M87, enhanced cooling of the gas, rather than heating by energy dissipations. Enhanced cooling may be explained either by disruption of previously condensed material in the cooling flow or by a higher cooling rate due to inhomogeneous gas distribution generated by plasma waves and instabilities.

Nulsen and Böhringer [119] used the ROSAT PSPC data and derived the mass profile of M87. The profile they found agrees well with that determined by the dynamics of stars in M87 (Sargent et al. 1978 [132]), of the globular clusters in M87 (Mould et al. 1990 [110]; though it is marginally consistent with Merritt and Tremblay 1993 [103]), and by the previous X-ray observation (Stewart et al. 1984 [140]), although it is marginally consistent with the results of Fabricant and Gorenstein (1983) [44] (figure 3.6).

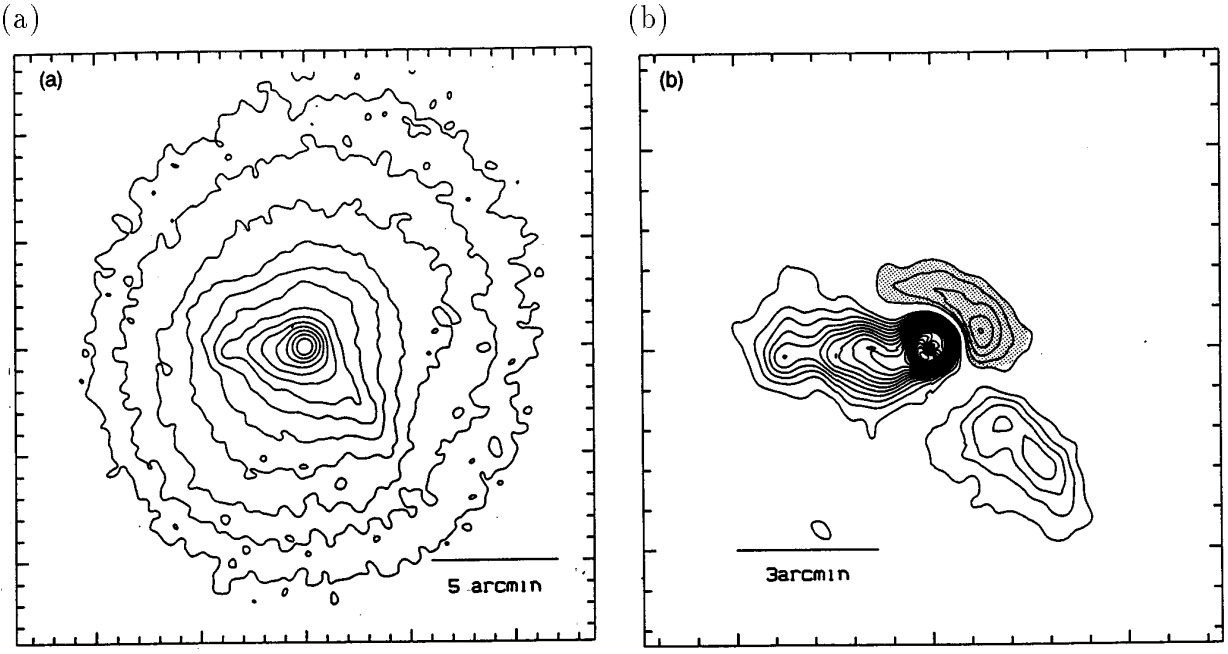

Figure 3.9: (a) ROSAT PSPC image of M87 in the 0.5 – 2 keV band. (b) Residuals of the X-ray image of the halo region of M87 after subtraction of a spherically symmetric model from figure (a).

Harris, Biretta, and Junor (1997) [62] analyzed higher-resolution X-ray images of M87 obtained by the multiple observations with the ROSAT HRI. They found the intensity of jet (knot A) as well as that of the core shows a time variability. Although the core variability is consistent with an AGN nuclei concept, the flux changes of the jet (knot A) provide constraints on the

X-ray emission process and geometry. Therefore they suggested that the X-ray morphology of the jet (knot A) is significantly different from the radio and optical structures.

We summarize below the previous results:

1. The distribution and temperature of the hot gas in M87 give strong evidence for a massive dark halo.

2. There is a cooling flow with 3 – 10 $M_{\odot}$/yr, and the mass accreting rate increases with increasing distance from the center of M87.

3. The innermost region of M87 exhibits spatially complex X-ray emissions with several components; a hot intracluster gas around M87, a jet-like structure, a compact nuclear source, and an asymmetrical component correlated with the radio halo.

4. The X-ray spectrum for the asymmetrical component can be expressed by a thermal plasma model of a temperature lower than that of the surrounding gas.

5. Both the X-ray intensities of the core and jet (knot A) show significant time variabilities.

6. The abundance ratio of oxygen to iron (O/Fe) is about 3 – 5 times larger than the solar ratio.

Chapter 4

Review of the Virgo Cluster of Galaxies

4.1 Optical Properties

The Virgo cluster is the closest and the best-studied cluster of galaxies, lying at a distance of approximately 15 Mpc. Cosmographycally, the Virgo cluster is the nucleus of the Local Supercluster of galaxies, in a outskirts of which, we are situated. We can observe a large number of galaxies in great detail, for all types and wide range of luminosities.

Therefore this cluster is an ideal laboratory for the systematic study of the galaxy properties. This may provide a fundamental stepping stone of the cosmological distance scale. Thus the Virgo cluster has been one of the most important objects for the extragalactic astronomy.

We show the map of the Virgo cluster in figure 4.1. The cluster covers a large, roughly circular sky area of approximately 10° diameter. The Virgo cluster is a fairly poor, loosely concentrated, irregularly shaped cluster of galaxies. Binggeli, Sandage, and Tammann (1985) [12] cataloged 2096 galaxies; 1277 and 574 of them are respectively considered to be the members and possible members of the Virgo cluster. Table 4.1 shows the classifications of the known member galaxies. The number of spiral galaxies is the largest among the bright galaxy members. This property can be seen in many poor clusters.

E and S0 galaxies are much rarer, although these are dominated in rich, dense, regularly shaped clusters . However, since the Virgo is the nearest cluster, we can detect fainter galaxies than those in any other clusters. Therefore the Virgo cluster is the richest cluster of galaxies in terms of the number of known member galaxies. As table 4.1 shows, dwarf galaxies, particularly dwarf ellipticals, are numerically the main population of Virgo.

Table 4.1: Known member galaxies if the Virgo cluster (Binggeli 1992)

Morphological Type	Number
Elliptical	30
S0	49
Spiral	128
Dwarf elliptical	828
Dwarf S0	30
Dwarf irregular	89
Dwarf irregular/elliptical	89
Other	34
Total	1277

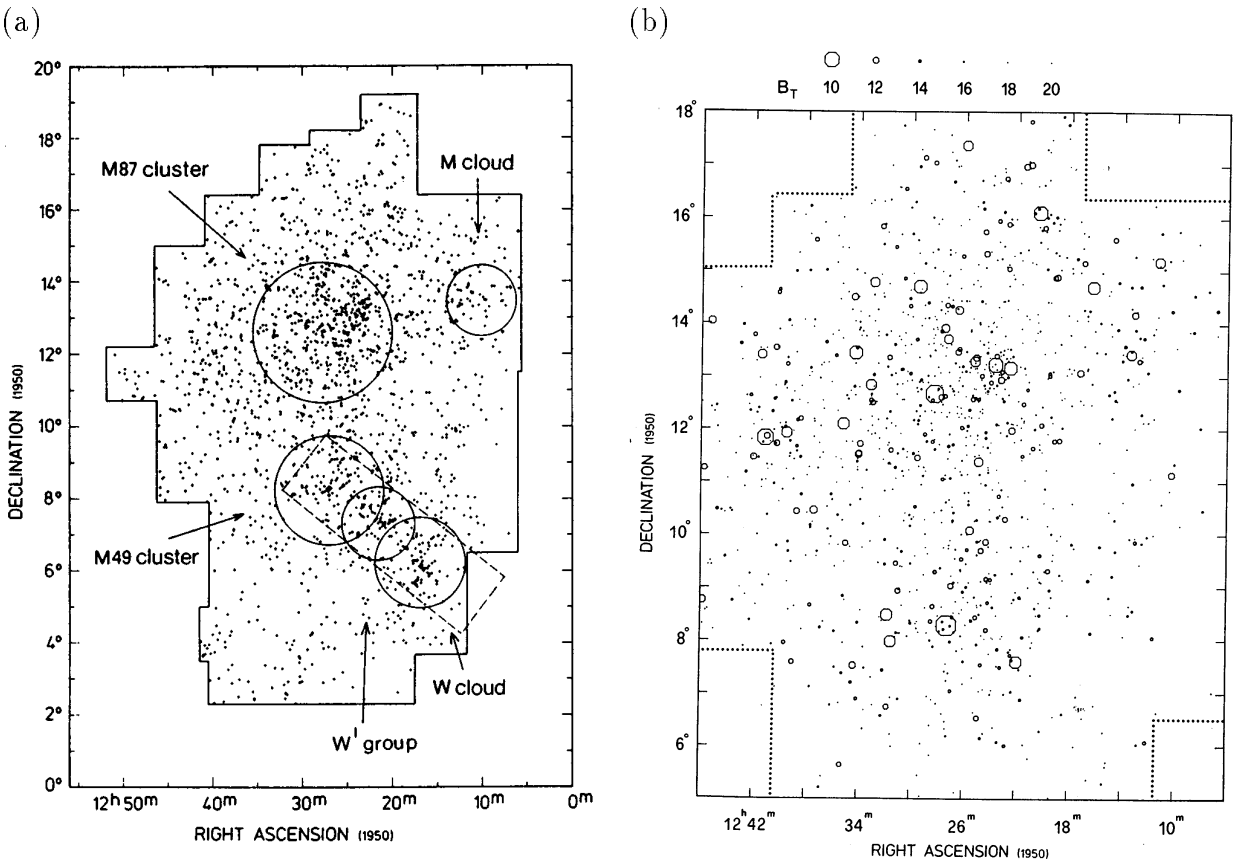

Figure 4.1: Plot of all members and possible members in the Virgo cluster: (a) Dots show the galaxies. Five main concentrations indicated by circles, are evident; (b) Luminosity-weighted map of the Virgo cluster. The symbol size (area) is proportional to the luminosity of the galaxy (Binggeli, Tammann, and Sandage, 1987).

Several sub-concentrations can be seen in figure 4.1. A major subcluster of galaxies exists around the giant E galaxy M87 (M87 cluster or subcluster A), and there is a smaller, less dense subcluster around the brightest member galaxy M49 (M49 cluster or subcluster B). Although M87 is often taken as the center of the Virgo cluster, it is 1° away from the density peak of the subcluster A toward the east. With respect to morphological type, the elliptical and S0 member galaxies are concentrated most strongly. Hence, they constitute the "skeleton" of the cluster. The E type galaxies, in particular, are distributed along an axis which is extended toward the east from the subcluster A. The jet of M87 is aligned with this axis. Spiral and irregular galaxies, on the other hand, are scattered over the whole region of the cluster with no obvious concentration. The irregular structure of the Virgo cluster suggests that the cluster is not in dynamical equilibrium, even at the central region. There is evidence that the cluster is still in the making.

From the radial velocities of about 400, attributable mostly to bright Virgo members, Binggeli, Popescu, and Tammann (1993) [14] derive a mean heliocentric, systematic velocity of the cluster of $\langle v_\odot \rangle = 1050 \pm 35$ km/s. The mean velocity of early-type galaxies (E+S0) is 1017 ± 68 km/s, and that of late-type galaxies (S+Im) is 1031 ± 54 km/s. Thus these two types have similar values. Only the dwarf early-type galaxies (dE + dS0) have systematically higher mean velocity of 1139 ± 67 km/s. However the velocity dispersion differs substantially for different galaxy types; late-type galaxies have a larger velocity dispersion of $\sigma_r \sim 737$ km/s than that of early-type galaxies of $\sigma_r \sim 589$ km/s. The late-type galaxies are thus more dispersed, not only in space, but also in velocity, than the early-type galaxies. This suggests that late-type galaxies have only recently (in the last few 10^9 yr) fallen, or are still falling into the cluster from the environment.

The subcluster A is made up predominantly of early-type galaxies, while the subcluster B contains mainly late-type galaxies. Though the subcluster B has a higher spiral abundance, the subcluster A has a larger velocity dispersion of $\sigma_r \sim 750$ km/s than the subcluster B which has $\sigma_r \sim 516$ km/s. The mean heliocentric velocities of the cluster A and B are 1044 ± 45 km/s and 1030 ± 57 km/s, respectively. Hence there is no difference. This is in good agreement with the result of Tammann (1988) [145] that there is no difference in distance modulus between the subcluster A and B.

The well concentrated early-type galaxies of the subcluster A is considered to be the oldest members. However, these galaxies do not constitute a dynamically relaxed cluster core. There are two massive subclumps of galaxies within the subcluster A; one is centered on M87 and the other is on M86. Although M87 has enormous mass, as is deduced by X-ray observations

(5×10^{13} $M_\odot$; e.g. Fabricant and Gorenstein 1983 [44]), M87 is off the cluster center in space and velocity ($\Delta v \sim 200$ km/s). However, the subclumps will rapidly merge. We may, in fact, be living in a very special time, shortly before ($\sim 10^9$ yr) the final formation of a relaxed cluster core in Virgo. An analysis of the velocity dispersion of galaxies around M86 by Binggeli, Popescu, and Tammann (1993) [14] has shown that there is an asymmetric blue-shifted tail in the distribution, consisting mainly of dwarf ellipticals, implying that M86 is actually part of a small subclump in the subcluster A. M86 is presumably falling into the cluster from behind.

Fukugita, Okamura, and Yasuda (1993) [53] and Yasuda, Fukugita and Okamura (1997) [162] carried out a Tully-Fisher analysis for a complete sample of spiral galaxies in the Virgo cluster. They presented the evidence that spiral galaxies in the Virgo cluster are distributed in an elongated region, like a filament, which extends from 13 to 30 Mpc almost along the line of sight with the maximum of the density distribution at around 15 Mpc. Furthermore, the luminosity function and surface brightness fluctuation of planetary nebulae indicate that bright ellipticals as typically represented by M87 are concentrated around 15 Mpc. Therefore, in this thesis, we use 15 Mpc as the distance of the Virgo cluster and M87, so that a radius of $1'$ corresponds to 4.4 kpc.

4.2 X-ray Properties

The X-ray emission from Virgo is strongly concentrated in the region around M87, and its extent is much smaller than that of the member galaxies (Malina et al. 1976 [92]; Gorenstein et al. 1977 [58]; Fabricant and Gorenstein 1983 [44]). Furthermore, the deduced gas temperature of 2.5 keV is cooler than is usually associated with cluster emission (Lea et al. 1982 [84]). Therefore, before the Ginga satellite, X-ray emission of Virgo had been considered to be associated with M87 itself, rather than the cluster as a whole.

The mapping observations with Ginga revealed the existence of a large scale extended X-ray emission which fills the whole region of the Virgo cluster for the first time (Takano et al. 1989 [142]; Takano 1990 [143]). The diffuse X-ray emission is strongly peaked at M87 rather than the density peak of the subcluster A. The surface brightness distribution is radially symmetric around M87, and is well described by the β model (Eq. (2.40)) with $R_c \sim 1'.62$ and $\beta \sim 0.436$, except for the southern outer part around M49 (figure 4.2). In the southern outer part, the X-ray surface brightness distribution shows significant flattening with $\beta \sim 0.357$. Figure 4.3 shows that the gas temperature around M87 is almost isothermal with $kT \sim 2.2$ keV, but the gas temperature at the southern outer region around M49 is 3.4 keV which is significantly larger

than that around M87 (Koyama, Takano and Tawara 1991 [82]; Takano 1990 [143]). These suggest that the ICM of the Virgo cluster consists of two components: one is associated with the subcluster A (M87 cluster), and the other is associated with the subcluster B (M49 cluster). Though the subcluster B has a lower velocity dispersion ($\sigma_r \sim 516$ km/s) than the subcluster A ($\sigma_r \sim 750$ km/s), the temperature is higher at the subcluster B, which is inconsistent with a general tendency that clusters with larger velocity dispersions have higher gas temperatures (e.g. Hatsukade 1989 [63]). This may suggest that the Virgo cluster is not a dynamically relaxed system. The physical parameters are summarized in table 4.2.

Table 4.2: Physical parameters of the subcluster A and B.

	A (M87 cluster)	B (M49 cluster)
Temperature	2.2 keV	3.4 keV
L_X†	3×10^{43} erg/s	4×10^{42} erg/s
Gas Mass	2×10^{13} $M_\odot$	5×10^{12} $M_\odot$

†: X-ray luminosity in the 2 – 10 keV band.

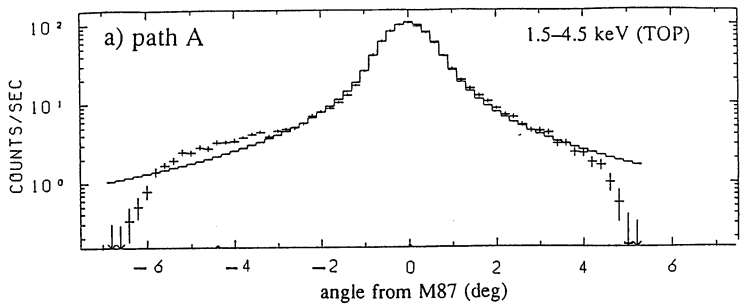

Figure 4.2: X-ray surface brightness obtained with Ginga (Takano 1990). The solid line denotes the expected profile by extrapolating the X-ray surface brightness distribution measured with the Einstein observation (Fabricant and Gorenstein (1983)).

One of the most important results of the Ginga observation is that the iron abundance increases towards the center of the Virgo cluster which is shown in figure 4.4 (Koyama, Takano, and Tawara 1991 [82]; Takano 1990 [143]). The iron abundance is at least about half of the cosmic value in the innermost region of the subcluster A and significantly decreases at outward regions.

The Virgo region was observed with ROSAT during the ROSAT all-sky survey between November 1990 and January 1991, and the results have been already published by Böhringer

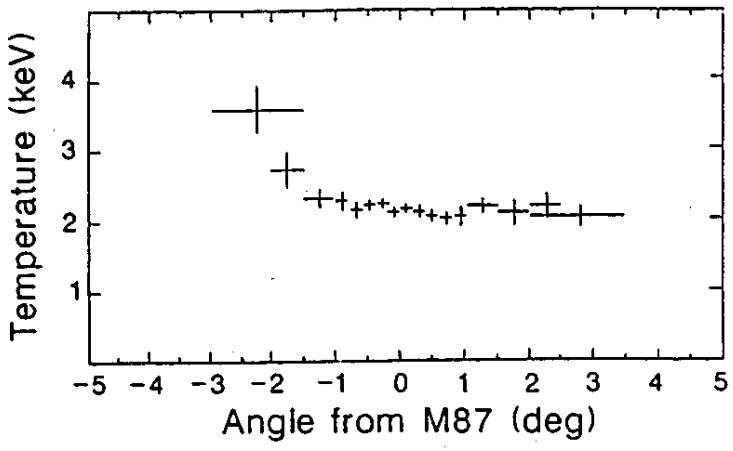

Figure 4.3: ICM temperature distribution obtained with Ginga (Koyama, Takano, and Tawara 1991).

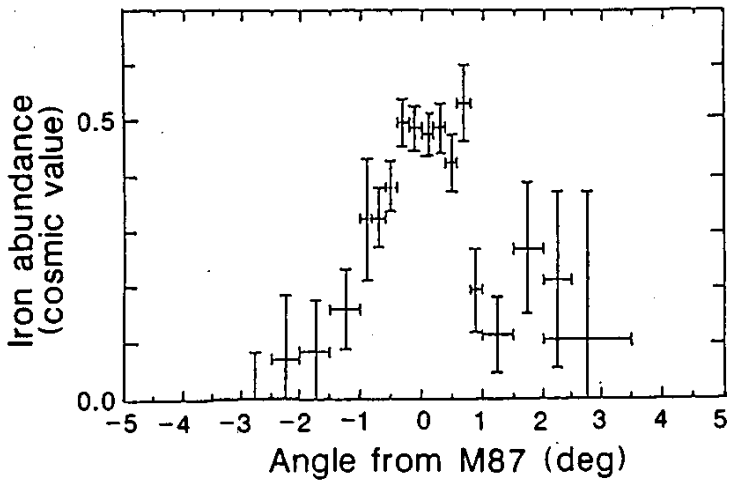

Figure 4.4: Iron abundance distribution obtained with Ginga (Koyama, Takano, and Tawara 1991).

et al. (1994) [16]. Figure 4.5 (a) and (b) show contour maps of the X-ray surface brightness of the Virgo cluster in the hard (0.4 – 2.4 keV) and soft (0.1 – 0.4 keV) bands, respectively. The X-ray morphology is very similar to the structure of the galaxy distribution (Binggeli, Sandage, and Tammann 1985 [12]). However, the M49 halo is much smaller in the X-ray image compared to the optical appearance of the subcluster B. The X-ray surface brightness around M87 can be fitted by the β model with $R_c = 2'.3$, and $\beta = 0.45$ (figure 4.6 (a)). The overall temperature determined for the region within 1° radius of M87 is $\sim$ 2.4 keV, which is consistent with the Ginga result. However, ROSAT found no evidence of the temperature increase around M49, which is inconsistent with the Ginga results (figure 4.6 (b)). ASCA will proceed mapping observations of the link-region between the subcluster A and B in 1998 to make clear whether the temperature gradient obtained with Ginga exists or not. From the ROSAT results one can estimate the total gravitating masses associated with the halos of M87, M86 and M49. They are (1.5 – 6)$\times 10^{14}$ $M_\odot$ for M87, and (1 – 3)$\times 10^{13}$ $M_\odot$ for both M86 and M49, respectively.

(a) (b)

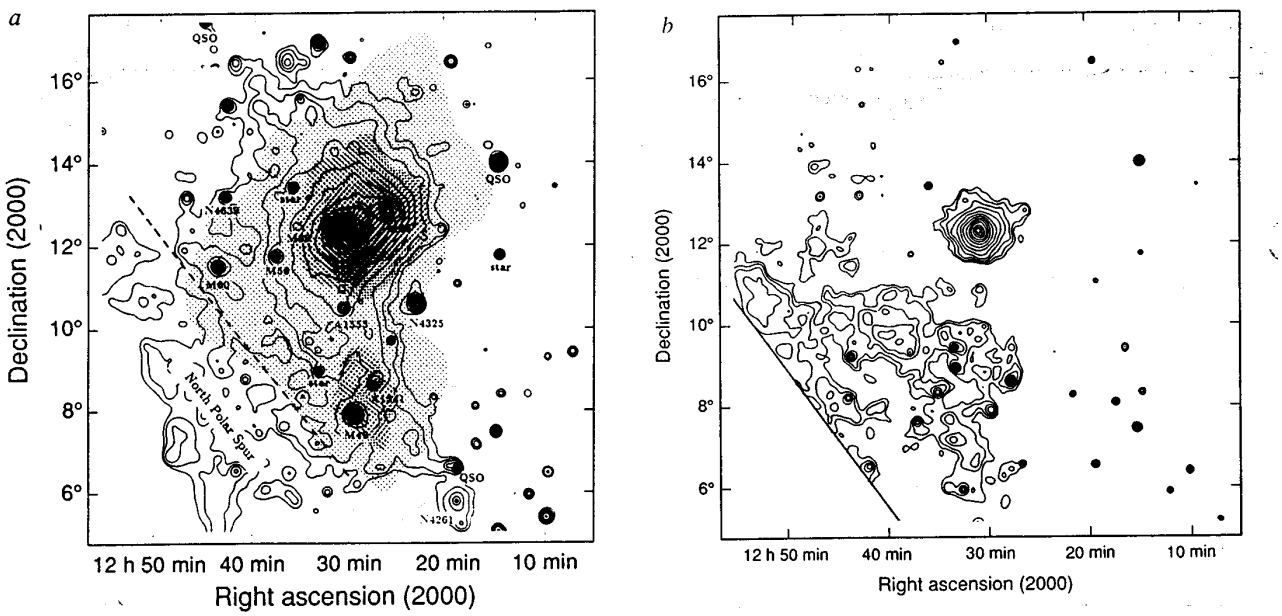

Figure 4.5: Contour Plot of the X-ray image of the Virgo cluster obtained with ROSAT (Böhringer et al. 1994): (a) 0.4 – 2.4 keV band, The galaxy density distribution is shown in grey scale; (b) 0.1 – 0.4 keV band.

M86 (NGC4406) is a dominant galaxy of a small subclump in the subcluster A. The peculiar X-ray morphology of an extended plume is thought to be evidence of ram-pressure interaction with the ICM of the Virgo cluster (figure 4.7). Iwasawa, White and Fabian (1996) [76] did detailed study of spatial variations in X-ray spectral properties with ASCA, and revealed that

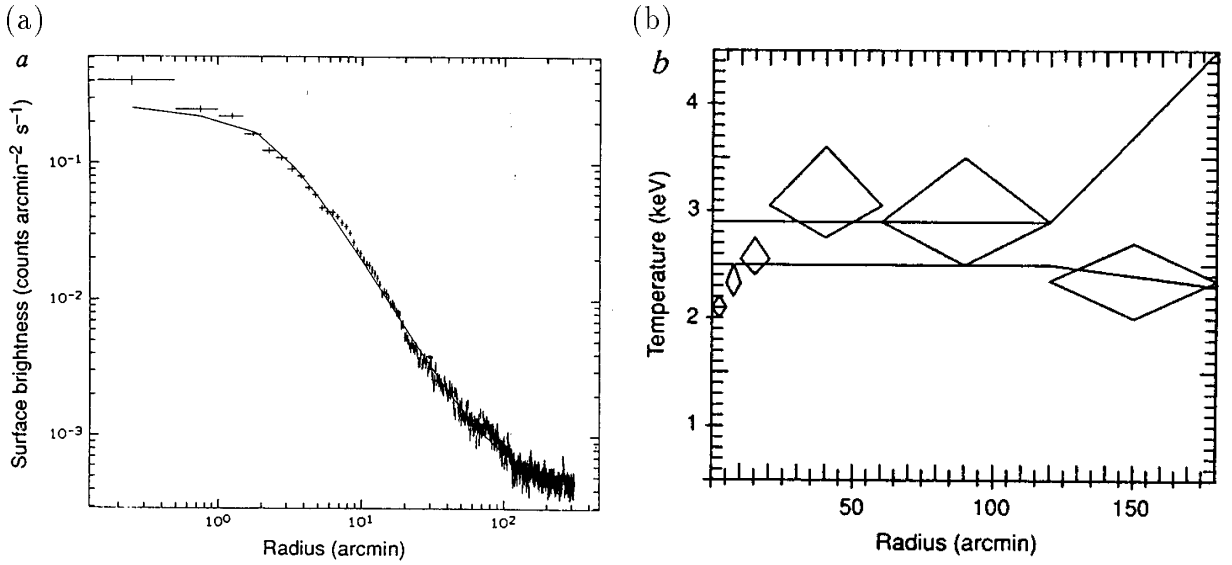

Figure 4.6: (a) Azimuthally averaged surface brightness profile for the X-ray halo around M87 (data points) and result of a fit of the β model to the data (line). (b) Radial temperature profile of the X-ray luminous halo around M87. The diamonds give the values determined from the ROSAT data, and continuous lines show the results obtained with Ginga. Both figures are from Böhringer et al. (1994).

the X-ray emission from the galaxy core region consists of at least two different temperature components ($\sim$ 0.6 keV and $\sim$ 1 keV), while that from the plume is well described by a single phase thermal emission, and has similar properties to those of the hot component associated with the galaxy main body. Since the hot component is the pre-cooling interstellar matter of M86, the ram-pressure stripping is a viable scenario to explain the X-ray morphology of M86.

4.3 Other Properties

In general, spiral and irregular galaxies contain neutral hydrogen gas which emits the 21-cm line, and isolated galaxies have similar mass of the neutral hydrogen with each others, if they have the same type and size. Radio observations of spiral galaxies of the Virgo cluster revealed that many members have smaller content of the neutral hydrogen than field galaxies and that those HI deficient galaxies are concentrated toward the center of the cluster (Giovanelli and Haynes 1983 [57]). This suggests that a sweeping mechanism that removes the interstellar gas from late-type galaxies plays a significant role in the cluster center.

The Extreme-UltraViolet Explorer (EUVE) observed the Virgo cluster in the 0.065 – 0.245 keV energy band and detected an extended emission halo of radius 20′ (Lieu et al. 1996b [88]).

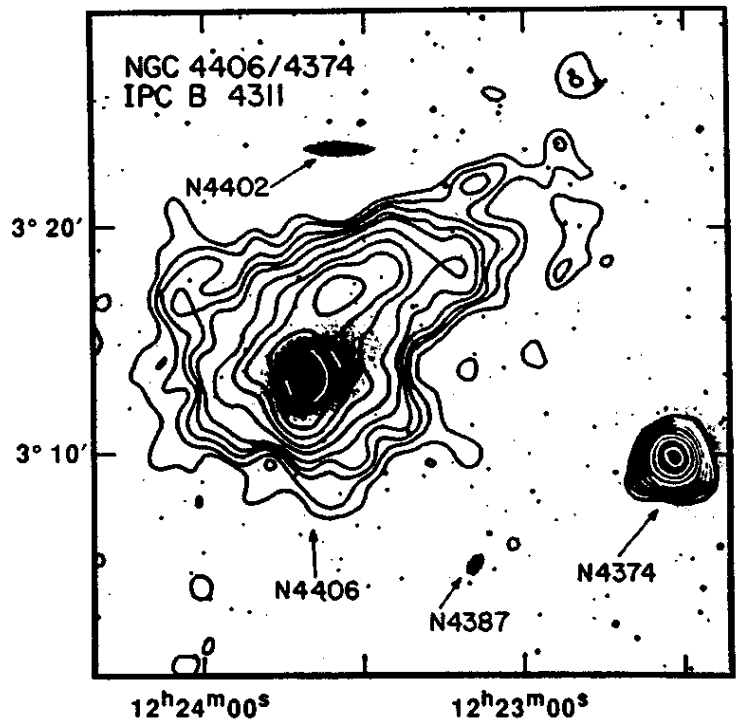

Figure 4.7: X-ray image of M86 (NGC4406) obtained with the Einstein IPC (Fabbiano, Kim and Trinchieri (1992)).

This is the first detection of cluster gas emission in the EUV band. After this discovery, Coma cluster (Lieu et al. 1996a [87]), A1795 (Mittaz, Lieu, and Lockman 1997 [108]), A2199 and A4038 (Bowyer, Lieu, and Mittaz 1997 [18]) were also found to have the EUV emission. The emission cannot be explained by the well-known cluster gas at X-ray temperatures. Though its origin is not clear so far, Sarazin and Lieu (1998) [131] suggest that the EUV emission is inverse Compton scattering of cosmic microwave background radiation by low energy cosmic ray electrons in the ICM.

Chapter 5

Instrumentation

5.1 The ASCA Satellite

The atmosphere of the Earth blocks the cosmic X-rays by photoelectric absorption, hence, we are required to use balloons, rockets, or satellites for the observations of cosmic X-ray sources.

Advanced Satellite for Cosmology and Astrophysics – ASCA – is the fourth Japanese X-ray astronomy satellite and was launched by the Institute of Space and Astronautical Science (ISAS) on 1993 February 20, with the M-3S-II rocket, and put into an approximately circular orbit with a perigee and apogee of 520 and 620 km, respectively, and an inclination of 31.1°. The orbital period is approximately 96 min. The schematic view of the ASCA satellite is shown in figure 5.1.

The spacecraft mass is 417 kg, and its length is 4.7 m along the telescope axis. The spacecraft is three-axis stabilized; the pointing accuracy is approximately 30″ with a stability of better than 10″. Orientation of the space craft is limited by the power constraint that the direction of the solar paddles must be within 30° from the Sun. This limits the observable sky at a time in a belt within which the Sun angle is between 60° and 120°. Thus the entire sky is accessible every half year.

ASCA carries the four X-Ray Telescopes (XRT), and four focal plane detectors, two of which are the Gas Imaging Spectrometers (GIS) and the other two are the Solid-state Imaging Spectrometers (SIS). All four detectors are operated simultaneously all the time, and data obtained from each of them are separately available. Overview of them are described below.

General descriptions of ASCA are given in Tanaka, Inoue, and Holt (1994) [147].

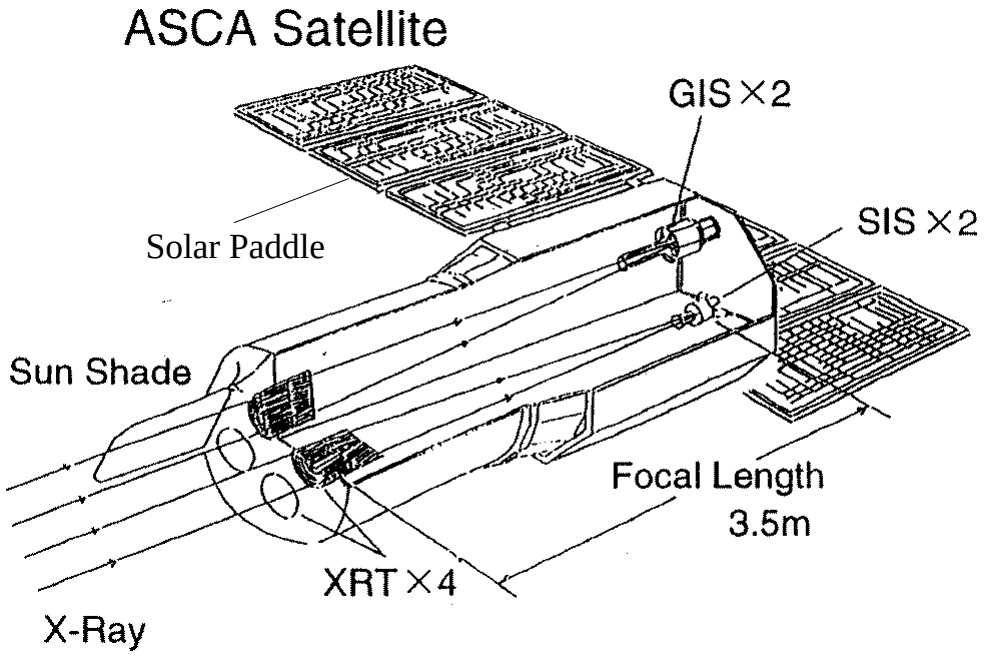

Figure 5.1: Schematic view of the ASCA satellite in orbit.

5.2 X-Ray telescope (XRT)

ASCA carries four identical grazing-incidence X-ray telescopes (XRT) each equipped with an imaging spectrometer at its focal plane. The telescope utilizes multi-nested (119 layers) thin-foil conical optics, a technology developed by Serlemitsos et al. (1995) [137]. This technology allows maximum use of the aperture for X-ray reflection, and enables a large effective area with small mass. We show the total effective area of four telescopes plotted as a function of photon energy in figure 5.2 (a). In this figure, we can also see that the effective area of the XRT depends on an incident angle as well as on energy of X-ray photon, which is called vignetting. In figure 5.2 (b), we compare the effective area of the ASCA XRT with those of other satellites.

The focal length of the telescopes is 3.5 m. These telescopes are mounted on an extensible optical bench. Because of the limited length available within the rocket nose fairing, the optical bench was held inside the spacecraft during launch and extended by 1.2 m in orbit to achieve the designed focal length.

The angular resolution of the telescope is modest, with a half power diameter (diameter which encircles 50% of the photons of a point source image) of approximately 3′. However, the point spread functions has a cusp-shaped peak, and 20% of photons are concentrated within a circle of 1′ diameter, producing a sharp core image . This feature allows us to resolve two

(a)

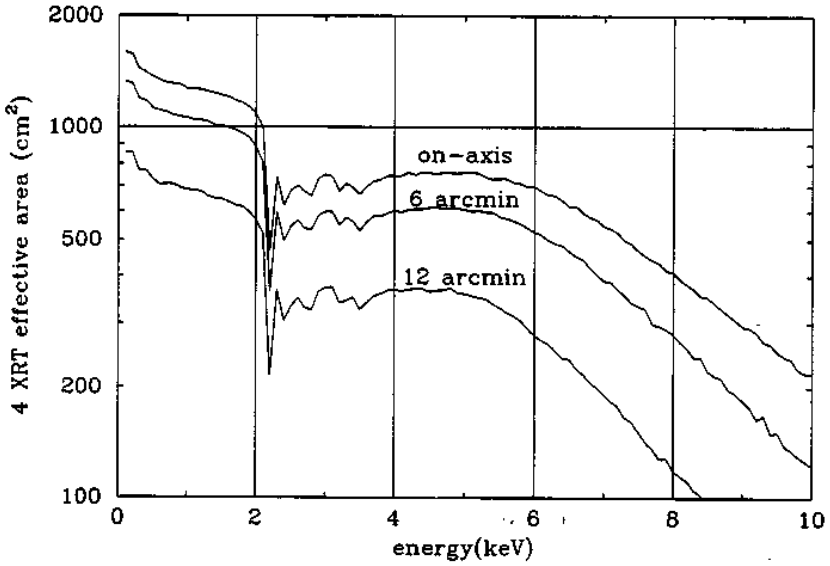

(b)

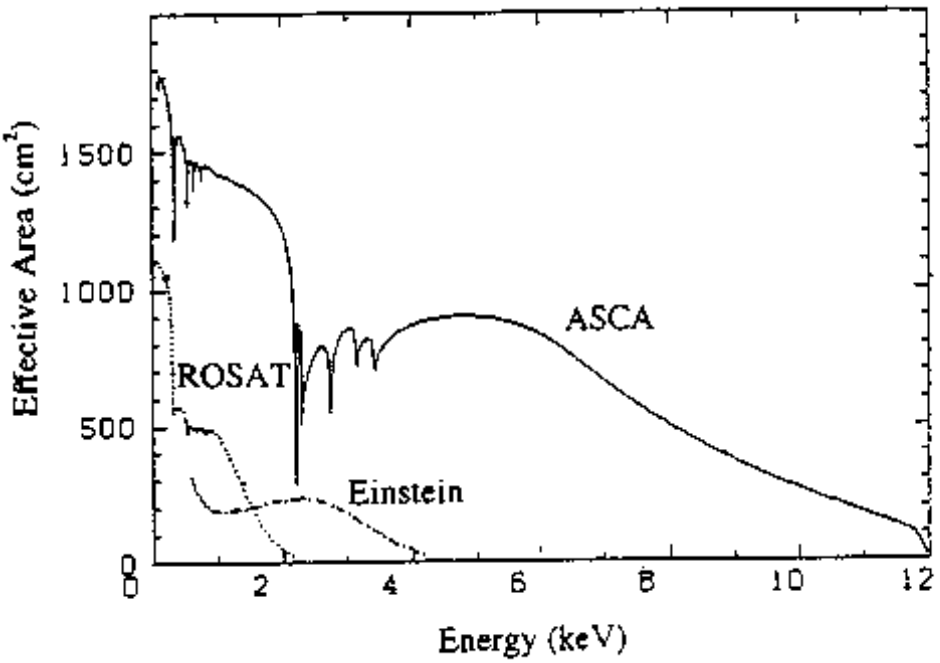

Figure 5.2: Effective area of XRT; (a) energy dependence at the three off-axis angles as indicated (Yamashita 1995). (b) comparison of the effective area with those of the Einstein satellite and ROSAT. Both show the total total effective area of four telescopes (Tanaka, Inoue, and Holt 1994).

sources separated by 1′. In figure 5.3, we show the point spread function (PSF) of the XRT.

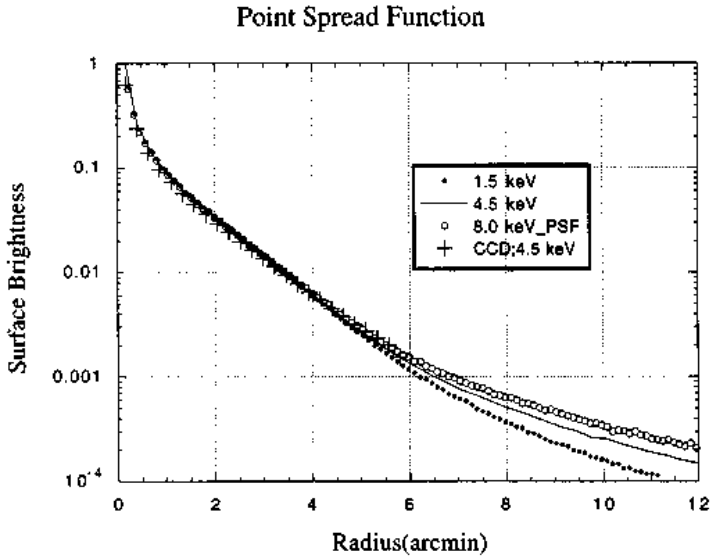

Figure 5.3: Simulated point spread function for photons of 1.5, 4.5, and 8.0 keV. Measured data for photons of 4.5 keV are also shown with crosses (Serlemitsos et al. 1995).

Even if a point source is outside the field of view, a fraction of the X-rays from the source arrive at the focal plane detectors. These X-rays are called the stray lights. Figure 5.4 shows an example of the stray lights observed with the GIS. The Crab nebulae is placed at the position of the filled circle, 60′ off-axis from the normal optical axis. When we analyze the data of the mapping observations of the Virgo cluster, we have to take the stray lights from M87 into account (chapter 7).

Details concerning the XRT can be found in Serlemitsos et al. (1995) [137].

5.3 Solid-state Imaging Spectrometer (SIS)

The Solid-state Imaging Spectrometer (SIS) is the first CCD camera for the X-ray astronomy. ASCA has two SISs (SIS0 and SIS1). Each SIS consists of 4 CCD chips, covering an X-ray detection area of 22 mm × 22 mm square. The depth of the depletion layer of each CCD chip is approximately 25 – 30 μm. We illustrate the quantum efficiency of the SIS as a function of X-ray energy in figure 5.5 (a). The hard X-ray efficiency is determined by the thickness of the depletion layer, while the soft X-ray efficiency is reduced due to X-ray absorption by the optical blocking filter, electrode and insulator of the CCD, and others placed in front of the depletion

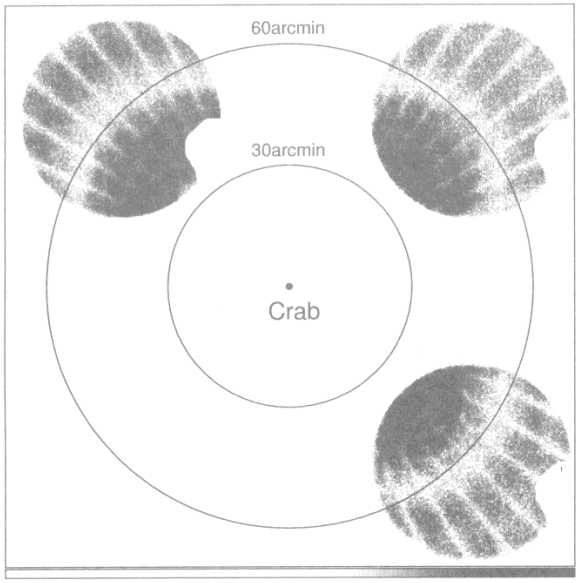

Figure 5.4: Three of the Crab stray light images taken by the GIS3 in the 0.7 – 10 keV band. The location of the Crab is indicated with a filled circle, and the optical axis for each observation is offset by 60′ from the Crab (Ishisaki 1996).

layer. The combination of the XRT and the SIS provides an X-ray imaging and spectral capability in the effective energy range of 0.4 – 10 keV. We also show the energy resolution of the SIS in figure 5.5 (b). The energy resolution of the SIS can be expressed as FWHM $\sim 2.0\sqrt{\frac{E}{5.9\mathrm{keV}}}$ % (120 eV at 5.9 keV) just after the launch, where E denotes energy. However, a few years after the launch, we found a significant degradation of the CCD performance, which was mainly caused by particle irradiation in orbit. For example, the energy resolution in the 1 CCD mode was degraded to 250 eV after 2.5 years in orbit (Yamashita 1995 [160]; Dotani et al. 1996 [32]). Due to the radiation damage, the quality of the Virgo mapping data are significantly worse than that of M87.

Details about the SIS can be found in Burke et al. (1991) [20].

5.4 Gas Imaging Spectrometer (GIS)

The Gas Imaging Spectrometer (GIS) is an imaging gas scintillation proportional counter. ASCA has two GISs (GIS2 and GIS3). The GIS has larger field of view ($\sim 50'$ in diameter), better time resolution, and higher efficiency at high energy range (above 3 keV) than those

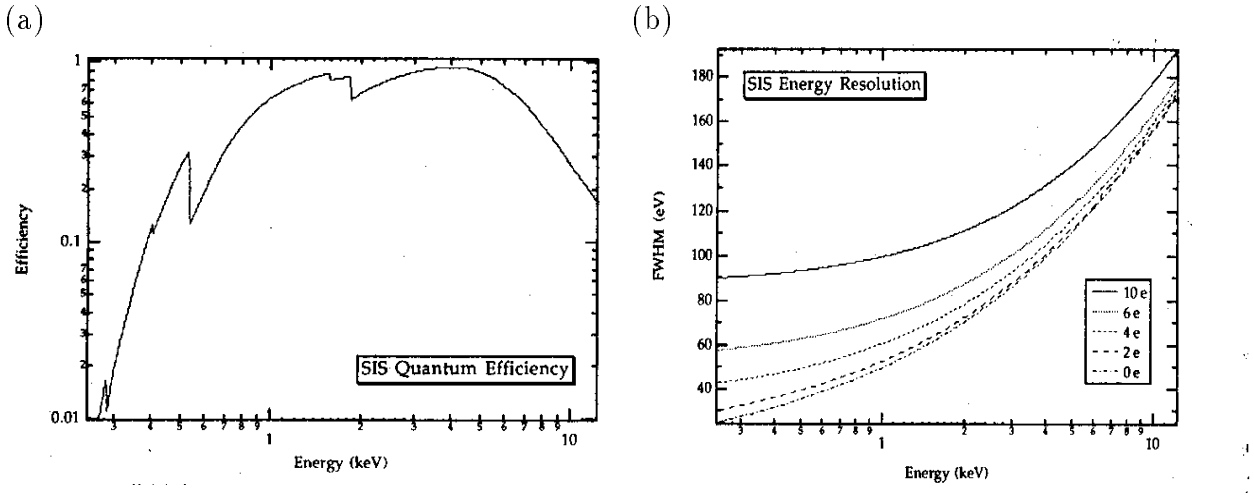

Figure 5.5: (a) Quantum efficiency of the SIS as a function of incident X-ray energy excluding the XRT response. (b) Energy resolution of the SIS as a function of incident X-ray energy. Energy resolutions with different read-out noise are plotted separately. The read-out noise levels are given as the equivalent number of electrons.

of the SIS. Therefore the GIS is a complementary detector of the SIS. We show the detection efficiency of the GIS in figure 5.6 (a) as a function of energy. The low-energy efficiency is determined by the beryllium entrance window of the GIS, while the high-energy efficiency is determined by the stopping power of the drift region. Figure 5.6 (b) shows the energy resolution of the GIS, which is expressed as FWHM $\sim 7.8\sqrt{\frac{E}{5.9\ \mathrm{keV}}}$ % (460 eV at 5.9 keV). The energy resolution of the GIS is worse by a factor 4 than that of the SIS.

Details concerning the instruments can be found in Makishima et al. (1996) [91], and Ohashi et al. (1996) [121].

We summarize the performance of the SIS and GIS in table 5.1.

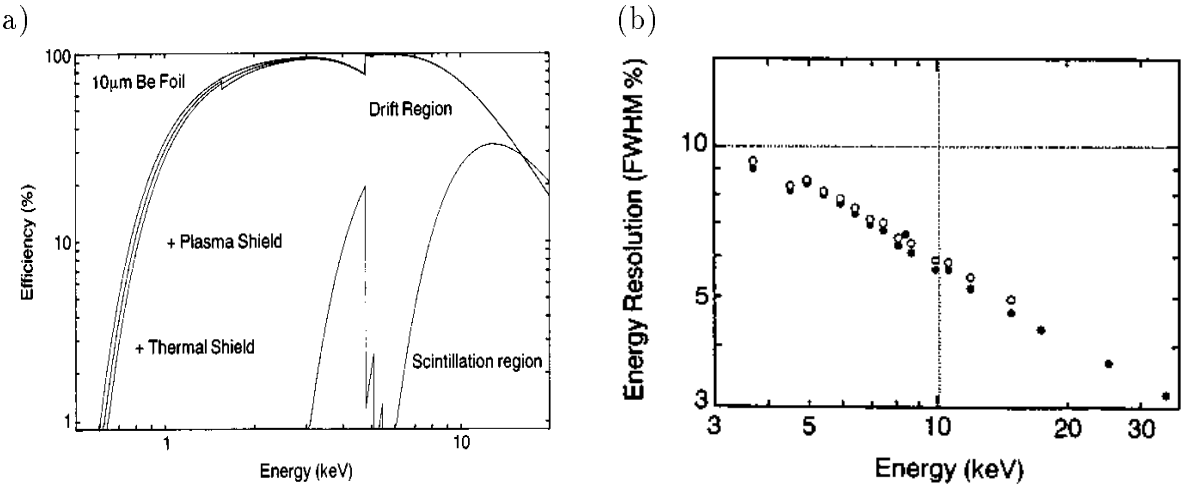

Figure 5.6: (a) Detection efficiency of the GIS as a function of energy, excluding the XRT response. Absorptions due to plasma shield in the GIS housing and due to thermal shield in front of the XRT are included in the actual observations (Ohashi et al. 1996). (b) Energy resolution of the GIS as a function of energy (Ohashi et al. 1996).

Table 5.1: Performance of the SIS and GIS.

Covered Energy Band†	0.4 – 10 keV	0.7 – 10 keV
Energy Resolution at 5.9 keV	2.0 %	7.8 %
Field of View	$20' \times 20'$	$50'$ in diameter
Pixel size	27 μm	0.5 mm§
Spatial Resolution†	$\sim 3'$	$\sim 3'$
Maximum Time Resolution	16 sec (4CCD mode)	60 μsec (PH mode)
Maximum Count Rate	500 cts/sec	10000 cts/sec

†: When used with the XRT.

§: Virtual pixel in the signal process.

Chapter 6

ASCA observation of M87

6.1 Observations and Data Reduction

M87 was observed on 1994 June 7 and 8, during the PV phase program, pointed at $(\alpha, \delta)_{J2000}$ = ($12^h30^m32^s$, $12°25'57''$). The observation was made with the two SISs and the two GISs at the foci of 4 thin-foil XRT onboard the ASCA satellite.

The SIS data were obtained mainly with the 4-CCD bright mode, including a small fraction of the 4-CCD faint mode. We therefore used the data taken with the 4-CCD bright mode. The GIS data were obtained with the normal PH mode. Both the SIS and GIS data were screened with the nominal selection criteria in order to exclude the data affected by the South Atlantic Anomaly, Earth occultation, and in the regions of low geomagnetic rigidity. We also excluded any data contaminated by stray lights from the bright Earth, removed hot and flickering pixels for the SIS data, and applied a rise-time rejection technique to reject particle events in the GIS data.

After the above mentioned data screening, we combined the SIS0 and SIS1 data from the 4-CCD chips, and the GIS2 and GIS3 data, after correcting for the pulse-height gain.

The X-ray image of M87 obtained with ASCA is shown in figure 6.1. In the higher-resolution X-ray images obtained with the Einstein and ROSAT satellites, we can see the X-ray emissions from the core of M87 which is thought to harbor massive black hole, jet, and radio halo (Schreier, Gorenstein, and Feigelson 1982 [138]; Feigelson et al. 1987 [45]; Böhringer et al. 1995 [17]; Harris, Biretta, and Junor 1997 [62]). However, we cannot see these structures in the ASCA image, because the spatial resolution of ASCA is worse than those of the Einstein and ROSAT satellites. Since the X-ray image obtained with ASCA is roughly circular, we assumed spherical symmetry for simplicity. For a further analysis, we divided the central region of M87

(the region within 10′ radius from M87) into 5 concentric annuli, each with a 2′ width, and obtained X-ray spectra from each annulus. We also analyzed the entire M87 spectrum from a circular region of 10′ radius centered on M87. These spectra are shown in figure A.1 (SIS) and A.2 (GIS).

Since the extent of the X-ray emission from the intracluster gas extends over a region larger than the field of view of ASCA, we used for the background spectrum data obtained from blank-sky regions provided by the ASCA Guest Observer Facility of NASA. We then rebinned the data so that each spectral bin contained at least 20 counts in order to use the χ^2 statistics.

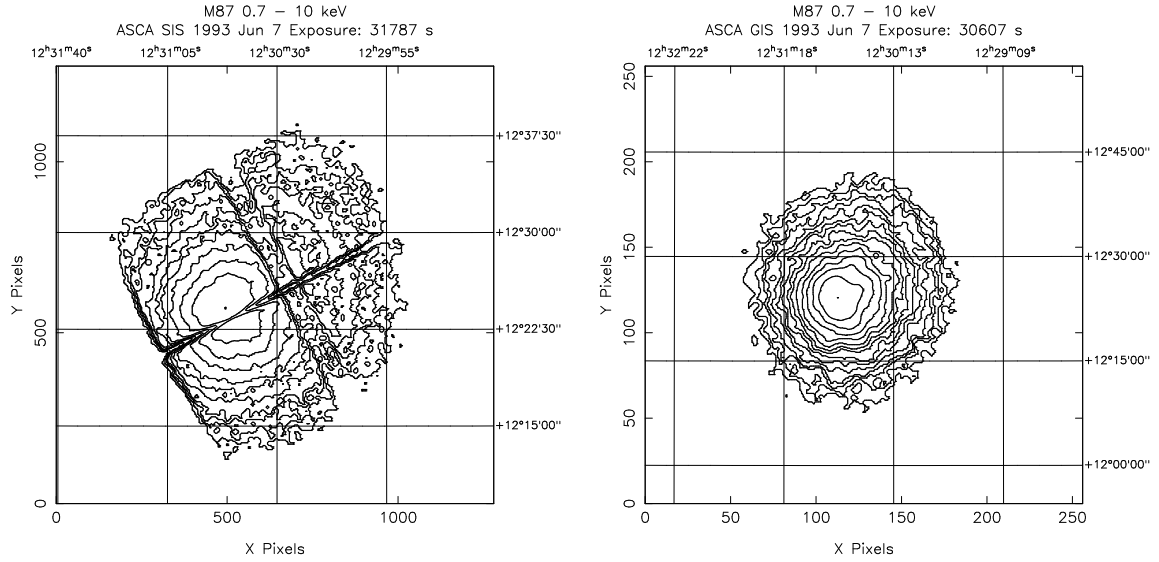

Figure 6.1: The X-ray image of M87 obtained with ASCA. The left and right panels show the SIS and GIS images respectively.

6.2 Spectral Analysis and Results

6.2.1 Response Matrix

In spectral fitting, we used the "XSPEC" spectral fitting package ver 9.0. The XSPEC calculates an expected pulse height distribution $S(PI)$ using a model spectrum $M(E)$ and the response matrix $K(PI, E)$ as follows;

$$S(PI) = \sum_E K(PI, E) M(E), \tag{6.1}$$

where E denotes energy, and PI represents pulse invariant, which is the pulse height after the gain corrections. The XSPEC search for model parameters so that $S(PI)$ gives the best-fit to the observed pulse height distribution.

The $K(PI, E)$ can be split into two parts, which are the redistribution matrix file (RMF) $RMF(PI, E)$ and ancillary response file (ARF) $ARF(E)$;

$$K(PI, E) = RMF(PI, E)ARF(E). \tag{6.2}$$

The RMF specifies channel probability distribution (pulse height distribution) for an incident photon of with energy of E, and the ARF specifies the telescope effective area and window absorption. Because the RMF is determined only by the elementary process in a detector, we need only one RMF for one detector. We used the standard RMF provided by the GIS team for the GIS data, while we generated the RMF of the SIS with the "sis_bldrsp2" package ver 1.6.

We calculated the ARF as follows;

$$ARF(E) = \int d\vec{r_1} S(\vec{r_1}) EA(E, \vec{r_1}) \int d\vec{r_2} P(E, \vec{r_1}, \vec{r_2}), \tag{6.3}$$

where $\vec{r_1}$ and $\vec{r_2}$ are direction vector of an incident X-ray photon and that of a reflected X-ray, respectively. $S(\vec{r_1})$ denotes a surface brightness distribution of an object which is normalized as $\int S(\vec{r_1}) d\vec{r_1} = 1$. $P(E, \vec{r_1}, \vec{r_2})$ represents reflection probability of an X-ray photon with energy E from the direction of $\vec{r_1}$ to $\vec{r_2}$ (i.e. point-spread function, PSF) including quantum efficiency. $EA(E, \vec{r_1})$ is the effective area of the XRT for an X-ray photon with an incident direction of $\vec{r_1}$ and energy of E. Since the PSF of the ASCA XRT is rather extended, X-rays in a annular region of the detector are contaminated by those from adjacent annuli (Ikebe 1996 [71]; Ikebe et al. 1997 [73]; Takahashi et al. 1995 [141]; Markevitch et al. 1996 [93]). To simulate this effect from the first approximation, we assume the observed X-ray image to be $S(\vec{r_1})$ and calculated the ARF for each annulus region using the "jbldarf" package ver 2.10.

6.2.2 Thermal Bremsstrahlung and Narrow line Model

As shown in figures A.1 and A.2, the X-ray spectra of M87 obtained with ASCA exhibit many emission lines, which contain crucial information for the physical state of the plasma. Since the emission-line structures in the high-energy band (1.6 – 10 keV) are simple compared to those in the lower energy band, we fitted the high-energy band spectra of the SIS extracted from the $0' - 10'$ region with a model of thermal bremsstrahlung plus several Gaussian profile lines. At

least 8 lines in the high-energy band are required with the best-fit energies of 1.84, 1.99, 2.45, 2.61, 3.12, 3.89, 6.67 and 7.86 keV. These lines can be assigned to be He-like Si Kα (Si XIII at 1.87 keV), H-like Si Kα (Si XIV at 2.01 keV), He-like S Kα (S XV at 2.46 keV), H-like S Kα (S XVI at 2.62 keV), He-like Ar Kα (Ar XVII at 3.14 keV), He-like Ca Kα (Ca XIX at 3.91 keV), He-like Fe Kα (Fe XXV at 6.67 keV), and blend of He-like Ni Kα (Ni XXVII at 7.80 keV) and He-like Fe Kβ (Fe XXV at 7.90 keV), respectively. The results of this model fitting is shown in figure 6.2.

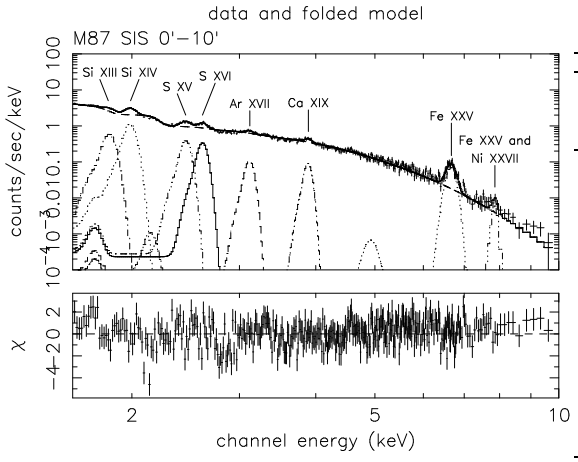

Brems kT(keV)	2.29 ± 0.03	
$\chi^2/d.o.f.$	475.4/355	
line center keV	equivalent width eV	identify
1.84±0.01	23±4	Si XIII
1.99±0.00	57±4	Si XIV
2.45±0.01	45±5	S XV
2.61±0.01	43±5	S XVI
3.12±0.02	21±6	Ar XVII
3.89±0.02	33±8	Ca XIX
6.67±0.01	1060±104	Fe XXV
7.86±0.09	277±127	Fe XXV and Ni XXVII

Figure 6.2: The best-fit model of a thermal bremsstrahlung plus Gaussian for the SIS spectrum in the $0' - 10'$ region. Errors are 90% confidence limit for one interesting parameter.

In figure 6.3, the SIS spectra of the two annulus regions of $0' - 2'$ and $8' - 10'$ and their ratio are given. We can see clear radial variations of the spectra. The most prominent change is found near at 1 keV.

For more quantitative study of the spectral variations, we fitted the spatially resolved spectra of the SIS in the limited high-energy to the same model as used to the full band spectrum: a thermal bremsstrahlung plus Gaussian lines. Since the lines of Ar XVII and Ca XIX, and the blend of Fe XXV and Ni XXVII are not very strong in the spatially resolved spectra, we fixed the center energies of these lines to be 3.12, 3.89 and 7.86 keV. The results are shown in table 6.1 and figure A.3.

For a consistency check, we also performed the same model fits to the GIS spectra in the 3 – 10 keV band, where the relevant lines are only Fe XXV and the blend of Fe XXV and Ni XXVII. The best-fit parameters are listed in table 6.2 and figure A.4. The results for the GIS data are consistent with those for the SIS data within the errors.

If the plasma is isothermal, we can estimate the plasma temperature using the line ratios of H-like to He-like ions of Si and S. For this purpose, we used the MEKAL code (Mewe,

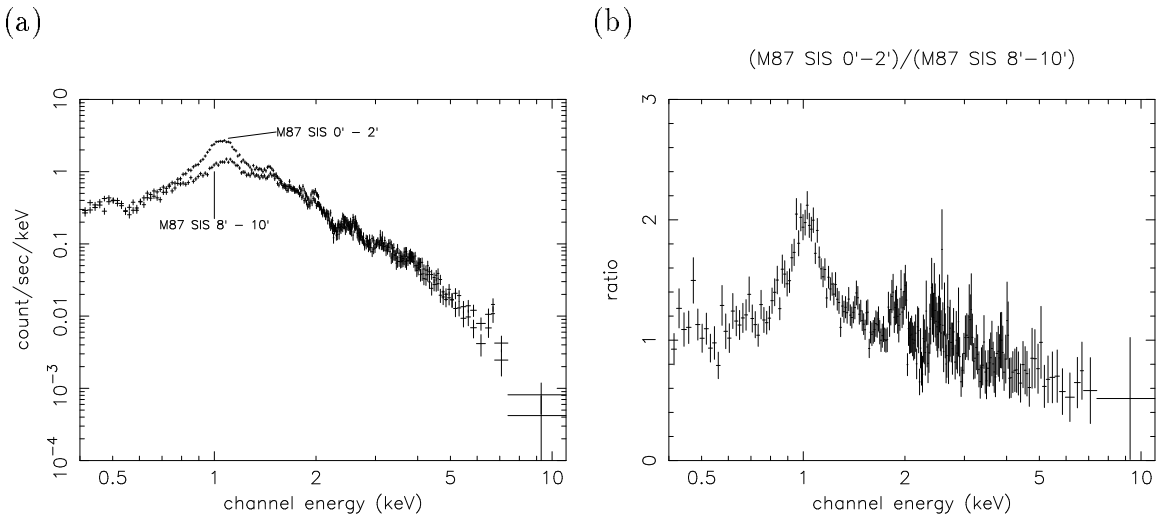

Figure 6.3: (a) SIS spectra of M87 from the $0' - 2'$ annulus and the $8' - 10'$ annulus. (b) Ratio of count rate of the $0' - 2'$ spectrum to that of the $8'$ - – 10 $'$ spectrum.

Gronenschild, and van den Oord 1985 [106]; Mewe, Lemen, and van den Oord 1986 [107]; Kaastra 1992 [78]; Liedahl, Osterheld, and Goldstein 1995 [86]; Arnaud and Rothenflug 1985 [4]). The results are given in figure 6.4, together with the best-fit bremsstrahlung temperature as a function of the radius from the M87 center. The temperatures inferred by the Si line ratio show good agreement with those deduced from the S line ratio. However, these temperatures are systematically lower than the bremsstrahlung temperature. Furthermore, the bremsstrahlung temperature gradually increases with the distance from the center. These suggest that the plasma in the M87 region is not isothermal, as has already been reported with the Einstein satellite (e.g. Canizares et al. 1982 [23]; Lea et al. 1982 [84]; Tsai 1994 [150]), and that the temperature in the outer region is higher than in the inner region.

We show the equivalent widths of emission lines as a function of the distance from the M87 center in figure 6.5. The equivalent widths of Si XIII and XIV, S XV and XVI, and Fe XXV rapidly decrease as the radius increases. This may indicate that the abundances of Fe, Si, and S are larger in the center of M87 than in the outer regions. On the other hand, equivalent widths of Ar XVII, Ca XIX and the blend of Ni XXVII and Fe XXV show no clear gradient, though the statistical errors are rather large.

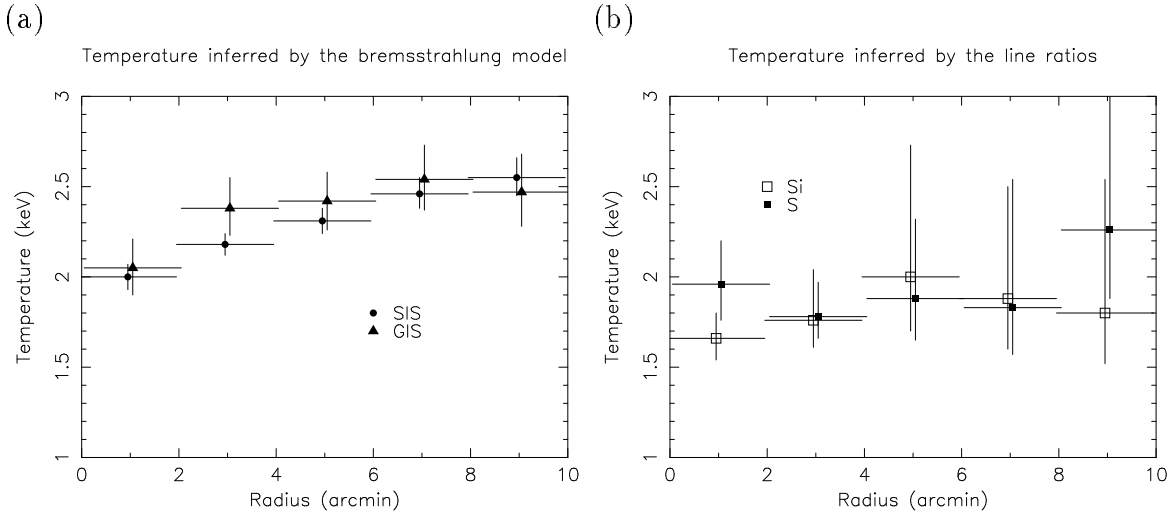

Figure 6.4: Temperature distribution as a function of the distance from the center of M87: (a) the temperature of thermal bremsstrahlung model for the SIS (circles) and GIS (triangles); (b) the temperature inferred by the line ratios of Si (closed squares) and S (open squares)

Table 6.1: The result of the thermal bremsstrahlung and narrow line model fitting to the SIS spectra.*

Radius	0′–2′	2′–4′	4′–6′	6′–8′	8′–10′	0′–10′	Identify
Brems kT	2.00	2.18	2.31	2.46	2.55	2.29	
(keV)	(1.93–2.07)	(2.12–2.24)	(2.24–2.38)	(2.38–2.55)	(2.45–2.66)	(2.25–2.32)	
$\chi^2/d.o.f.$	240.1/206	328.7/251	279.4/253	262.1/246	239.3/231	475.4/355	
Center	1.83	1.84	1.84	1.86	1.81	1.84	Si XIII
(keV)	(1.83–1.84)	(1.83–1.85)	(1.83–1.87)	(1.83–1.90)	(1.76–1.84)	(1.83–1.84)	
Flux	1.71	1.72	0.78	0.61	0.41	4.62	
(10^{-4}ph cm^{-2} s^{-1})	(1.43–1.98)	(1.25–2.18)	(0.42–1.10)	(0.36–0.86)	(0.23–0.60)	(3.75–5.54)	
Equivalent Width	43	30	18	17	14	23	
(eV)	(36–51)	(24–38)	(10–26)	(10–25)	(8–21)	(19–28)	
Center	1.98	1.99	1.99	1.99	1.98	1.99	Si XIV
(keV)	(1.97–1.98)	(1.99–2.00)	(1.98–1.99)	(1.99-2.00)	(1.97–1.99)	(1.99–1.99)	
Flux	2.77	3.23	1.96	1.33	0.82	9.67	
(10^{-4}ph cm^{-2} s^{-1})	(2.47–3.08)	(2.94–3.53)	(1.70–2.21)	(1.09–1.55)	(0.63–1.01)	(9.11–10.24)	
Equivalent Width	84	73	53	44	34	57	
(eV)	(73–93)	(66–80)	(45–60)	(36–50)	(26–43)	(53–60)	
Center	2.43	2.46	2.46	2.45	2.44	2.45	S XV
(keV)	(2.42–2.44)	(2.45–2.47)	(2.45–2.48)	(2.42–2.48)	(2.38–2.48)	(2.44–2.46)	
Flux	1.46	1.82	0.80	0.55	0.37	4.71	
(10^{-4}ph cm^{-2} s^{-1})	(1.21–1.72)	(1.57–2.08)	(0.59–1.01)	(0.36–0.74)	(0.21–0.54)	(4.23–5.20)	
Equivalent Width	73	68	36	29	25	45	
(eV)	(59–86)	(58–78)	(26–45)	(19–39)	(13–36)	(40–50)	
Center	2.59	2.62	2.62	2.62	2.62	2.61	S XVI
(keV)	(2.58–2.60)	(2.61–2.63)	(2.60–2.64)	(2.59–2.65)	(2.60–2.64)	(2.61–2.62)	
Flux	1.28	1.26	0.63	0.41	0.46	3.86	
(10^{-4}ph cm^{-2} s^{-1})	(1.05–1.51)	(1.04–1.48)	(0.44–0.82)	(0.24–0.58)	(0.31–0.62)	(3.43–4.29)	
Equivalent Width	74	55	33	25	36	43	
(eV)	(61–89)	(45–64)	(23–42)	(15–36)	(24–50)	(38–48)	
Center	3.12(fix)	3.12(fix)	3.12(fix)	3.12(fix)	3.12(fix)	3.12	Ar XVII
(keV)	—	—	—	—	—	(3.10–3.14)	
Flux	0.40	0.54	0.08	0.24	0	1.18	
(10^{-4}ph cm^{-2} s^{-1})	(0.25–0.55)	(0.38–0.70)	(<0.21)	(0.11–0.37)	(<0.07)	(0.88–1.48)	
Equivalent Width	39	37	6	23	0	21	
(eV)	(24–55)	(26–49)	(<17)	(11–35)	(<9)	(16–26)	
Center	3.89(fix)	3.89(fix)	3.89(fix)	3.89(fix)	3.89(fix)	3.89	Ca XIX
(keV)	—	—	—	—	—	(3.87–3.90)	
Flux	0.22	0.36	0.14	0.18	0.07	1.00	
(10^{-4}ph cm^{-2} s^{-1})	(0.10–0.33)	(0.24–0.48)	(0.04–0.24)	(0.08–0.28)	(<0.15)	(0.76–1.22)	
Equivalent Width	42	48	21	32	15	33	
(eV)	(20–64)	(32–64)	(5–37)	(15–49)	(<34)	(26–41)	
Center	6.69	6.65	6.68	6.68	6.64	6.67	Fe XXV
(keV)	(6.67–6.72)	(6.62–6.69)	(6.66–6.70)	(6.67–6.70)	(6.62–6.66)	(6.66–6.68)	
Flux	0.69	0.83	0.68	0.78	0.54	4.44	
(10^{-4}ph cm^{-2} s^{-1})	(0.54–0.85)	(0.68–0.98)	(0.55–0.82)	(0.64–0.92)	(0.42–0.66)	(4.04–4.83)	
Equivalent Width	1154	824	735	906	739	1060	
(eV)	(888–1455)	(674–1000)	(587–897)	(734–1088)	(568–921)	(958–1165)	
Center	7.86(fix)	7.86(fix)	7.86(fix)	7.86(fix)	7.86(fix)	7.86	Fe XXV
(keV)	—	—	—	—	—	(7.75–7.92)	and Ni XXVII
Flux	0.23	0.10	0.31	0.20	0.14	0.55	
(10^{-4}ph cm^{-2} s^{-1})	(0.05–0.41)	(<0.22)	(0.17–0.46)	(0.06–0.35)	(0.02–0.25)	(0.30–0.79)	
Equivalent Width	860	220	711	474	378	277	
(eV)	(196–1572)	(<493)	(371–1066)	(134–829)	(61–712)	(152–405)	

* The errors in the brackets are at 90% confidence level.

Table 6.2: The result of the thermal bremsstrahlung and narrow line model fitting to the GIS spectra.*

Radius	0′–2′	2′–4′	4′–6′	6′–8′	8′–10′	0′–10′	Identify
Brems kT	2.05	2.38	2.42	2.54	2.47	2.31	
(keV)	(1.90–2.21)	(2.23–2.55)	(2.26–2.58)	(2.37–2.73)	(2.28–2.68)	(2.24–2.39)	
$\chi^2/d.o.f.$	163.8/128	173.2/176	193.4/185	150.8/178	196.8/164	404.3/356	
Center	6.64	6.69	6.63	6.60	6.60	6.63	Fe XXV
(keV)	(6.59–6.69)	(6.63–6.74)	(6.57–6.69)	(6.55–6.65)	(6.54–6.67)	(6.60–6.65)	
Flux	1.05	0.83	0.78	0.81	0.59	4.20	
(10^{-4}ph cm^{-2} s^{-1})	(0.86–1.23)	(0.67–1.00)	(0.62–0.94)	(0.66–0.97)	(0.45–0.74)	(3.77–4.64)	
Equivalent Width	1415	807	733	834	712	944	
(eV)	(1098–1777)	(617–1015)	(562–929)	(652–1031)	(517–926)	(825–1074)	
Center	7.82(fix)	7.82(fix)	7.82(fix)	7.82(fix)	7.82(fix)	7.82	Fe XXV
(keV)	—	—	—	—	—	(7.75–7.90)	and Ni XXVII
Flux	0.30	0.27	0.30	0.13	0.16	1.10	
(10^{-4}ph cm^{-2} s^{-1})	(0.16–0.45)	(0.13–0.41)	(0.16–0.44)	(0.01–0.25)	(0.03–0.28)	(0.83–1.39)	
Equivalent Width	897	521	580	276	388	527	
(eV)	(432–1438)	(242–835)	(295–895)	(24–553)	(79–736)	(382–681)	

* The errors in the brackets are at 90% confidence level.

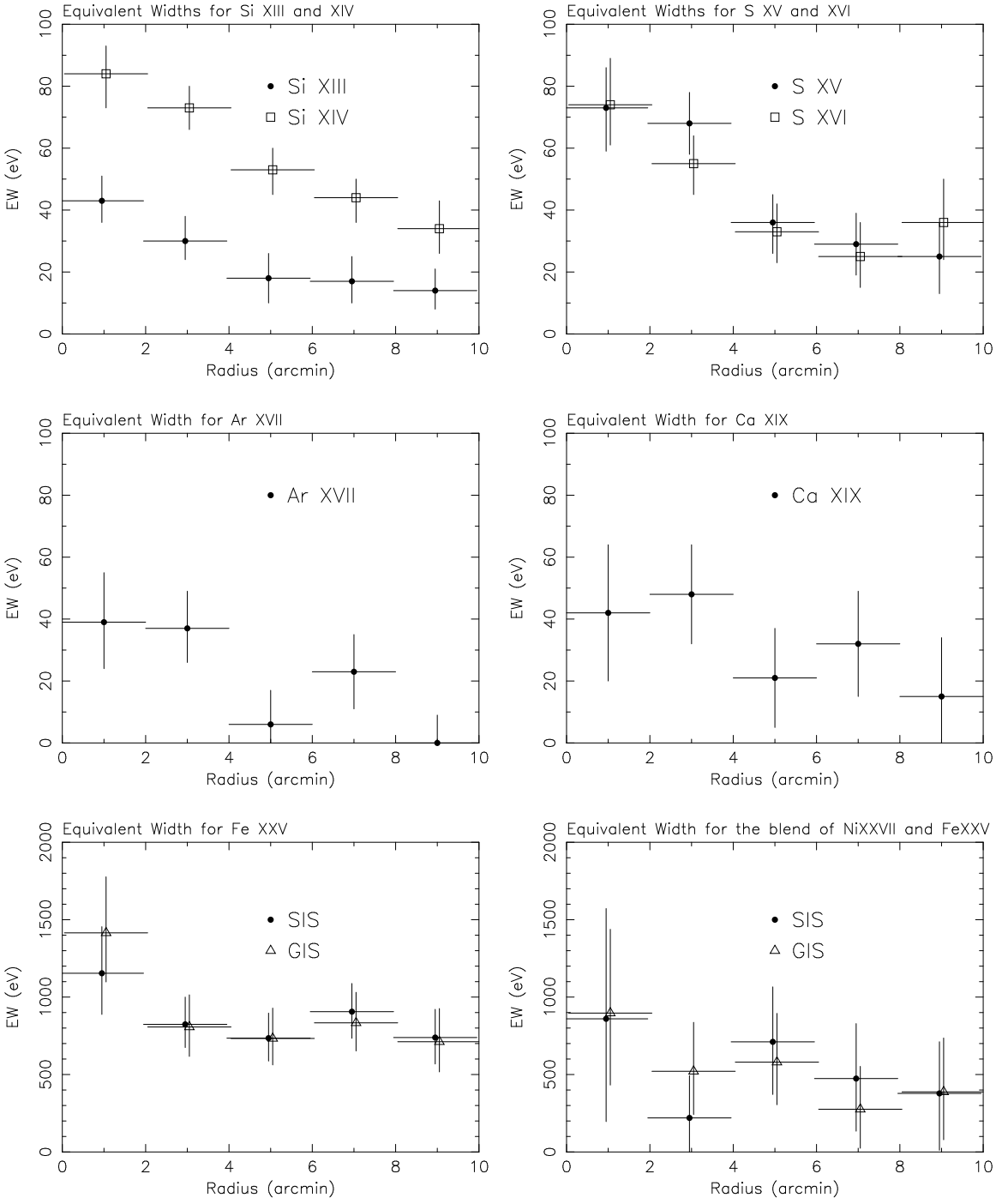

Figure 6.5: Equivalent width of emission lines plotted as a function of radius from the center of M87.

6.2.3 Thin Thermal Plasma Model

Many emission lines detected with ASCA tell us that the X-ray emission of M87 is due to an optically thin plasma. Therefore, we tried to fit the SIS and GIS spectra simultaneously with a thin thermal plasma model modified by interstellar absorption over the entire energy band of 0.4 – 10 keV for the SIS and 0.7 – 10 keV for the GIS. The plasma temperature, normalizations (i.e. emission integral; hereafter EI) for the SIS and GIS, interstellar absorptions for the SIS and GIS and metal abundances of O, Mg, Si, S, Ar, Ca, and Fe were free parameters.

We use the solar abundances given by Anders and Grevesse (1989) [2] to be the unit value (table E.1), hence the abundances means those relative to the solar values.

We fixed the abundances of C, N and Ne to be the same as that of O. Furthermore, we set the Ni abundance equal to that of Fe. The other elements in table E.1 like He, Na, Al and so on are fixed to the solar values. For the plasma model, we used the Raymond-Smith model (hereafter RS model; the revised version of Raymond and Smith (1977) [122]). Comparison between the RS model and MEKAL model is given in Appendix B.

The best-fit $\chi^2/d.o.f$ is given in table 6.3. This model is rejected in view of the large values of $\chi^2/d.o.f.$. In figure A.5, we give best-fit model curves and their residuals. Significant residuals were found around 1 keV and above 7 keV; also, the isothermal model gave a poorer fit in the inner regions rather than in the outer regions.

Table 6.3: The $\chi^2/d.o.f$ values of the one-temperature RS model fitting.

	$0'$–$2'$	$2'$–$4'$	$4'$–$6'$	$6'$–$8'$	$8'$– $10'$
$chi^2/d.o.f.$	1821/629	1882/716	1209/726	985.1/712	914.5/682

We are then forced to apply more complicated model: a plasma with hot and cool components (a two-temperature model).

At first we tried this model with free-abundances for both the components, then found that no constraint is given on the abundances. Thus we assumed the same metal abundances, other than Fe, between the hot and cool plasmas. In this case, we can obtain reasonable constraint on the abundances. However we should note that the results of Fe abundances strongly depends on plasma model. In figure 6.6, we show confidence contours of Fe abundance of the innermost region of M87 ($0'$ – $2'$), obtained with the RS and MEKAL model. The RS model gives almost the same Fe abundance between the cool and hot components, while the MEKAL model gives significantly larger Fe abundance in the hot component than that in the cool component. This

difference between the RS and MEKAL model is due to the large uncertainty of the atomic data of the Fe-L shell emission complex.

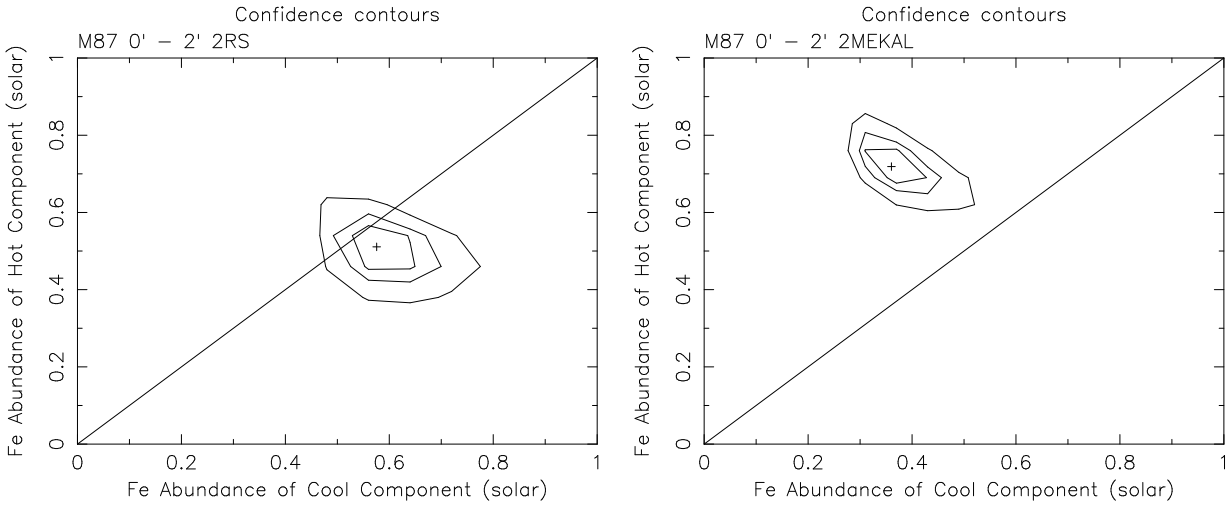

Figure 6.6: Confidence contours of Fe abundance when we fitted the spectra of the innermost region of M87 (0′–2′) with the two-temperature plasma model. The horizontal axis shows the Fe abundance of cool component, and the vertical shows that of hot component. Three contours of each panel show $\Delta\chi^2 = 2.71, 4.61, 9.21$: (a) RS model, (b) MEKAL model.

Consequently, we decided to assume all the metal abundances are the same between the two components. In this case, we find no abundance difference between the RS and MEKAL model (see Appendix B).

Thus, in the final two-components model, the free parameters were the temperatures of the hot and cool components, the abundances of O, Si, S, Ar, Ca, and Fe, the normalizations of the hot component for the SIS and the GIS, the ratio of normalization of the cool component to that of the hot component, and the interstellar absorptions for the SIS and the GIS .

The two-temperature model gives a significant improvement on the single-temperature model. For details, one should refer Appendix A, where we demonstrate the best-fit model curves in figure A.6, which can be compared to figure A.5. The best-fit parameters from each region are given in table 6.4. The derived kT for the lower temperature component is consistent with that derived by the Einstein SSS (Lea et al. 1982 [84]).

We should note, however, the two-temperature model is still rejected with the χ^2 statistics. We therefore further tried a three-temperature model, but obtained no improvement in the $\chi^2/d.o.f.$ value. The large χ^2 values come primarily from residuals near to 1 keV and 0.5 keV.

Table 6.4: The results of the two-temperature RS model fitting.*

Radius	0′–2′	2′–4′	4′–6′	6′–8′	8′–10′
$N_{\rm H}$(SIS)	5.78	6.59	6.25	5.04	5.41
(10^{20}cm^{-2})	(5.22–6.36)	(6.14–6.96)	(5.78–6.74)	(4.53–5.56)	(4.82–6.02)
$N_{\rm H}$(GIS)	3.37	3.18	2.29	0.48	2.06
(10^{20} cm^{-2})	(1.86–4.90)	(1.84–3.98)	(0.89–3.71)	(<2.05)	(0.03–3.85)
kT_1	1.17	1.36	1.41	1.44	1.43
(keV)	(1.14–1.24)	(1.33–1.38)	(1.38–1.44)	(1.43–1.61)	(1.34–1.67)
kT_2	2.51	3.32	3.20	3.27	3.09
(keV)	(2.37–2.81)	(3.01–4.01)	(2.92–3.57)	(3.06–3.80)	(2.78–3.90)
Abundance (Solar)					
O	0.32	0.35	0.44	0.33	0.29
	(0.23–0.42)	(0.27–0.43)	(0.34–0.54)	(0.23–0.45)	(0.17–0.43)
Mg	0.00	0.00	0.00	0.00	0.00
	(<0.01)	(<0.01)	(<0.02)	(<0.03)	(<0.11)
Si	0.76	0.68	0.60	0.62	0.47
	(0.68–0.83)	(0.62–0.74)	(0.54–0.67)	(0.55–0.69)	(0.39–0.55)
S	0.74	0.66	0.49	0.50	0.42
	(0.66–0.82)	(0.60–0.73)	(0.42–0.55)	(0.42–0.58)	(0.33–0.52)
Ar	0.57	0.74	0.33	0.53	0.34
	(0.34–0.80)	(0.54–0.88)	(0.13–0.53)	(0.29–0.77)	(0.09–0.60)
Ca	0.89	0.96	0.36	0.54	0.38
	(0.55–1.24)	(0.65–1.18)	(0.07–0.65)	(0.21–0.87)	(0.04–0.73)
Fe	0.55	0.45	0.37	0.35	0.29
	(0.51–0.59)	(0.42–0.48)	(0.34–0.40)	(0.32–0.38)	(0.26–0.33)
EI(SIS)§	7.89	7.25	7.24	6.80	6.08
(10^{64} cm^{-3})	(6.19–8.73)	(5.57–8.50)	(6.09–8.35)	(4.81–7.47)	(3.70–7.32)
EI(GIS)§	8.48	6.33	7.38	6.75	6.81
(10^{64} cm^{-3})	(6.65–9.40)	(4.94–7.43)	(6.21–8.52)	(4.77–7.42)	(4.18–8.21)
EI ratio‡	0.94	1.76	1.14	0.80	0.60
(cool-kT/hot-kT)	(0.72–1.52)	(1.32–2.68)	(0.83–1.59)	(0.62–1.55)	(0.31–1.65)
Cool Component					
Fx(10^{-11} erg/s/cm^2)†					
SIS	2.40	3.83	2.39	1.58	0.99
GIS	2.71	3.57	2.64	1.71	1.19
Lx(10^{41} erg/s)††					
SIS	7.29	11.71	7.28	4.68	2.97
GIS	7.84	10.23	7.43	4.64	3.33
Hot Component					
Fx(10^{-11} erg/s/cm^2)†					
SIS	3.08	3.15	3.03	2.89	2.43
GIS	3.42	2.86	3.25	3.04	2.85
Lx(10^{41} erg/s)††					
SIS	8.99	9.17	8.83	8.28	7.02
GIS	9.65	8.00	9.00	8.22	7.87
$\chi^2/d.o.f.$	1016/627	1127/714	971.2/724	850.5/710	851.4/680

* The errors in the brackets are at 90% confidence level.

§ EI is Emission Integral of hot component.

‡ Ratio of EI of cool component to that of hot component.

† X-ray flux in the 0.5 – 10 keV band from each annulus.

†† X-ray luminosity in the 0.5 – 10 keV band from each annulus.

The large residuals around 1 keV is consistent with an origin in the Fe-L complex. Since the atomic data of these lines still have considerable ambiguity, the residual structure may depend on thin thermal model codes. For a comparison, we tried the MEKAL model but found no essential difference from the RS model (Appendix B). We nevertheless not go into detail on the 1 keV structure, until more reliable iron L-shell data become available to the thin plasma codes.

For the large residuals around 0.5 keV, Yamashita (1995) [160] reported that many objects show the structures like this and concluded that this is possibly due to a calibration problem of the SIS. Accordingly, we presently consider the two-temperature plasma to be the most reasonable model to describe the Virgo spectra.

We found that the temperatures of the hot and cool components are almost constant within the M87 region which are shown in figure 6.7. The mean values of the best-fit temperature of the hot and cool components weighted using relative errors are 2.9 and 1.4 keV.

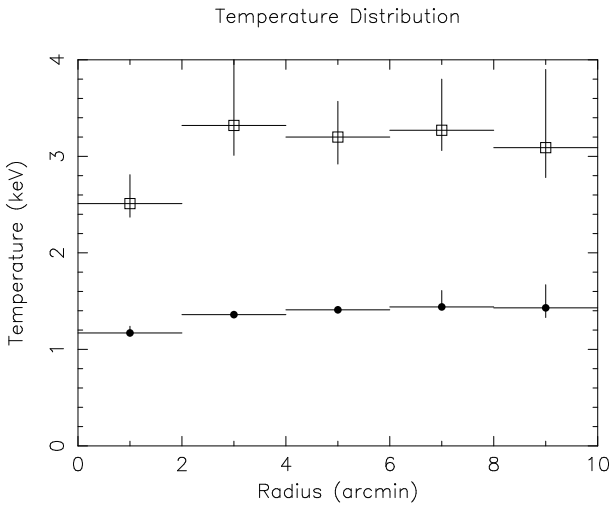

Figure 6.7: Temperature distribution of the two-temperature RS model.

We show in figure 6.8 (a) the distribution of the ratio of EI (Emission Integral) of the cool component to that of the hot component. There is only weak evidence of a radial variation of the EI ratio within its large errors. However, since the EI and temperature of each component are strongly coupled in the fitting procedure, we fixed the temperature of the hot component to be its mean value (2.9 keV) and re-evaluated the spectral parameters. The best-fit parameters and the model curves are shown in table 6.5 and figure A.7. Except for EI, flux, luminosity of each component and EI ratio, we can see no essential differences between table 6.4 and 6.5. However, in figure 6.8 (b), we can find that the EI of the cool component decreases more rapidly than that of the hot component.

Plots of the radial distribution of the best-fit abundances for each element are given in figure

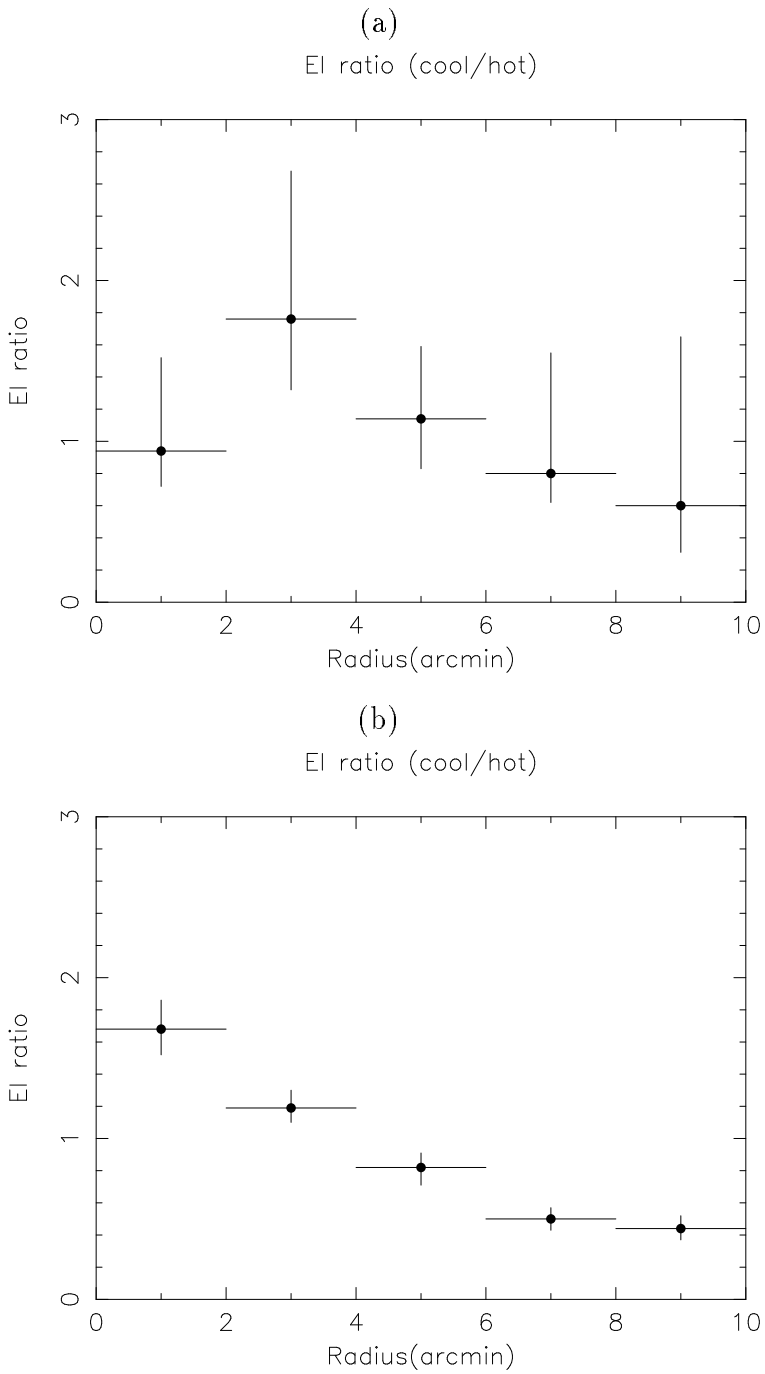

Figure 6.8: Ratio of emission integral of the cool component to that of the hot component plotted as a function of the radius from the center of M87: (a)both temperatures of the hot and cool components are free parameters, (b)temperature of the hot component is fixed to be 2.9 keV.

Table 6.5: The results of the two-temperature RS model fitting. The temperature of the hot component is fixed to 2.9 keV.*

Radius	0′–2′	2′–4′	4′–6′	6′–8′	8′–10′
$N_{\rm H}$(SIS)	5.95	6.45	6.17	4.99	5.35
(10^{20}cm^{-2})	(5.39–6.52)	(6.02–6.89)	(5.71–6.63)	(4.49–5.49)	(4.77–5.93)
$N_{\rm H}$(GIS)	3.48	3.18	2.25	0.51	2.80
(10^{20} cm^{-2})	(1.97–5.02)	(1.72–4.39)	(0.85–3.65)	(<2.07)	(0.29–3.83)
kT_1(keV)	1.25	1.33	1.39	1.42	1.40
	(1.23–1.27)	(1.31–1.34)	(1.36–1.41)	(1.39–1.47)	(1.34–1.44)
kT_2(keV)	2.9(fix)	2.9(fix)	2.9(fix)	2.9(fix)	2.9(fix)
Abundance (Solar)					
O	0.29	0.38	0.46	0.40	0.31
	(0.21–0.39)	(0.29–0.46)	(0.36–0.56)	(0.29–0.52)	(0.18–0.45)
Mg	0.00	0.00	0.00	0.00	0.00
	(<0.01)	(<0.01)	(<0.03)	(<0.04)	(<0.13)
Si	0.71	0.72	0.63	0.65	0.48
	(0.65–0.77)	(0.67–0.77)	(0.58–0.69)	(0.58–0.73)	(0.41–0.57)
S	0.72	0.69	0.50	0.50	0.43
	(0.64–0.80)	(0.62–0.76)	(0.43–0.57)	(0.41–0.58)	(0.33–0.52)
Ar	0.65	0.68	0.29	0.46	0.32
	(0.42–0.88)	(0.49–0.87)	(0.10–0.48)	(0.23–0.68)	(0.07–0.57)
Ca	0.97	0.87	0.33	0.50	0.36
	(0.61–1.33)	(0.60–1.15)	(0.06–0.60)	(0.20–0.80)	(0.03–0.69)
Fe	0.52	0.48	0.39	0.37	0.31
	(0.49–0.55)	(0.45–0.50)	(0.36–0.41)	(0.35–0.40)	(0.28–0.33)
EI(SIS)§	5.84	8.91	8.40	8.02	6.69
(10^{64} cm^{-3})	(5.52–6.16)	(8.55–9.27)	(8.06–8.74)	(7.69–8.35)	(6.38–7.04)
EI(GIS)§	6.28	7.78	8.57	7.96	7.51
(10^{64} cm^{-3})	(5.94–6.61)	(7.47–8.09)	(8.23–8.92)	(7.64–8.27)	(7.17–7.85)
EI ratio‡	1.68	1.19	0.82	0.50	0.44
(low-kT/high-kT)	(1.52–1.86)	(1.10–1.30)	(0.71–0.91)	(0.43–0.57)	(0.37–0.52)
Cool Component					
Fx(10^{-11} erg/s/cm^2)†					
SIS	3.07	3.29	2.02	1.19	0.83
GIS	3.47	3.07	2.23	1.29	0.96
Lx(10^{41} erg/s)††					
SIS	9.32	10.05	6.16	3.52	2.41
GIS	10.03	8.79	6.29	3.50	2.70
Hot Component					
Fx(10^{-11} erg/s/cm^2)†					
SIS	2.42	3.66	3.39	3.26	2.61
GIS	2.68	3.34	3.64	3.45	3.06
Lx(10^{41} erg/s)††					
SIS	7.02	10.71	9.88	9.37	7.55
GIS	7.54	9.36	10.09	9.31	8.47
$\chi^2/d.o.f.$	1020/628	1131/715	974.1/725	858.9/711	852.7/681

* The errors in the brackets are at 90% confidence level.

§ EI is Emission Integral of hot component.

‡ Ratio of EI of cool component to that of hot component.

† X-ray flux in the 0.5 – 10 keV band from each annulus.

†† X-ray luminosity in the 0.5 – 10 keV band from each annulus.

6.9. We can see that the abundances of Si, S, and Fe have a strong concentration toward the M87 center, as suggested in subsection 6.2.2. On the other hand, the O abundance is rather constant from place to place. We can say no definite statement on the distributions of Ar and Ca, because the errors are relatively large. No significant variation of S/Fe , nor Si/S is found over the entire image. The observed Si/Fe ratio is similar to that found in clusters of galaxies (Mushotzky et al. 1996 [118]).

The obvious spectral distinctions between the "cluster gas" and the gas associated with M87 is due to the increases of the absolute abundance and the flux of the cool component.

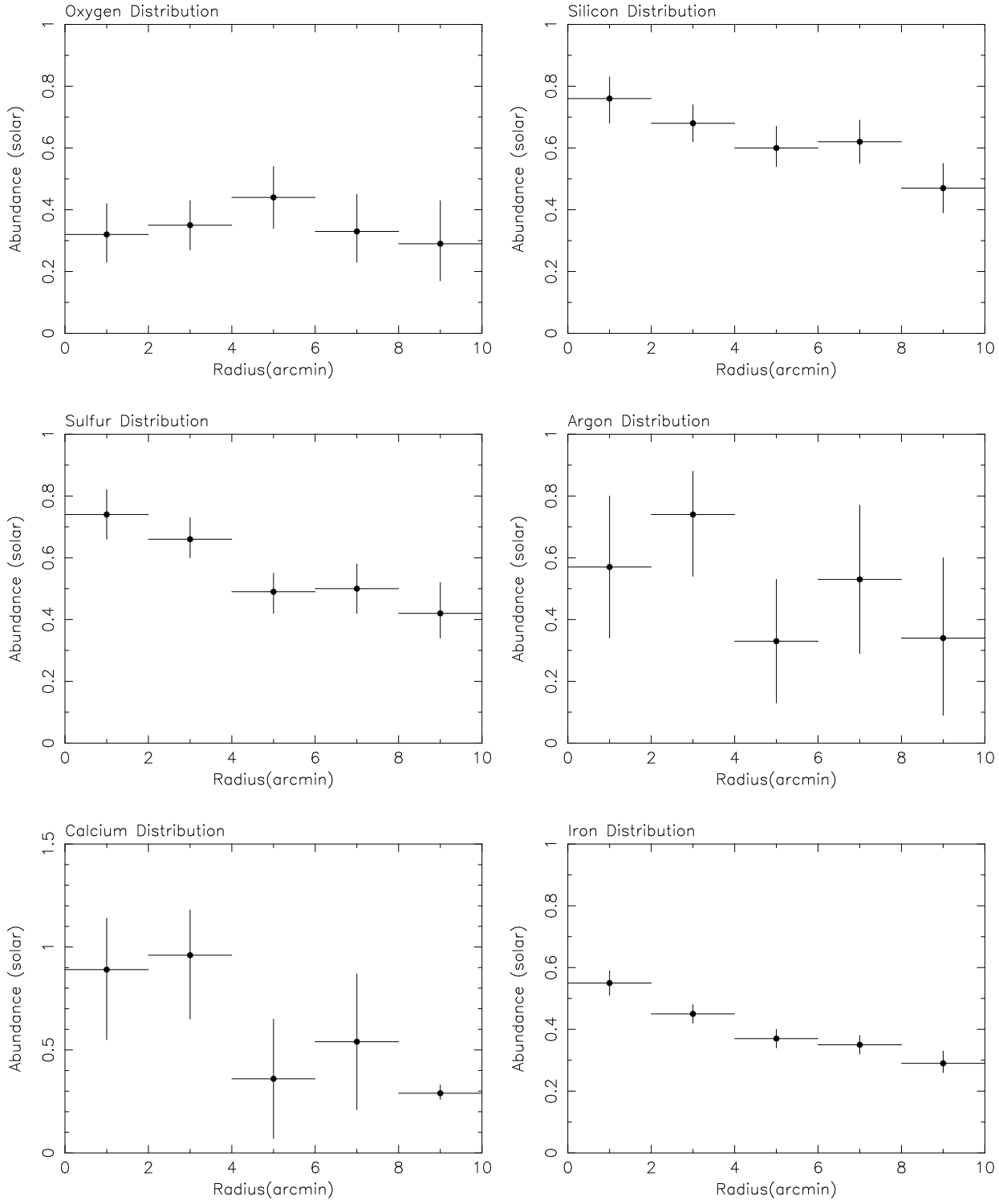

Figure 6.9: Abundance distribution of O, Si, S, Ar, Ca, and Fe. In this analysis, the temperature of each component is a free parameter.

6.2.4 X-ray Emission from AGN of M87

A power-law component, probably due to an AGN located in the nucleus of M87, has previously been reported with HEAO-1, Einstein, and Ginga (e.g. Lea et al. 1981 [85]; Schreier et al. 1982 [138]; Takano 1990 [143]; Takano and Koyama 1991 [144]; Hatsukade 1989 [63]). We therefore examined for the presence or absence of this power-law component in the ASCA spectra and image.

The power-law component dominates the Ginga spectra above the 4 keV band (Takano 1990 [143]; Takano and Koyama 1991 [144]; Hatsukade 1989 [63]). Therefore we study the hard band image of M87. In figure 6.10 (a), we show the X-ray image of M87 taken with the GIS in the 7 – 10 keV band. Figure 6.10 (b) shows the radial profile of this image and the point spread function (PSF). Since the radial profile is much broader than the PSF, we concluded that we can see no point-like object at the position of M87 in the ASCA image.

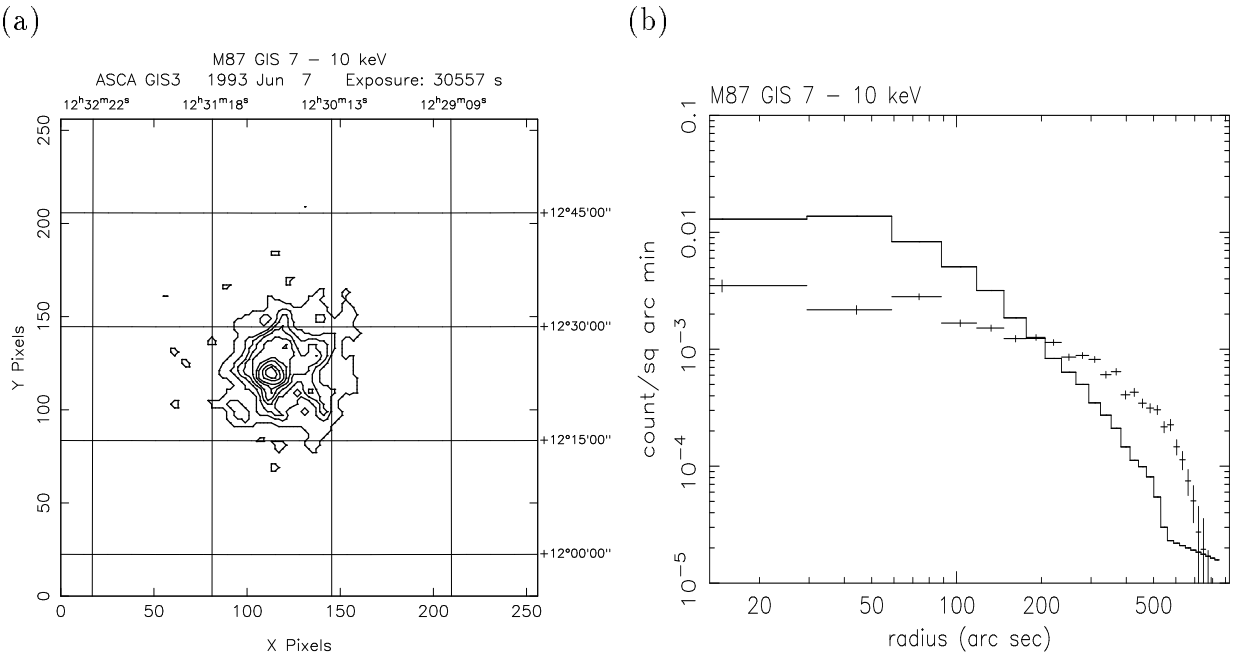

Figure 6.10: (a) Hard band (7 – 10 keV) X-ray image of M87 taken with the GIS; (b) Radial profile of (a). The solid line shows the expected radial profile for a point-like source.

When we fitted the ASCA spectra of the innermost region of M87 with the two-temperature thermal plasma model, there is no significant residual in the high energy band, which can be seen in figure A.6 and A.7. Therefore we concluded that we can find no power-law component in the ASCA spectra.

To estimate the upper limit of the flux of the power-law component, we added a power-law model to the two-temperature RS model and fitted the ASCA spectra of the innermost region

of M87 with this model. The photon index of the power-law component is fixed to be 1.7, which is the typical value for AGN (Mushotzky et al. 1993 [114]). Furthermore, because the flux of the power-law component and the temperature of the hot component are strongly coupled, we fixed the temperature of the hot component to be 2.9 keV. The upper limit of the absorption-corrected fluxes in the 0.5 – 10 keV band of the power-law component are determined to be 2.2×10^{-12} erg/cm^2/s for the SIS and 2.7×10^{-12} erg/cm^2/s for the GIS.

6.2.5 Cooling Flow Model

Many X-ray observations of M87 reported the existence of the cooling flow at the center of M87 with the mass deposition rate of 3 – 20 $M_\odot$/yr (Fabricant et al. 1980 [43]; Fabricant and Gorenstein 1983 [44]; Canizares et al. 1979 [22]; Canizares et al. 1982 [23]; Lea et al. 1982 [84]; Mushotzky 1984 [112]; Stewart et al. 1984 [140]).

Therefore we fitted both the SIS and GIS spectra within 10′ radius from the center with the constant-pressure cooling flow model (hereafter "cflow" model) (Mushotzky and Szymkowiak 1988 [113]; see section 2.3.4) plus an additional thermal plasma model modified by interstellar absorption; this model is expressed as

$$AB(N_H) \times [CF(\dot{M}, T_{min}, T_{max}, \text{Abundances}) + P(T_{max}, \text{Abundances}, \text{EI})], \qquad (6.4)$$

where AB is the interstellar absorption model, CF is the cflow model and P is the additional thermal plasma model which represents the hot plasma that has not yet cooled down. CF is a function of the mass deposition rate $\dot{M}$, the maximum temperature T_{max} from which the gas cools down, the minimum temperature T_{min} to which the gas cools. The temperature is distributed continuously from T_{max} to T_{min} and each temperature component has emission integral (EI) which is inversely proportional to the total emissivity of that temperature. The additional thermal plasma component must have the same temperature as T_{max}. In this fitting, the free parameters were the normalization of the cflow model (i.e. $\dot{M}$) for the SIS and GIS, T_{max}, the abundances of O, Si, S, Ar, Ca, and Fe, the ratio of the normalization of the additional thermal component (i.e. EI) to that of the cflow model, and the interstellar absorptions for the SIS and the GIS. We tied the abundance of each element of the additional thermal plasma component to be the same as that of the cflow model. Because $\dot{M}$ and T_{min} are strongly coupled, we have to fix T_{min}. According to Fabian et al. 1994 [40], the lowest temperature of the cooling flow should be below 0.1 keV, hence T_{min} is fixed to be 0.1 keV.

This cooling flow mode, however, is found to be rejected with large residuals and $\chi^2/d.o.f.$. Nevertheless, we show the best-fit parameters and model curves in figure 6.11 and table 6.6.

We suspected that the failure of the fitting is due to simplified cflow modeling:

1. although the nominal cooling radius is larger than 10′ (Stewart et al. 1984 [140]), we assumed that X-rays from the cooling flow are entirely in the detectors field of view,
2. the mass "dropping out" effect is not taken into account,
3. the abundances are assumed to be constant with the radius, and
4. the plasma pressure is assumed to be constant.

Further detailed modeling for the cooling flow, however, is beyond the scope of the paper.

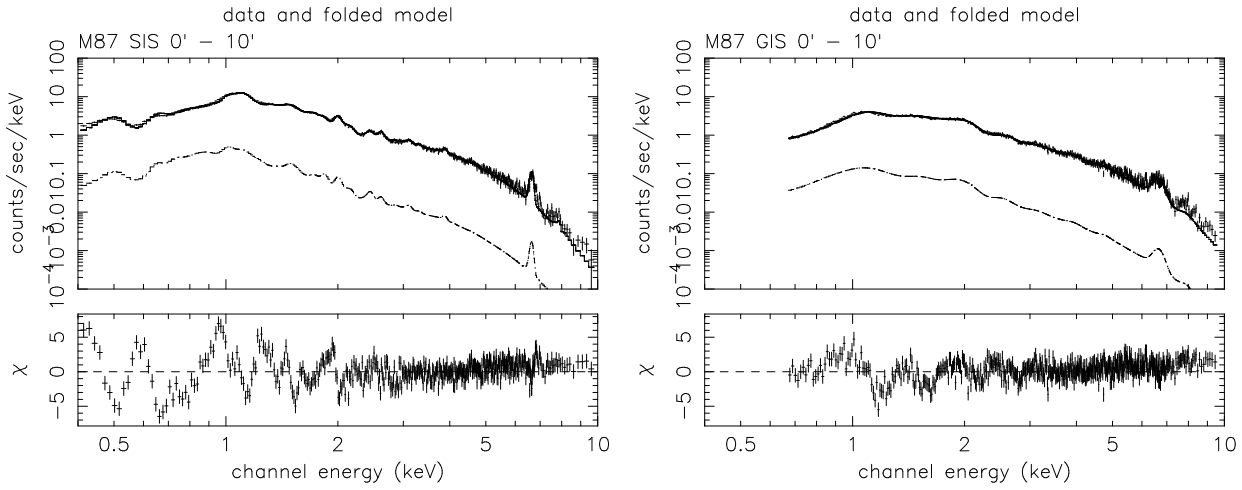

Figure 6.11: The ASCA spectrum of M87 in the 0′– 10′ region. The solid line shows the best-fitting cooling flow plus additional thermal plasma model.

Table 6.6: Results of the cflow model fitting

N_H(SIS) (cm^{-2})	(6.1±0.3)×10^{20}
N_H(GIS) (cm^{-2})	(2.4±0.7)×10^{20}
kT_{min} (keV)	0.1(fix)
kT_{max} (keV)	2.1±0.01
Abundance (solar)	
O	0.68±0.05
Mg	0(<0.06)
Si	0.69±0.03
S	0.57±0.04
Ar	0.40±0.10
Ca	0.71±0.13
Fe	0.48±0.01
$\dot{M}$ (SIS)(M$_\odot$/yr)	1.0±0.3
$\dot{M}$ (GIS)(M$_\odot$/yr)	1.2±0.3
norm ratio†	0.3±0.1
$\chi^2/d.o.f.$	2579/1006

The errors are at 90% confidence level.

†norm ratio = $\frac{\text{norm of additional thermal plasma model}}{\text{norm of cflow model}}$

6.3 Discussion

6.3.1 Interstellar Absorption

The column density for the interstellar absorption due to our Galaxy is $N_H = 2.6\times10^{20}$ cm^{-2} (Heiles 1975 [65]). In fact, the HEAO-1 observation (Lea et al. 1979 [83]) and the Einstein IPC observation (Fabricant, Gorenstein 1983 [44]) gave this value. The Einstein SSS spectrum gives higher values of $(5 - 20)\times10^{20}$ cm^{-2} (Lea et al. 1982 [84]) and 17.5×10^{20} cm^{-2} (White et al. 1991 [158]). However, Tsai (1994) [150] found no evidence that the absorption is larger than the Galactic value in the SSS spectrum, and claimed that the large value of the previous report may have been due to remaining calibration problems.

In our analysis, although the column densities determined with the GIS are consistent with the Galactic value, those from the SIS are $\sim 5\times10^{20}$ cm^{-2}, twice the Galactic absorption. Since the thickness of the thermal shield of the XRT and SiO_2 of the CCD electrode is equivalent to $\sim 3.5\times10^{21}$ cm^{-2} (Miyata et al. 1994 [109]), the SIS is insensitive by the small Galactic absorption. Therefore we suspect this difference of column density between the SIS and GIS is within the calibration errors.

We should note that the GIS data give a lower column density for the mapping observations of the Virgo cluster (see chapter 7). This suggests that the absorption seen in the central regions of the M87 region may be real, and larger than that at the regions far from M87. This may be attributable to the cooling flow (White et al. 1991 [158]).

6.3.2 Nuclear Activity of M87

We detected no strong X-ray attributable to the AGN of M87. Since M87 has the nuclear black hole of 3×10^9 $M_\odot$(Ford et al. 1994 [46]; Harms et al. 1994 [61]), accretion from the ICM with $\dot{M} \sim 10M_\odot$/yr, for example, may produce a luminosity of $\sim 1\times10^{46}$ erg/s, comparable to that of a quasar. Hence no apparent AGN activity of M87 is puzzling. Reynolds et al. (1996) [125] adopted a model of the advection-dominated accretion disc and found that the model can explain the core flux from the radio through to the X-ray wavelengths.

Some of previous X-ray observations of M87 reported the luminosity of the power-law component or the upper limit of this component (Schreier, Gorenstein and Feigelson 1982 [138]; Lea et al. 1982 [84]; Hanson et al. 1990 [60]; Takano and Koyama 1991 [144]). We converted these values to those in the 0.5 – 10 keV band assuming the distance to M87 is 15 Mpc and show them in table 6.7 and figure 6.12. We find a long-term variability of the nucleus flux of

M87, from the HEAO-1 to the ASCA observations.

Table 6.7: Luminosity of the power-law component in the 0.5 – 10 keV band.

Detector	Observation	L_X(erg/s)†	Reference
HEAO-1 A2 + A4	1977 Dec. 17–31	$(3.1\pm1.0)\times10^{43}$	Lea et al. 1981 [85]
HEAO-1 A2 + A4	1978 June 13 – 26	$(8.1\pm3.7)\times10^{42}$	Lea et al. 1981 [85]
Einstein SSS	1978 June 22 – 26	$(2.6\pm0.4)\times10^{42}$	Lea et al. 1982 [84]
HEAO-1 A2 + A4	1978 Dec. 16 – 1979 Jan. 1	$(7.4\pm2.1)\times10^{43}$	Lea et al. 1981 [85]
Einstein HRI	1979 July 5 – 9	$<1.4\times10^{41}$	Schreier et al. 1982 [138]
SL2XRT	1985 July 29 & Aug 6	$<3.6\times10^{41}$	Hanson et al. 1990 [60]
Ginga LAC	1988 June 6 – 9	$(6.6\pm1.1)\times10^{41}$	Takano et al. 1991 [144]
ASCA SIS and GIS	1993 June 7	$<6.6\times10^{40}$	This thesis

†Luminosity in the 0.5 – 10 keV band. We assume the distance to M87 is 15 Mpc.

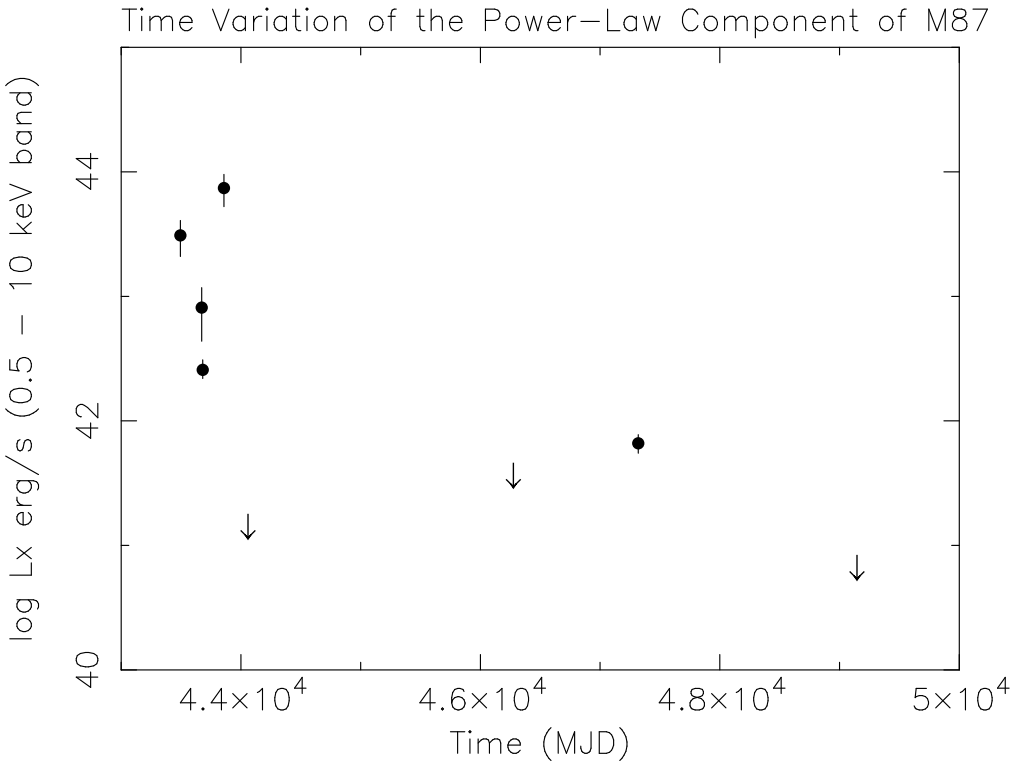

Figure 6.12: Time variability of the power law component of M87. The downward arrows show the upper limit.

6.3.3 Temperature Structure

We found that the X-ray emitting plasma in the M87 region require at least two spectral components. The temperature of the hot component is found to be about 2.9 keV, with no significant radial variation. This temperature is slightly higher than that found with Ginga (Takano 1990 [143]; Takano, Koyama 1991 [144]; Hatsukade 1989 [63]).

In order to compare the Ginga results, we fit the ASCA data above the 2 keV band with a single-temperature model, since Ginga is only sensitive for the X-rays above 2 keV. Then we derive a temperature consistent with the Ginga result. Böhringer et al. (1994) [16] fitted isothermal models to the ROSAT data, and derived a slightly lower temperature than that found with ASCA. However, the sensitive energy band of ROSAT is below 2.5 keV, and the energy resolution is limited. We simulated the ROSAT result by fitting a single-temperature plasma to the ASCA data in the limited energy band below 2.5 keV, after smoothing the energy bins to become comparable to the energy resolution of ROSAT. We find a kT consistent with the Böhringer et al. (1994) [16] result. Therefore, the apparent difference in the estimated temperatures between the ASCA, Ginga, and ROSAT are due to the difference in the energy bands, energy resolution, and fitted model.

Since the temperature of the hot component obtained with ASCA is almost the same as that obtained with non-imaging instruments with a wider field of view than ASCA, and since the hot component extends beyond $40'$ from the center (see chapter 7), we conclude that the hot component is due to the intracluster plasma which pervades the Virgo cluster with a nearly constant temperature of 2.9 keV [however, we note that the temperature near to the M49 subcluster has been reported to be higher than that of the M87 main cluster (Koyama, Takano, and Tawara 1991 [82]; Takano 1990 [143])]. Since the EI of the cool component drops more rapidly with distance from M87 than that of the hot component, and the temperature of the cool component is also constant within the $10'$ region centered on M87, we conclude that the cool component is not associated with the intracluster gas, but is confined in the M87 galaxy. Alternatively, the cool component could be directly associated with the postulated cooling flow, since the cooling times in the central region are very small: based on our spatially resolved spectra, less than 2×10^9 yr in the central $2'$ radius. If we attribute the luminosity of the cool component to the cooling flow, we can estimate the mass deposition rate ($\dot{M}$) using the relation of

$$L_{cool} = \frac{5}{2}\frac{\dot{M}}{\mu m_p}kT \tag{6.5}$$

(see Eq. (2.58)), where L_{cool} is bolometric X-ray luminosity of the cool component which is

equal to the energy loss rate of the cooling flow, and kT is the temperature at the cooling radius. Substitute our results to this equation, we get $\dot{M} \sim 1$ $M_\odot$/yr. Since the cooling radius of M87 is larger than $10'$ and we do not see the whole cooling region, this value should be the lower limit, and is consistent with the previous observations.

6.3.4 Abundance Structure

Although a marked gradient in the Fe abundance has been found in some clusters of galaxies (Ohashi et al. 1994 [120]; Fukazawa et al. 1994 [49]; Ikebe 1996 [71]), no gradient of Si nor S abundance has been previously reported.

We have confirmed the Ginga (Koyama, Takano, and Tawara 1991 [82]; Takano 1990 [143]) result that Fe is concentrated toward the M87 center, and have extended this result to the inner region of M87. However, the O abundance shows no significant radial variation.

With the ASCA data of M87, the Fe abundance is determined by both the Fe K and L lines. Therefore this Fe concentration is due not only to the increase of equivalent width of the Fe-K emission (figure 6.5) but also to the Fe-L emissions. This is confirmed by Hwang et al. (1997) [70], who reported that the Fe abundance derived only by the Fe-K line is consistent with that derived only by the Fe-L lines using the ASCA M87 data. This consistency of abundance measurements between Fe K and Fe L is also reported by Mushotzky et al. (1996) [118] and Fukazawa (1997) [51] using ASCA data of other clusters of galaxies.

We fitted the abundance profile of iron with an analytic function of the form,

$$A_{Fe}(r) = A_{0Fe} - A_s \left[1 - \exp(-\frac{r}{\lambda})\right]. \tag{6.6}$$

The best-fitting parameters and errors are 0.62 ± 0.07 solar for A_{0Fe}, 0.38 ± 0.11 solar for A_s and $5'.2\pm4'.5$ for λ. Assuming that the density profile of the plasma of M87 is the beta profile, we can estimate the mass of iron within $10'$ from the center. According to the results of the Einstein observation, we assumed the central proton density, beta and core radius are 3.6×10^{-2} cm^{-3}, 0.44 and $1'.6$, respectively (Fabricant and Gorenstein 1983 [44]), and estimated the iron mass within $10'$ to be 4.3×10^7 $M_\odot$. On the other hand, we can estimate the iron mass to be 3.6×10^7 $M_\odot$, under the assumption of spatially uniform iron abundance of 0.3 solar, the abundance of the outermost region. The excess of the former above the latter is about 0.7×10^7 $M_\odot$. This "extra" mass of iron would be due to the recent mass loss from M87, hence is compared it with the results of the stellar mass loss rate; the standard mass-loss rate is $1.5\times10^{-11}M_\odot/L_B$/yr, where L_B is a B-band luminosity of a galaxy in a Solar unit (Awaki et al. 1994 [7]; Ciotti et al.

1991 [25]). According to the luminosity profile of de Vaucouleurs and Nieto (1978) [30] with an assumption of B-band absorption of 0.06 mag (Tsai 1993 [149]), and adopting the B-band luminosity (L_B) of M87 of $\sim 4.5\times10^{10}$ within 10′, we can estimate the mass loss rate of M87 to be 0.68 $M_\odot$/yr. If the iron abundance in the stellar mass-loss gas is one solar, the stellar mass time is required to be $\sim 4\times10^9$ yr to accumulate the "extra" iron.

We found that the abundance ratio between Fe, Si, and S does not change towards the center. This fact strongly limits the contribution of a type-I SN to the 'extra" iron, because type-I SN preferentially produce a large amount of Fe, hence would largely change the abundance ratios.

A detailed calculation of the metallicity gradient should be also taken into account of effects of the cooling flow (Reisenegger, Miralda-Escudé, and Waxman 1996 [123]).

For the abundance profiles of O, Si, and S, we also adopted Eq. (6.6) and estimated the total masses of them. They are summarized in table 6.8.

Table 6.8: The total masses of metals within 10′ radius from the center of M87.

element	mass ($M_\odot$)
gas	6.1×10^{10}
oxygen	2.2×10^8
silicon	2.6×10^7
sulfur	1.2×10^7
iron	4.3×10^7

The abundance ratio of O/Fe is found to be smaller than the solar value, which disagrees with the Einstein FPCS result; the O/Fe ratio is 3 – 5 times the solar value (Canizares et al. 1982 [23]; Tsai 1994 [150]).

One may argue that the abundance of oxygen strongly depends on the column density of the interstellar absorption. To make this clear, we performed a two-temperature analysis for the 0′ – 10′ spectrum, in which the column density was assumed to be 1×10^{21} cm^{-2}, about two-times larger than the maximum value of the best-fit $N_{\rm H}$s. Still the ratio of O/Fe is found to be at most 1.5 the solar value. Therefore, the smaller O/Fe in the ASCA data compared to the Einstein result is not an artifact due to a possible ambiguity in the fitted column density.

For a further check of whether the line fluxes detected with FPCS (table 6.9 which is from the table 1 of Canizares et al. 1982 [23]) are consistent with the ASCA SIS spectrum in the 0′ – 10′ region, we simulated a FPCS spectrum, convolved it with the SIS response and compared it with the ASCA SIS spectrum in the 0.4 – 6 keV band. We made a convolved FPCS spectrum by applying a thermal bremsstrahlung model for a continuum modified by interstellar absorption,

then added 10 narrow lines with the fixed-flux ratio given in table 6.9. To this spectrum we further added narrow lines whose center energies are outside of the energy band of FPCS (> 1.2 keV) one by one until we obtained no significant decrease in the χ^2 value. Figure 6.13 is the result of this "simulation spectrum" together with the real SIS spectrum of the M87 region. The best-fit "simulated" values of the column density and temperature were found to be $N_{\rm H} = 9.6\times10^{20}$ cm^{-2} and $kT = 2.1$ keV, respectively. This column density is about 4 – 5 times the Galactic value. Even with this unreasonable large $N_{\rm H}$, we found a large model excess of around 0.65 keV at the energy of the O VIII Lyα line. This suggests that the flux of the O VIII Lyα line estimated by Canizares et al. (1982) [23] is significantly larger than that seen in the ASCA spectrum.

Table 6.9: X-ray lines from M87 detected with the Einstein FPCS (Canizares et al. 1982)

Line	Rest Energy (eV)	Corrected Line Flux† 10^{-3} ph cm^{-2} s^{-1}	Dominant Ions
O VIII Lyα	654	9.4±3.1	O VIII
O VIII Lyβ	774	<1.2	O VIII
Blend 1	945 – 978	2.1±0.4	Fe XX, XXI, XXII
Blend 1.5	980 – 999	<0.56	...
Blend 2	1000 – 1029	1.9±0.4	Ne X, Fe XVII, XX, XXI, XXII
Blend 3	1030 – 1052	1.6±0.4	Fe XXI, XXII
Blend 4	1116 – 1138	0.9±0.4	Fe XIX
Blend 5	1145 – 1192	1.0±0.2	Fe XIX, XXIV
Blend 6	1194 – 1223	0.6±0.3	Fe XX
Fe XVII	826	1.2±0.5	Fe XVII

† Corrected for a column density of 2×10^{20} cm $^{-2}$.

On the other hand, we noticed that there is an excess of data compared to the model at the O VII K-α line energy of 0.56 keV. One may argue that, adding this line to the above model and increasing the column density, the residuals around 0.65 keV may disappear. We therefore estimated the flux of the O VII K-α line to be one-fifth of that of the O VIII Lyα line using the EI distribution of Canizares et al. (1982) [23], and added this line to the above model. However, the result essentially did not change. We also noticed a large excess compared to the best fit two-temperature model around 1.07 keV, which is attributable to the L-shell transitions of Fe XXII – XXIII. Since FPCS did not detect any strong emission lines near to 1.07 keV, this may be another discrepancy between the ASCA and FPCS data. One possible explanation of this apparent discrepancy is attributable to the different fields of view between the ASCA and FPCS. However, in this case, we are required to postulate large and asymmetric abundance

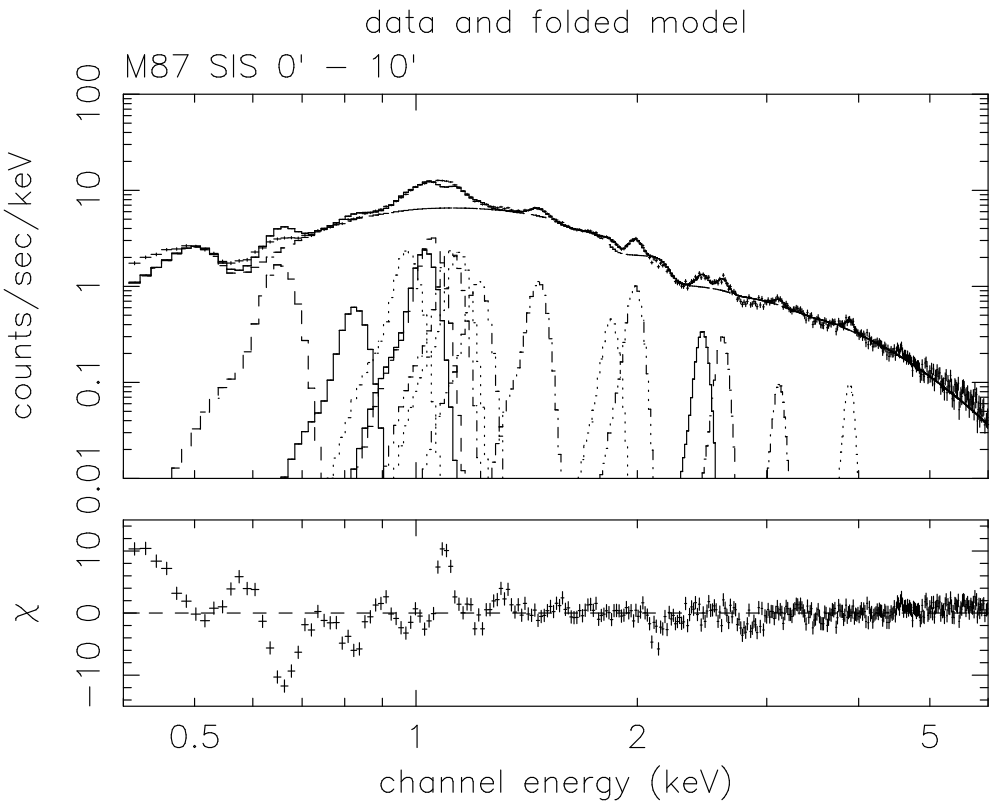

Figure 6.13: Result of bremsstrahlung and line-emission model fitting, where some of the lines are in accordance with table 3.8.

variations within about 30′ regions of M87, which are not clear in our data, and are inconsistent with the ROSAT analysis of Böhringer et al. (1995) [17]. Note that the discrepancy between the ASCA data and simulated FPCS spectrum is almost the same as that between the FPCS and SSS data (Tsai 1994; figure 3.8). Thus, we suspect that some unknown problems may exist in the FPCS data rather than in the ASCA data.

We found that the abundances of S and Si in the inner regions are larger than those of O and Fe, with no significant gradients on the ratios of Si/Fe and S/Fe. The ratio Si/Fe is rather similar to that found in rich clusters, while the ratio S/Fe is rather larger (Mushotzky et al. 1996 [118]; Fukazawa 1997 [51]).

The abundance ratio of O/Fe is smaller than the solar ratio. Current model of the chemical evolution can hardly explain the low O/Fe associated with high Si/Fe, because both O and Si are produced in the stars of nearly the same mass (Loewenstein and Mushotzky 1996 [90]).

Chapter 7

ASCA Mapping Observations of the Virgo Cluster

7.1 Observations and Data Reduction

ASCA observed the region 40′ northwest of M87 (hereafter "M87NW") on 1994 June 8. Furthermore, ASCA proceeded mapping observations of the Virgo cluster from 1996 December 25 to 28 and from 1997 June 14 to 18. The log and positions of the observations are shown in table 7.1 and figure 7.1.

The SIS data were obtained with the 4-CCD bright mode for the M87 NW region, and the 2-CCD faint mode for the other observations. However, since the SIS was heavily damaged by proton irradiation while in orbit, the energy resolution and dark current of the SIS at the time of the Virgo mapping observations were significantly degraded and increased compared with those just after the launch of ASCA (Yamashita 1995 [160]; Dotani et al. 1996 [32]; Tomida et al. 1997 [148]). Therefore we did not used the SIS data.

The GIS data were obtained with the normal PH mode. We excluded the data affected by the South Atlantic Anomaly, Earth occultation, and regions of low geomagnetic rigidity. We also applied a rise-time rejection to exclude particle events.

Using the ROSAT results (Böhringer et al. 1994 [16]), we predict that the X-ray flux from the Virgo cluster at the position far from M87 (like P1, P7, P8 and P9) is comparable to the background level (i.e. sum of the Cosmic X-ray Background (CXB) and Non X-ray Background (NXB)). Therefore, we further apply the "flare-cut" criteria to exclude the NXB events as many as possible (Ishisaki 1996 [74]; Ishisaki et al. 1997 [75]).

After the above mentioned data screening, we corrected the pulse height gain, and combined

Table 7.1: Log of ASCA observations of the Virgo cluster.

Filed	Position(J2000)		Distance	Date (UT)†		Exposure§	N_H‡
	RA(H M S)	DEC(D M S)	arcmin¶	Start	End	(sec)	(10^{20} cm^{-2})
M87 NW	12 28 24.14	12 38 50.64	37.78	93/06/08 07:11	93/06/08 18:36	27528	2.62
P1	12 22 56.21	13 41 53.16	138.51	96/12/25 19:15	96/12/26 11:20	39054	3.00
P2	12 23 33.29	13 07 13.80	114.13	96/12/26 11:20	96/12/26 22:19	39044	2.88
P3	12 25 15.38	13 32 32.28	105.85	96/12/26 22:21	96/12/27 15:20	40644	2.92
P4	12 27 34.03	13 23 21.84	75.66	96/12/27 15:21	96/12/27 20:30	17914	2.78
P5	12 29 15.82	13 48 50.04	87.67	96/12/27 20:30	96/12/28 03:47	17302	2.73
P7	12 24 02.98	14 41 27.60	168.86	97/06/14 22:05	97/06/15 15:51	53200	2.70
P8	12 24 36.48	14 07 56.28	137.51	97/06/15 16:26	97/06/16 06:44	39156	2.86
P9	12 26 19.03	14 32 45.60	144.25	97/06/16 06:15	97/06/16 20:46	37890	2.67
P10	12 26 58.08	13 59 48.48	110.78	97/06/16 21:18	97/06/17 09:25	39136	2.79
P11	12 28 34.06	14 22 36.12	122.91	97/06/17 08:56	97/06/18 01:47	34818	2.63
P12	12 30 12.98	13 18 25.56	55.05	97/06/14 11:37	97/06/14 22:10	20052	2.65

¶ Distance from the center of M87. The coordinate of the center of M87 is $(\alpha, \delta)_{J2000}$ = (12 30 46.46, 12 23 59.28).

† The start and end time of observation in year/month/day hour:minutes.

§ Total exposure time of the GIS 2 and 3 after the data screening described in section 7.1.

‡ Galactic line of sight column density from Einstein On-line Service($EINLINE$)

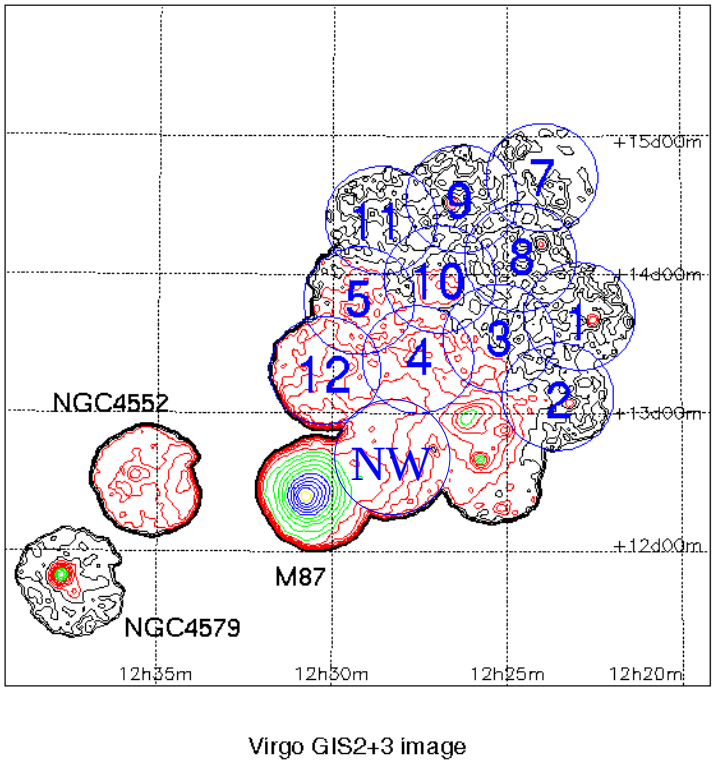

Figure 7.1: X-ray image of the Virgo cluster obtained with the GIS (Kikuchi 1997).

the GIS2 and GIS3 data.

7.2 Analysis and Results

7.2.1 Source Detection

The GIS images in the 0.7 – 10 keV and 3 – 10 keV bands are shown in figure C.1. We can see some X-ray peaks in these images.

To study the X-ray spectrum from the ICM in the Virgo cluster, contamination of the X-ray point sources should be removed. Therefore we did point source search in the images of the 0.7 – 10 keV band. We extracted a peak count rate from a $1'.3 \times 1'.3$ square region, and estimated background counts using a source-free region near to the peak in the same field of view. After subtracting the background count rate from that of the peak, we regarded the peak with signal-to-noise ratio greater than 5.0 to be an X-ray source. We calculated the real source count rate correcting for the point spread function (the $1'.3 \times 1'.3$ square region includes about 36% of the incident flux) and the XRT vignetting. We then converted these count rates to absorption corrected X-ray fluxes assuming photon indices of their spectra are equal to 1.7 which is the typical value for AGN (Mushotzky, Done and Pounds 1993 [114]) and Galactic column densities shown in table 7.1. We summarized the results in table 7.2. In table 7.3, we list candidates of X-ray sources (possible detection), whose S/N ratios are in between 4.5 to 5.0. In these tables, we also showed the source count rates estimated using images in the 3 – 10 keV band. Note that the three sources in P12 are extremely brighter than the other sources. Since P12 is close to the bright source M87, the region is heavily contaminated by the stray lights from M87. Furthermore, all the positions of the three sources are at the nearest side of M87. Therefore possibility that these are artifacts due to the stray lights from M87 can not be excluded.

Using the sources in table 7.2, we derived the Log N - Log S relation. The number of sources (N) with flux greater than S is normalized by the net area of $\Omega(S)$, in which the sensitivity limit should be lower than S (e.g. Ueda 1996 [156]),

$$N(>S) = \frac{\text{Number of Sources (flux} > S)}{\Omega(S)}. \tag{7.1}$$

Therefore we have to estimate the completeness of the source detection in the area $\Omega(S)$. Since the sensitivity limit depends on parameters such as the exposure, vignetting, and background level, it is different from one point to another point even in the same field of view. Thus

elaborated works are required to accurately estimate $\Omega(S)$ (Ueda 1996 [156]), which is beyond the scope of this thesis. For a simplicity, we assume the net observed area as $\Omega(S)$. In this case, $N(>S)$ is regard to be the lower limit. Excluding the regions of M87NW and P12 because these two are largely contaminated by the stray lights from M87, $\Omega(S)$ is 3.3 deg^2. Then we can get the Log N - Log S relation, which is shown in figure 7.2. Note again that the solid line is the lower limit, hence allowed region is above this line. In this figure, we also show the result of the ASCA CXB study (Ueda 1996 [156]). Although the solid line (our results) is the lower limit, it is almost the same as that of the ASCA CXB study above 1.0×10^{-13} erg/cm^2/s in the 2 – 10 keV band. Since the difference between our $\Omega(S)$ and the real $\Omega(S)$ is expected to decrease as S increases, our estimation of $N(>S)$ is a good approximation of the real $N(>S)$ in a high flux region.

From figure 7.2, we see that although there are many galaxies in the Virgo cluster, most of them emit no strong X-rays. This can be seen in figure C.1, where positions of most of the VCC sources (Binggeli et al. 1985 [12]) are not coincident with X-ray structures detected with ASCA.

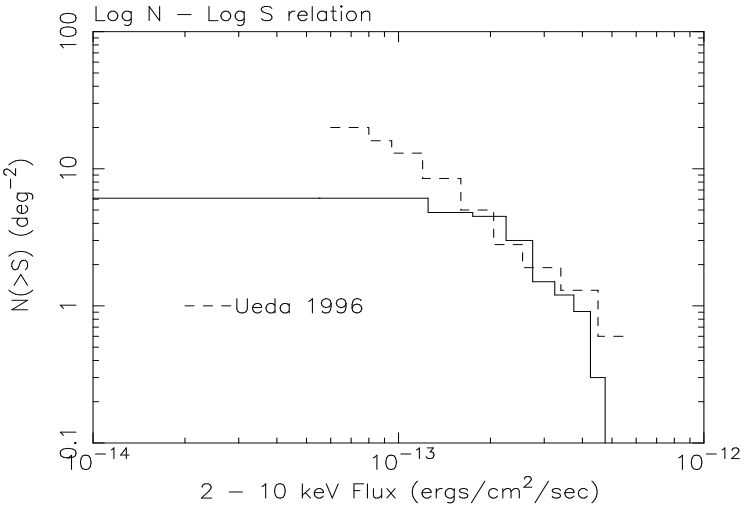

Figure 7.2: Log N - Log S relation derived by the Virgo mapping observation. Note that the region upper than the solid line is allowed by our analysis. Dashed line shows the result of the ASCA CXB analysis (Ueda 1996).

Table 7.2: ASCA GIS detections in the Virgo Cluster Region.

Filed	No.	Position(J2000)		Count Rate‡		Flux¶		S/N§	ID	Ref†
		RA	DEC	All Band	Hard Band					
		H M S	D M S	(0.7-10keV)	(3-10keV)	(0.5-10keV)	(2-10keV)			
1	1	12 22 21.8	13 48 15.8	8.77±1.56	2.44±0.81	4.0±0.7	2.6±0.5	5.61	121957+135702	BBN91
1	2	12 23 22.5	13 41 38.2	5.27±0.96	2.26±0.57	2.4±0.4	1.6±0.3	5.52		
1	3	12 22 30.9	13 40 09.8	9.53±1.52	6.34±0.89	4.3±0.7	2.8±0.4	6.23		
2	1	12 23 11.1	13 04 09.8	9.74±1.27	3.02±0.70	4.4±0.6	2.9±0.4	7.65	PGC40202	RC3
2	2	12 23 51.9	13 04 09.8	4.88±0.96	1.22±0.52	2.2±0.4	1.4±0.3	5.11		
2	3	12 24 16.6	13 01 05.5	9.94±1.63	3.94±0.96	4.5±0.7	2.9±0.5	6.11	VCC0723	VCC
3	1	12 26 06.4	13 24 18.2	10.3±2.02	3.23±1.11	4.7±0.9	3.0±0.6	5.09		
3	2	12 26 02.3	13 20 52.1	15.9±2.55	1.58±1.10	7.2±1.2	4.7±0.7	6.21		
3	3	12 25 26.5	13 23 19.6	7.77±1.50	0.48±0.65	3.5±0.7	2.3±0.4	5.18		
5	1*	12 29 31.5	13 46 00.0	14.6±1.98	3.32±1.06	6.6±0.9	4.3±0.6	7.39	1227+140	HB89
5	2*	12 29 27.9	13 44 32.2	14.2±1.94	4.11±1.13	6.5±0.9	4.2±0.6	7.32		
7	1	12 23 47.7	14 39 00.7	3.77±0.68	1.41±0.42	1.7±0.3	1.1±0.2	5.52		
8	1	12 24 02.5	14 12 57.8	7.79±1.31	3.14±0.81	3.5±0.6	2.3±0.4	5.95		
8	2	12 24 50.7	14 15 47.3	7.40±1.35	2.37±0.78	3.4±0.6	2.2±0.4	5.47	1222+145	HB89
8	3	12 24 32.4	14 07 11.8	4.63±0.85	1.30±0.47	2.1±0.4	1.4±0.3	5.43	1222+143	TXS
9	1	12 26 08.4	14 33 37.5	4.31±0.78	1.75±0.48	2.0±0.4	1.3±0.2	5.54		
9	2	12 26 36.3	14 31 02.9	12.5±1.27	3.57±0.70	5.7±0.6	3.7±0.4	9.81		
10	1*	12 26 53.0	13 55 37.6	8.95±1.13	2.80±0.60	4.1±0.5	2.6±0.3	7.90		
10	2*	12 26 31.8	13 52 55.5	6.96±1.24	1.99±0.64	3.2±0.6	2.0±0.4	5.60	122400.4+140831 or VCC924	87GB VCC
10	3*	12 26 28.2	13 55 08.0	7.81±1.28	3.05±0.71	3.6±0.6	2.3±0.4	6.13		
12	1	12 30 47.2	13 02 13.6	49.1±7.50	4.48±3.04	22.3±3.4	14.4±2.2	6.55		
12	2	12 30 05.9	13 02 58.0	47.1±5.85	2.72±2.17	21.4±2.7	13.8±1.7	8.04		
12	3	12 29 42.7	13 03 05.3	32.8±6.16	1.91±2.52	14.9±2.8	9.6±1.8	5.33	VCC1229	VCC

*: Contaminates with each other.

‡: After corrections of the point spread function and the vignetting. The unit is 10^{-3} counts/sec.

§: Signal-to-Noise ratio in the 0.7 – 10 keV band. Only the sources with S/N > 5.0 are shown in this table.

¶: Absorption corrected X-ray flux calculated from the count rate in the 0.7 - 10 keV band assuming the photon index of 1.7 and Galactic column density in table 7.1. The unit is 10^{-13} erg/sec/cm^2

†: VCC = Binggeli, Sandage and Tammann 1985 [12]
BBN91 = Batuski et al. 1991 [10]
RC3 = de Vaucouleurs et al. 1991 [31]
HB89 = Hewitt and Burbidge 1989 [68]
TXS = Douglas et al. 1996 [33]
87GB = Gregory and Condon 1991 [59]

Table 7.3: Source candidates detected with the ASCA GIS in the Virgo Cluster Region.

Field	No.	Position(J2000)		Count Rate‡		Flux¶		S/N§	ID	Ref†
		RA	DEC	All Band	Hard Band					
		H M S	D M S	(0.7-10keV)	(3-10keV)	(0.5-10keV)	(2-10keV)			
1	4	12 22 48.1	13 49 00.2	5.14±1.06	0.96±0.54	2.3±0.5	1.5±0.3	4.83		
2	4	12 24 18.1	13 07 21.1	6.78±1.38	2.11±0.78	3.1±0.6	2.0±0.4	4.90		
3	4	12 25 15.4	13 34 37.2	4.35±0.92	2.32±0.56	2.0±0.4	1.3±0.3	4.72		
3	5	12 26 08.4	13 27 07.6	8.86±1.80	1.55±0.89	4.0±0.8	2.6±0.5	4.91		
3	6	12 25 16.9	13 16 56.7	10.4±2.19	1.35±1.04	4.7±1.0	3.1±0.6	4.74	VCC0789	VCC
3	7	12 25 11.9	13 22 42.8	6.57±1.45	1.25±0.67	3.0±0.7	1.9±0.4	4.52		
7	2	12 24 39.0	14 53 44.3	7.18±1.45	0.62±0.71	3.3±0.7	2.1±0.4	4.94		
7	3	12 24 20.7	14 40 21.7	3.83±0.78	1.19±0.46	1.7±3.5	1.1±0.2	4.92		
7	4	12 23 27.4	14 38 23.7	4.07±0.85	1.33±0.50	1.9±0.4	1.2±0.3	4.78		
10	4	12 27 27.9	13 56 58.5	6.45±1.41	2.98±0.78	2.9±0.6	1.9±0.4	4.56	122457.8+141307	87GB
10	5	12 27 23.4	13 53 10.2	6.98±1.49	3.21±0.82	3.2±0.7	2.1±0.4	4.70		

‡: After corrections of the point spread function and the vignetting. The unit is 10^{-3} count/sec.

§: Signal-to-Noise ratio in the 0.7 – 10 keV band. The candidates for the sources with 4.5 < S/N < 5.0 are shown in this table.

¶: Absorption corrected X-ray flux calculated from the count rate in the 0.7 – 10 keV band assuming the photon index of 1.7 and Galactic column density in table 7.1. The unit is 10^{-13} erg/sec/cm^2

†: VCC = Binggeli, Sandage and Tammann 1985 [12]
87GB = Gregory and Condon 1991 [59]

7.2.2 Spectral Analysis

For the data of each pointing, we made an X-ray spectrum of the ICM using the events within $18'$ from the center of the field of view after excluding contaminations from the sources in table 7.2 and 7.3. To exclude the contamination from each source, we discard the events within the circular region cantered on the source whose radius is typically $3'$. For bright sources, we used larger radius than $3'$.

We could not use the same background as that in the case of the analysis of M87, because the background data are made with no flare-cut criteria. Therefore we used other observations for the background sky. Since the Galactic latitude of the Virgo cluster is rather high (the Galactic coordinate of the Virgo cluster is (l, b) = (279.7, 74.5)), we selected the regions of high Galactic latitude to exclude contamination from the Galactic ridge emission. We found three regions, QSF3, Lockman Hole and Jupiter, as are shown in table 7.4, where in the "Jupiter" region, Jupiter itself was found to be very faint, hence can be used as a background sky. As for QSF3, we combined the data of the 4 pointings. These background sky have following characteristics,

1. All are high Galactic-latitude skys.

2. Jupiter and Lockman Hole are at the north side of the Galactic plane, while QSF3 is at the south side.

3. The date of observation of Jupiter is near to those of QSF3, while that of Lockman Hole was 1997. Therefore, by these background comparison, we can study the effect due to the long-term increase of NXB (Ishisaki 1996 [74]; Ishisaki et al. 1997 [75]).

For these background data, we adopted the same criteria of the data screening as those for the Virgo cluster to exclude the data affected by the South Atlantic Anomaly, Earth occultation, regions of low geomagnetic rigidity, and flare events. We also applied a rise-time rejection to exclude particle events. We then performed point-source search in the same way as described in the subsection 7.2.1. We found 2, 6, and 5 sources in the Jupiter, QSF3 and Lockman Hole fields. After excluding these sources, we extracted X-ray spectrum from each background sky using the events within $18'$ radius from the center of the field of view. We show the GIS spectra of the background skys in figure 7.3.

To evaluate the spectral variation among the backgrounds, we show the ratio of count rate between the backgrounds in figure 7.4. We found that the spectral shapes of the backgrounds are almost identical. However, the absolute count rate of Lockman Hole is larger than those of

Table 7.4: Log of observation of the background region.

Name	Date	Position*		Exposure†	count rate†	PI§
	YY/MM/DD	l	b	(sec)	c/s/detector	
Jupiter	93/06/06	286.2	61.2	62160	0.219	PV
QSF3	93/07/11	250.8	-52.0	67778	0.207	PV
QSF3	93/09/10	250.8	-52.0	41481		PV
QSF3	93/09/15	250.8	-52.0	47069		PV
QSF3	93/09/21	250.8	-52.0	35836		PV
Lockman Hole	97/04/29	149.2	53.2	170384	0.265	Ishisaki, Y.

* Galactic coordinates of the center of the field of view.
† The sum of exposure time of the GIS2 and 3 after data screening.
† Count rate after correcting differences of the spectral extraction area.
§ Principal Investigator. PV means observations in the Performance Verification phase.

Jupiter and QSF3, while the latter two have almost the same absolute fluxes; after correcting the differences of the spectral extraction area, the count rates in the 0.7 – 10 keV band of Jupiter, QSF3 and Lockman Hole are 0.219, 0.207 and 0.265 counts/sec/detector, respectively.

One may argue that the difference between the count rates is due to the long-term increase of NXB (Ishisaki 1996 [74]; Ishisaki et al. 1997 [75]). To study this, we made the X-ray spectra of night Earth in June 1993 and June 1997 using the data of the pointing observations of QSF3, NGC4365, NGC4472, and NGC720 in 1993 and the Virgo mapping observations in 1997. We screened the data affected by the South Atlantic Anomaly, regions of low geomagnetic rigidity. We also excluded the flare events and applied a rise-time rejection to exclude particle events. After the above data screening, we extracted X-ray spectra using the data obtained while ASCA was looking at the night Earth, which are shown in figure 7.5. Although the spectral shape of them are almost identical, the count rates of NXB in 1993 and 1997 are 0.070 and 0.085 counts/sec/detector, respectively. This increase of the NXB count rate is consistent with that reported by Ishisaki (1996) [74] and Ishisaki et al. (1997) [75], and is too small to explain the differences of count rates between QSF3, Jupiter and Lockman hole. Therefore we conclude the differences of the count rates between QSF3, Jupiter and Lockman Hole are due to the fluctuation of the CXB. According to the CXB analysis done by Ishisaki (1996) [74], the fluxes of Jupiter and QSF3 are consistent with the average flux of the CXB + NXB within the errors. However, the count rate of Lockman Hole is 3 σ brighter than that of the average CXB + NXB. Therefore we regard that Jupiter and QSF3 represent a standard background, and Lockman Hole is an extremely bright example.

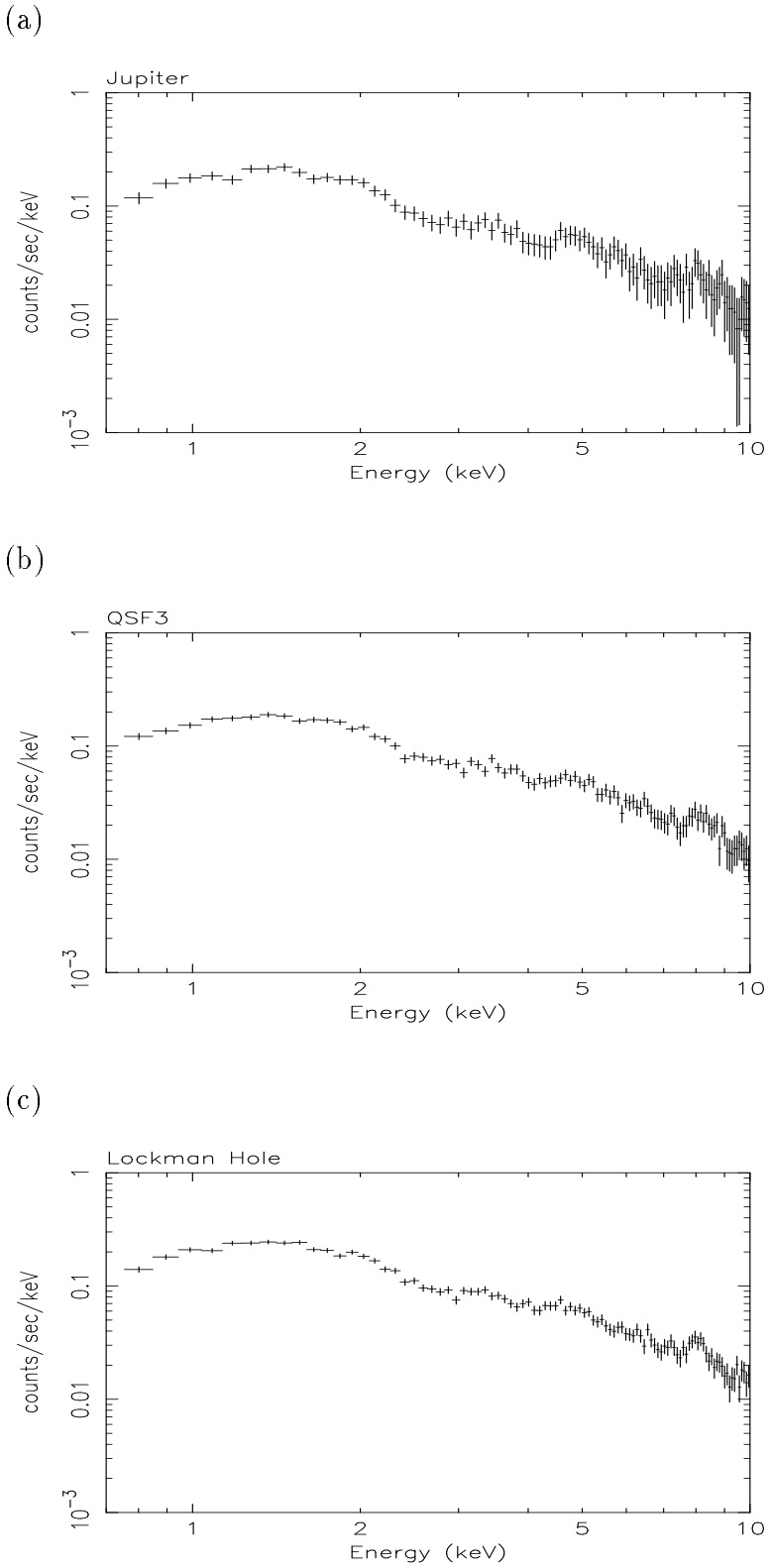

Figure 7.3: GIS spectra used as a background; (a) Jupiter, (b) QSF3, and (c) Lockman Hole.

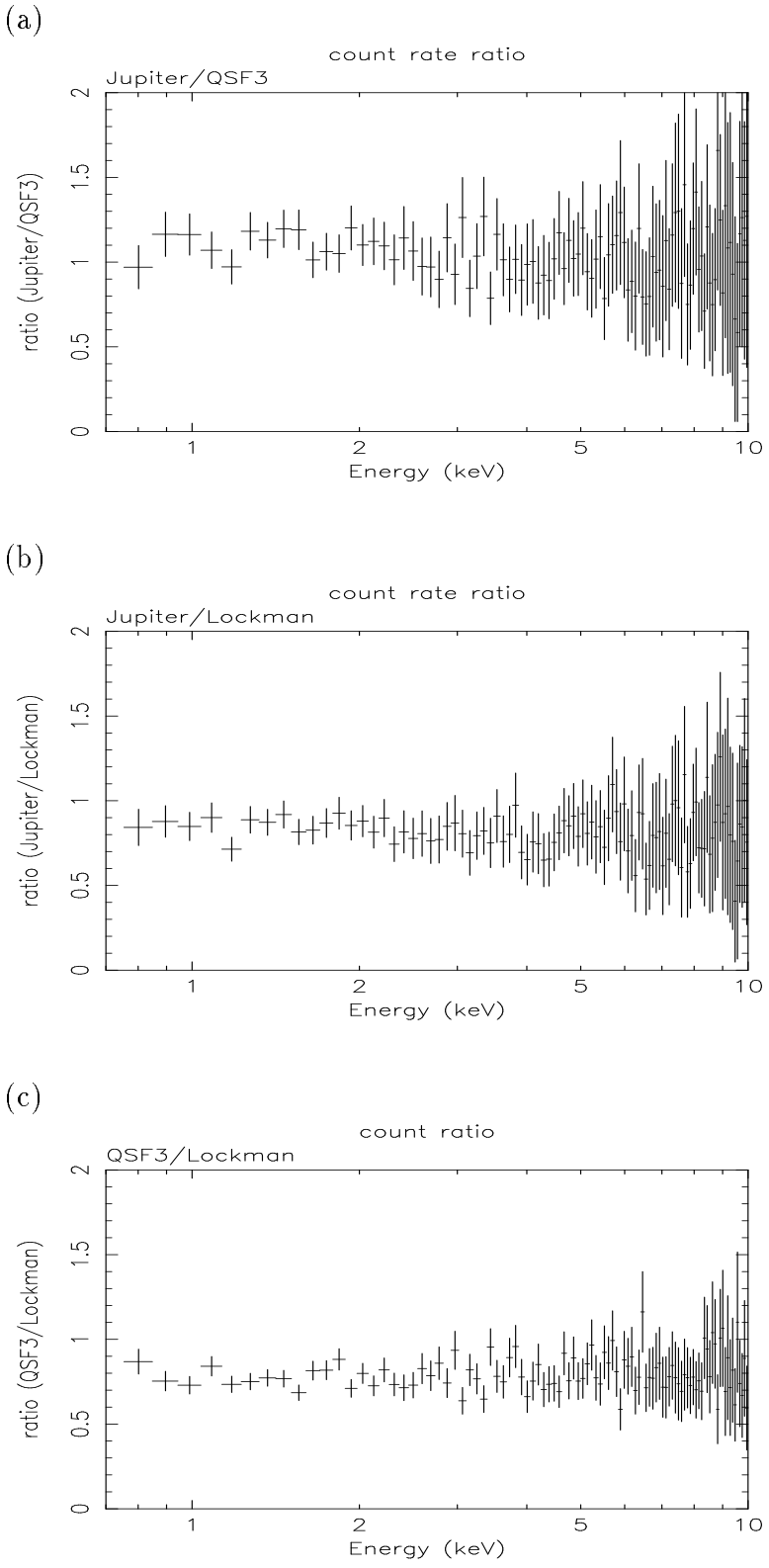

Figure 7.4: Ratio of count rate between Jupiter, QSF3, and Lockman Hole; (a) Jupiter/QSF3, (b) Jupiter/Lockman Hole, and (c) QSF3/Lockman Hole.

(a)

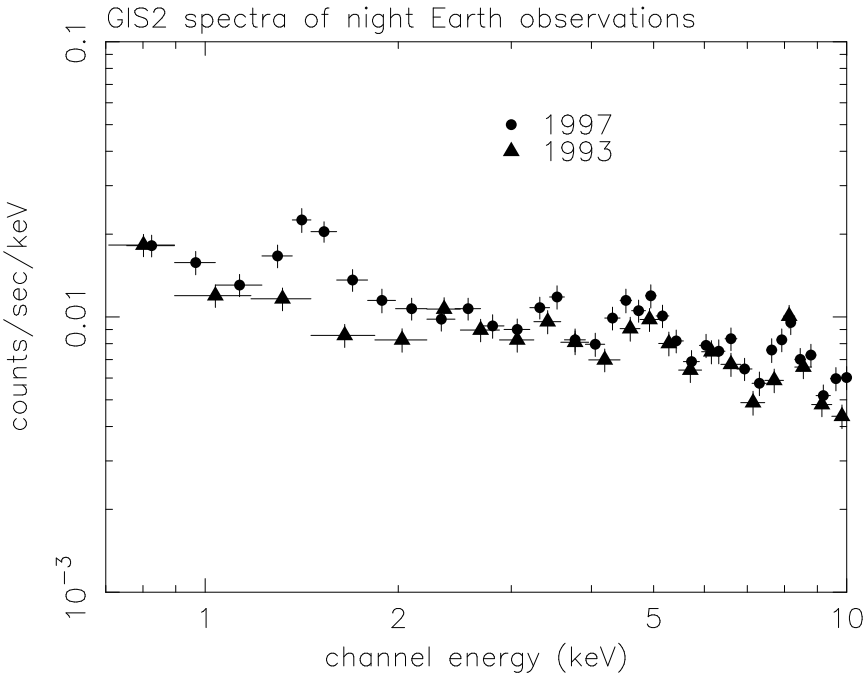

(b)

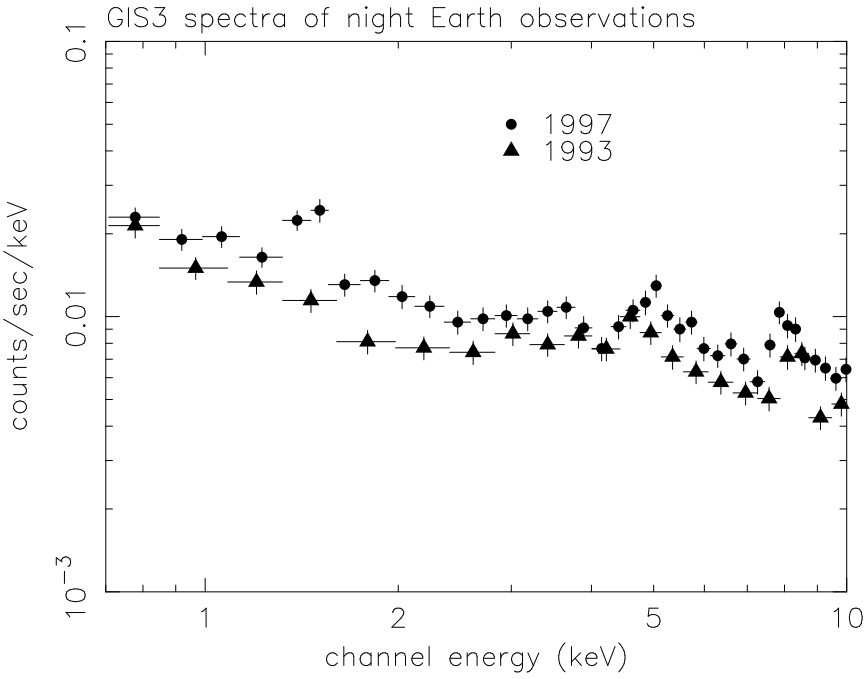

Figure 7.5: GIS spectra of night Earth in 1993 and 1997; (a) GIS2, (b) GIS3.

Since the X-ray emission of the Virgo cluster extends over a region much larger than the ASCA field of view, stray lights occupy a significant fraction of the photons detected at each region. For example, in the case of the uniformly extended CXB, if we integrate X-ray photons within the radius of 20 $'$ from optical axis, the number ratio of the X-ray photons which come from the region outer than 20 $'$ to that of the total X-ray photons is about 45 % at 1 keV (Ishisaki 1996 [74]). In our case, M87 is extremely brighter than the surface brightness of each region, the ratio of the contamination is expected to be larger than 45 % at 1 keV. Therefore we have to take the stray light effect into account for the Virgo analysis. According to Ishisaki (1996) [74], it is enough to take into account stray lights which come from the region within 180 $'$ from the optical axis. To do this approximately, we assumed the beta model as $S(\vec{r_1})$ in Eq. (6.3), setting the core radius and beta equal to $2'.3$ and 0.45, respectively, according to the results of the ROSAT observation (Böhringer et al. 1994 [16]). To calculate the ARF, we used the "SimARF" package. We used the standard RMF provided by the GIS team.

We then fitted the X-ray spectra in the 0.7 – 10 keV band with a one-temperature RS model modified by interstellar absorption. Free parameters are the plasma temperature, metal abundance, and normalization. We assumed that the relative ratios of abundances between heavy elements are the same as the solar ratios (table E.1). If we set the interstellar absorption to be free, the best-fit values are 0 in all the observed regions. Comparing with the results of M87 (chapter 6), this suggests that the interstellar absorption toward the center of M87 is larger than that toward the region far from M87. However, since the statistical errors are large and the confidence ranges are consistent with the Galactic values in table 7.1, we fixed them to the Galactic values. The best-fit parameters and model curves are shown in table 7.5 and figure D.1. The best-fit χ^2 values show this model can fit the data quite well.

The temperature and abundance distributions are shown in figure 7.6. Though the statistical errors are very large, both the temperature and abundance distribution seem to have spherical symmetry. Therefore, to improve the statistics, we simultaneously fitted the spectra from the regions with approximately the same angular distance from M87, with a one-temperature RS model.

The plasma temperature, abundance, and normalization are free parameters, while the column density is fixed to of the Galactic value given in table 7.1. This gives a good fitting as is indicated by the best-fit $\chi^2/d.o.f.$ given in table 7.6. The spatial distributions of the temperature and abundance are shown in figure 7.7.

The metal abundance is primary determined by the Fe L lines. Therefore we should regard this metal abundance as that of Fe. Though the statistical errors are rather large, the abundance

Table 7.5: The best-fit parameters and 90% confidence errors from the one-temperature RS model fitting.

Name	BGD¶	Temperature (keV)	Abundance (solar)	Surface Brightness† (erg/cm^2/s/amin^2)	$\chi^2/d.o.f$
M87NW	J	$2.67^{+0.12}_{-0.10}$	$0.26^{+0.12}_{-0.08}$	$3.80^{+0.07}_{-0.06}\times10^{-14}$	233.5/274
	Q	$2.65^{+0.10}_{-0.10}$	$0.25^{+0.10}_{-0.08}$	$3.82^{+0.05}_{-0.05}\times10^{-14}$	234.7/274
	L	$2.52^{+0.10}_{-0.11}$	$0.22^{+0.09}_{-0.09}$	$3.65^{+0.05}_{-0.06}\times10^{-14}$	235.1/274
P1	J	$1.73^{+0.67}_{-0.27}$	$0.17^{+0.59}_{-0.17}$	$4.57^{+0.24}_{-0.25}\times10^{-15}$	54.00/59
	Q	$1.70^{+0.45}_{-0.23}$	$0.13^{+0.31}_{-0.13}$	$4.89^{+0.23}_{-0.24}\times10^{-15}$	58.53/59
	L	$1.23^{+0.19}_{-0.23}$	$0.07^{+0.15}_{-0.07}$	$3.76^{+0.22}_{-0.22}\times10^{-15}$	45.38/59
P2	J	$2.19^{+0.54}_{-0.39}$	$0.33^{+0.58}_{-0.27}$	$5.43^{+0.26}_{-0.26}\times10^{-15}$	46.06/76
	Q	$2.10^{+0.36}_{-0.35}$	$0.25^{+0.33}_{-0.22}$	$5.70^{+0.25}_{-0.24}\times10^{-15}$	48.51/76
	L	$1.41^{+0.31}_{-0.21}$	$0.06^{+0.21}_{-0.06}$	$4.38^{+0.22}_{-0.23}\times10^{-15}$	39.09/76
P3	J	$2.18^{+0.45}_{-0.29}$	$0.28^{+0.39}_{-0.21}$	$6.37^{+0.25}_{-0.24}\times10^{-15}$	62.88/80
	Q	$2.13^{+0.31}_{-0.26}$	$0.22^{+0.25}_{-0.16}$	$6.61^{+0.23}_{-0.30}\times10^{-15}$	68.86/80
	L	$1.61^{+0.19}_{-0.21}$	$0.13^{+0.17}_{-0.11}$	$5.32^{+0.21}_{-0.21}\times10^{-15}$	65.37/80
P4	J	$2.39^{+0.28}_{-0.27}$	$0.32^{+0.25}_{-0.19}$	$1.31^{+0.03}_{-0.04}\times10^{-14}$	53.74/81
	Q	$2.35^{+0.25}_{-0.24}$	$0.29^{+0.22}_{-0.18}$	$1.33^{+0.04}_{-0.03}\times10^{-14}$	56.06/81
	L	$2.07^{+0.20}_{-0.20}$	$0.21^{+0.19}_{-0.13}$	$1.21^{+0.04}_{-0.04}\times10^{-14}$	51.77/81
P5	J	$2.17^{+0.47}_{-0.30}$	$0.27^{+0.37}_{-0.20}$	$8.99^{+0.35}_{-0.35}\times10^{-15}$	51.39/56
	Q	$2.15^{+0.39}_{-0.29}$	$0.24^{+0.30}_{-0.18}$	$9.22^{+0.34}_{-0.34}\times10^{-15}$	49.15/56
	L	$1.72^{+0.34}_{-0.21}$	$0.15^{+0.23}_{-0.13}$	$7.96^{+0.31}_{-0.32}\times10^{-15}$	45.14/56
P7	J	$3.17^{+1.13}_{-1.18}$	$1.13^{+2.71}_{-1.07}$	$2.78^{+0.25}_{-0.24}\times10^{-15}$	22.41/39
	Q	$2.49^{+0.86}_{-0.72}$	$0.35^{+0.91}_{-0.35}$	$2.87^{+0.19}_{-0.19}\times10^{-15}$	31.61/39
	L	$1.09^{+0.31}_{-0.23}$	$0.09^{+0.40}_{-0.09}$	$1.53^{+0.16}_{-0.17}\times10^{-15}$	28.76/39
P8	J	$3.24^{+0.69}_{-0.72}$	$1.08^{+1.42}_{-0.78}$	$4.97^{+0.30}_{-0.28}\times10^{-15}$	34.25/37
	Q	$2.94^{+0.58}_{-0.61}$	$0.73^{+0.86}_{-0.55}$	$5.11^{+0.25}_{-0.25}\times10^{-15}$	38.46/37
	L	$1.67^{+0.49}_{-0.33}$	$0.18^{+0.46}_{-0.18}$	$3.34^{+0.22}_{-0.22}\times10^{-15}$	29.50/37
P9	J	$2.86^{+0.84}_{-0.70}$	$0.62^{+1.33}_{-0.57}$	$4.47^{+0.28}_{-0.28}\times10^{-15}$	15.62/35
	Q	$2.55^{+0.66}_{-0.54}$	$0.31^{+0.67}_{-0.31}$	$4.65^{+0.24}_{-0.25}\times10^{-15}$	17.26/35
	L	$1.55^{+0.29}_{-0.32}$	$0.06^{+0.33}_{-0.06}$	$3.17^{+0.22}_{-0.22}\times10^{-15}$	15.90/35
P10	J	$2.54^{+0.39}_{-0.38}$	$0.43^{+0.48}_{-0.28}$	$7.65^{+0.28}_{-0.28}\times10^{-15}$	29.22/46
	Q	$2.42^{+0.34}_{-0.33}$	$0.32^{+0.33}_{-0.23}$	$7.86^{+0.27}_{-0.26}\times10^{-15}$	38.83/46
	L	$1.78^{+0.31}_{-0.20}$	$0.13^{+0.23}_{-0.12}$	$6.32^{+0.24}_{-0.24}\times10^{-15}$	27.27/46
P11	J	$2.46^{+0.45}_{-0.42}$	$0.35^{+0.48}_{-0.29}$	$6.04^{+0.27}_{-0.27}\times10^{-15}$	27.18/41
	Q	$2.27^{+0.42}_{-0.29}$	$0.21^{+0.34}_{-0.19}$	$6.24^{+0.24}_{-0.24}\times10^{-15}$	35.26/41
	L	$1.72^{+0.29}_{-0.23}$	$0.14^{+0.24}_{-0.14}$	$4.80^{+0.24}_{-0.23}\times10^{-15}$	34.68/41
P12	J	$2.27^{+0.29}_{-0.16}$	$0.17^{+0.20}_{-0.11}$	$1.74^{+0.04}_{-0.05}\times10^{-14}$	100.8/95
	Q	$2.24^{+0.25}_{-0.15}$	$0.16^{+0.16}_{-0.12}$	$1.76^{+0.05}_{-0.04}\times10^{-14}$	96.57/95
	L	$2.08^{+0.17}_{-0.16}$	$0.12^{+0.13}_{-0.10}$	$1.65^{+0.03}_{-0.04}\times10^{-14}$	88.95/95

¶ : Backgroud used for the analysis.
"J", "Q", and "L" represent Jupiter, QSF3, and Lockman Hole, respectively.

† : Absoption corrected value in the 0.5 – 10 keV band.

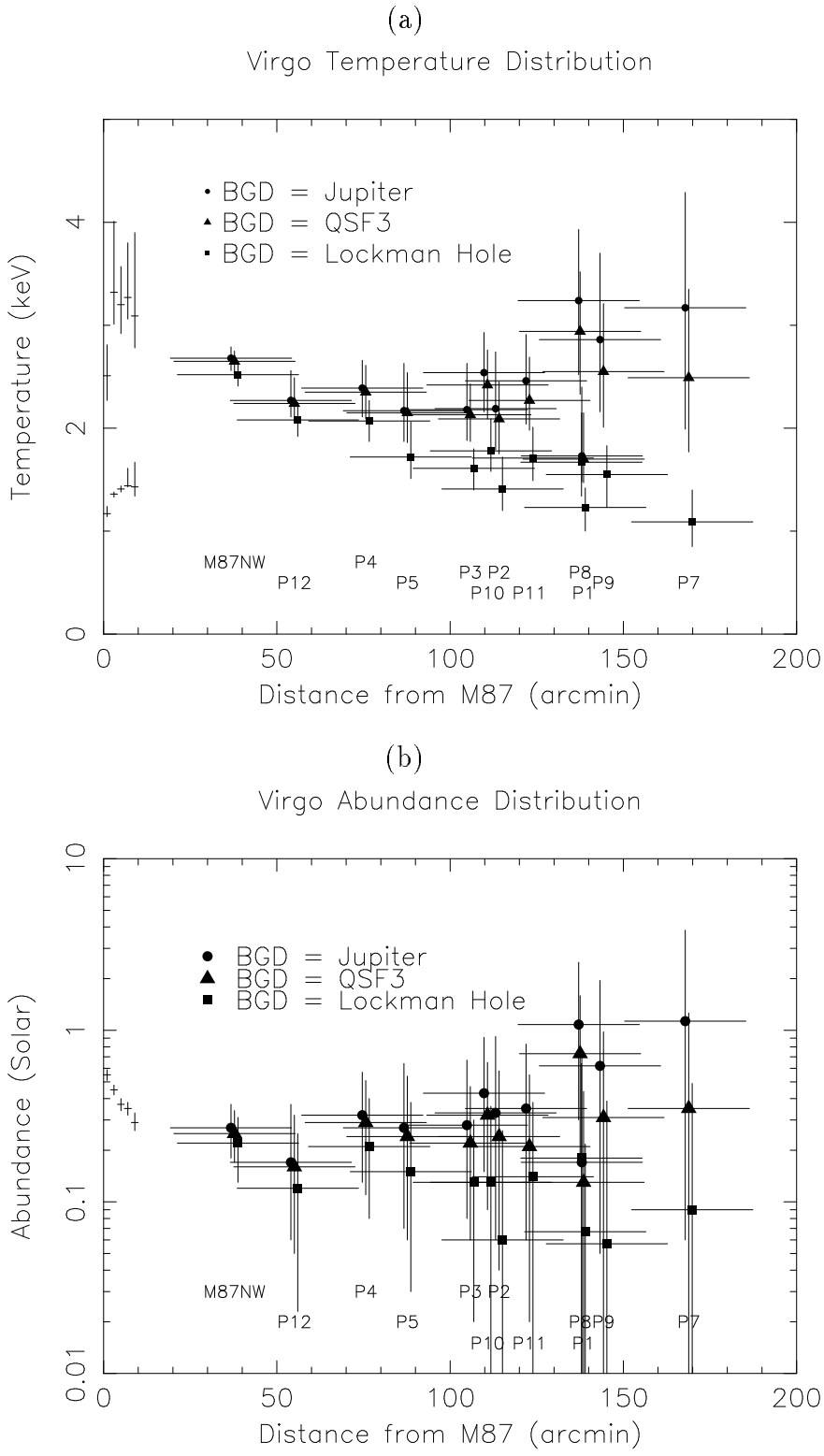

Figure 7.6: Results of the one-temperature model fitting of the Virgo cluster; (a) temperature, and (b) abundance. We also plot the results of M87. Dots, triangles and squares represent the cases that we used the data of Jupiter, QSF3, and Lockman Hole as a background.

Table 7.6: The best-fit parameters and 90 % confidence errors of the one-temperature model fitting. In this case, we fitted the data of the regions having the similar radii from the center of M87 simultaneously.

Region	BGD¶	Temperature (keV)	Abundance (solar)	$\chi^2/d.o.f.$
M87NW	J	$2.67^{+0.12}_{-0.10}$	$0.26^{+0.12}_{-0.08}$	233.5/274
	Q	$2.65^{+0.10}_{-0.10}$	$0.25^{+0.10}_{-0.08}$	234.7/274
	L	$2.52^{+0.10}_{-0.11}$	$0.22^{+0.09}_{-0.09}$	235.1/274
P12	J	$2.27^{+0.29}_{-0.16}$	$0.17^{+0.20}_{-0.11}$	100.8/95
	Q	$2.24^{+0.25}_{-0.15}$	$0.16^{+0.16}_{-0.12}$	96.57/95
	L	$2.08^{+0.17}_{-0.16}$	$0.12^{+0.13}_{-0.10}$	88.95/95
P4+P5	J	$2.27^{+0.30}_{-0.17}$	$0.29^{+0.22}_{-0.14}$	105.8/139
	Q	$2.24^{+0.26}_{-0.16}$	$0.26^{+0.18}_{-0.12}$	105.7/139
	L	$1.99^{+0.17}_{-0.17}$	$0.20^{+0.14}_{-0.10}$	99.37/139
P2+P3+P10+P11	J	$2.39^{+0.22}_{-0.25}$	$0.37^{+0.21}_{-0.18}$	167.3/249
	Q	$2.21^{+0.18}_{-0.14}$	$0.24^{+0.13}_{-0.10}$	193.4/249
	L	$1.66^{+0.11}_{-0.11}$	$0.12^{+0.09}_{-0.06}$	170.1/249
P1+P8+P9	J	$2.64^{+0.41}_{-0.41}$	$0.61^{+0.56}_{-0.34}$	110.9/135
	Q	$2.24^{+0.47}_{-0.21}$	$0.29^{+0.38}_{-0.17}$	123.5/135
	L	$1.40^{+0.24}_{-0.13}$	$0.08^{+0.15}_{-0.06}$	96.60/135
P7	J	$3.17^{+1.13}_{-1.18}$	$1.13^{+2.71}_{-1.07}$	22.41/39
	Q	$2.49^{+0.86}_{-0.72}$	$0.35^{+0.91}_{-0.35}$	31.61/39
	L	$1.09^{+0.31}_{-0.23}$	$0.09^{+0.40}_{-0.09}$	28.76/39

¶: Backgroud used for the analysis.
"J", "Q", and "L" represent Jupiter, QSF3, and Lockman Hole, respectively.

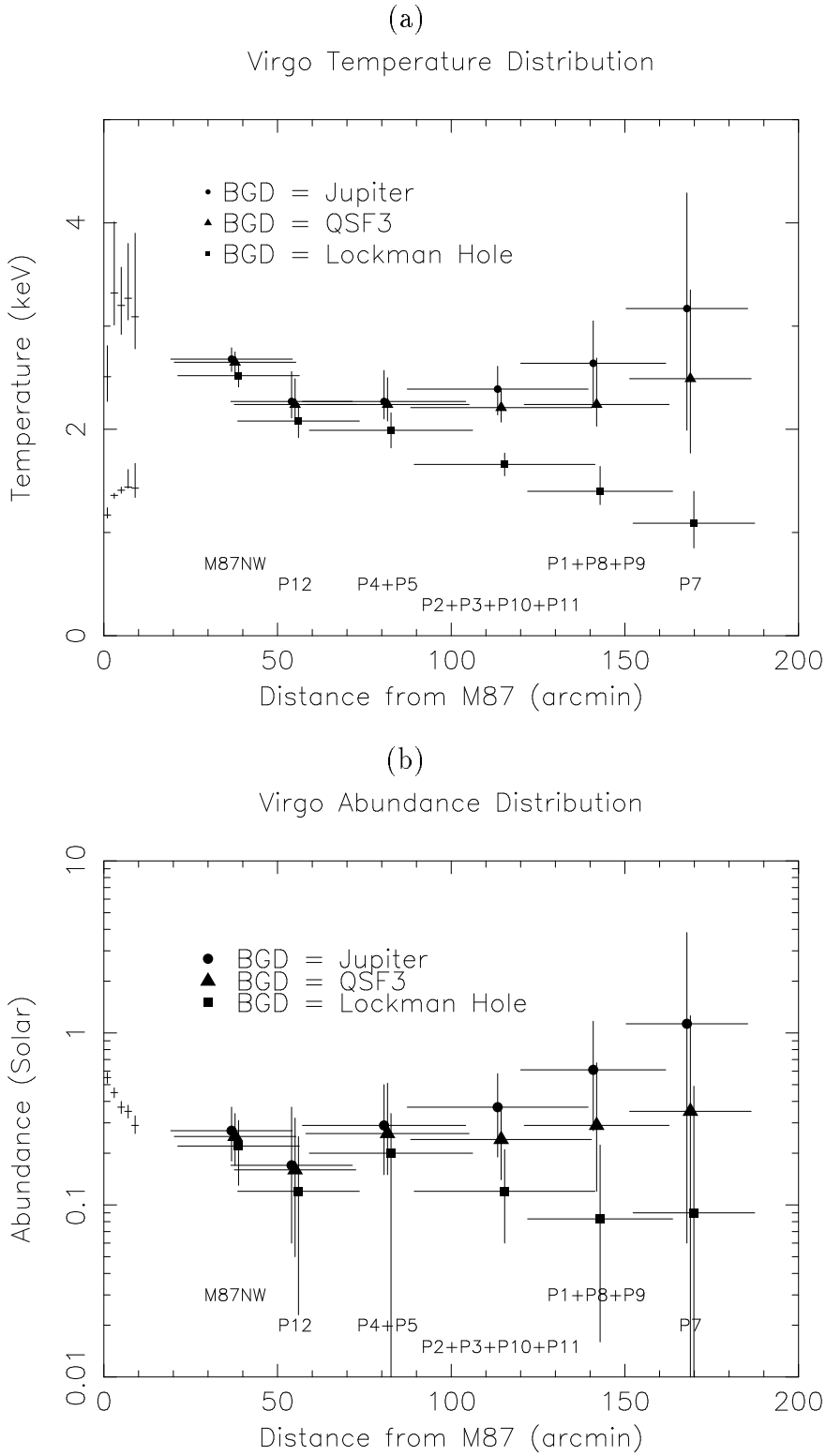

Figure 7.7: (a) Temperature and (b) abundance distribution of the Virgo cluster. We also plot the results of M87. In this case, we fitted the data of the regions having the similar radii from the center of M87 simultaneously. Dots, triangles and squares represent the cases that we used the data of Jupiter, QSF3, and Lockman Hole as a background.

of each region is less than that at the central region of M87 and consistent with a spatially constant profile in all cases of the background selection. Therefore we can conclude that the Fe abundance decreases with radius from the center of M87 to 40′ radius. Beyond this radius, the metallicity is almost spatially constant at 0.3 solar.

7.3 Discussion

7.3.1 Mass Distribution

The surface brightness distribution are shown in figure 7.8, in which we also show the result of the two-temperature model fitting to the data of M87 fixing the temperature of the hot component to be 2.9 keV (table 6.5). We can see that the hot component of M87 can be smoothly extrapolated to the ICM of the Virgo cluster, which suggests that the hot and cool components are the gases associated with the Virgo cluster and M87, respectively. This is the same situation as other clusters of galaxies having cool components at the regions of the central dominant galaxies (Ikebe 1996 [71], Fukazawa 1997 [51]).

We fitted these profiles from $40'$ to $200'$ with the beta model fixing the core radius to be $2'.3$ (Böhringer 1994 [16]). The best-fit parameters are summarized in table 7.7, which are consistent with the previous observations (Fabricant and Gorenstein 1983 [44]; Böhringer 1994 [16]; Fukazawa 1997 [51]). We converted the central surface brightness, $S_X(0)$, to the central proton density, $n(0)$, assuming the temperature and abundance of the ICM are the same as their averaged values; 2.55 keV and 0.27 solar for the case of Jupiter, 2.47 keV and 0.24 solar for the case of QSF3, and 1.94 keV and 0.15 solar for the case of Lockman Hole.

We fitted the radial temperature profile of figure 7.7 (b) with an analytic function of the form,

$$T(r) = T_0 - T_s \left[1 - \exp(-\frac{r}{\lambda})\right]. \tag{7.2}$$

We fixed the central temperature, T_0 to be 2.9 keV. The free parameters are λ and T_s. The best-fit parameters are summarized in table 7.8.

Table 7.7: Surface brightness fit with the beta model†.

BGD	β	$S_X(0)$ erg/cm^2/s/amin^2	$n(0)$§ cm^{-3}
Jupiter	0.43±0.1	$(2.9\pm0.4)\times10^{-12}$	$(3.00\pm0.03)\times10^{-2}$
QSF3	0.43±0.1	$(3.3\pm0.2)\times10^{-12}$	$(3.10\pm0.02)\times10^{-2}$
Lockman Hole	0.47±0.1	$(6.5\pm0.7)\times10^{-12}$	$(3.09\pm0.03)\times10^{-2}$

†: From expression surface brightness $S_X = S_X(0)[1 + (r/r_c)^2]^{(-3\beta+0.5)}$. We fixed r_c to be $2'.3$.

§: Central proton density.

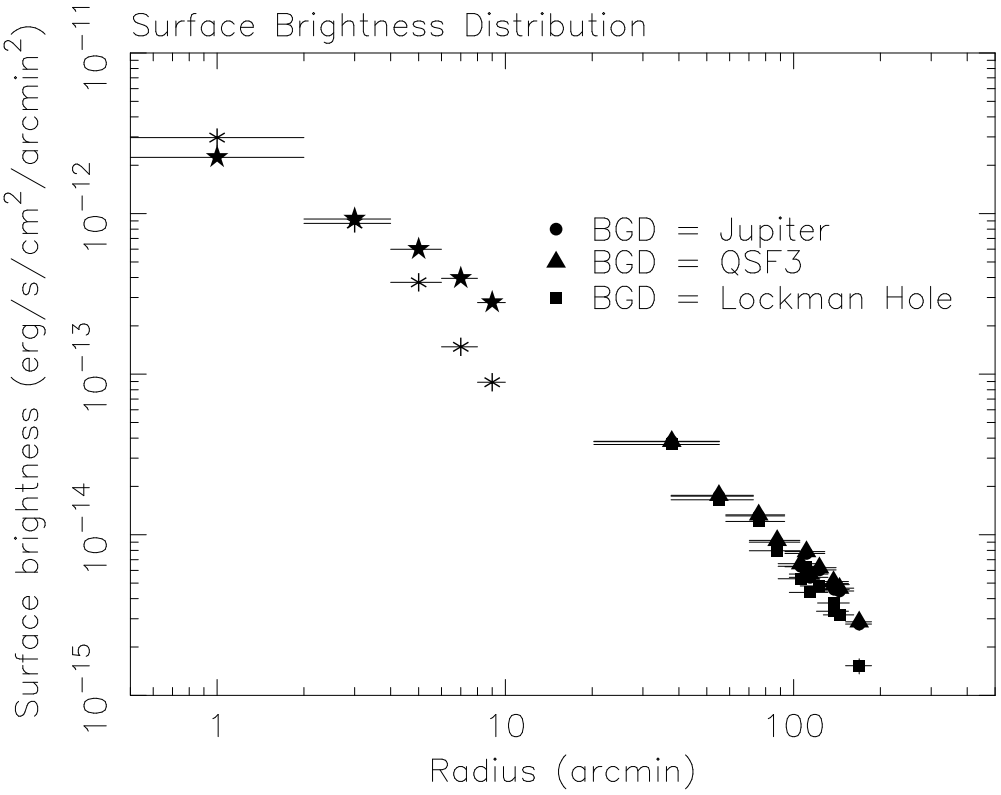

Figure 7.8: The 0.5 – 10 keV surface brightness profile of the Virgo cluster. Dots, triangles and squares represent the cases we used the data of Jupiter, QSF3, and Lockman Hole as a background, respectively. Stars and diamonds show those of the hot and cool components in M87, respectively. In this case, we fitted the spectra of M87 with the two-temperature RS model fixing the temperature of the hot component to be 2.9 keV.

Table 7.8: Analytic form of the radial temperature profile†.

BGD¶	T_s (keV)	λ (arcmin)
Jupiter	0.53±0.34	49.3(<111.8)
QSF3	0.97±0.80	96.1(<218.9)
Lockman Hole	6.9(<20.9)	575.8(<1867)

†: We fitted the radial temperature profile of figure 7.7 with a function of

$$T(r) = T_0 - T_s\,(1 - \exp(-r/\lambda)).$$

We fixed T_0 to be 2.9 keV.

¶: Data used for the background.

Substituting these results for Eq. (2.44), we calculated the integrated mass profiles of the total gravitating matter and ICM. We also calculated the stellar mass distribution using the optical brightness data of Binggeli, Sandage, Tammann (1985), [12] assuming the mass-to-light ratio is equal to 5. In figure 7.9, we show the integrated mass profiles of various components in the Virgo cluster. The mass of the ICM dominates the baryon mass beyond $20'$ ($\sim$ 87 kpc) from the center. However, beyond $50'$ from the center, the ratio of the mass of the ICM to that of the stellar mass keeps a constant value of about 5. The baryon fraction is gradually increases with radius from 0.06 at $40'$ ($\sim$ 170 kpc) to 0.18 at $200'$ ($\sim$ 870 kpc), because the slope of the ICM is steeper than that of the total gravitating mass.

7.3.2 Temperature Distribution

Whatever background we use, the temperature of the Virgo cluster decreases with radius from 2.9 keV at the center of M87 to 2.2 keV at $50'$ radius ($\sim$ 220 kpc) from the center. The temperature profile at larger radius, however, depends on the background data we selected. If we used the data from the regions of Jupiter or QSF3 which we regarded as a standard background, the temperature is almost spatially constant with radius beyond $50'$. In the case of Lockman Hole, the temperature continues to decrease beyond $50'$. However, we should note that the Lockman Hole is extremely bright background sky.

The temperature decrease with radius can be seen in many rich clusters of galaxies (Markevitch et al. 1997 [95]; Sarazin, Wise, and Markevitch 1997 [130]). Though the averaged profile of rich clusters is consistent with our profile within large errors, the profile of rich clusters seems

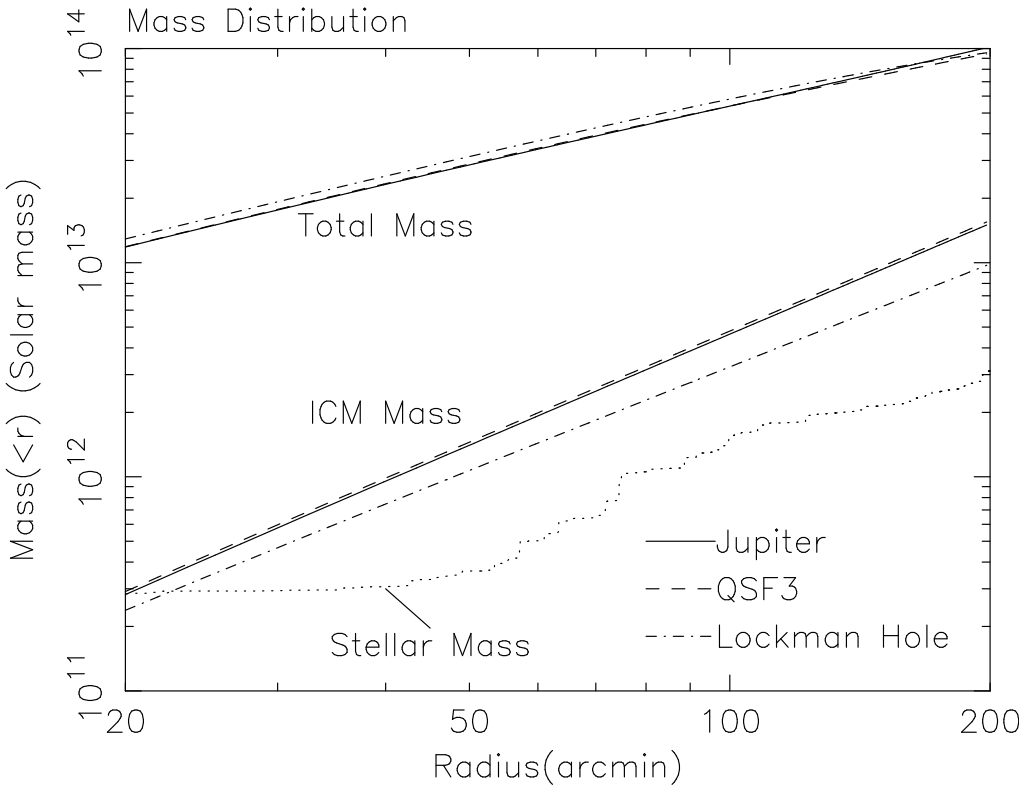

Figure 7.9: The integrated mass profiles of various components in the Virgo cluster. The upper three lines and middle three lines show distributions of the total gravitating matter, and ICM. The solid, dashed and dash-dotted lines represent that we used the data of Jupiter, QSF3 and Lockman Hole as the backgrounds, respectively. The lowest dotted line shows the stellar mass distribution.

to be steeper than that of Virgo. This may suggest that the rich clusters have steeper profiles than those of low mass clusters.

An entropy distribution of ICM sometimes provides a physical bases to diagnose the merging clusters (Markevitch Sarazin, and Irwin 1996 [94]). Assuming the ICM is an ideal gas of a monatomic molecule, the entropy per particle, s, is expressed as

$$s(n,T) = \frac{3}{2}k \ln \left(\frac{T}{n^{\frac{2}{3}}} \right) + a, \tag{7.3}$$

where n is the number density of ICM, and a is the chemical constant which is independent from T and n. We then define the extra entropy, Δs as follows,

$$\Delta s \equiv s - s_0 = \frac{3}{2}k \ln \left[\left(\frac{T}{T_0} \right) \left(\frac{n}{n_0} \right)^{-\frac{2}{3}} \right], \tag{7.4}$$

where the subscript zero denotes values at any fiducial region in the cluster. Approximating $n/n_0 \sim \sqrt{S_X/S_{X0}}$ for a qualitative estimate, where S_X is the X-ray surface brightness of the cluster, we get an approximate expression as

$$\Delta s \sim \frac{3}{2}k \ln \left[\left(\frac{T}{T_0} \right) \left(\frac{S_X}{S_{X0}} \right)^{-\frac{1}{3}} \right]. \tag{7.5}$$

We chose the central point as the fiducial region, and substituted 2.9 keV and the best-fit value of S_{X0} in table 7.7 for T_0 and S_{X0}, respectively. We thus got the entropy distribution of the Virgo cluster, which is shown in figure 7.10.

In the cases using the Jupiter and QSF3 background, the entropy increases with radius, which is usually seen in many clusters of galaxies (David, Jones and Forman 1996 [28]). This profile is mainly due to the decrease of the gas density with radius.

In an extreme case of the Lockman Hole background, the entropy distribution become almost constant, because the temperature decrease cancels the density decrease. Then we infer that the ICM of the Virgo cluster is heated adiabatically; the ICM would be recently mixed via merging, and was followed adiabatic compression to hydrostatic equilibrium, which make the temperature gradient.

Although P1, P8 and P9 have almost the same radii, the temperature at P1 is lower than those at P8 and P9 as is seen in figure 7.6 (a), hence P1 shows significantly lower entropy than P8 and P9. The ROSAT observation shows that P1 has the lowest level of the X-ray surface brightness, i.e. P1 is the edge of the X-ray emission (Böhringer et al. 1994 [16]). Suppose that primordial gas is infalling into the Virgo cluster, and make a strong shock near the positions of P1, P8 and P9. We then suggest that ICM gas at P1 is under the shock heating process, while those at P8 and P9 are immediately after the shock heating.

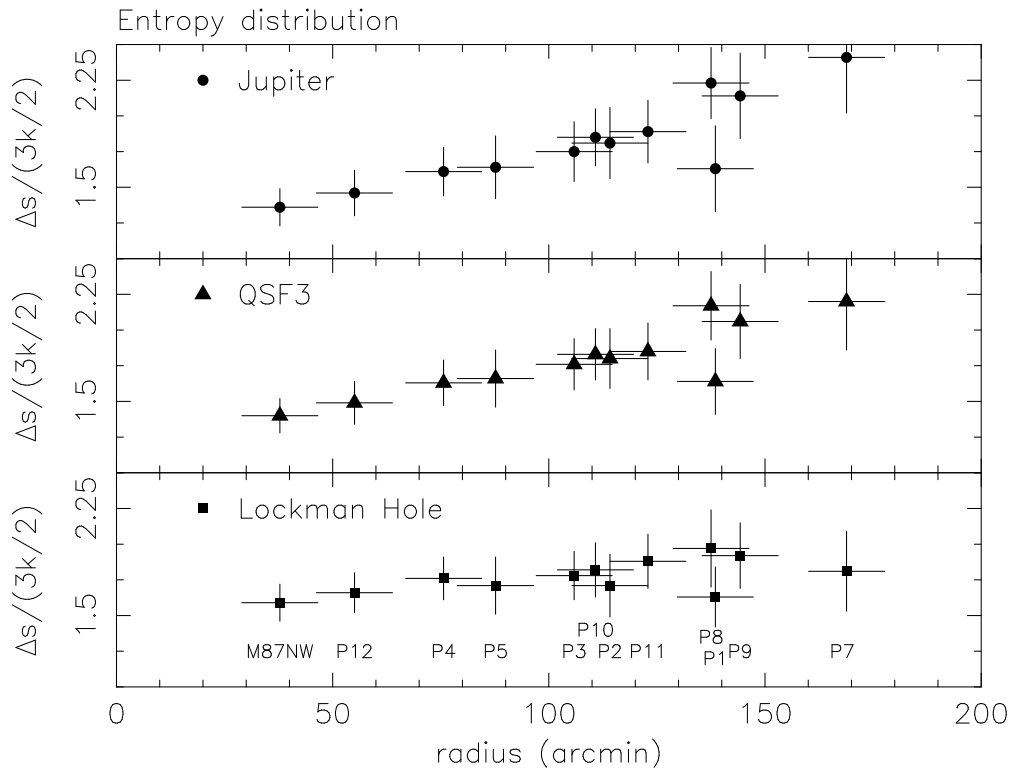

Figure 7.10: Entropy distribution relative to the central value. The upper, middle and lower panel show the cases that we used the data of Jupiter, QSF3, and Lockman hole as a background, respectively.

7.3.3 Abundance Distribution

We discovered an abundance gradient in the Virgo cluster. Since iron is a heavy atom, the iron ions would concentrate to the core of the cluster.

Suppose that a "test particle" with the mass m and charge Ze moves at a velocity v through an ionized gas in the ICM. All the ICM particles are assumed to have the same mass, m_f, and charge, $Z_f e$, with the number density of n_f and temperature of T. Then the thermal velocity of the ICM particles, v_f, is defined as

$$v_f = \sqrt{\frac{2kT}{m_f}}. \tag{7.6}$$

The velocity slow-down rate of the test particle by interaction with the ICM particles, Δv, can be expressed as,

$$\Delta v = -\frac{A_D}{v_f^2}\left(1+\frac{m}{m_f}\right) G\left(\frac{v}{v_f}\right), \tag{7.7}$$

where the diffusion constant A_D is defined by using the Coulomb logarithm Λ as,

$$A_D = \frac{8\pi e^4 n_f Z^2 Z_f^2 \ln\Lambda}{m^2}. \tag{7.8}$$

The function $G(x)$ is defined in terms of the usual error function, $\Phi(x)$,

$$G(x) = \frac{\Phi(x) - x\Phi'(x)}{2x^2}, \tag{7.9}$$

where $\Phi(x)$ is

$$\Phi(x) = \frac{2}{\sqrt{\pi}}\int_0^x e^{-y^2} dy \tag{7.10}$$

(Spitzer 1962 [139]). If $x \ll 1$, substituting $1-y^2$ for e^{-y^2} in Eq. (7.10), we get

$$\Phi(x) \sim \frac{2}{\sqrt{\pi}}(1-x^2) \tag{7.11}$$

and

$$G(x) \sim \frac{2x}{3\sqrt{\pi}}. \tag{7.12}$$

Therefore, if the velocity of the test particle, v, is much smaller than the thermal velocity of the ICM particle, v_f, we get

$$\Delta v = -\frac{16\sqrt{\pi}e^4 n_f Z^2 Z_f^2 \ln\Lambda}{3m^2 v_f^3}\left(1+\frac{m}{m_f}\right) v. \tag{7.13}$$

In a stationary state, the dynamical friction force should be in balance with the inward gravitational force. Thus we can estimate the drift speed of the test particle, v_D, by equating Δv with the cluster gravitational acceleration, g,

$$g = -\frac{16\sqrt{\pi}e^4 n_f Z^2 Z_f^2 \ln\Lambda}{3m^2 v_f^3}\left(1+\frac{m}{m_f}\right) v_D. \tag{7.14}$$

g can be expressed as

$$g = \frac{GM(< r)}{r^2}, \tag{7.15}$$

where $M(< r)$ is the total gravitating mass within a radius r. In our case, the test and ICM particles are iron and proton, respectively, and $1 + m/m_f \sim A$, where A is the mass number of iron (A $\simeq$ 56). Therefore the drift speed of the test particle can be written,

$$v_D = \frac{3}{16\sqrt{\pi}} \frac{Am_p^2 v_f^3 g}{Z^2 e^4 n_f \ln \Lambda}, \tag{7.16}$$

where m_p is the proton mass (Fabian and Pringle 1977 [41]). We also have to take collisions with helium nuclei into account in a real situation, which reduce the drift speed by a factor of 1.8. Thus we get the iron drift velocity numerically,

$$v_D = 1.4 \times 10^{-2} T^{\frac{3}{2}} g/n_f \text{ cm/sec} \tag{7.17}$$

(Rephaeli 1978 [124]). Using this relation, we estimated the travel distance of iron within the Hubble time ($\sim 10^{10}$ yr) in the Virgo cluster, which is shown in figure 7.11. We used the results shown in table 7.8, table 7.7, and figure 7.9 to estimate T, n_f, and g. The travel distance of iron is rather short in all the three cases. Magnetic fields in the Virgo ICM would further reduce the travel distance. Therefore we expect that the iron nuclei have not moved largely from the initial positions of the iron productions (i.e. the member galaxies), and that there should be a correlation between the ICM abundance (Fe) and the positions of member galaxies. We show distributions of luminosity densities of member galaxies calculated using the data of Binggeli et al. (1985) [12] in figure 7.12, where dots represent early-type galaxies (E + S0 + dE + dS0), while triangles show late-type galaxies (S + Irr). The abundance profile is roughly consistent with the distributions of the luminosity density of early-type galaxies, and extremely different from that of spiral galaxies. This suggests the origin of iron in the ICM of the Virgo cluster is early-type galaxies, which support the conclusions of Arnaud et al. (1992) [5] and Tsuru (1993) [153].

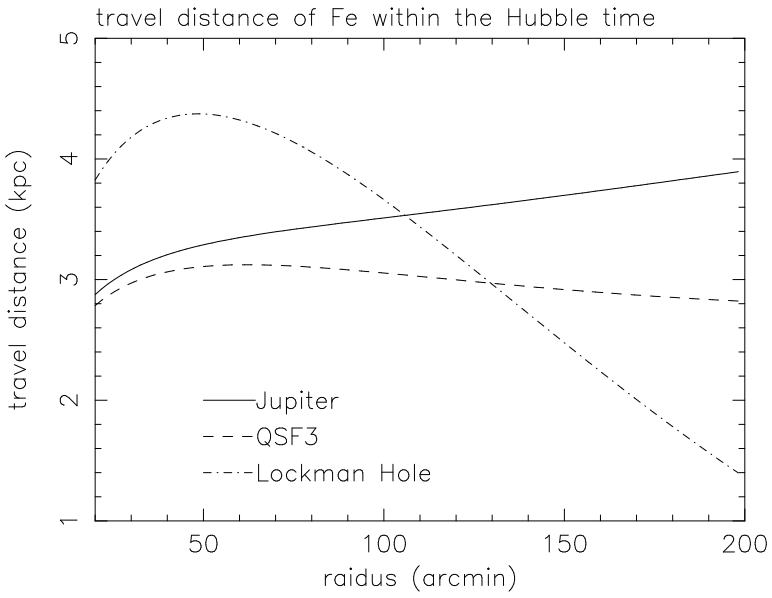

Figure 7.11: Travel distance of iron within the Hubble time in the Virgo cluster.

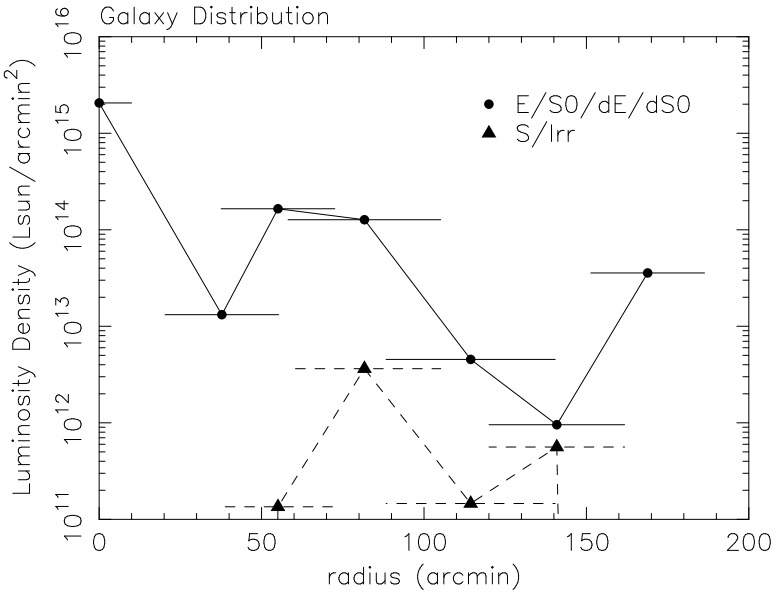

Figure 7.12: Distribution of the luminosity density of member galaxies. Dots show that of early type galaxies (E + S0 + dE + dS0), while triangles show that of late type galaxies (S + Irr).

Chapter 8

Conclusion

We summarize our observational results of the Virgo cluster of galaxies with ASCA.

1. We detected two-temperature plasma components from the region near to M87. On the other hand, the ICM of the Virgo cluster at a region beyond $40'$ from M87 is found to be one-temperature plasma.

2. The temperature of the hot component of M87 is about 2.9 keV and is nearly constant from $0'$ to $10'$. The surface brightness of the hot component is smoothly extrapolated to that of the ICM beyond $40'$. Therefore the hot component is likely to be the ICM of the Virgo main body.

3. The temperature of the ICM decreases with radius from $10'$ to $50'$ from M87. Beyond $50'$, the temperature is almost constant at 2.2 keV.

4. The temperature of the cool component of M87 is ~ 1.3 keV, and shows no variation over the field of M87. The flux of the cool component is more concentrated toward the center of M87 than that of the hot component.

5. We found clear gradient of abundances of Fe, Si, and S. The iron abundance is 0.5 solar at the M87 center, and gradually decreases to about 0.2 – 0.3 at $40'$ from M87, then stay almost constant beyond the distance of $40'$. No significant radial variation of the oxygen abundance, however, is found.

6. We found that the abundances of S and Si in the inner regions are larger than those of O and Fe, with no significant gradient on the ratios of Si/ Fe and S/Fe. The ratio of Si/Fe is rather similar to, while that of S/Fe is rather larger than, those found in rich clusters (Mushotzky et al. 1996 [118]),

7. The abundance ratio of O/Fe is smaller than the solar ratio. Since the current theory predict that O and Si come from nearly same mass progenitors, the co-existence of low O/Fe and high Si/Fe is puzzling (Loewenstein, and Mushotzky 1996 [90]),

8. The abundance distribution in the Virgo cluster is consistent with the distribution of luminosity density of early-type galaxies. This suggests the origin of iron in the ICM of the Virgo cluster is early type galaxies.

9. We found a low-temperature region at $140'$ from M87. This suggests the ICM at the region is now undergoing shock heating.

10. We found no strong nuclear activity from M87. The upper limit of the absorption-corrected flux of the power-law component is $\sim 2.5\times10^{-12}$ erg cm^{-2} s^{-1} in the 0.5 – 10.0 keV band. Compared with the previous results, we suggest a long-term variability of the AGN activity of M87.

Appendix A

ASCA spectra of M87

A.1 The spatially resolaved ASCA spectra of M87

We show the spatially resolved X-ray specta of M87 taken with the SIS and GIS. The background spectrum is subtracted from each spectrum.

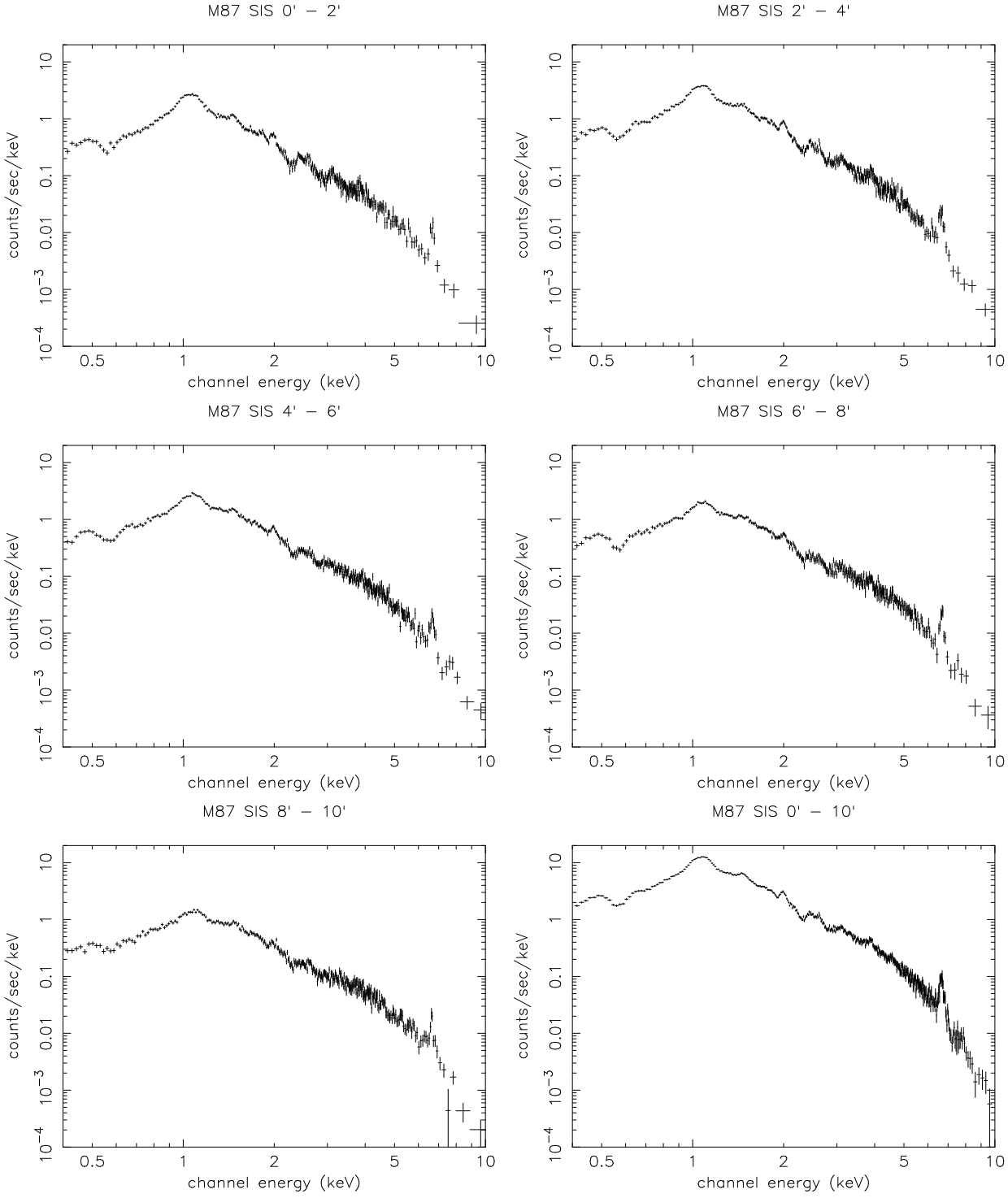

Figure A.1: The SIS spectra of M87 taken from different annular regions of the radius 0′– 2′, 2′– 4′, 4′– 6′, 6′– 8′, 8′– 10′, and 0′– 10′.

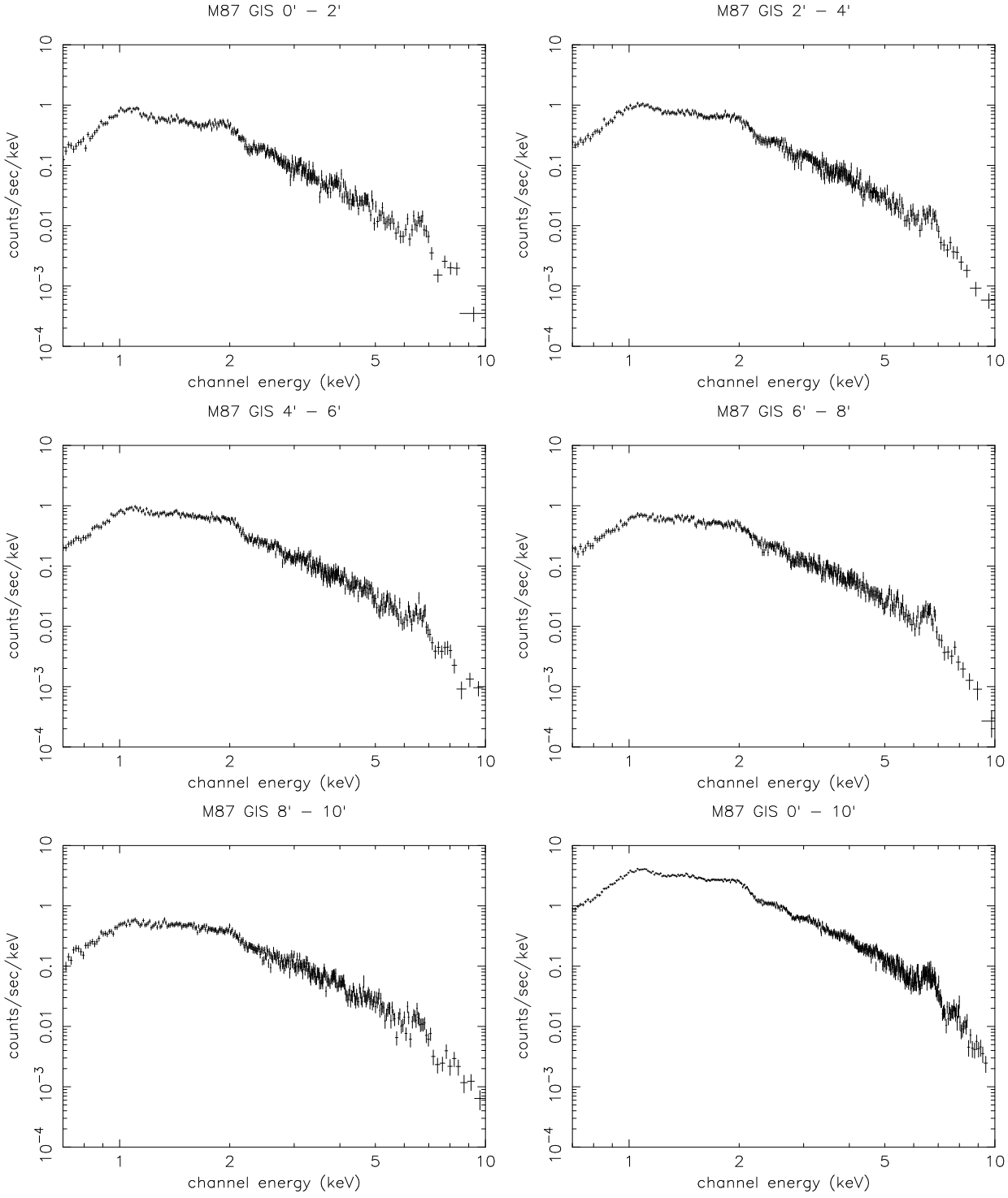

Figure A.2: The GIS spectra of M87 taken from different annular regions of the radius 0′– 2′, 2′– 4′, 4′– 6′, 6′– 8′, 8′– 10′, and 0′– 10′.

A.2 The bremsstrahlung plus Gaussian lines model fitting

We fitted the SIS (1.6 – 10 keV) and GIS (3.0 – 10 keV) spectra of M87 with the thermal bremsstrahlung continuum and Gaussian lines model. We show the best-fit model and its residuals in figure A.3 and A.4.

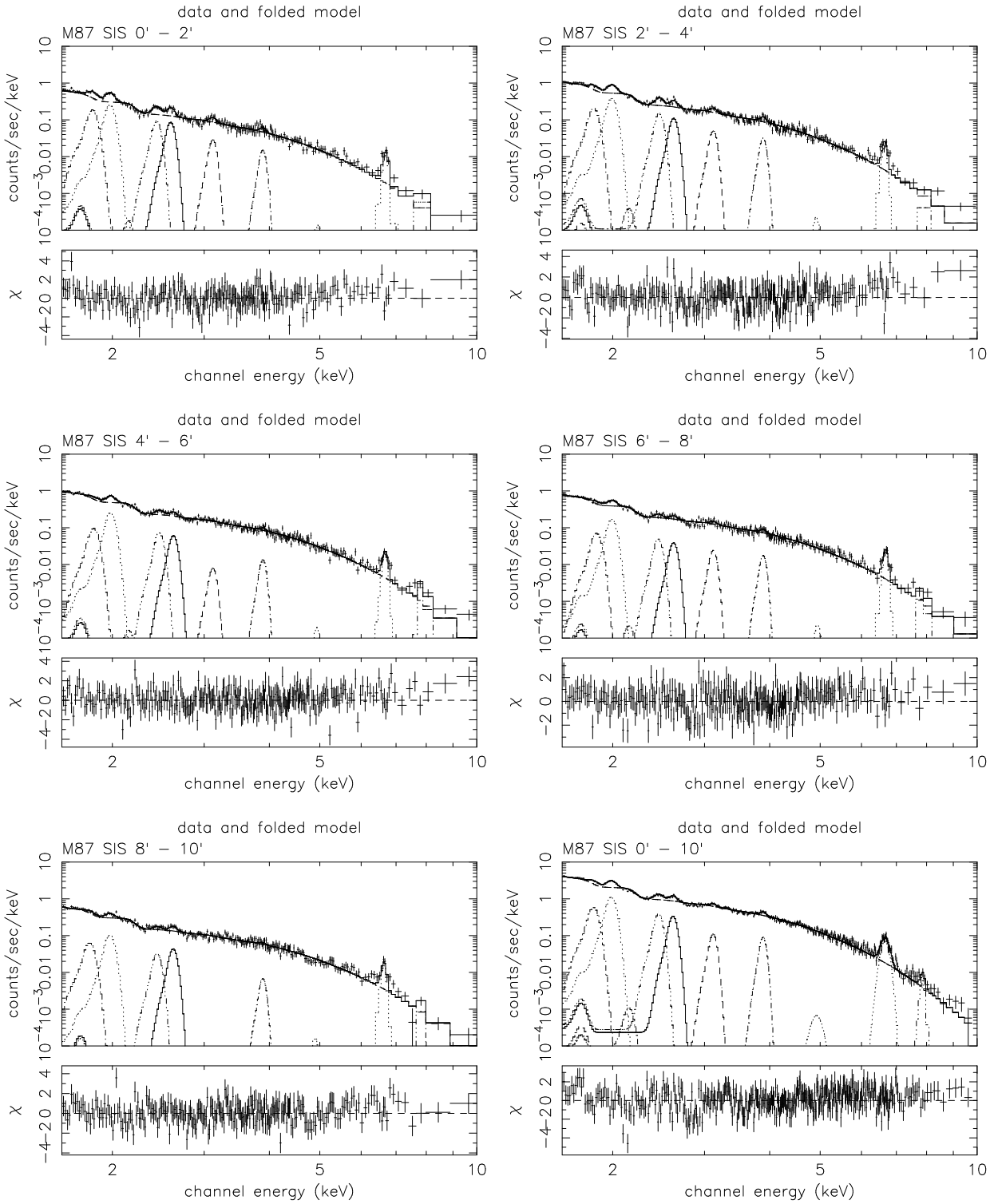

Figure A.3: The result of the thermal bremsstrahlung plus Gaussian lines model fitting to the spatially resolved SIS spectra of the high-energy band (1.6 – 10 keV).

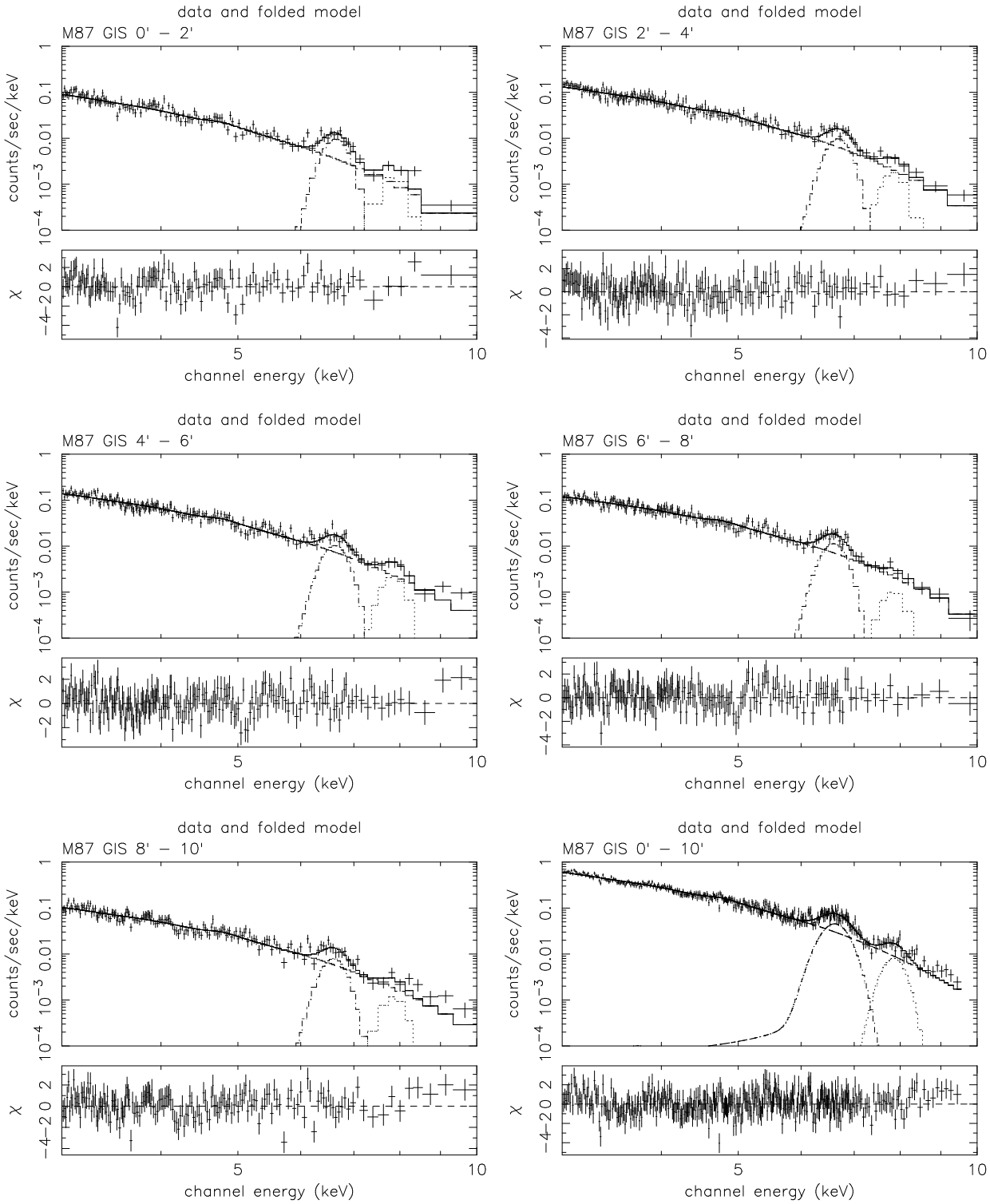

Figure A.4: The result of the thermal bremsstrahlung plus Gaussian lines model fitting to the spatially resolved GIS spectra of the high-energy band (3 – 10 keV).

A.3 The spectra of M87 fitted with the one-temperature RS model

We fitted the SIS (0.4 – 10 keV) and GIS (0.7 – 10 keV) spectra of M87 simulatneously with the one-temperature RS model. The plasma temperature, normalizations for the SIS and GIS, the interstellar absorptions for the SIS and GIS and metal abundances of O, Mg, Si, S, Ar, Ca, and Fe were free parameters.

Figure A.5: The spatially resolved SIS and GIS spectra of M87. The solid line shows the best-fitting one-temperature RS model. The model was fitted with the SIS and GIS data simultaneously. However, for clarity, we show the SIS and GIS spectra in the left and right columns separately.

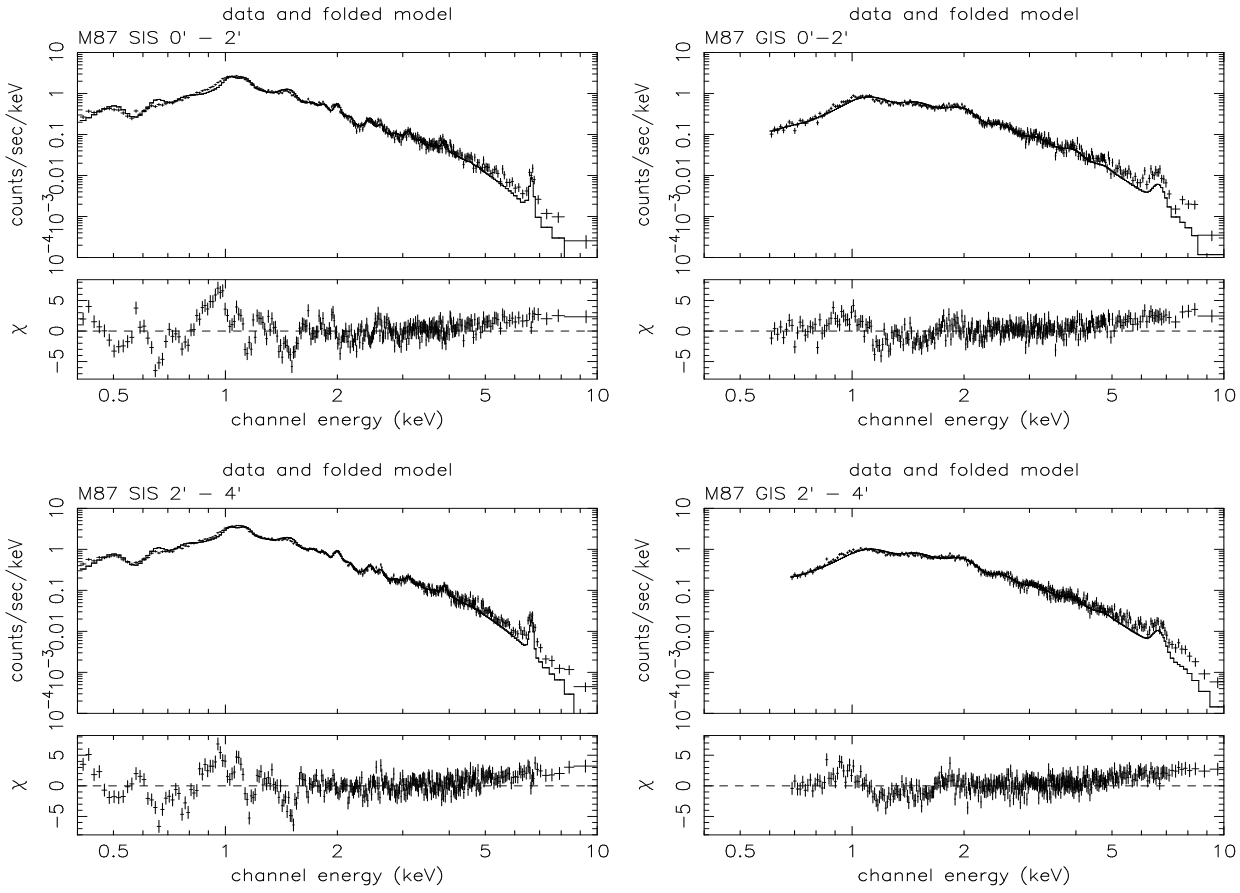

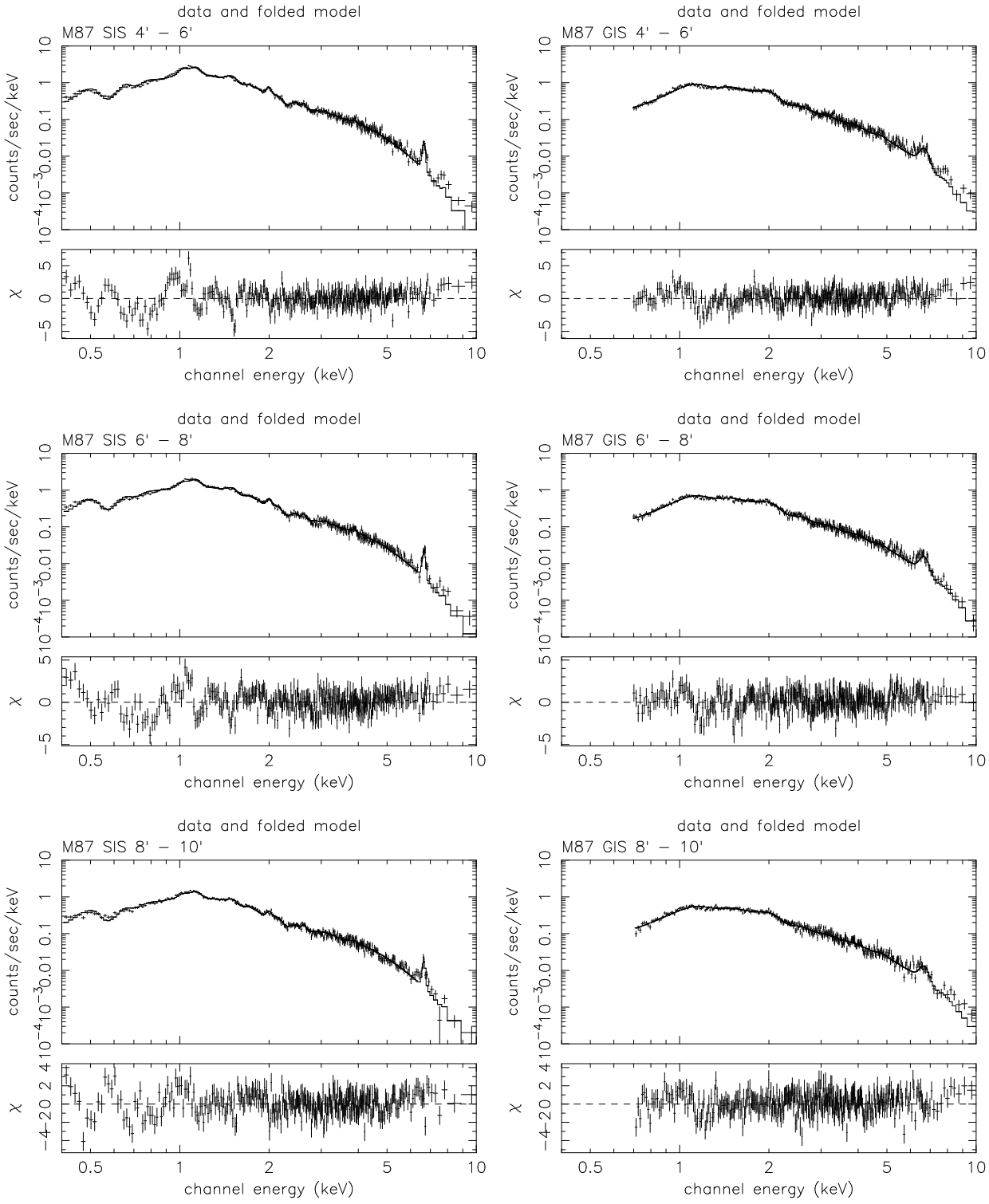
data and folded model
M87 SIS 4' – 6'
counts/sec/keV
χ
channel energy (keV)
data and folded model
M87 GIS 4' – 6'
counts/sec/keV
χ
channel energy (keV)
data and folded model
M87 SIS 6' – 8'
counts/sec/keV
χ
channel energy (keV)
data and folded model
M87 GIS 6' – 8'
counts/sec/keV
χ
channel energy (keV)
data and folded model
M87 SIS 8' – 10'
counts/sec/keV
χ
channel energy (keV)
data and folded model
M87 GIS 8' – 10'
counts/sec/keV
χ
channel energy (keV)

A.4 The two temperature RS model fitting (I)

We fitted the SIS (0.4 – 10 keV) and GIS (0.7 – 10 keV) spectra of M87 simulatneously with the two-temperature RS model. In this case, both temperatures of the hot and cool components are free parameters.

The other free parameters were the abundances of O, Si, S, Ar, Ca, and Fe, the normalizations of the hot component for the SIS and the GIS, the ratio of normalization of the cool component to that of the hot component, and the interstellar absorptions for the SIS and the GIS. We assumed that the metal abundances for the cool component is the same as that of the hot component.

Figure A.6: The spatially resolved SIS and GIS spectra of M87. The solid line shows the best-fitting two-temperature RS model. The model was fitted with the SIS and GIS data simultaneously. However, for clarity, we show the SIS and GIS spectra in the left and right columns separately.

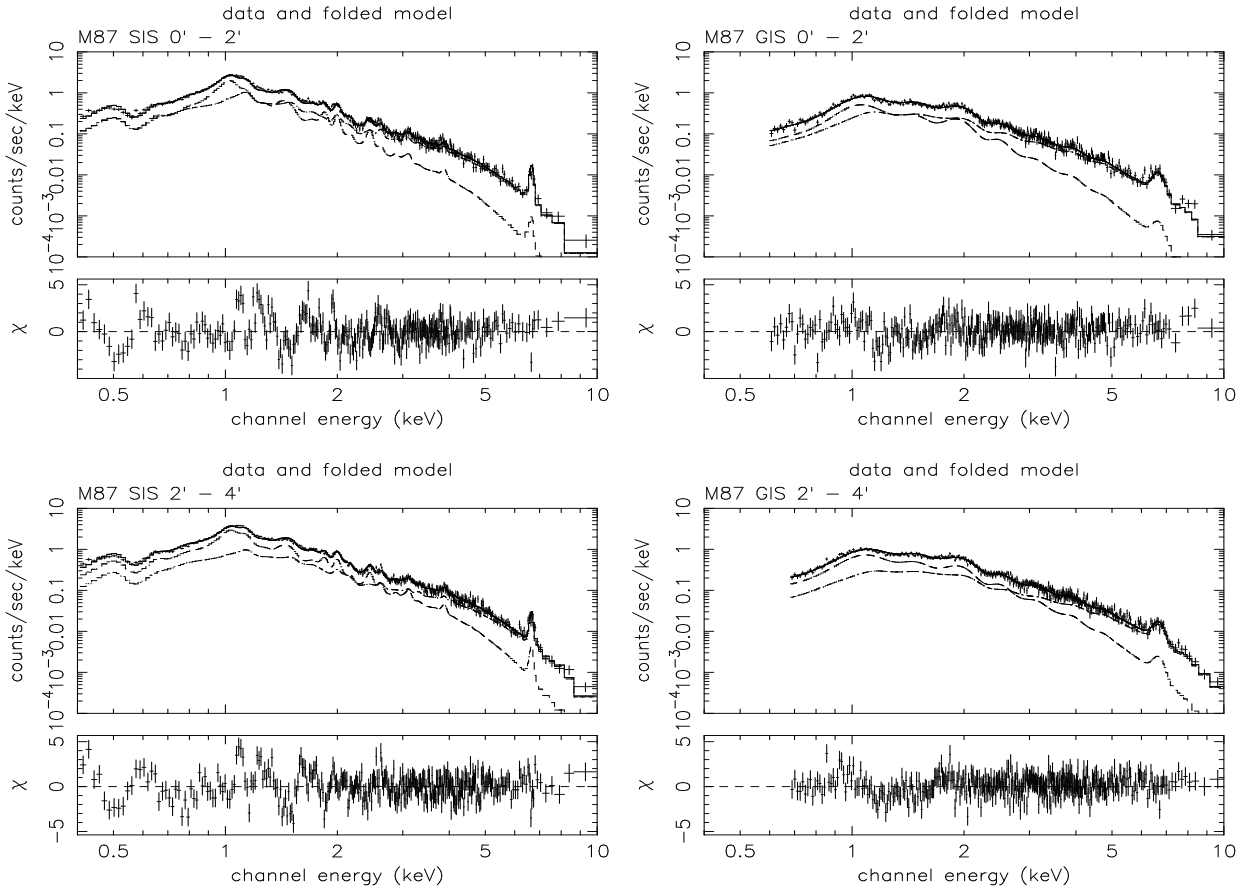

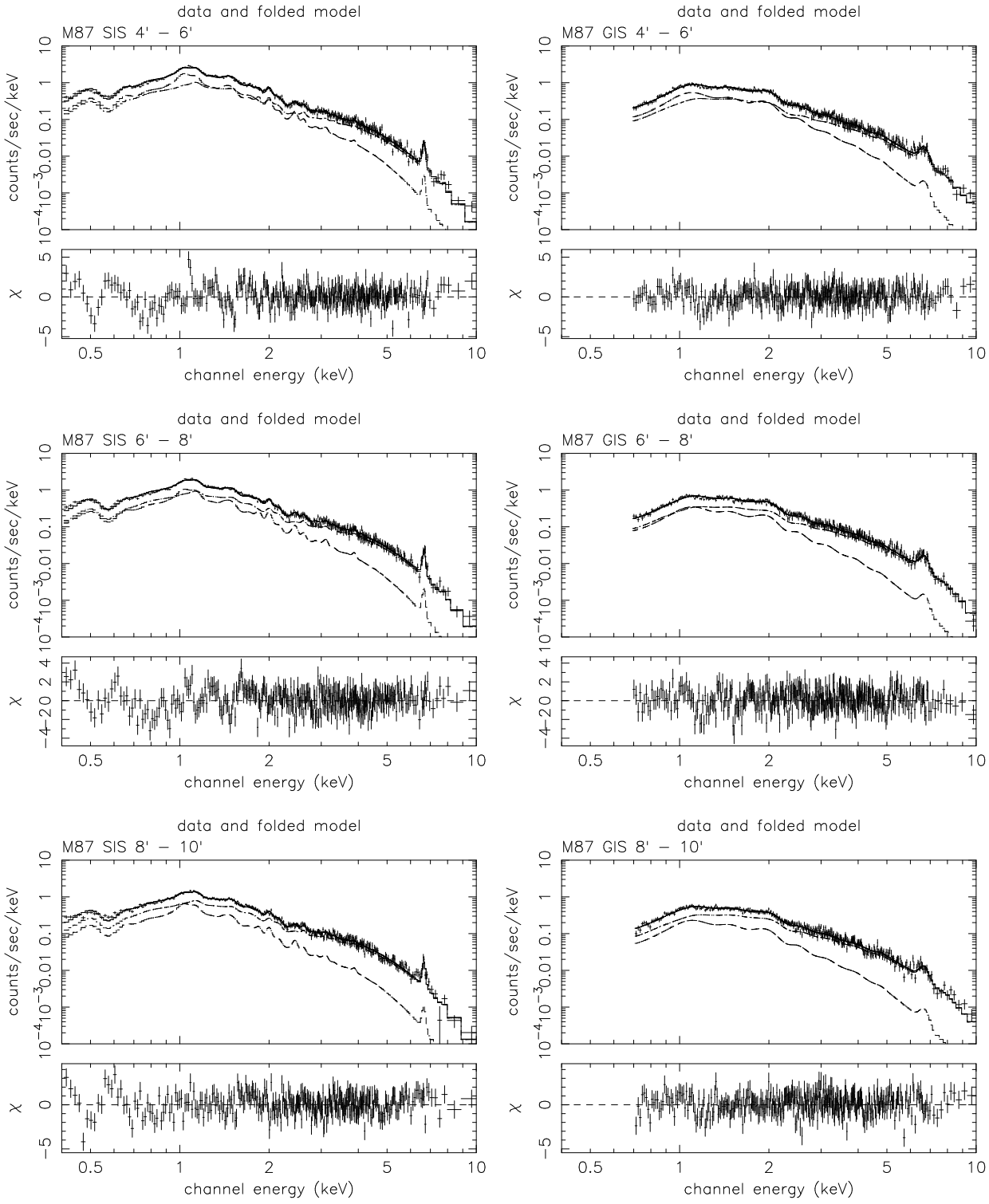
data and folded model
M87 SIS 4' – 6'
counts/sec/keV
χ
channel energy (keV)
data and folded model
M87 GIS 4' – 6'
counts/sec/keV
χ
channel energy (keV)
data and folded model
M87 SIS 6' – 8'
counts/sec/keV
χ
channel energy (keV)
data and folded model
M87 GIS 6' – 8'
counts/sec/keV
χ
channel energy (keV)
data and folded model
M87 SIS 8' – 10'
counts/sec/keV
χ
channel energy (keV)
data and folded model
M87 GIS 8' – 10'
counts/sec/keV
χ
channel energy (keV)

A.5 The two temperature RS model fitting (II)

We fitted the SIS (0.4 – 10 keV) and GIS (0.7 – 10 keV) spectra of M87 simulatneously with the two-temperature RS model. In this case, the temperature of the hot component is fixed to 2.9 keV.

The free parameters were the temperature of the cool component, the abundances of O, Si, S, Ar, Ca, and Fe, the normalizations of the hot component for the SIS and the GIS, the ratio of normalization of the cool component to that of the hot component, and the interstellar absorptions for the SIS and the GIS. We assumed that the metal abundances for the cool component is the same as that of the hot component.

Figure A.7: The spatially resolved SIS and GIS spectra of M87. The solid line shows the best-fitting two-temperature RS model. In this case, the temperature of the hot component is fixed to 2.9 keV. The model was fitted with the SIS and GIS data simultaneously. However, for clarity, we show the SIS and GIS spectra in the left and right columns separately.

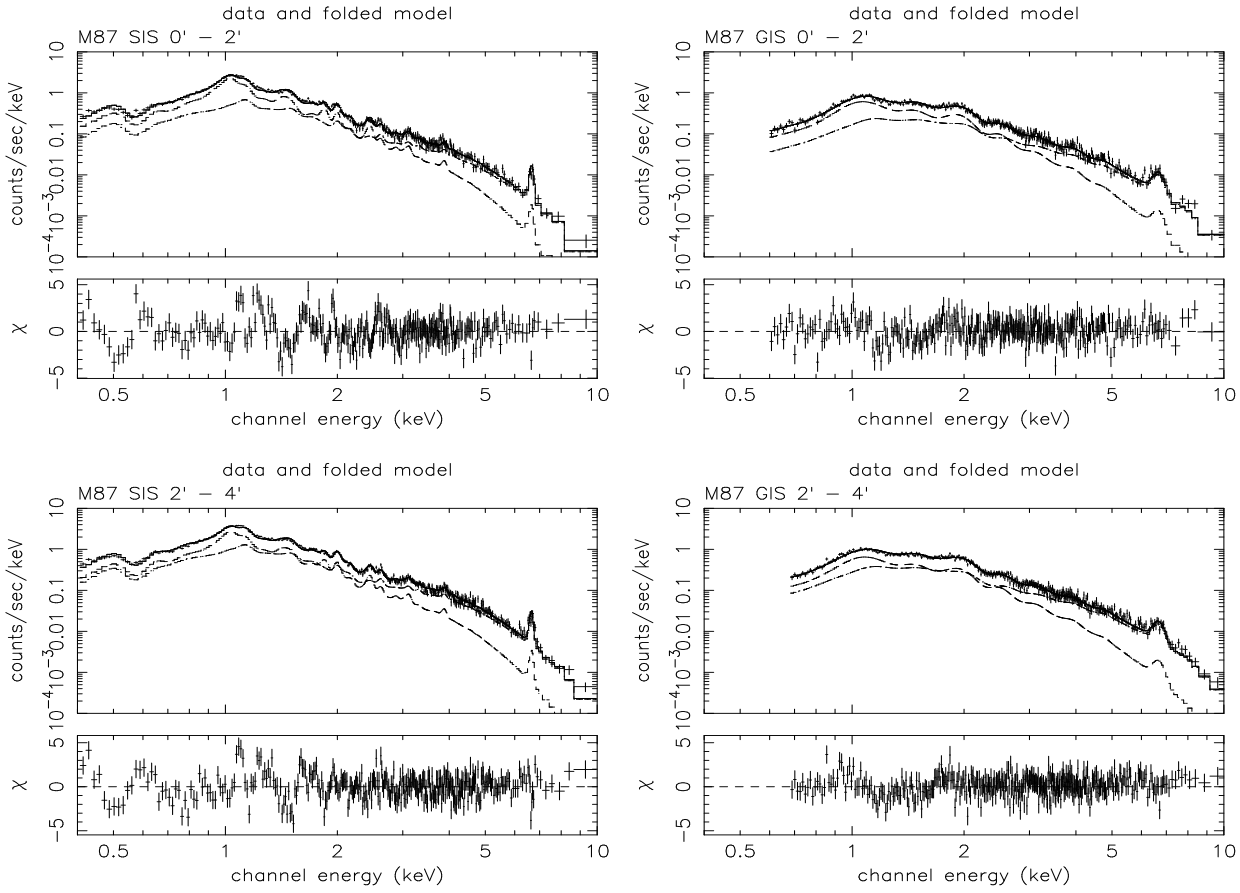

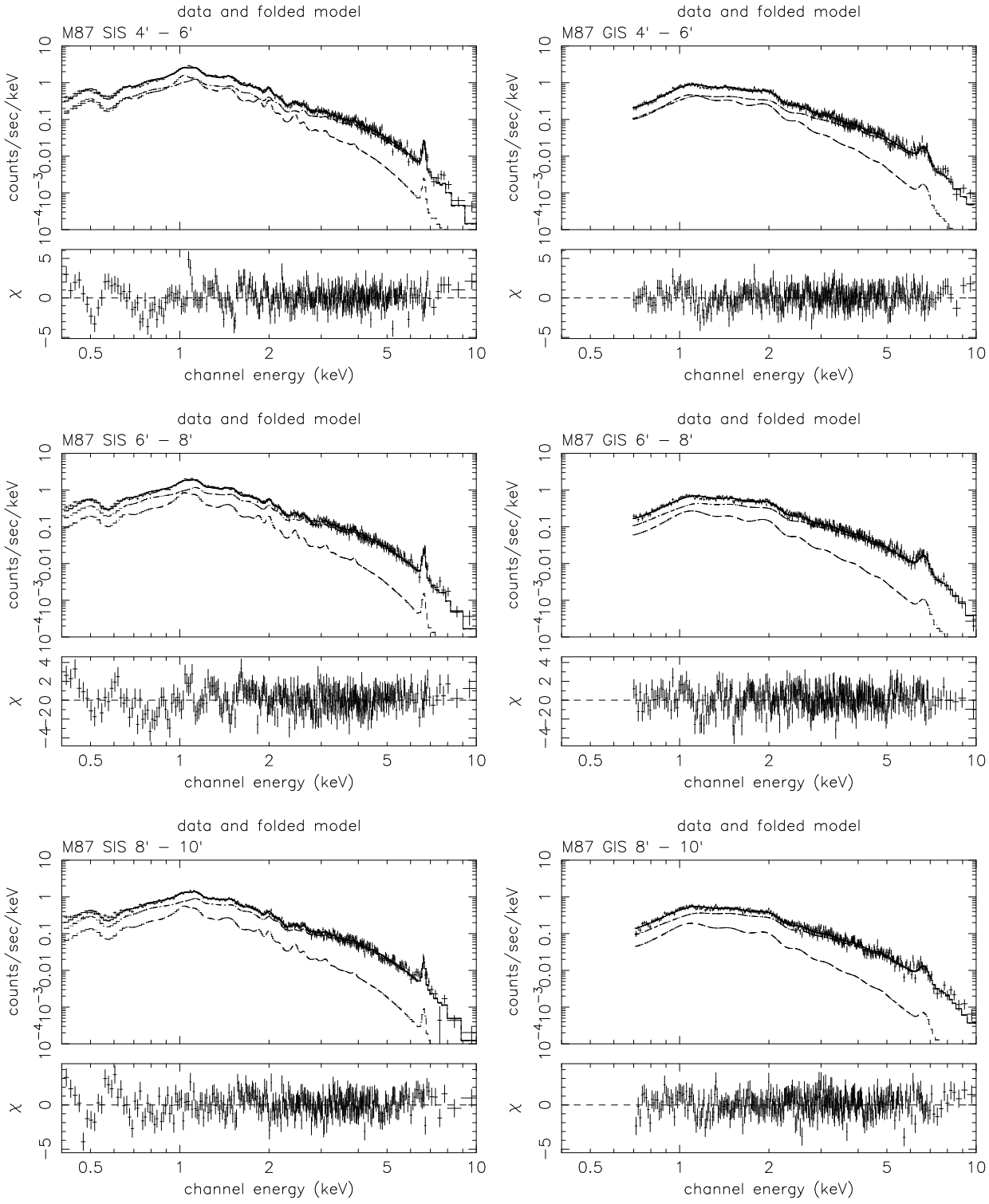
data and folded model
M87 SIS 4' – 6'
counts/sec/keV
χ
channel energy (keV)
data and folded model
M87 GIS 4' – 6'
counts/sec/keV
χ
channel energy (keV)
data and folded model
M87 SIS 6' – 8'
counts/sec/keV
χ
channel energy (keV)
data and folded model
M87 GIS 6' – 8'
counts/sec/keV
χ
channel energy (keV)
data and folded model
M87 SIS 8' – 10'
counts/sec/keV
χ
channel energy (keV)
data and folded model
M87 GIS 8' – 10'
counts/sec/keV
χ
channel energy (keV)

Appendix B

The MEKAL model fitting

B.1 RS model vs MEKAL model

In figure B.1, we show model spectra from thin thermal plasma. The temperature of it is 1.4 keV, which is almost the same temperature of the cool component of M87. The abundance of it is 1.0 solar. We can see clear differences between the RS and MEKAL models around 0.8 – 2 keV. Because this may significantly change our results with the RS model, we used the MEKAL model to fit the spectra of M87.

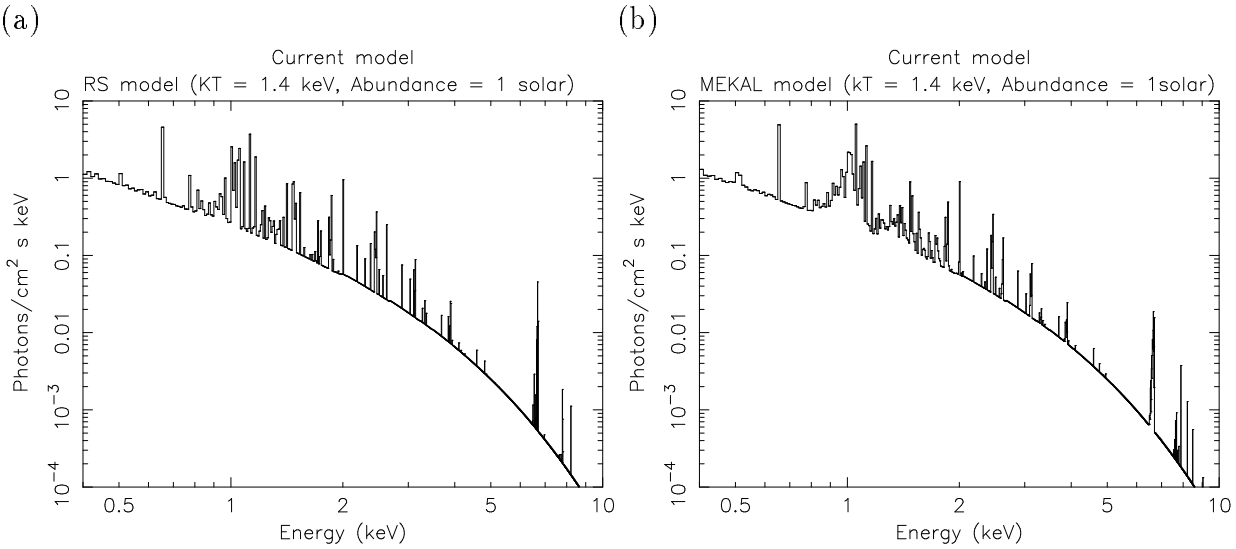

Figure B.1: Model spectra from thin thermal plasma of whose temperature metal abundance are 1.4 keV and 1.0 solar; (a) RS model; (b) MEKAL model.

B.2 The one-temperature MEKAL model

First we fitted the spatially spectra taken with the SIS and GIS simultaneously with the one-temperature MEKAL model modified by interstellar absorption. The free and fixed parameters are the same as those of the one-temperature RS model (p. 74). The best-fit model curves and spectra are shown in figure B.2. We show the best-fit $\chi^2/d.o.f.$ in table B.1 which can be compared with table 6.3. Though the values are significantly smaller than those of the RS model fitting, the fit is not satisfactory. Therefore we tried the two-temperature MEKAL model.

Table B.1: The $\chi^2/d.o.f$ values of the one-temperature MEKAL model fitting.

	$0'$–$2'$	$2'$–$4'$	$4'$–$6'$	$6'$–$8'$	$8'$–$10'$
$chi^2/d.o.f.$	1284/629	1250/716	969.4/726	840.7/712	835.3/682

Figure B.2: The spatially resolved SIS and GIS spectra of M87. The solid line shows the best-fitting one-temperature MEKAL model. The model was fitted with the SIS and GIS data simultaneously. However, for clarity, we show the SIS and GIS spectra in the left and right columns separately.

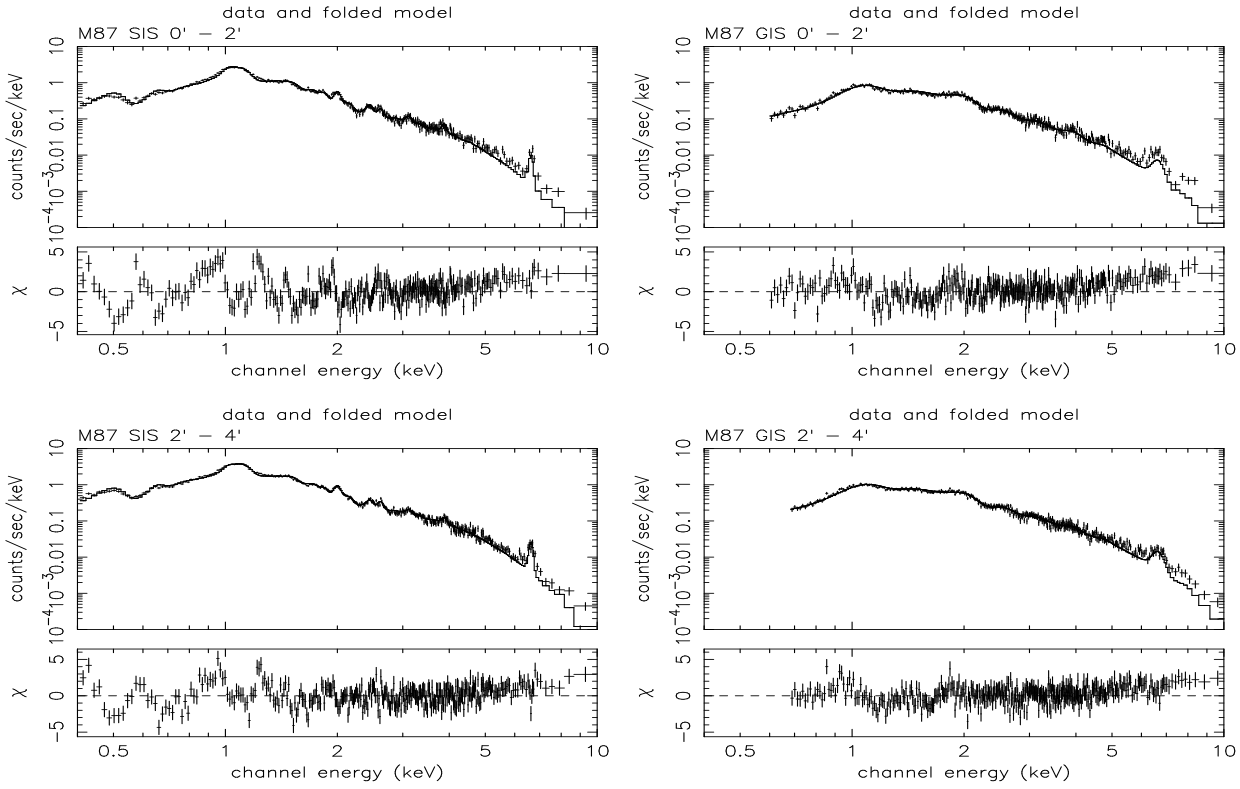

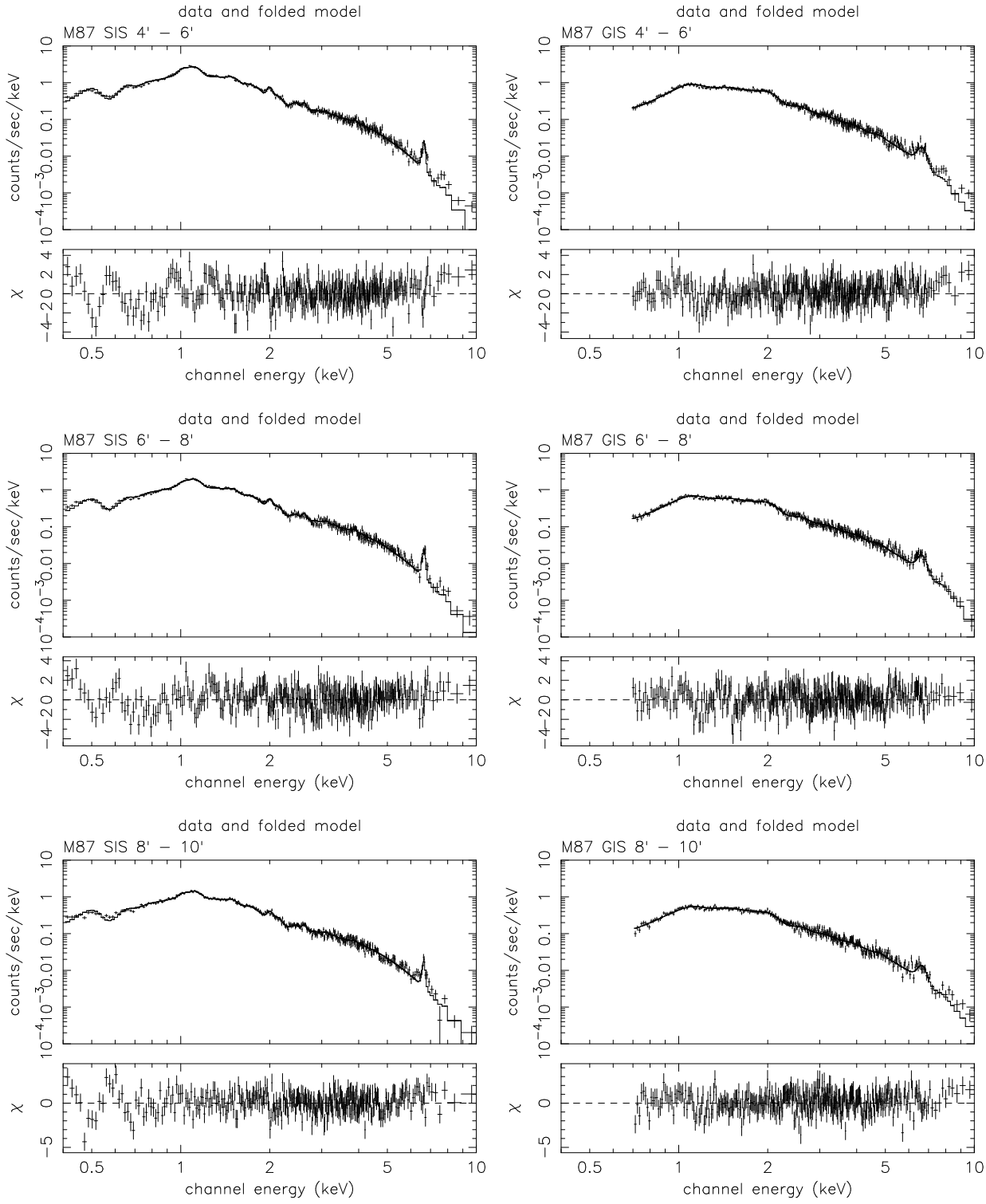
data and folded model
M87 SIS 4' – 6'
counts/sec/keV
χ
channel energy (keV)
data and folded model
M87 GIS 4' – 6'
counts/sec/keV
χ
channel energy (keV)
data and folded model
M87 SIS 6' – 8'
counts/sec/keV
χ
channel energy (keV)
data and folded model
M87 GIS 6' – 8'
counts/sec/keV
χ
channel energy (keV)
data and folded model
M87 SIS 8' – 10'
counts/sec/keV
χ
channel energy (keV)
data and folded model
M87 GIS 8' – 10'
counts/sec/keV
χ
channel energy (keV)

B.3 The two-temperature MEKAL model

The one-temperature could not fit the spectra, we then tried the two-temperature MEKAL model. The free and fixed parameters are the same as those of the two-temperature RS model (p. 75) except for the temperature of the hot component. In the case of this model fitting, the temperature of the hot component is much strongly coupled with the ratio of normalization of the cool component to that of the hot component than in the case of the RS model. We thus fixed the temperature of the hot component to be 2.9 keV, which is the average temperature of the hot component obtained by the two-temperature RS model fitting. The best-fit parameters and model curves are shown in table B.2 and figure B.3, respectively.

Comparing table B.2 with table 6.5, the χ^2 values are significantly smaller than those of the RS model. However, there is no essential difference between the RS and MEKAL model as summarized below;

1. Though the temperatures of the cool component of the MEKAL model are slightly higher than those of the RS model, they are almost spatially constant.
2. The *EI* of the cool component is more concentrated toward the center of M87 than that of the hot component.
3. The abundaces of Si, S and Fe show strong concentration toward the M87 center.
4. The abundace of O is almost spatially constant.
5. The abundance ratio of O/Fe is smaller than the solar ratio.
6. The abundance ratios of Si:S:Fe are almost spatially constant.

We thus conclude that the results of our thesis are not essentially changed even if we used the MEKAL model instead of the RS model.

Table B.2: The results of the two-temperature MEKAL model fitting. The temperature of the hot component is fixed to 2.9 keV.*

Radius	0′–2′	2′–4′	4′–6′	6′–8′	8′–10′
$N_{\rm H}$(SIS)	5.49	5.99	5.54	4.49	4.76
(10^{20}cm^{-2})	(4.94–5.96)	(5.54–6.41)	(5.09–5.99)	(4.02–4.98)	(4.20–5.33)
$N_{\rm H}$(GIS)	2.72	2.34	1.35	0.00	1.17
(10^{20} cm^{-2})	(1.22–4.18)	(1.03–3.66)	(0.00–2.74)	(<1.49)	(<2.93)
kT_1(keV)	1.41	1.53	1.66	1.74	1.75
	(1.39–1.43)	(1.50–1.56)	(1.60–1.73)	(1.64–1.86)	(1.60–1.82)
kT_2(keV)	2.9(fix)	2.9(fix)	2.9(fix)	2.9(fix)	2.9(fix)
Abundance (Solar)					
O	0.21	0.29	0.43	0.32	0.32
	(0.13–0.30)	(0.21–0.38)	(0.34–0.54)	(0.20–0.44)	(0.18–0.39)
Mg	0.09	0.06	0.17	0.12	0.21
	(<0.18)	(0.00–0.15)	(0.07–0.27)	(0.00–0.25)	(0.06–0.36)
Si	0.74	0.76	0.68	0.69	0.52
	(0.68–0.81)	(0.70–0.82)	(0.62–0.75)	(0.61–0.77)	(0.44–0.61)
S	0.70	0.68	0.51	0.52	0.46
	(0.63–0.78)	(0.61–0.75)	(0.44–0.59)	(0.43–0.61)	(0.36–0.57)
Ar	0.50	0.58	0.21	0.41	0.29
	(0.28–0.72)	(0.39–0.76)	(<0.41)	(0.18–0.65)	(0.04–0.55)
Ca	0.98	0.90	0.27	0.49	0.37
	(0.61–1.32)	(0.62–1.18)	(<0.56)	(0.16–0.82)	(<0.74)
Fe	0.46	0.44	0.38	0.37	0.31
	(0.44–0.49)	(0.42–0.46)	(0.36–0.40)	(0.35–0.40)	(0.28–0.34)
EI(SIS)§	5.16	7.73	7.13	7.14	5.87
(10^{64} cm^{-3})	(5.02–5.28)	(7.19–8.23)	(6.38–7.70)	(6.33–7.77)	(4.90–6.50)
EI(GIS)§	5.53	6.74	7.27	7.11	6.57
(10^{64} cm^{-3})	(5.35–5.94)	(6.28–7.19)	(6.52–7.86)	(6.30–7.74)	(5.50–7.27)
EI ratio‡	1.99	1.51	1.07	0.64	0.57
(low-kT/high-kT)	(1.75–2.25)	(1.33–1.70)	(0.91–1.31)	(0.51–0.85)	(0.42–0.87)
Cool Component					
Fx(10^{-11} erg/s/cm^2)†					
SIS	3.34	3.75	2.46	1.50	1.05
GIS	3.77	3.50	2.71	1.62	1.26
Lx(10^{41} erg/s)††					
SIS	9.99	11.27	7.34	4.37	3.08
GIS	10.12	9.83	7.48	4.34	3.45
Hot Component					
Fx(10^{-11} erg/s/cm^2)†					
SIS	2.13	3.19	2.93	2.94	2.36
GIS	2.37	2.92	3.17	3.11	2.78
Lx(10^{41} erg/s)††					
SIS	6.15	9.27	8.49	8.40	6.77
GIS	6.59	8.08	8.66	8.35	7.58
$\chi^2/d.o.f.$	977.6/628	997.8/715	892.2/725	806.8/711	819.0/681

* The errors in the brackets are at 90% confidence level.

§ EI is Emission Integral of hot component.

‡ Ratio of EI of cool component to that of hot component.

† X-ray flux in the 0.5 – 10 keV band from each annulus.

†† X-ray luminosity in the 0.5 – 10 keV band from each annulus.

Figure B.3: The spatially resolved SIS and GIS spectra of M87. The solid line shows the best-fitting two-temperature MEKAL model. The model was fitted with the SIS and GIS data simultaneously. However, for clarity, we show the SIS and GIS spectra in the left and right columns separately.

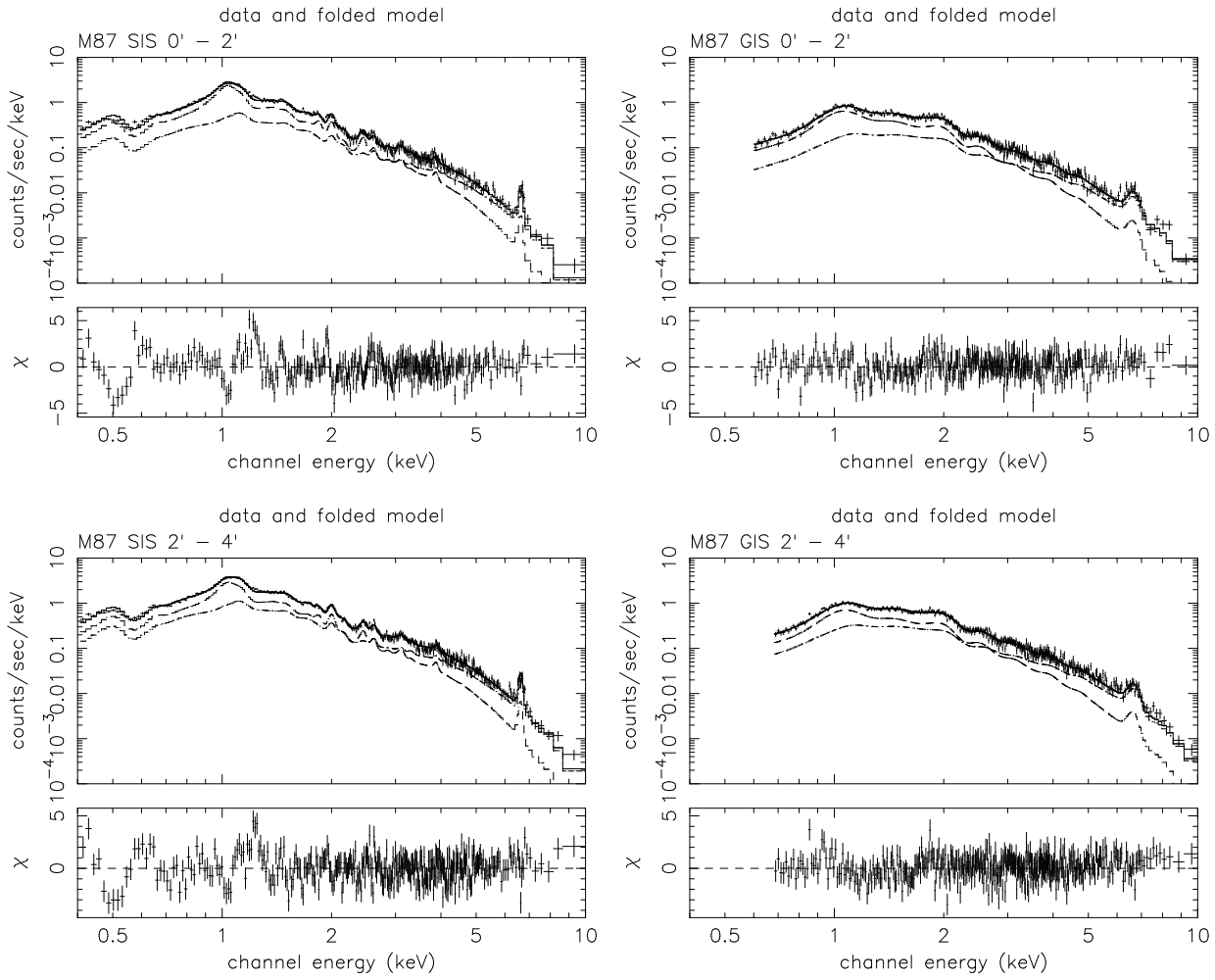

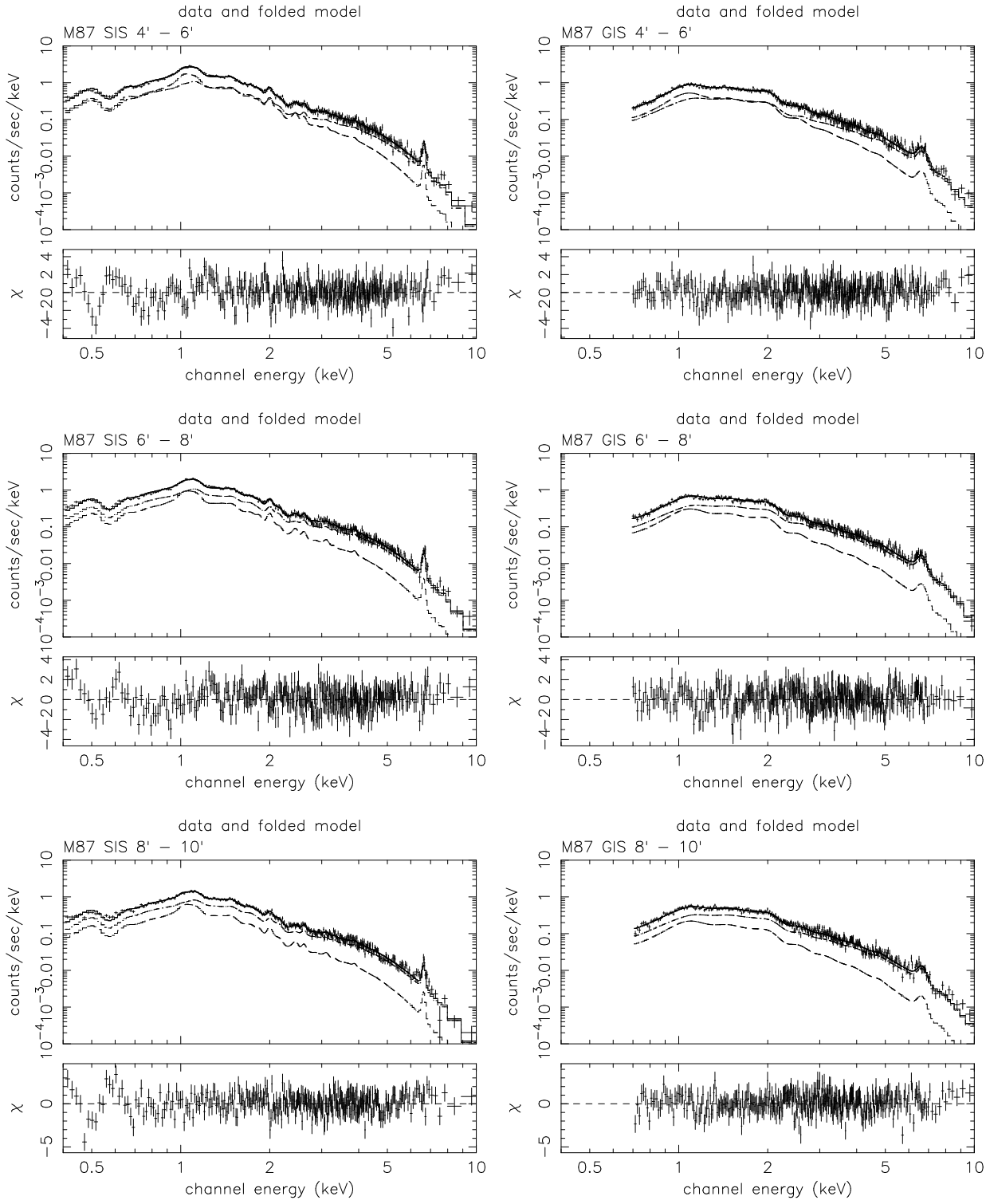
data and folded model
M87 SIS 4' – 6'
counts/sec/keV
χ
channel energy (keV)
data and folded model
M87 GIS 4' – 6'
counts/sec/keV
χ
channel energy (keV)
data and folded model
M87 SIS 6' – 8'
counts/sec/keV
χ
channel energy (keV)
data and folded model
M87 GIS 6' – 8'
counts/sec/keV
χ
channel energy (keV)
data and folded model
M87 SIS 8' – 10'
counts/sec/keV
χ
channel energy (keV)
data and folded model
M87 GIS 8' – 10'
counts/sec/keV
χ
channel energy (keV)

Appendix C

ASCA GIS images of the Virgo cluster

We show the X-ray images of the Virgo cluster obtained with the GIS. The all band (0.7 – 10 keV) images are shown in the left column, while the hard band (3 – 10 keV) images are shown in the right column. Dots show sources with S/N ratios greater than 5.0, while triangles show candidates for sources whose S/N ratios are in between 4.5 and 5.0. Crosses shows the VCC sources (Binggeli, Sandage and Tammann 1985 [12]).

Figure C.1: The GIS images of the Virgo clusters.

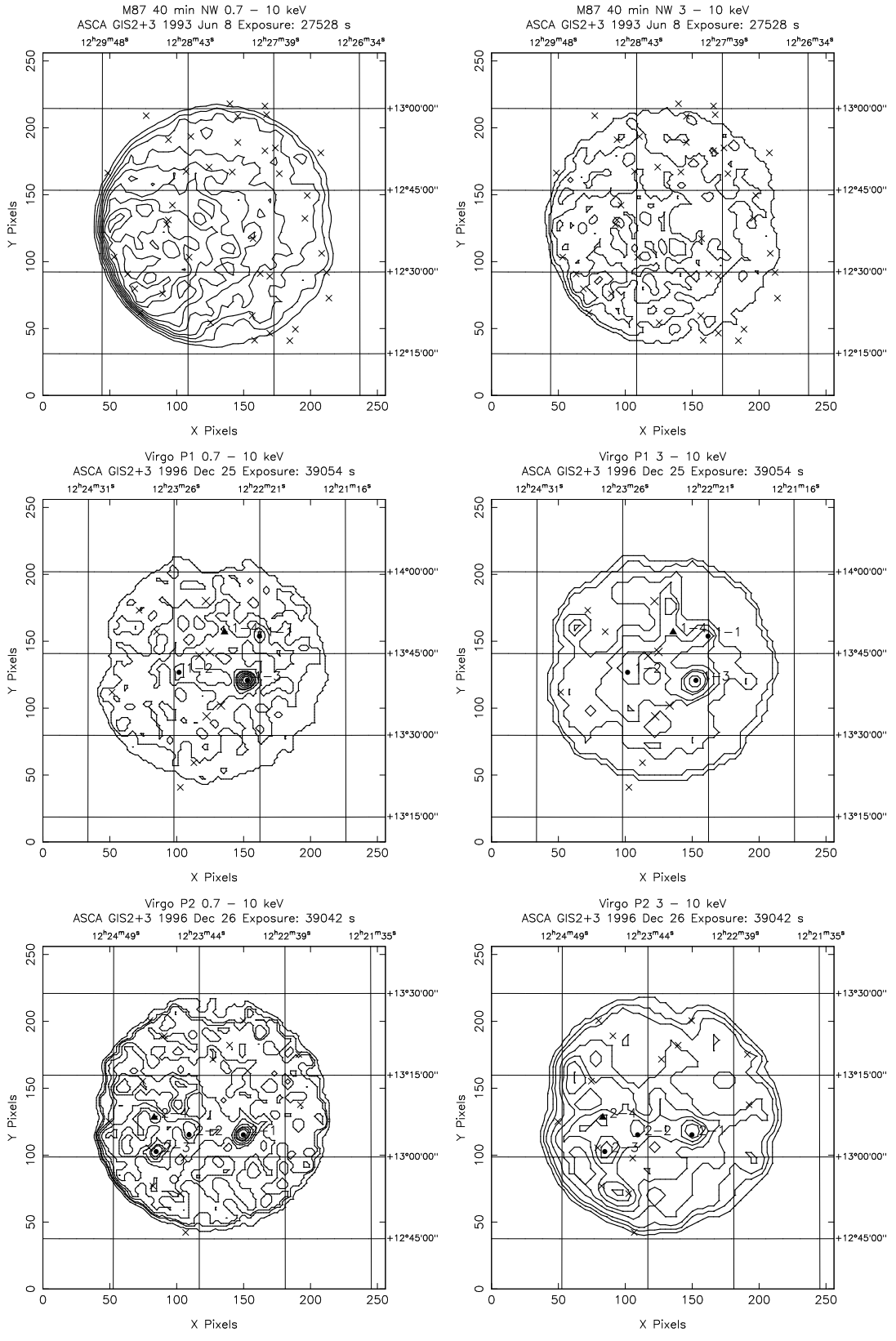

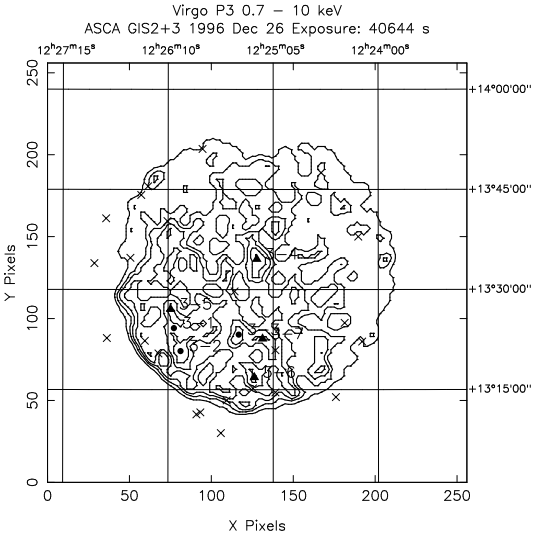
Virgo P3 0.7 – 10 keV
ASCA GIS2+3 1996 Dec 26 Exposure: 40644 s
12h27m15s
12h26m10s
12h25m05s
12h24m00s
+14°00'00"
+13°45'00"
+13°30'00"
+13°15'00"
Y Pixels
X Pixels

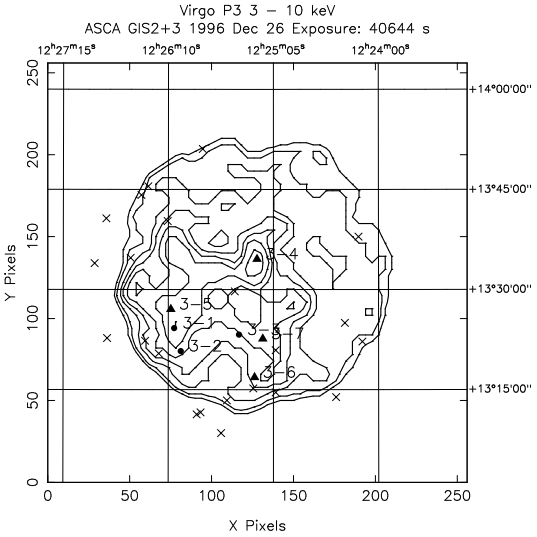
Virgo P3 3 – 10 keV
ASCA GIS2+3 1996 Dec 26 Exposure: 40644 s
12h27m15s
12h26m10s
12h25m05s
12h24m00s
+14°00'00"
+13°45'00"
+13°30'00"
+13°15'00"
Y Pixels
X Pixels

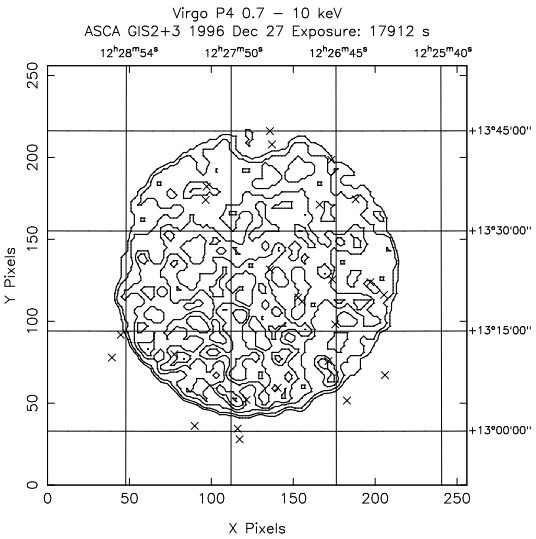
Virgo P4 0.7 – 10 keV
ASCA GIS2+3 1996 Dec 27 Exposure: 17912 s
12h28m54s
12h27m50s
12h26m45s
12h25m40s
+13°45'00"
+13°30'00"
+13°15'00"
+13°00'00"
Y Pixels
X Pixels

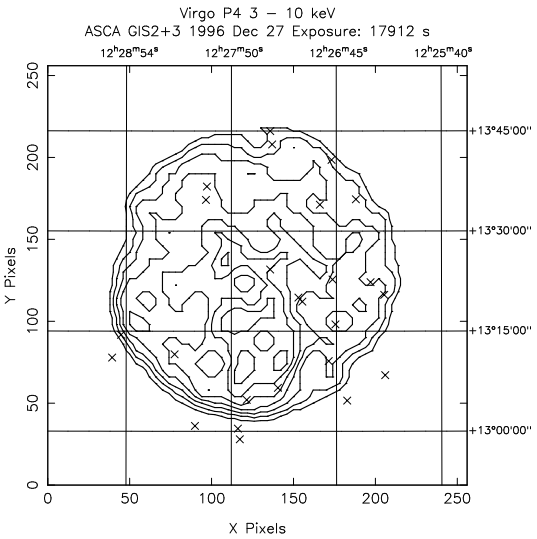
Virgo P4 3 – 10 keV
ASCA GIS2+3 1996 Dec 27 Exposure: 17912 s
12h28m54s
12h27m50s
12h26m45s
12h25m40s
+13°45'00"
+13°30'00"
+13°15'00"
+13°00'00"
Y Pixels
X Pixels

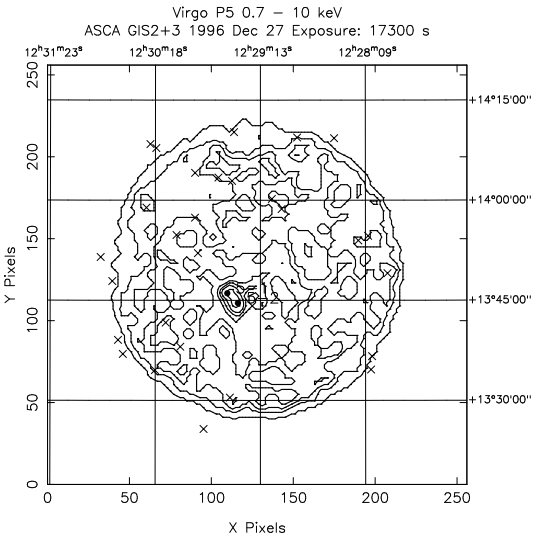
Virgo P5 0.7 – 10 keV
ASCA GIS2+3 1996 Dec 27 Exposure: 17300 s
12h31m23s
12h30m18s
12h29m13s
12h28m09s
+14°15'00"
+14°00'00"
+13°45'00"
+13°30'00"
Y Pixels
X Pixels

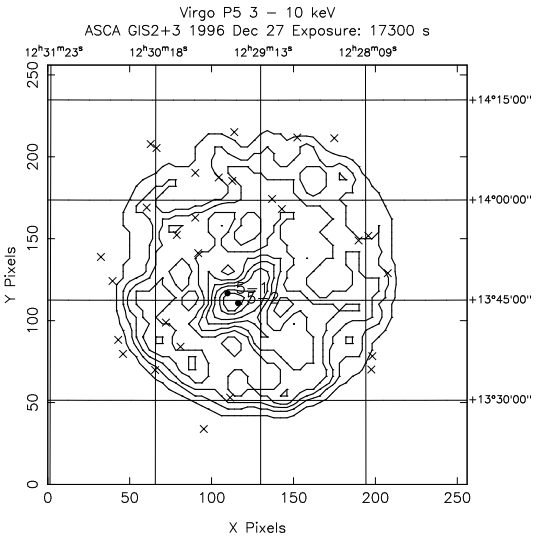
Virgo P5 3 – 10 keV
ASCA GIS2+3 1996 Dec 27 Exposure: 17300 s
12h31m23s
12h30m18s
12h29m13s
12h28m09s
+14°15'00"
+14°00'00"
+13°45'00"
+13°30'00"
Y Pixels
X Pixels

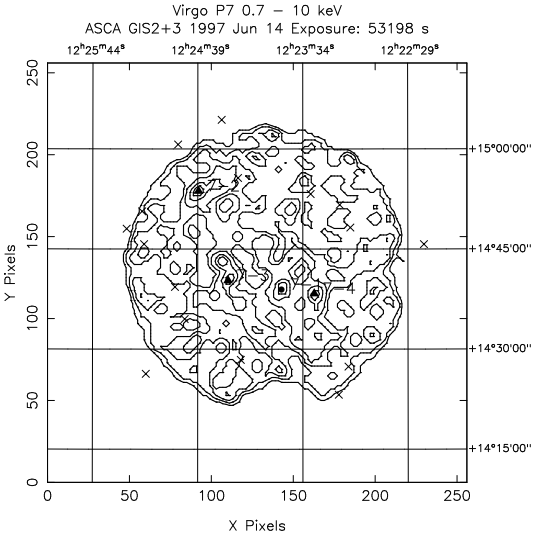
Virgo P7 0.7 – 10 keV
ASCA GIS2+3 1997 Jun 14 Exposure: 53198 s
12h25m44s
12h24m39s
12h23m34s
12h22m29s
+15°00'00"
+14°45'00"
+14°30'00"
+14°15'00"
Y Pixels
X Pixels

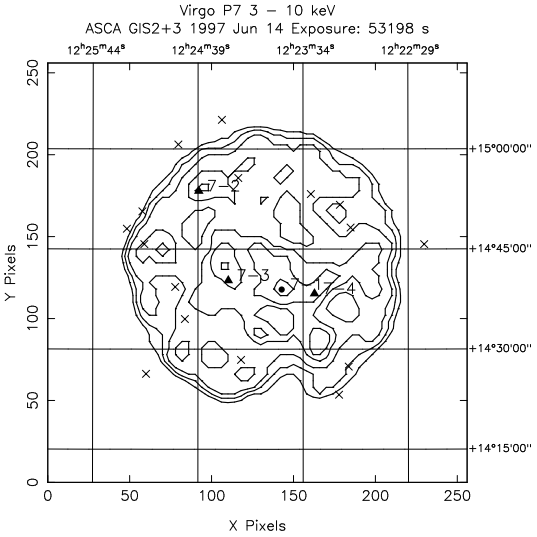
Virgo P7 3 – 10 keV
ASCA GIS2+3 1997 Jun 14 Exposure: 53198 s
12h25m44s
12h24m39s
12h23m34s
12h22m29s
+15°00'00"
+14°45'00"
+14°30'00"
+14°15'00"
Y Pixels
X Pixels

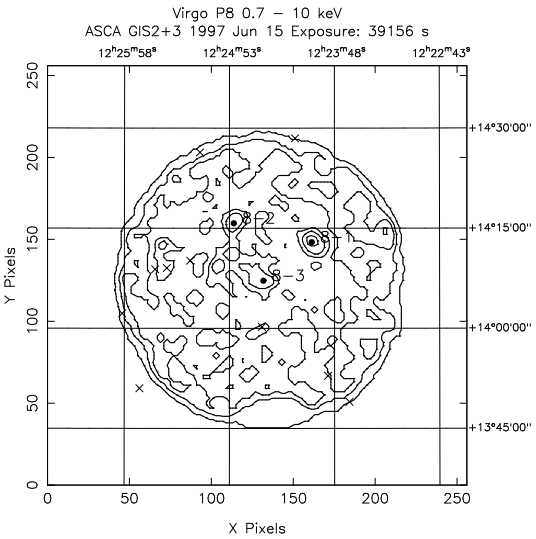
Virgo P8 0.7 – 10 keV
ASCA GIS2+3 1997 Jun 15 Exposure: 39156 s
12h25m58s
12h24m53s
12h23m48s
12h22m43s
+14°30'00"
+14°15'00"
+14°00'00"
+13°45'00"
Y Pixels
X Pixels

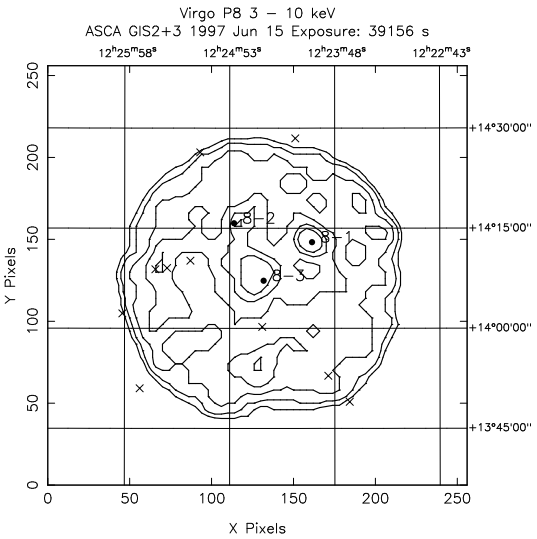
Virgo P8 3 – 10 keV
ASCA GIS2+3 1997 Jun 15 Exposure: 39156 s
12h25m58s
12h24m53s
12h23m48s
12h22m43s
+14°30'00"
+14°15'00"
+14°00'00"
+13°45'00"
Y Pixels
X Pixels

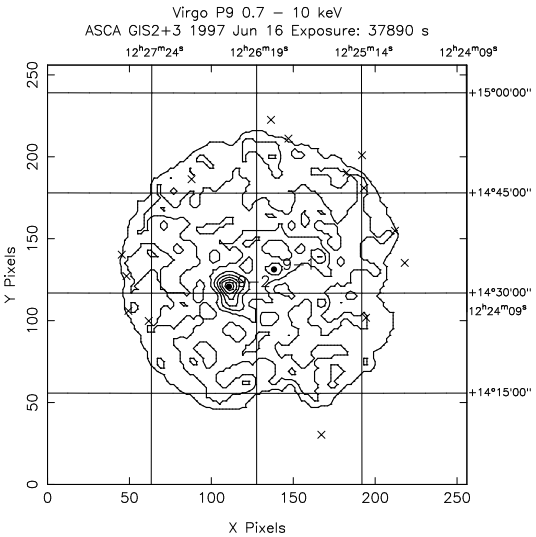
Virgo P9 0.7 – 10 keV
ASCA GIS2+3 1997 Jun 16 Exposure: 37890 s
12h27m24s
12h26m19s
12h25m14s
12h24m09s
+15°00'00"
+14°45'00"
+14°30'00"
+14°15'00"
Y Pixels
X Pixels

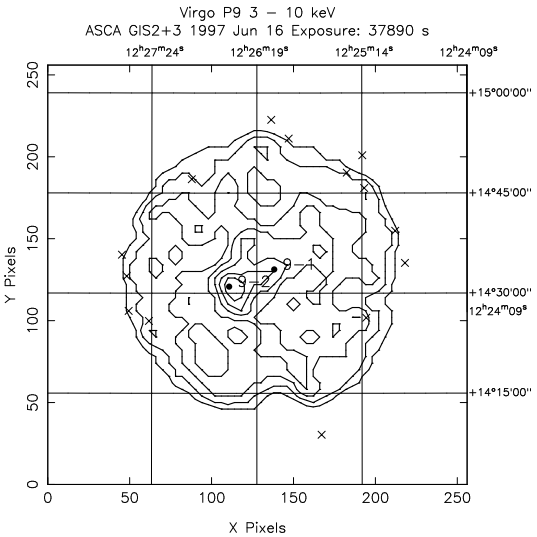
Virgo P9 3 – 10 keV
ASCA GIS2+3 1997 Jun 16 Exposure: 37890 s
12h27m24s
12h26m19s
12h25m14s
12h24m09s
+15°00'00"
+14°45'00"
+14°30'00"
+14°15'00"
Y Pixels
X Pixels

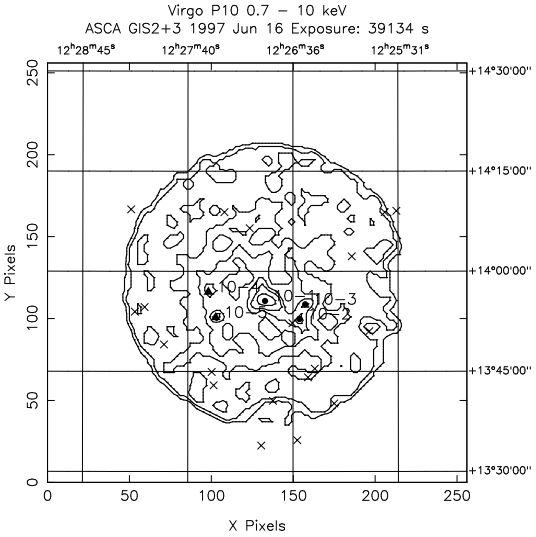
Virgo P10 0.7 – 10 keV
ASCA GIS2+3 1997 Jun 16 Exposure: 39134 s
12h28m45s
12h27m40s
12h26m36s
12h25m31s
+14°30'00"
+14°15'00"
+14°00'00"
+13°45'00"
+13°30'00"
Y Pixels
X Pixels

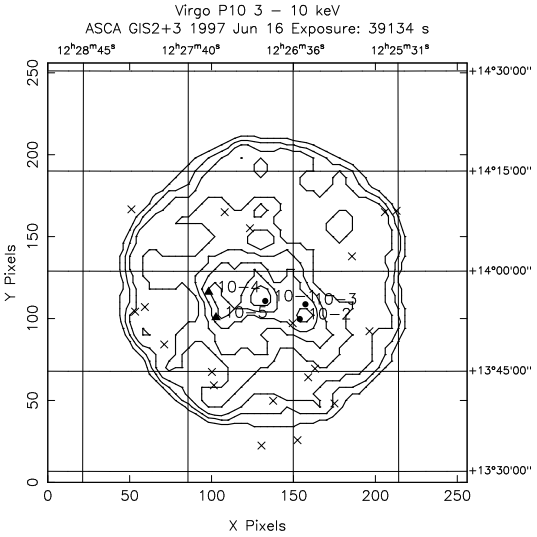
Virgo P10 3 – 10 keV
ASCA GIS2+3 1997 Jun 16 Exposure: 39134 s
12h28m45s
12h27m40s
12h26m36s
12h25m31s
+14°30'00"
+14°15'00"
+14°00'00"
+13°45'00"
+13°30'00"
Y Pixels
X Pixels

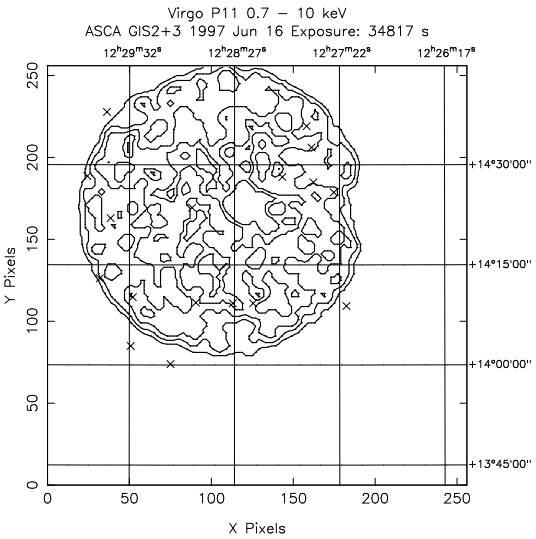
Virgo P11 0.7 – 10 keV
ASCA GIS2+3 1997 Jun 16 Exposure: 34817 s
12h29m32s
12h28m27s
12h27m22s
12h26m17s
+14°30'00"
+14°15'00"
+14°00'00"
+13°45'00"
Y Pixels
X Pixels

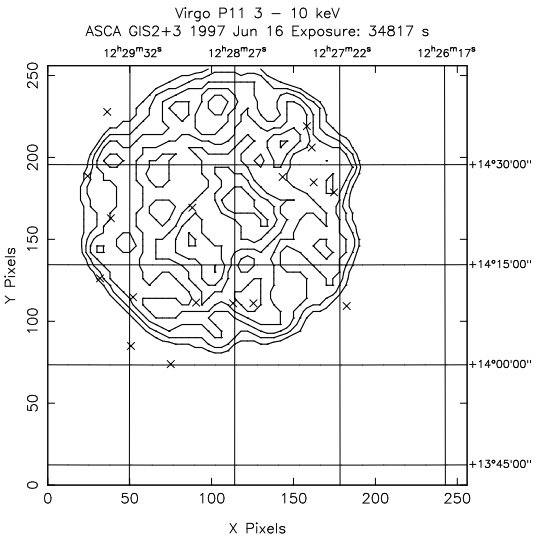
Virgo P11 3 – 10 keV
ASCA GIS2+3 1997 Jun 16 Exposure: 34817 s
12h29m32s
12h28m27s
12h27m22s
12h26m17s
+14°30'00"
+14°15'00"
+14°00'00"
+13°45'00"
Y Pixels
X Pixels

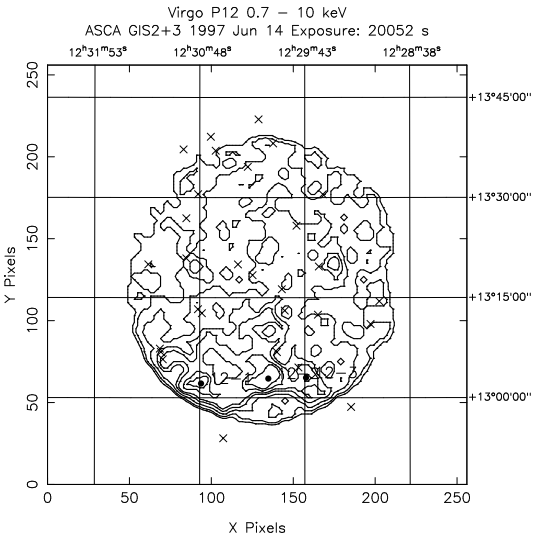
Virgo P12 0.7 – 10 keV
ASCA GIS2+3 1997 Jun 14 Exposure: 20052 s
12h31m53s
12h30m48s
12h29m43s
12h28m38s
+13°45'00"
+13°30'00"
+13°15'00"
+13°00'00"
Y Pixels
X Pixels

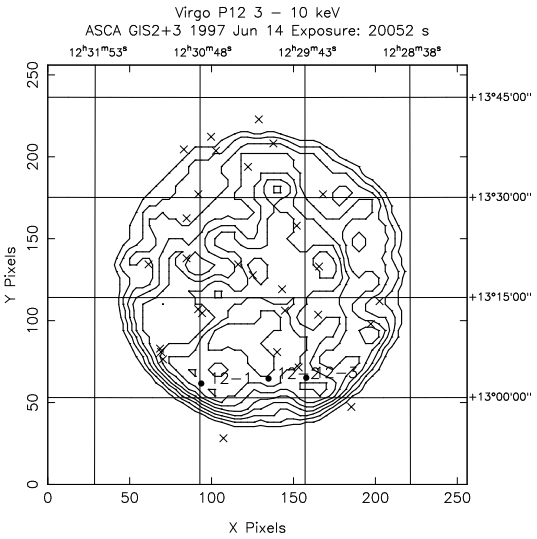
Virgo P12 3 – 10 keV
ASCA GIS2+3 1997 Jun 14 Exposure: 20052 s
12h31m53s
12h30m48s
12h29m43s
12h28m38s
+13°45'00"
+13°30'00"
+13°15'00"
+13°00'00"
Y Pixels
X Pixels

Appendix D

ASCA GIS spectra of the Virgo cluster

We show the GIS spectra of the Virgo mapping observations with the best-fit one-temperature RS model curves. We used the data of Jupiter, QSF3, and Lockman Hole as a background, which are shown in the left, middle, and right columns, respectively.

Figure D.1: ASCA GIS spectra of the Virgo cluster.

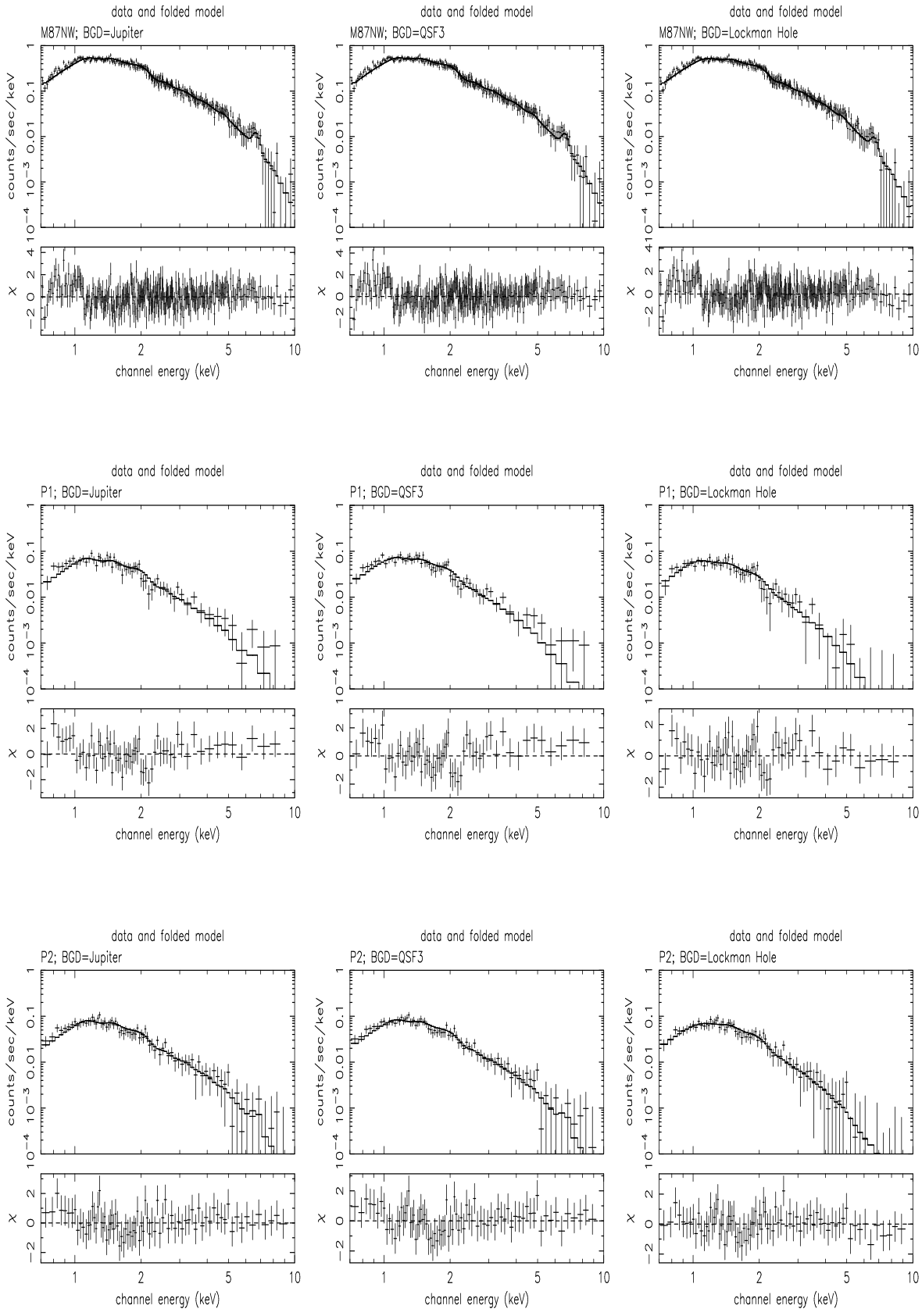

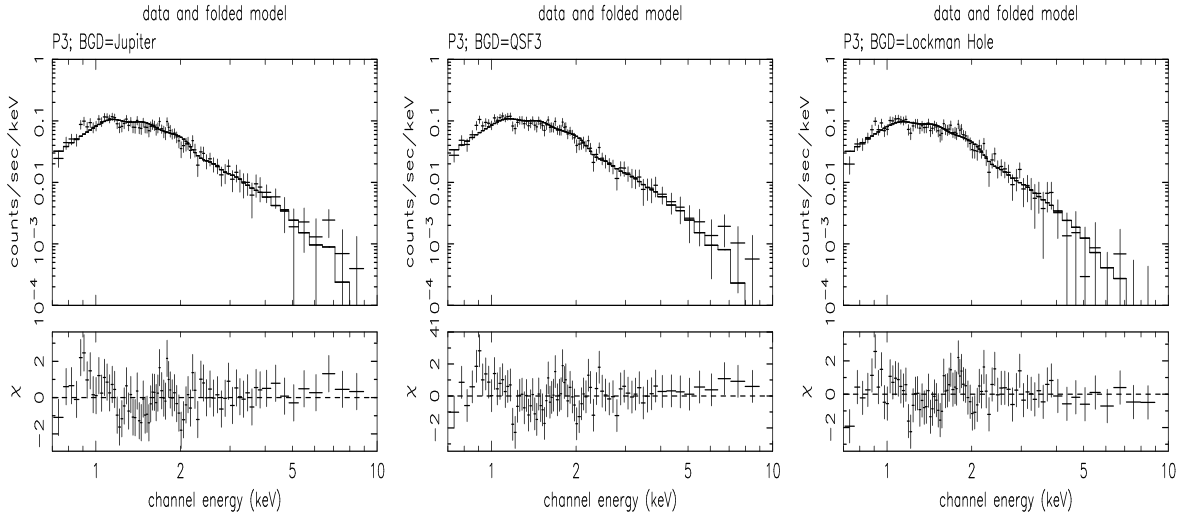
data and folded model
P3; BGD=Jupiter
counts/sec/keV
χ
channel energy (keV)

data and folded model
P3; BGD=QSF3
counts/sec/keV
χ
channel energy (keV)

data and folded model
P3; BGD=Lockman Hole
counts/sec/keV
χ
channel energy (keV)

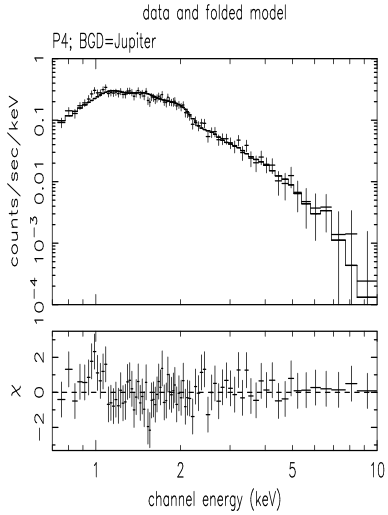
data and folded model
P4; BGD=Jupiter
counts/sec/keV
χ
channel energy (keV)

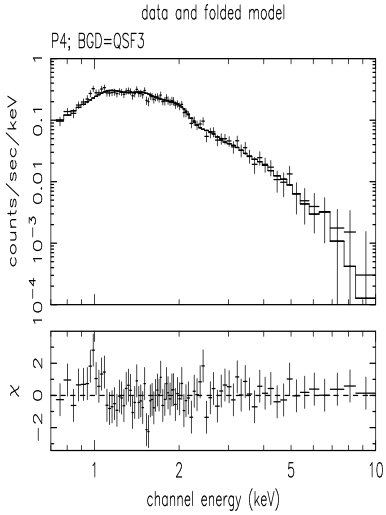
data and folded model
P4; BGD=QSF3
counts/sec/keV
χ
channel energy (keV)

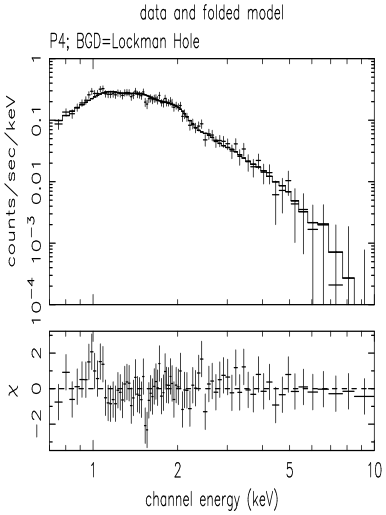
data and folded model
P4; BGD=Lockman Hole
counts/sec/keV
χ
channel energy (keV)

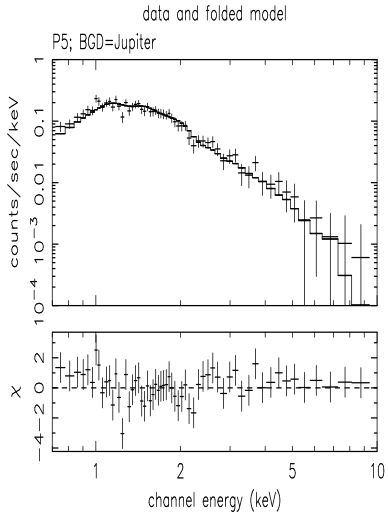
data and folded model
P5; BGD=Jupiter
counts/sec/keV
χ
channel energy (keV)

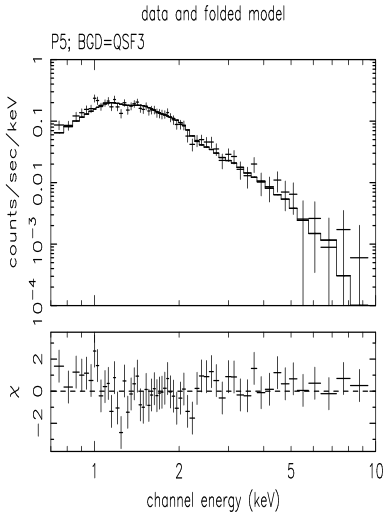
data and folded model
P5; BGD=QSF3
counts/sec/keV
χ
channel energy (keV)

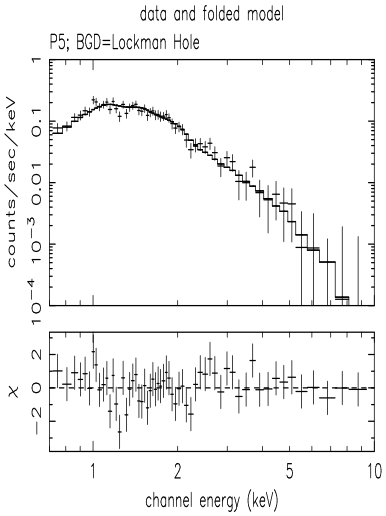
data and folded model
P5; BGD=Lockman Hole
counts/sec/keV
χ
channel energy (keV)

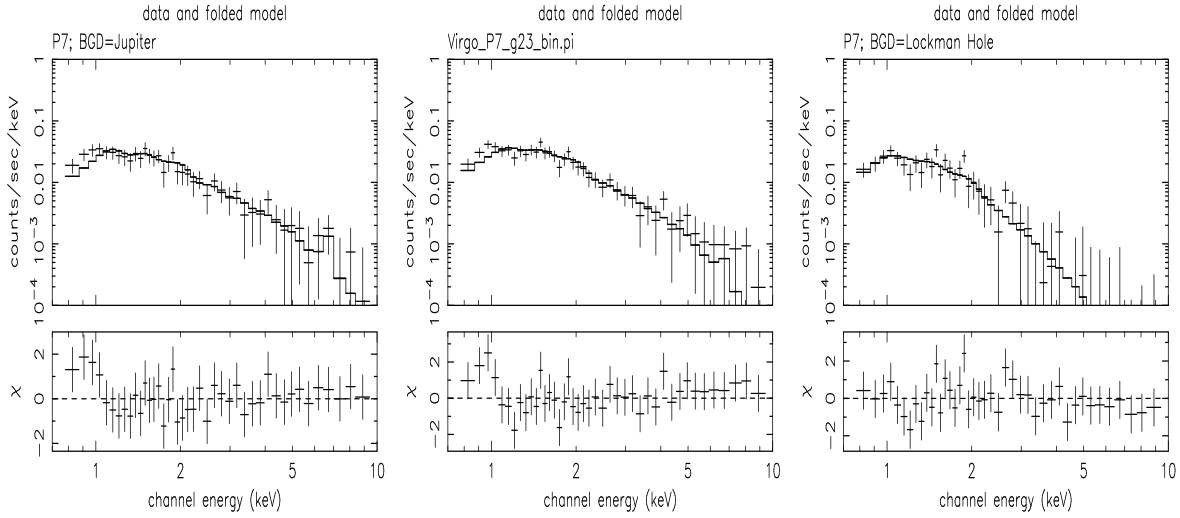
data and folded model
P7; BGD=Jupiter
data and folded model
Virgo_P7_g23_bin.pi
data and folded model
P7; BGD=Lockman Hole
counts/sec/keV
χ
channel energy (keV)

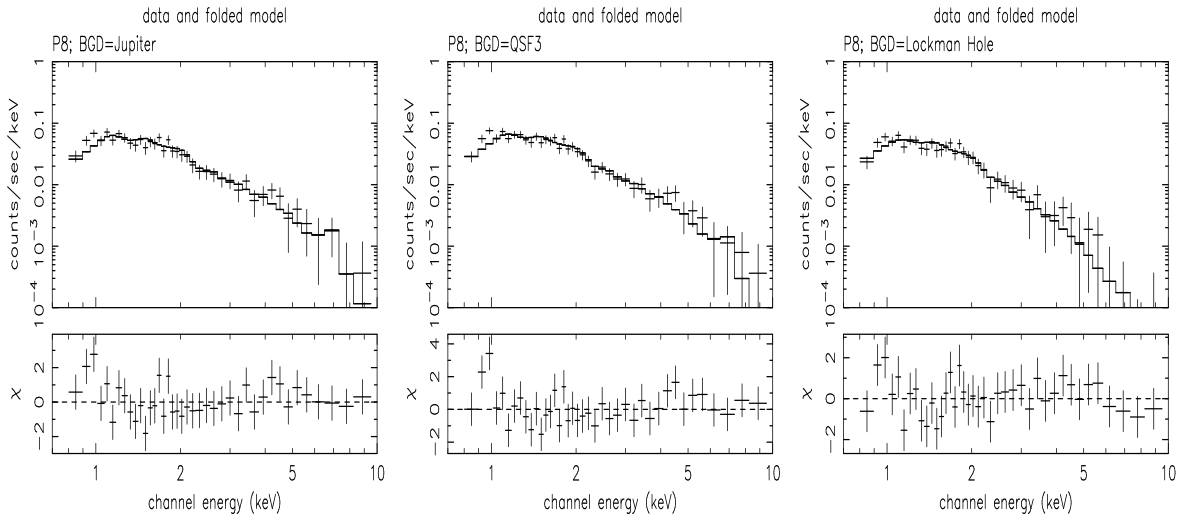
data and folded model
P8; BGD=Jupiter
data and folded model
P8; BGD=QSF3
data and folded model
P8; BGD=Lockman Hole
counts/sec/keV
χ
channel energy (keV)

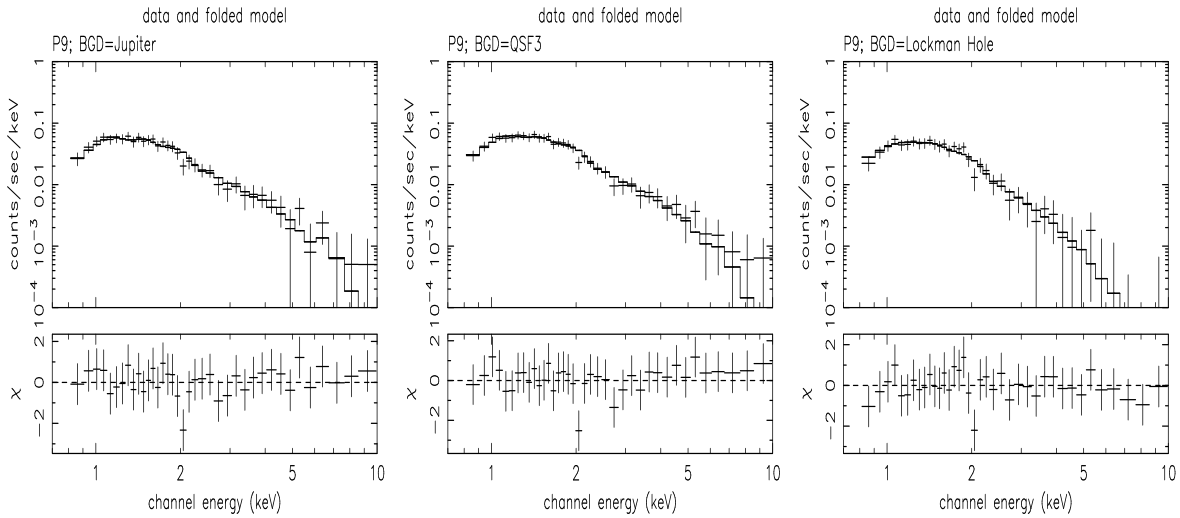
data and folded model
P9; BGD=Jupiter
data and folded model
P9; BGD=QSF3
data and folded model
P9; BGD=Lockman Hole
counts/sec/keV
χ
channel energy (keV)

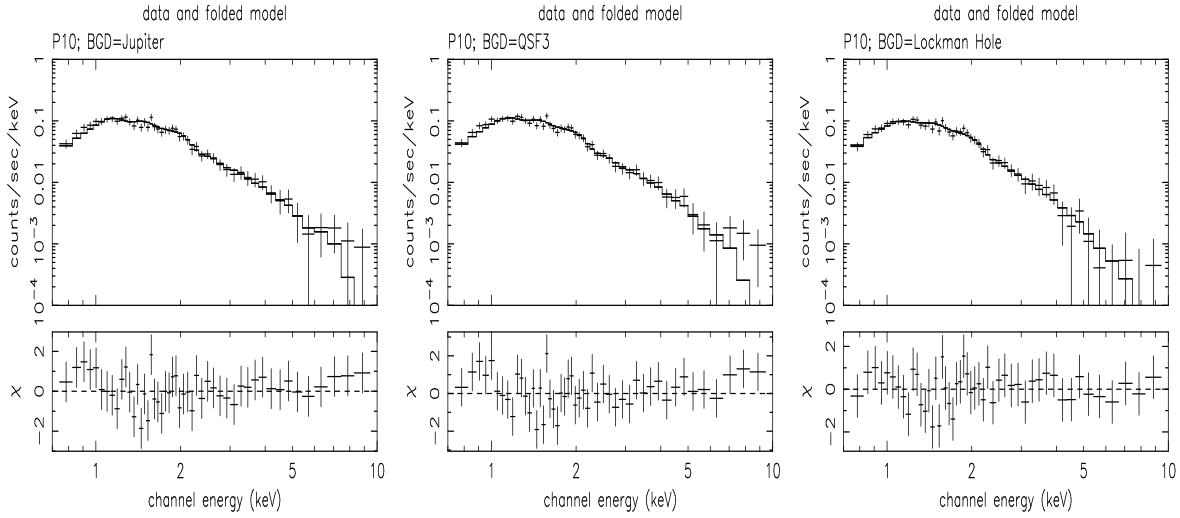
data and folded model
P10; BGD=Jupiter
counts/sec/keV
χ
channel energy (keV)

data and folded model
P10; BGD=QSF3
counts/sec/keV
χ
channel energy (keV)

data and folded model
P10; BGD=Lockman Hole
counts/sec/keV
χ
channel energy (keV)

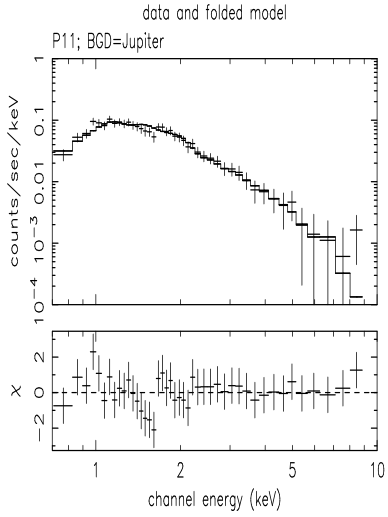
data and folded model
P11; BGD=Jupiter
counts/sec/keV
χ
channel energy (keV)

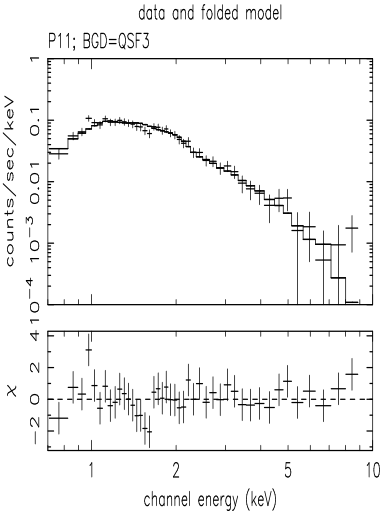
data and folded model
P11; BGD=QSF3
counts/sec/keV
χ
channel energy (keV)

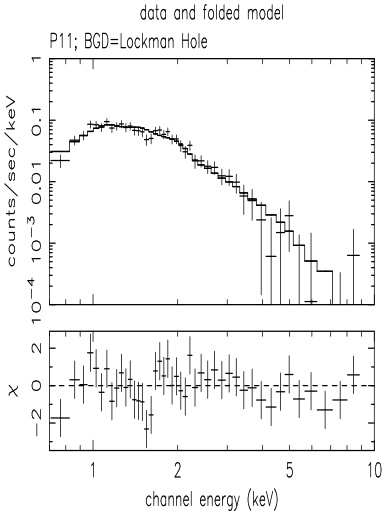
data and folded model
P11; BGD=Lockman Hole
counts/sec/keV
χ
channel energy (keV)

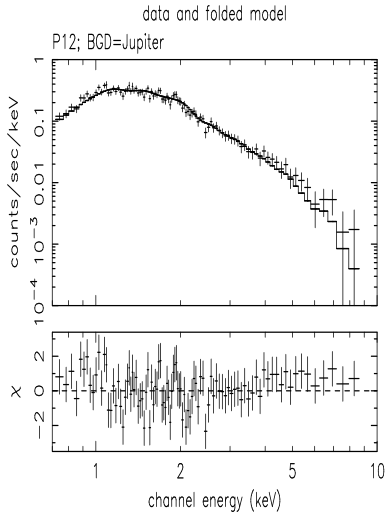
data and folded model
P12; BGD=Jupiter
counts/sec/keV
χ
channel energy (keV)

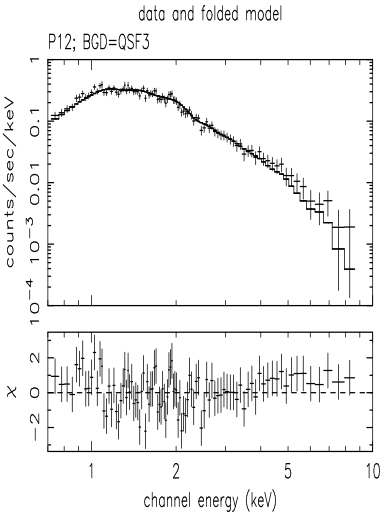
data and folded model
P12; BGD=QSF3
counts/sec/keV
χ
channel energy (keV)

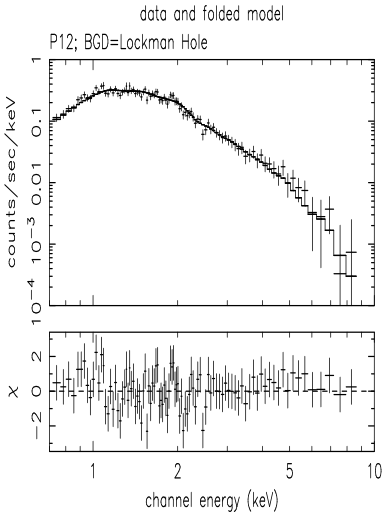
data and folded model
P12; BGD=Lockman Hole
counts/sec/keV
χ
channel energy (keV)

Appendix E

The Solar Abundance

Table E.1: The number ratios of various elements relative to Hydrogen, which are used as the Solar abundance ratios throughout this thesis. These are from Anders and Grevesse (1989).

H	1.00
He	9.77×10^{-2}
C	3.63×10^{-4}
N	1.12×10^{-4}
O	8.51×10^{-4}
Ne	1.23×10^{-4}
Na	2.14×10^{-6}
Mg	3.80×10^{-5}
Al	2.95×10^{-6}
Si	3.55×10^{-5}
S	1.62×10^{-5}
Cl	1.88×10^{-7}
Ar	3.63×10^{-6}
Ca	2.29×10^{-6}
Cr	4.84×10^{-7}
Fe	4.68×10^{-5}
Ni	1.78×10^{-6}
Co	8.60×10^{-8}

Bibliography

[1] Allen, C. W. 1973, in Astrophysical Quantities (3d ed.; London :Athlone), 30

[2] Anders, E., and Grevesse, N. 1989, Geochim. Cosmochim. Acta, 53, 197

[3] Arimoto, N., Matsushita, K., Ishimaru, Y., Ohashi, T. and Renzini, A. 1997, ApJ, 477, 128

[4] Arnaud, M., and Rothenflug, M. 1985, A&AS, 60, 425

[5] Arnaud, M., Rothenflug, M., Boulade, O., Vigroux, L., and Vangioni-Flam, E. 1992, A&A, 254, 49

[6] Audouze, J. and Israël, G. 1994, "The Cambridge Atlas of Astronomy", third edition, Cambridge University Press

[7] Awaki, H., Mushotzky, R. F., Tsuru, T., Fabian, A. C., Fukazawa, Y., Loewenstein, M., Makishima, K., Matsumoto, H. et al. 1994, PASJ, 46, L65

[8] Bahcall, J. N., and Sarazin, C. L., 1977, ApJ, 213, L99

[9] Bahcall, N. A., and Lubin, L. M. 1994, ApJ, 426, 513

[10] Batuski, D. J., Burns, J., Newberry, M. V., Hill, J. M., Deeg, H.-J., Laubscher, B. and Elston, R. J. 1991, AJ, 101, 1983

[11] Binggeli, B., 1992, in "The Astronomy and Astrophysics Encyclopedia", ed. Maran, S. P., Van Nostrand Reinhold, New York

[12] Binggeli, B., Sandage, A., and Tammann, G. A. 1985, AJ, 90, 1681

[13] Binggeli, B., Tammann, G. A., and Sandage, A. 1987, AJ, 94, 251

[14] Binggeli, B., Popescu, C. C., and Tammann, G. A. 1993, A&AS, 98, 275

[15] Biretta, J. A., Stern, C. P., and Harris, D. E. 1991, AJ, 101, 1632

[16] Böhringer, H., Briel, U. G., Schwartz, R. A., Voges, W., Hartner, G., and Trümper, J. 1994, Nature, 368, 828

[17] Böhringer, H., Nulsen, P. E. J., Braun, R., and Fabian, A. C. 1995, MNRAS, 274, L67

[18] Bower, S., Lieu, R., and Mittaz, J. 1997, preprint

[19] Bradt, H., Mayer, W., Naranan, S., Rappaport, S., and Spada, G. 1967, ApJ, 150, L199

[20] Burke, B. E., Mountain, R. W., Harrison, D. C., Bautz, M. W., Doty, J. P., Ticker, G. R., and Daniels, P. J. 1991, IEEE Trans. ED-38, 1069

[21] Byram, E. T., Chubb, T. A., and Friedman, H. 1966, Science, 152, 66

[22] Canizares, C. R., Clark, G. W., Markert, T. H., Berg, C. Smedira, M., Bardas, D., Schnopper, H., and Kalata, K. 1979, ApJ, 234, L33

[23] Canizares, C. R., Clark, G. W., Jernigan, J. G., and Markert, T. H. 1982, ApJ, 262, 33

[24] Castander, F. J., Bower, R. G., Ellis, R. S., Aragón-Sakamanca, A., Mason, K. O., Hasinger, G., McMahon, R. G., Carrera, F. J., Mittaz, J. P. D., Pérez-Fournon, I., and Lehto, H. J. 1995, Nature, 377, 39

[25] Ciotti, L., D'Ercole, A., Pellegrini, S., and Renzini, A. 1991, ApJ, 376, 380

[26] Collins, C. A., Burke, D. J., Romer, A. K., Sharples, R. M., and Nichol, R. C. 1997, ApJ, 479, L117

[27] David, L .P., Slyz, A., Jones, C., Forman, W., Vrtilek, S. D., and Arnaud, K. A. 1993, ApJ, 412, 479

[28] David, L. P., Jones, C., and Forman, W. 1996, ApJ, 473, 692

[29] Davis, D., Mulchaey, J., Mushotzky, R., amd Burstein, D. 1996, ApJ, 456, 80

[30] de Vaucouleurs, G., and Nieto, J.-L. 1978, ApJ, 220, 449

[31] de Vaucouleurs, G., de Vaucouleurs, A., Corwin, H. G., Jr., Buta, R. J., Paturel, G., and Fouqué, P. 1991, Third Reference Catalogue of Bright Galaxies (New York: Springer)

[32] Dotani, T., Mitsuda, K., Yamashita, A., Ezuka, H., Hayashida, K., Torii, K., Miura, N., Otani, C., Crew, G., Rasmussen, A., and Gendreau, K. 1996, ASCA News No. 4., p3 (ASCA Guest Observer Facility, NASA, Goddard Space Flight Center)

[33] Douglas, J. N., Bash, F., Bozyan, F. A., Torrence, G. W., and Wolfe, C. 1996, AJ, 111, 1945

[34] Ebeling, H., Edge, A. C., Fabian, A. C., Allen, S. W., and Crawford, C. S. 1997, ApJ, 479, L101

[35] Edge, A., and Stewart, G. 1991, MNRAS, 252, 428

[36] Edge, A. C., Stewart, G. C., and Smith, A. 1988, in "Hot Thin Plasmas in Astrophysics", ed. R. Pallavicini (Dordrecht: Kluwer)

[37] Eilek, J. A. 1992, in "The Astronomy and Astrophysics Encyclopedia", ed. Maran, S. P., Van Nostrand Reinhold, New York

[38] Ezawa, H., Fukazawa, Y., Makishima, K., Ohashi, T., Takahara, F., Xu, H., and Yamasaki, N. Y. 1997, ApJ, 490, L33

[39] Fabian, A. C. 1994, ARAA, 32, 277

[40] Fabian, A.C., Arnaud, K. A., Bautz, M. W., and Tawara, Y. 1994, ApJ, 436, L63

[41] Fabian, A. C. and Pringle, J. E. 1977, MNRAS, 181, *Short Communication*, 5p

[42] Fabbiano, G., Kim, D. -W., and Trinchieri, G. 1992, ApJS, 80, 531

[43] Fabricant, D., Lecar, M., and Gorenstein, P. 1980, ApJ, 241, 552

[44] Fabricant, D., and Gorenstein, P. 1983, ApJ, 267, 535

[45] Feigelson, E. D., Wood, P. A., Schreier, E. J., Harris, D. E., and Reid, M. J. 1987, ApJ, 312, 101

[46] Ford, H. C., Harms, R. J., Tsvetanov. Z. I., Hartig, G. F., Dressel. L. L., Kriss, G. A., Bohlin, R. C., Davidsen, A. F., Margon, B., and Kochhar, A. K. 1994, ApJ, 435, L27

[47] Forman, W., and Jones, C. 1982, ARAA, 20, 547

[48] Forman, W., Jones, C., and Tucker, W. 1985, ApJ, 293, 102

[49] Fukazawa, Y., Ohashi, T., Fabian, A. C., Canizares, C. R., Ikebe, Y., Makishima, K., Mushotzky, R. F., and Yamashita, K. 1994, PASJ, 46, L55

[50] Fukazawa, Y., Makishima, K., Matsushita, K., Yamasaki, N., Ohashi, T., Mushotzky, R. F., Sakima, Y., Tsusaka, Y., and Yamashita, K. 1996, PASJ, 48, 395

[51] Fukazawa, Y. 1997, Ph.D. thesis, the University of Tokyo

[52] Fukazawa, Y., Makishima, K., Tamura, T., Ezawa, H., Xu, H., Ikebe, Y., Kikuchi, K., and Ohashi, T. 1998, PASJ, 50, 187

[53] Fukugita, M., Okamura, S., and Yasuda, N. 1993, ApJ, 412, L13

[54] Galileo Galilei 1600, private communication

[55] Gehrels, N., and Williams, E. D. 1993, ApJ, L25

[56] Gioia, I. M., Henry, J. P., Maccacaro, T., Morris, S. L., Stocke, J. T., and Wolter, A. 1990, ApJ, 356, L35

[57] Giovanneli, R. and Haynes, M. P. 1983, AJ, 88, 881

[58] Gorenstein, P., Fabricant, D., Topka, K., Tucker, W., and Harnden, F. R. 1977, ApJ, 216, L95

[59] Gregory, P. C., and Condon, J. J. 1991, ApJS, 75, 1011

[60] Hanson, C. G., Skinner, G. K., Eyles, C. J., and Willmore, A. P. 1990, MNRAS, 242, 262

[61] Harms, R. J., Ford, H. C., Tsvetanov. Z. I., Hartig, G. F., Dressel. L. L., Kriss, G. A., Bohlin, R., Davidsen, A. F., Margon, B., and Kochhar, A. K. 1994, ApJ, 435, L35

[62] Harris, D. E., Biretta, J. A., and Junor, W. 1997, MNRAS, 284, L21

[63] Hatsukade, I. 1989, Ph.D. Thesis, Osaka University

[64] Hattori, M., Ikebe, Y., Takeshima, T., Mihara, T., Böringer, H., Asaoka, I., Schindler, S., Neumann, D., Tsuru, T., and Tamura, T. 1997, Nature, 388, 146

[65] Heiles, C. 1975, A&AS, 20, 37

[66] Henriksen, M. J., and Mushotzky, R. F. 1985, ApJ, 292, 441

[67] Henry, J. P., Gioia, I. M., Maccacaro, T., Morris, S. L., Stocke, J. T., and Wolter, A. 1992, ApJ, 386, 408

[68] Hewitt, A. and Burbidge, G. 1989, ApJS, 69, 1

[69] Honda, H., Hirayama, M., Watanabe, M., Kunieda, H., Tawara, Y., Yamashita, K., Ohashi, T., Hughes, J. P., and Henry, J. P. 1996, ApJ, 473, L71

[70] Hwang, U., Mushotzky, R. F., Loewenstein, M., Markert, T. H., Fukazawa, Y., and Matsumoto, H. 1997, ApJ, 476, 560

[71] Ikebe, Y. 1996, Ph.D. thesis, University of Tokyo

[72] Ikebe, Y., Ezawa, H., Fukazawa, Y., Hirayama, M., Ishisaki, Y., Kikuchi, K., Kubo, H., Makishima, K., Matsushita, K., Ohashi, T., Takahashi, T., and Tamura, T. 1996, Nature, 379, 427

[73] Ikebe, Y., Makishima, K., Ezawa, H., Fukazawa, Y., Mihara, M., Honda, H., Ishisaki, Y., Kikuchi, K., Kubo, H., Murakami, T., Ohashi, T., Takahashi, T. and Yamashita, K. 1997, ApJ, 481, 660

[74] Ishisaki, Y. 1996, Ph.D. thesis, University of Tokyo

[75] Ishisaki, Y., Ueda, Y., Kubo, H., Ikebe, Y., Makishima, K. and the GIS team 1997, ASCA News No. 5., p26 (ASCA Guest Observer Facility, NASA, Goddard Space Flight Center)

[76] Iwasawa, K., White, D. A., and Fabian, A. C. 1996, MNRAS submitted.

[77] Jones, C. and Forman, W., 1984, ApJ, 276, 38

[78] Kaastra, J. S. 1992, An X-Ray Spectral Code for Optically Thin Plasmas (Internal SRON-Leiden Report, updated version 2.0)

[79] Kent, S. M., and Sargent, W. L. W. 1983, AJ, 88, 697

[80] Kikuchi, K. 1997, private communication

[81] King, I. 1962, 67, 471

[82] Koyama, K., Takano, S., and Tawara, Y. 1991, Nature, 350, 135

[83] Lea, S. M., Mason, K. O., Reichert, G., Charles, P. A., and Riegler G. 1979, ApJ, 227, L67

[84] Lea, S. M., Mushotzky, R., and Holt, S. S. 1982, ApJ, 262, 24

[85] Lea, S. M., Reichert, G., Mushotzky, R. F., Baity, W. A., Gruber, D. E., Rothschild, R., and Primini, F. A. 1981, ApJ, 246, 369

[86] Liedahl, D. A., Osterheld, A. L., and Goldstein, A. L. 1995, ApJL, 438, 115

[87] Lieu, R., Mittaz, J. P. D., Bowyer, S., Breen, J. O., Murphy, E. M., Lockman, F. J., and Hwang, C. -W. 1996a, Science, 274, 1335

[88] Lieu, R., Mittaz, J. P. D., Bowyer, S., Lockman, F. J., Hwang, C. -W., and Schmitt, J. H. M. M. 1996b, ApJ, 458, L5

[89] Loewenstein, M., Mushotzky, R. F., Tamura, T., Ikebe, Y., Makishima, K., Matsushita, K., Awaki, H., and Serlemitsos, P. J. 1994, ApJ, 436, L75

[90] Loewenstein, M., and Mushotzky, R. F. 1996, ApJ, 466, 695

[91] Makishima, K., Tashiro, M., Ebisawa, K., Ezawa, H., Fukazawa, Y., Gunji, S., Hirayama, M., Idesawa, E. et al. 1996, PASJ, 48, 171

[92] Maline, R., Lampton, M., and Bowyer, S. 1976, ApJ, 209, 678

[93] Markevitch, M., Mushotzky, R., Inoue, H., Yamashita, K., Furuzawa, A., and Tawara, Y. 1996, ApJ, 456, 437

[94] Markevitch, M. L., Sarazin, C. L., and Irwin, J. A. 1996, ApJ, 472, L17

[95] Markevitch, M., Forman, W. R., Sarazin, C. L., and Vikhlinin, A. 1997, ApJ, submitted

[96] Masai, K. 1994, ApJ, 188, 335

[97] Mathews, W. G., and Bregman, J. N. 1978, ApJ, 233, 498

[98] Matsumoto, H., Koyama, K., Awaki, H., Tsuru, T., Loewenstein, M., and Matsushita, K. 1997, ApJ, 482, 133

[99] Matsushita, K., Makishima, K., Awaki, H., Canizares, C. R., Fabian, A. C., Fukazawa, Y., Loewenstein, M., Matsumoto, H. et al. 1994, ApJ, 436, L41

[100] Matsushita, K. 1997, Ph.D. Thesis, The University of Tokyo

[101] Matsushita, K., Makishima, K., Rokutanda, E., Yamasaki, N. Y., and Ohashi, T. 1997, ApJ, 488, L125

[102] Matsushita, K., Makishima, K., Ikebe, Y., Rokutanda, E., Yamasaki, N. Y., and Ohashi, T. 1998, ApJ, L13

[103] Merritt, D., and Tremblay, B. 1993, AJ, 106, 2229

[104] Metzler, C. A. and Evrard, A. E. 1994, ApJ, 437, 564

[105] Mewe, R., and Gronenschild, E. H. B. M. 1981, A&AS, 45, 11

[106] Mewe, R., Gronenschild, E. H. B. M., and van den Oord G. H. J. 1985, A&AS, 62, 197

[107] Mewe, R., Lemen, J. R., and van den Oord G. H. J. 1986, A&AS, 65, 511

[108] Mittaz, J. P. D., Lieu, R., and Lockman, F. J. 1997, preprint

[109] Miyata, E., Tsunemi, H., Pisarski, R., and Kissel, S. E. 1994, PASJ, L101

[110] Mould, J. R., Oke, J. B., De Zeeuw, P. T., and Nemec, J. M. 1990, AJ, 99, 1823

[111] Mushotzky, R. F., Serlemitsos, P. J., Smith, B. W., Boldt, E. A., and Holt, S. S. 1978, ApJ, 225, 21

[112] Mushotzky, R. F. 1984, Phys. Scr., T7, 157

[113] Mushotzky, R. F., and Szymkowiak, A. E. 1988, in "Cooling Flows and Galaxies," ed. Fabian, A. C. (Dordrecht: Kluwer), p53 – 62

[114] Mushotzky, R. F., Done, C., and Pounds, K. A. 1993, ARA&A 31, 717

[115] Mushotzky, R. F., Loewenstein, M., Awaki, H., Makishima, K., Matsushita, K., and Matsumoto, H. 1994, ApJ, 436, L41

[116] Mushotzky, R. F., and Loewenstein, M. 1997, ApJ, 481, L63

[117] Mushotzky, R. F., and Scharf, C. A. 1997, ApJ, 482, L13

[118] Mushotzky, R. F., Loewenstein, M., Arnaud, A., Tamura, T., Fukazawa, Y., Matsushita, K., Kikuchi, K., and Hatsukade, I. 1996, ApJ, 466, 686

[119] Nulsen, P. E. J., and Böhringer, H. 1995, MNRAS, 274, 1093

[120] Ohashi, T., Fukazawa, Y., Ikebe, Y., Ezawa, H., Tamura, T., and Makishima, K. 1994, in "New Horizon of X-Ray Astronomy", ed F. Makino, T. Ohashi (Universal Academy Press, Tokyo) p273

[121] Ohashi, T., Ebisawa, K., Fukazawa, Y., Hiyoshi, K., Horii, M., Ikebe, Y., Ikeda, H., Inoue, H. et al. 1996, PASJ, 48, 157

[122] Raymond, J. C., and Smith, B. W. 1977, ApJS, 35, 419

[123] Reisenegger, A., Miralda-Escudé, J. M., and Waxman, E. 1996, ApJL, 457, 11

[124] Rephaeli, Y. 1978, ApJ, 225, 335

[125] Reynolds, C. S. Matteo, T., Di, Fabian, A. C., Hwang, U., and Canizares, C. R. 1996, MNRAS, 283, L111

[126] Romer, A. K., Nichol, R. C., Collins, C. A., Burke, D. J., Holden, B. P., Metevier, A., Ulmer, M. P., and Pildis, R. 1997, preprint (astro-ph/9701233)

[127] Rothenflug, R., and Arnaud, M. 1985, A&A, 144, 431

[128] Rybicki, G. B., and Lightman, A. P. 1979, in "Radiative Processes in Astrophysics", Jone Wiley & Sons, Inc.

[129] Sarazin, C. L. 1986, Rev. Mod. Phys., 58, 1

[130] Sarazin, C. L., Wise, M. W., and Markevitch, M. L. 1997, ApJ, in press

[131] Sarazin, C. L., and Lieu, R. 1998, ApJ, 494, L177

[132] Sargent, W. L. W., Young, P. J., Boksenberg, A., Shortridge, K., Lynds, C. R., and Hartwick, F. D. A. 1978, ApJ, 221, 731

[133] Scharf, C. A., and Mushotzky, R. F. 1997, ApJ, 485, L65

[134] Scaharf, C. A., Jones, L. R., Perlman, E., Ebeling, H., Wegner, G., Malkan, M., and Horner, D. 1997, preprint (astro-ph/9702009)

[135] Schombert, J. M. 1986, ApJS, 60, 603

[136] Serlemitsos, P. J., Smith, B. W., Boldt, E. A., Holt, S. S., Swank, J. H. 1977, ApJ, 211, L63

[137] Serlemitsos, P. J., Jalota, L., Soong, Y., Kunieda, H., Tawara, Y., Tsusaka, Y., Suzuki, H., Sakima, Y. et al. 1995, PASJ, 47, 105

[138] Schreier, E. J., Gorenstein, P., and Feigelson, E. D. 1982, ApJ, 261, 42

[139] Spitzer, L. Jr. 1962, in "Physics of Fully Ionized Gases" (Interscience Publishers; a division of John Wiley & Sons, Inc.)

[140] Stewart, G. C., Canizares, C. R., Fabian, A. C., and Nulsen, P. E. J. 1984, ApJ, 278, 536

[141] Takahashi, T., Markevitch, M., Fukazawa, Y., Ikebe, Y., Ishisaki, Y., Kikuchi, K., Makishima, K., Tawara, Y., and ASCA Image analysis working group, 1995, ASCA News No. 3., p34 (ASCA Guest Observer Facility, NASA, Goddard Space Flight Center)

[142] Takano, S., Awaki, H., Koayama, K., Kunieda, H., Tawara, Y., Yamauchi, S., Makishima, K., and Ohashi, T. 1989, Nature, 340, 289

[143] Takano, S. 1990, Ph.D. Thesis, The University of Tokyo

[144] Takano, S., and Koyama, K. 1991, PASJ, 43, 1

[145] Tammann, G. A. 1988, in "The Extragalactic Distance Scale", APS conference series vol. 4, ed. S. van den Bergh and J. Pritchet, p282

[146] Tamura, T., Day, C. S., Fukazawa, Y., Hatsukade, I., Ikebe, Y., Makishima, K., Mushotzky, R. F., Ohashi, T., Takenaka, K., and Yamashita, K. 1996, PASJ, 48, 671

[147] Tanaka, Y., Inoue, H., and Holt, S. S. 1994, PASJ, 46, L37

[148] Tomida, H., Matsumoto, H., Ozaki, M., Tazawa, Y., Awaki, H., Tsuru, T., Koyama, K., Tsunemi, H. and Yamamoto, K 1997, PASJ, 49, 405

[149] Tsai, J. C. 1993, ApJ, 413, L59

[150] Tsai, J. C. 1994, ApJ, 423, 143

[151] Tsai, J. C. 1994b, ApJ, 429, 119

[152] Tsujimoto, T., Nomoto, K., Yoshii, Y., Hashimoto, M., Yanagida, S., Thielemann, F. -K. 1995, MNRAS, 277, 945

[153] Tsuru, T. 1993, Ph.D. Thesis, University of Tokyo

[154] Tsuru, T., Koyama, K., Hughes, J. P., Arimoto, N., Kii, T., and Hattori, M. 1997a, in "X-ray imaging and spectroscopy of cosmic hot plasmas", ed. Makino, F. and Mitsuda, K. (Universal Academy Press, Inc.: Tokyo, Japan)

[155] Tsuru, T., Matsumoto, H., Koyama, K., Tomida, H., Fukazawam Y., Hattori, M., and Hughes, J. P. 1997b, preprint

[156] Ueda, Y. 1996, Ph.D. thesis, 1996

[157] Vikhlinin, A., McNamara, B. R., Forman, W., Jones, C., Quintana, H., and Hornstrup, A. 1998, ApJ, 498, L21

[158] White, D. A., Fabian, A. C., Johnstone, R. M., Mushotzky, R. F., and Arnaud, K. A. 1991, MNRAS 252, 72

[159] Xu, H., Ezawa, H., Fukazawa, Y., Kikuchi, K., Makishima, K., Ohashi, T., and Tamura, T. 1997, PASJ, 49, 9

[160] Yamashita, A. 1995, Master Thesis, The University of Tokyo (in Japanese)

[161] Yamashita, K. 1992, in "Frontiers of X-ray Astronomy", ed. Tanaka, Y. and Koyama, K. (Tokyo: Universal Academy Press)

[162] Yasuda, N., Fukugita, M., and Okamura, S. 1997, ApJS, 108, 417

Acknowledgment

I am grateful to Prof. K. Koyama for his support and guidance throughout my graduate school period for five years. I am also grateful to Dr. Awaki and Dr. Tsuru, who have continuously supported and encouraged me. I thank the other staff of the cosmic-ray laboratory in Kyoto University, Prof. T. Maihara, Dr. Y. Tazawa, and Dr. F. Iwamuro.

I also express my thank to Prof. T. Ohashi, who planned the mapping observation of the Virgo cluster and allow me to use the data. I am also grateful to Mr. K. Kikuchi who kindly teach me the way to use the software and present me the figures, and Dr. Y. Ishisaki who allow me to analyze his data.

I wish to thank all my colleagues and friends, particularly to Dr. S. Ueno, Dr. H. Sogawa, Dr. M. Ozaki, Dr. I. Hayashi, Dr. Y. Maeda, Dr. M. Imanishi, Mr. H. Tomida, Ms. Y. Tsuboi, Mr. H. Terada, Mr. M. Sakano, Mr. K. Motohara, Ms. M. Goto, Mr. K. Hamaguchi, Ms. M. Nishiuchi, Mr. J. Iwai, Mr. H. Murakami, Mr. J. Yokogawa, and Mr. H. Tanabe.

I would like to thank all of the members of the ASCA team and duty scientists whose efforts made these observations and data analysis possible.

This work was supported by the grants for JSPS Research Fellowships for Young Scientists.

I thank my family for encouraging and supporting me. Finally I dedicate this thesis to the memory of my father.